Doctoral theses at NTNU, 2022:347

Aleksander Sendrowicz

Investigation and modelling of plastic deformation aided by in situ monitoring techniques

Doctoral thesis

NTNU
Norwegian University of Science and Technology
Thesis for the Degree of Philosophiae Doctor
Faculty of Engineering
Department of Mechanical and Industrial Engineering

NTNU
Norwegian University of Science and Technology

Aleksander Sendrowicz

Investigation and modelling of plastic deformation aided by in situ monitoring techniques

Thesis for the Degree of Philosophiae Doctor

Trondheim, November 2022

Norwegian University of Science and Technology
Faculty of Engineering
Department of Mechanical and Industrial Engineering

NTNU
Norwegian University of
Science and Technology

NTNU
Norwegian University of Science and Technology

Thesis for the Degree of Philosophiae Doctor

Faculty of Engineering
Department of Mechanical and Industrial Engineering

ISBN 978-82-326-6591-4 (printed ver.)
ISBN 978-82-326-6272-2 (electronic ver.)
ISSN 1503-8181 (printed ver.)
ISSN 2703-8084 (online ver.)

Doctoral theses at NTNU, 2022:347

Printed by NTNU Grafisk senter

Preface

This PhD work was sponsored by Norwegian University of Science and Technology, Department of Mechanical and Industrial Engineering, and supported by SINTEF industry through their laboratory facilities and services. The project was supervised by Professor Alexei Vinogradov, and Professor Filippo Berto.

The initial experimental work, was to investigate fatigue crack growth through three in situ methods, infrared thermography, optical imaging combined with digital image correlation, and acoustic emission. The work was expanded and converted into a PhD project, motivated by understanding material damage, fatigue behaviour and plastic deformation, through intrinsic variables.

Acknowledgements

This project would not have been possible without its creator, Professor Alexei Vinogradov. His knowledge, curiosity and kindness convinced me to join this work. Without his support and contribution, this project would not succeed. The final outcome is the result of countless hours of discussions, collaboration, and supervision from his side. I will never be able to describe my appreciation for his help, and will always be grateful for his motivational guidance during this challenging time. Thank You!

Next, I would like to recognise the invaluable assistance of SINTEF staff, especially Antonio Alvaro and Tore Andre Kristensen, for access to their laboratory facilities, equipment, technical support during experimental work, and especially for their help in manufacturing equipment and specimen.

I am also very grateful to my co-supervisor, Professor Filippo Berto, for the support and guidance he provided, and especially for his help regarding the use of university laboratories.

A special thanks goes to my colleagme, Aleksander Omholt Myhre, for spending enormous amounts of time in the laboratories and performing the experimental work with me. Solving problems related to acoustic emission allowed us to collect good data sets used in this work.

Further, I would like to acknowledge the help provided by Berit Vinje Kramer in specimen preparation, and for being a role model regarding helping other students and employees. Thanks to Professor Roy Johnsen for providing the Inconel 625 alloy, and Wieland Werke AG (Germany) for providing the CuZn alloys.

I am extremely grateful to my family and friends, especially Magdalena Elnes for the release of oxytocin and other neurotransmitters when I needed it. My parents, Beata and Janusz Sendrowicz, for taking the life choices and hard work needed for providing a proper environment for the early development of my neural network, and doing their best answering my questions.

Finally, I have to thank my sister, Sabina Sendrowicz, for choosing a relatively prestigious career as a physician, and therefore motivating me to pursue a PhD in order to become a real Doctor.

Abstract

A synergy from three modern in situ techniques - infrared thermography, digital image correlation, and acoustic emission - used concurrently has been obtained to gain deeper insight into deformation kinetics and energy partitioning in monotonic tensile tests performed on various representative structural materials. Multiple experimental challenges have been addressed, and the specific methodological procedures developed to mitigate them are described in great detail. The original experimental setup designed in the present work is used to unite a wealth of data acquired to meet the above stated objective. Integrated in the experimental design, a thermodynamic modelling methodology is presented, based on the first law of thermodynamics and informed by the dislocation evolution theory inspired by the classic Kocks and Mecking formalism. The advantage of the model is that only physically motivated variables are used, and the outcome, a successful prediction of energy partitioning in materials with dislocation mediated plasticity in monotonic deformation. On the basis of the unifying thermodynamic principles and the first-order dislocation kinetics, interlinked models are proposed for the energy storage as well as dissipation in the form of heat and acoustic emission. The model strategy is verified using austenitic 316L stainless steel and a set of CuZn alloys with varying Zn content and stacking fault energies, controlling dislocation mobility. The combination of infrared thermography and acoustic emission is used to characterise the evolution of dislocation ensembles through the developed model link providing direct access to the fundamental properties of dislocation kinetics. The factors controlling the dislocation production and dynamic recovery rates in the strain hardening process, are recovered for the first time from the model-based acoustic emission, and infrared thermography analyses respectively. Consequently, the developed toolset can be used as a powerful means for prediction of the strain hardening behaviour and quantitative evaluation of the dislocation kinetics in situ.

Contents

List of Figures

List of Abbreviations

AE	Acoustic Emission. 5, 6, 17–24, 26–29
ASKC	Adaptive Sequential k-means Clustering. 18, 20–22
DFT	Discrete Fourier Transform. 18–20
DIC	Digital Image Correlation. 5, 7, 8, 10–12, 24, 27
FCG	Fatigue Crack Growth. 29
FFT	Fast Fourier Transform. 20, 22
IRT	Infrared Thermography. 5, 6, 11–13, 24, 26–28
KM	Kocks & Mecking. 26, 28
PLC	Portevin–Le Chatelier. 3, 4
PSD	Power Spectral Density. 18, 20–22
ROI	Region Of Interest. 8, 10, 13, 24

List of Symbols

Sign	Description	Unit
B_λ	Spectral radiance	$\mathrm{W\,sr^{-1}\,m^{-3}}$
E_s	Stored energy density	$\mathrm{J\,m^{-3}}$
G	Shear modulus	MPa
H	Gauge length	mm
N	Number of sampled points	–
P_d	Dissipation power density	$\mathrm{W\,m^{-3}}$
P_e	Expansion power density	$\mathrm{W\,m^{-3}}$
P_s	Storage power density	$\mathrm{W\,m^{-3}}$
Q	Heat energy released by a thermodynamic system	J
T_{body}	Temperature of the body	K
T_{ds}	Time duration of a data segment	s
T_{sample}	Sampling interval	s
T_s	Temperature of the surroundings	K
T	Temperature	K
U	Internal energy of a thermodynamic system	J
W	Work done on a thermodynamic system	J
Φ	Heat flux	$\mathrm{W\,m^{-2}}$
α_T	Coefficient of linear thermal expansion	$\mathrm{K^{-1}}$
α	Strain rate sensitivity	–
$\dot{q}_{CD}$	Heat flow due to conduction	$\mathrm{W\,m^{-3}}$
$\dot{q}_{CV}$	Heat flow due to convection	$\mathrm{W\,m^{-2}}$
$\dot{q}_{RD}$	Heat flow due to radiation	$\mathrm{W\,m^{-2}}$
$\dot{q}_{TE}$	Energy change due to thermoelasticity	$\mathrm{W\,m^{-3}}$
$\dot{q}_d$	Heat production power density	$\mathrm{W\,m^{-3}}$
ϵ_{body}	Emissivity function	–
λ	Wavelength	m
ρ_0	Initial dislocation density	$\mathrm{m^{-2}}$

Sign	Description	Unit
ρ_{mat}	Density	$\mathrm{kg\,m^{-3}}$
ρ	Dislocation density	$\mathrm{m^{-2}}$
σ_I	Initial stress	MPa
σ_{SB}	Stefan-Boltzmann constant	$\mathrm{W\,m^{-2}\,K^{-4}}$
σ	Stress	MPa
ε	Strain	–
b	Magnitude of Burger's vector	nm
c_p	Specific heat capacity	$\mathrm{J\,kg^{-1}\,K^{-1}}$
c	Speed of light	$\mathrm{m\,s^{-1}}$
f_{m_h}	Frequency of a harmonic number	Hz
$f_{resolution}$	Frequency resolution	Hz
f_{sample}	Sampling frequency	Hz
h_c	Heat transfer coefficient	$\mathrm{W\,m^{-2}\,K^{-1}}$
h	Planck constant	$\mathrm{J\,Hz^{-1}}$
k_1	Rate of dislocation production	–
k_2	Rate of dislocation dynamic recovery	–
k_B	Boltzmann constant	$\mathrm{J\,K^{-1}}$
k	Thermal conductivity	$\mathrm{W\,m^{-1}\,K^{-1}}$
m_h	Harmonic number	–
s	First stress invariant	MPa
t	Time	s
$\mathbf{D}$	Rate of deformation	–
$\boldsymbol{\sigma}$	Cauchy stress tensor	MPa

Part I

1 Introduction

Plastic deformation is the permanent distortion occurring in a material when the local stresses exceed the material's yield strength [1]. Structural distortions are associated with the persistent defects of the crystal lattice, generated and stored in the course of plastic deformation. Plastic deformation of metals is a physical process that is inherently irreversible, spatially inhomogeneous, and temporally intermittent in nature due to a discrete origin of crystallographic slip caused by linear lattice defects - dislocations having long-range stress fields [2–8]. The discreteness of dislocation processes is known as the root cause of local fluctuations in stress and strain. However, a typical experimentally recorded stress–strain curve appears to be smooth (at least for pure metals) within the accuracy of modern equipment. It is because a global stress-strain curve is a result of averaging over deforming volume and time and as such it does not reveal the intermittency of the plastic flow - unless macroscopic plastic instabilities manifest themselves through spatiotemporal strain patterns, such as Lüders bands or Portevin–Le Chatelier (PLC) bands [9–11]. A classical explanation of the deformation behaviour of metals is based on the assumption of uncorrelated uniform motion of independent dislocation segments or dislocation loops. This concept can be challenged in light of the current understanding of the complexity associated with the behaviour of dislocations and their interactions with themselves and other crystal lattice defects at various length scales [4–8]. The complexity bears its origin from long-range elastic stress fields of dislocations, which decay as an inverse of the distance from the dislocation line, as well as short-range nonlinear dislocation-dislocation interactions [2, 3]. A further degree of complexity is associated with the fact that plastic flow of a deforming crystal is a dissipative and non-equilibrium process driven by external stresses. This process gives rise to self-organisation of dislocation ensembles into distinct patterns at different length scales, with considerable spatial and temporal variation in the dislocation density. A crystal containing lattice dislocations is not in thermal equilibrium due to

self-energy of dislocations. Furthermore, a large fraction of the mechanical work expended to generate dislocations and induce their motion to ensure plastic deformation is dissipated as heat. This indicates that plasticity is a highly irreversible dissipative process and that the resulting dislocation arrangements are far from equilibrium.

Dislocations are produced in the crystals under load by a variety of generating processes, of which the Frank-Reed mechanism, the dislocation nucleation at the grain boundaries, climb and cross-slip (double cross-slip) are to be mentioned first. The accumulation and interactions of dislocations cause strain hardening [12]. Depending on the magnitude of plastic deformation, dislocation patterning occurs on various scales. This process is strongly affected by high dislocation mobility, which is, in turn, controlled by the stacking fault energy [13]. When the materials are short in active slip systems, e.g., hcp metals such as Mg, Zn, Ti, etc., or when the mobility of dislocations is limited, e.g., in the materials with the low stacking fault energy, the alternative deformation mechanisms such as twinning or the formation of stacking faults and phase transformations may occur [14]. These mechanisms complicate the deformation process substantially and therefore they are outside of the scope of the present work, which is confined to the basic dislocation mechanisms.

The increase in dislocation density contributes to energy storage, though it is only a small fraction of the total energy expended during deformation as most of it is converted into heat due to dislocation annihilation in the bulk or at the free surface [15–18]. Energy can be stored in this system in a variety of ways, however, the first law of thermodynamics, axiomatically states that an increment of work δW done on a system, increases its internal energy dU, and in case of a non-adiabatic process causes a heat transfer δQ from the system to the reservoir:

$$\delta W = dU + \delta Q \tag{1.1}$$

To be able to better understand strain hardening, plastic instabilities such as macroscopic necking, local Lüders bands, the PLC effect, or fatigue strength, it is critical to understand the mechanisms governing plastic deformation. The present work focuses on the in situ investigation of plastic deformation mediated by dislocation processes - nucleation, motion and annihilation, which collectively govern the heat dissipation and energy storage in the deforming materials. In order to investigate the plastic activity from a thermodynamics point of view, a rate blend of contemporary experimental methods

has been chosen for the present study; these methods include Digital Image Correlation (DIC), Infrared Thermography (IRT), and Acoustic Emission (AE), which are complemented by characterisation of the grain structure and dislocation arrangement.

Although the main results of the present work will be illustrated for monotonic uni-axial deformation of various structural materials, the developed methodology based on the synchronised use of the above-mentioned techniques can be applied to cyclic deformation and fatigue crack growth investigations.

The main objective of this work is to gain deeper insight into the mechanisms governing plastic deformation, based on the intrinsic properties of the material. Our microstructurally-informed approach is motivated by the desire to predict a material's mechanical response from its fundamental properties. A side goal vital in doing so is to develop a practical toolbox that enables investigating these properties in a non-destructive in situ approach.

Article I focuses on the methodology. It describes all the methods used in great detail sufficient for reproduction. A few experimental aspects missed in that article are elaborated in chapter 2. This includes the estimates the heat transfer mechanisms other than conductivity: namely convection and radiation. Besides, the effect of AE processing software settings on the results are briefly outlined along with basic recommendations for these settings. The article addresses several challenges that might be encountered when using the methods individually, or in combination, and considers good practices based on our first hand experience.

Article II endeavours to propose a phenomenological thermodynamic modelling methodology inspired and informed by the dislocation evolution theory, and corroborates it with experimental measurements based on methodology from article I. The results show very good agreement between the two, and give new insight into mechanical energy partitioning influenced by dislocation reactions during plastic flow. The proposed modelling strategy and the obtained results serve as a basis for the next article.

Article III bridges the thermodynamic and dislocation kinetics models developed in article II with the phenomenological dislocation-based AE model. Thus, this work "closes the loop" by unifying the single internal variable strain hardening theory with the acoustic emission and heat dissipation analytical models. For the first time, this permitted us to obtain the kinetic parameters governing the evolution of the total dislocation density and

the overall strain hardening behaviour from two independent experimental methods, IRT and AE, yielding the results comparable to what is conventionally obtained from the model approximations of the stress-strain curves.

2 Methodology

A detailed description of the most essential aspects of the methodology developed in the present work is provided in article I. Some considerations, which were omitted there for brevity and which are deemed important for practicality, are elaborated in this chapter.

2.1 Digital image correlation

The DIC technique utilises images recorded by imaging systems, usually optical cameras, for software tracking procedures. The intention is to accurately measure changes occurring in images due to deformation of an object of interest. 2D and 3D DIC systems can be distinguished. 2D systems utilise a single camera, and measure in plane motion and deformation of planar objects. 3D systems require stereoscopic vision, the knowledge of the placement and orientation of the cameras, and their fields of view, allows to track a point in 3D space, and the requirement for planar objects is no longer necessary. Independent of the system used, the goal is to provide displacement and strain fields. There are two major approaches when it comes to obtaining deformation data, a local, subset based approach [19, 20], and a global finite element one [21]. This work focuses on 2D subset based DIC, as it is sufficient for the current work, and it has some advantages over finite element based algorithms [22], an appreciated, well performing [20] open source software developed by Blaber *et al.* [19] is also freely available.

When acquiring images, the temporal resolution, or frame rate, is limited by the sensors acquisition rate, and is related to some other key parameters, namely exposure time, aperture, and illumination. To achieve a satisfactory sensor filling, exposure time must be long enough to ensure sufficient light passing through the optics and aperture during acquisition [23], but should be limited by the speed of the recorded object to avoid motion blur. In other words, the motion of the object during acquisition, should be small compared to the spatial resolution of the system. In high speed imaging

systems, capable of achieving frame rates in the order of $1 \times 10^6\,\mathrm{s}^{-1}$ [24], illumination is often the limiting factor [25]. In case of out of plane motion, it is also important to have sufficient depth of field, which relies on the focal length, aperture, distance to object and more. An fully open aperture, allows more light to reach the sensor, therefore allowing for a shorter exposure time, but it reduces the depth of field, which might in some cases be problematic.

Spatial resolution depends on the whole imaging system [26], however, in case of optical DIC systems it is often determined by the pixel size and reproduction ratio of the lens. The resolution obtained from DIC analysis is however not the same as the resolution of the imaging system. Many factors will affect the resolution and precision of DIC measurements, algorithm used [22], pattern applied to the surface [27–30], subset size [31], order of shape function for subsets [32], and lens distortion [33] to mention some.

The principle behind the analysis is following. The Region Of Interest (ROI) is partitioned into small regions, each with their own image coordinates, these are called subsets. The software compares two images at a time, and the first task is to find approximately the same point in the two images, called a *seed*, an example of a seed is illustrated in fig. 2.1(a), and the belonging subsets of the reference image and the deformed image in figs. 2.1(b) and 2.1(c). Thus, a stochastic, high contrast pattern on the surface throughout the entire test is beneficial to obtain a unique, high correlation. The subset belonging to the seed (fig. 2.1(e)), will then be transformed through a shape function, which should have a sufficient degree to describe the deformation occurring within the subset. Since a subset is consisting of discrete pixels, the data must be interpolated in order to compare an undeformed subset, to a deformed, transformed subset. This is often achieved by the use of splines. This permits to compare the two subsets (figs. 2.1(d) and 2.1(e)) through a correlation criterion. Subsequently the deformation vector is modified in an iterative process to achieve better correlation, thus causing DIC to principally be an iterative optimisation problem. Once a sufficient correlation is found for a subset, its deformation vector is used as an initial guess for the neighbouring subset, and the process is repeated until the whole ROI has been processed. This way the position of each subset can be tracked.

The difference in coordinates between the subsets in sequential images is used as the displacement field given in image coordinates, as a function of time. These coordinates are further transformed to world coordinates, a process that translates the displacement from units of pixels to a measure of length, and which accounts for various distortions, e.g., lens distortion.

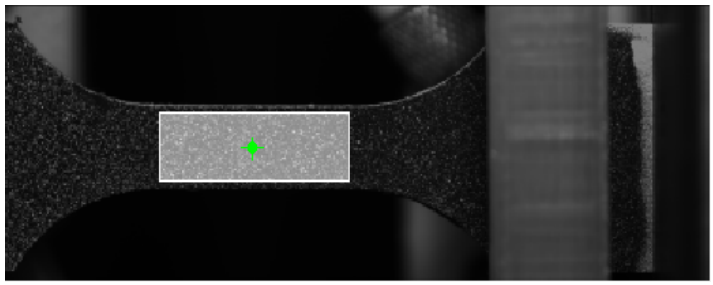

(a) ROI and seed

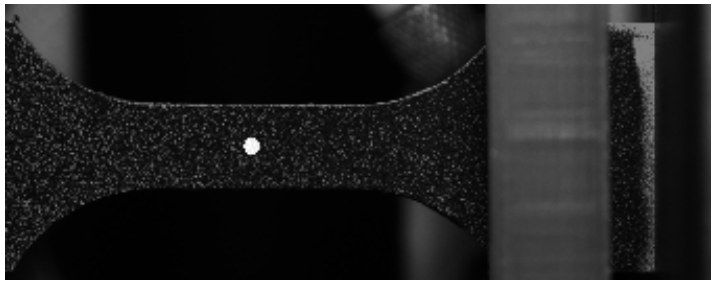

(b) Seed in undeformed image

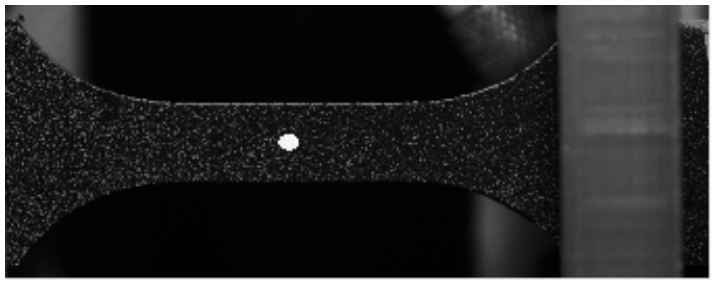

(c) Seed in deformed image

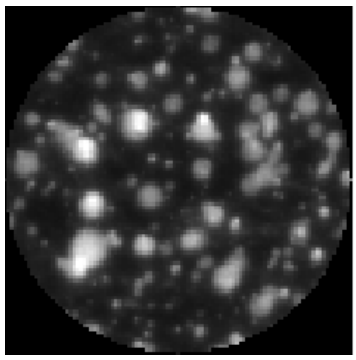

(d) Reference seed

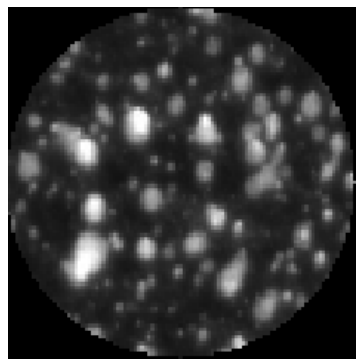

(e) Transformed deformed seed

Figure 2.1: DIC processing

The result is a global displacement field.

The previously mentioned open source 2D DIC software *Ncorr* [19], was modified in this work to account for lens distortions through the algorithm described by Pan *et al.* [33]. For interested readers, a summary of various aspects of 2D DIC processing can be found in [19, 34].

2.1.1 DIC settings

There are several settings affecting the DIC analysis. The most common and significant ones are described here.

Subset spacing is the distance between subsets in pixels. The resulting DIC data has fewer spatial measurement points when the spacing is increased. If the spacing is set low, it will not necessarily improve the results, as the subsets will strongly overlap, and the data will be blurred. On the contrary, it should also not be set too high, as the deformation might not be captured precisely, especially in case of strong deformation gradients. Low spacing also increases the computational time.

Subset radius is the size of the subset as shown in fig. 2.1(d). If the radius is small, there is more noise in capturing the deformation of the subset, which causes poor precision of the DIC data. An upper limit might be set based on two criteria, the first being the processing time which increases with the radius, and the second depends on the order of the shape function. If the shape function is not capable of capturing the deformation occurring in the subset, it might introduce an error in the measurements. Overmatched shape functions might escalate errors at small radius [35], and undermatched shape functions might cause systematic errors proportional to the square of the subset size [36].

Other settings include settings related to the iterative process, dividing the ROI into smaller regions enabling parallel processing, or seed propagation when the correlation becomes poor. They are however not described here as they will vary with the particular software used.

2.1.2 Applications of DIC

Due to the simplicity of acquiring DIC data, it is a very popular in situ technique with various applications in materials science. It can be implemented for structural health monitoring [37–39], tensile tests [40], fatigue

tests including measurement of plastic zone, crack closure, and crack opening displacements [41, 42], fracture toughness [43, 44], or high temperature tests [45] where use of other equipment is inconvenient. It is also flexible with regards to the imaging system used, as the only requirement is to have a distinct, unique pattern, and can be applied to images obtained by scanning electron microscopy [45], or infrared thermography [46].

2.1.3 Expended mechanical energy

The details regarding DIC measurements, and calculation of stress and strain tensors are explained in article I. The key property is the expended mechanical power density P_e measured by the method:

$$P_e = \boldsymbol{\sigma} : \mathbf{D} \tag{2.1}$$

where $\boldsymbol{\sigma}$ is the stress tensor, and $\mathbf{D}$ is the conjugate displacement rate tensor.

2.2 Infrared thermography

All bodies with a temperature above 0 K emit electromagnetic radiation (from now on radiation), and the spectral radiance as a function of temperature and wavelength for a black body (emissivity of 1) in thermodynamic equilibrium is described by Planck's radiation law [47]:

$$B_\lambda(\lambda, T) = \frac{2hc^2}{\lambda^5} \frac{1}{\exp \frac{hc}{\lambda k_B T} - 1} \tag{2.2}$$

In addition to the radiation emitted by a body, irradiation hitting a body can be absorbed, reflected from the surface, or transmitted through the body, proportions of which are described through the bodies absorptivity, reflectivity, and transmissivity, fractions that sum up to unity. According to Kirchhoff [48], absorptivity, and emissivity are the same for a given wavelength and temperature, and all of the abovementioned properties are a function of wavelength and temperature. Radiation does also interact with the surrounding atmosphere, as some will be absorbed through atmospheric attenuation, and some will be emitted due to the atmospheres temperature.

IRT utilises the radiation emitted by a body to extract thermal information, this process however requires several steps of processing to obtain reliable and physically sound results. Sensors in thermal cameras usually do not

distinguish between wave numbers, and are sensitive only in a limited spectral range. Sensors and optics are carefully selected for their environment, to avoid, for example, atmospheric attenuation, and are calibrated to give a precise temperature reading under the black body assumption. The calibration procedure accounts for the sensor response, transmissivity of the optics, etc. Both the effect of atmosphere, and lack of "true" black body conditions can be to some extent corrected for, but since atmosphere is not thick enough to affect measurements in this work in any significant amount, only the latter is described in article I. The outcome is a surface temperature distribution of an object.

2.2.1 Application of infrared thermography in materials science and engineering

The two main approaches of IRT in materials science are related to obtaining the stress fields from temperature data, and to investigate dissipative processes accompanying plastic deformation and fracture of materials. Mountain & Webber [49] utilised the temperature change caused by stress change, or the thermoelastic effect [50], to conduct full field, non contact, thermoelastic stress analysis for a cyclically loaded component. This phenomenon has later been utilised by several researchers to measure stress field surrounding a crack [51–54]. There have also been applications of IRT to measure fatigue limit, in both cyclic and monotonic tests, as well as fatigue life [55–64]. The methods can be used to relate thermomechanical behaviour to microstructure [65], or to perform DIC analysis on IRT data [46].

2.2.2 Thermal energy dissipation - considerations omitted in the articles

The internal heat energy per unit volume Q is related to the temperature T through specific heat capacity c_p and density ρ_{mat}:

$$\frac{\partial Q}{\partial t} = c_p \rho_{mat} \frac{\partial T}{\partial t} \tag{2.3}$$

Since the energy is conserved, the change in the thermal energy is equal to the heat production in the system, and heat flow into the system. Heat production, and heat flow can be divided into several terms, originating from different mechanisms. There are three sources of heat flow into a solid body, electromagnetic radiation from a free surface $\dot{q}_{RD}$, convection in case a surface is in contact with a fluid $\dot{q}_{CV}$, and heat conduction $\dot{q}_{CD}$

caused by heat flow within the solid. Factors affecting heat generation during a tensile test are heat dissipation due to plastic deformation $\dot{q}_d$, and temperature change due to thermoelastic effect $\dot{q}_{TE}$. Consequently, the following expression is formulated:

$$\rho_{mat} c_p \frac{\partial T}{\partial t} = \overbrace{\dot{q}_{CD} + \dot{q}_{CV} + \dot{q}_{RD}}^{flow} + \overbrace{\dot{q}_d + \dot{q}_{TE}}^{production} \tag{2.4}$$

To obtain the amount of energy dissipated as heat through plastic deformation, the different terms must be determined, and some can be neglected. The two terms that have not been described in article I are heat transfer through convection and radiation.

2.2.2.1 Convective heat transfer

Convective heat transfer is a complex problem to describe precisely for a general case of tensile tests, as it will depend on a variety of factors. More detailed information on the mechanisms and background can be found in the book by Bergman *et al.* [66]. To simplify the problem, Newton's law of cooling is used since it reduces the complex problem to one coefficient, the heat transfer coefficient h_c.

$$\dot{q}_{CV} = 2h_c(T_s - T_{body}) \tag{2.5}$$

In eq. (2.4) the number of spatial dimensions was not specified, as a general solution for the heat equation was used. Heat accumulation and production are given per volume, surface effects are however given per area. This requires to either use a complex 3D implementation with boundary conditions on the surfaces, or, a 2D simplification. The latter has several advantages, specifically considering the experimental information at hand. IRT provides surface measurements, and since the specimen is relatively thin, the properties are assumed to be uniform through the thickness.

The assumptions and simplifications in equation eq. (2.5) are:

- h_c is uniform for the whole ROI
- Each point on the 2D body has two surfaces, hence the factor 2 in eq. (2.5)
- The convective heat exchange occurs through natural convection

For illustrative purposes, the heat transfer coefficient was estimated according to the following equation [67]:

$$h_c = 1.42 \left(\frac{|T_{body} - T_s|}{H} \right)^{0.25} \tag{2.6}$$

where H is the height of the hot part in millimetres, here set to gauge length for a conservative estimate. The resulting heat exchange is shown for the most conservative specimen in figure 2.2, where it is approximately two orders of magnitude lower than the measured heat dissipation.

2.2.2.2 Radiation

Since the considerations regarding dimensionality were already discussed in 2.2.2.1, the implementation of the term for radiative loss is effortless. According to Stefan–Boltzmann law the power of emitted radiation is proportional to the fourth power of temperature

$$\dot{q}_{RD} = \sigma_{SB} \epsilon_{body} ({T_s}^4 - {T_{body}}^4) \tag{2.7}$$

where Stefan–Boltzmann constant σ_{SB} is the proportionality constant. The only challenge of this equation is the emissivity ϵ_{body}. The emissivity correction for thermal measurements is limited to a narrow spectrum, whereas this relation accounts for the whole radiated spectrum, and is a function of wavelength and temperature. An approximation of the heat transfer due to electromagnetic emissions is also shown in figure fig. 2.2, where it is approximately two orders of magnitude lesser than the measured heat dissipation.

2.2.2.3 Fraction of plastic work dissipated as heat

The left hand side of equation eq. (2.4) is known, as well as all terms on the right hand side except of $\dot{q}_d$ which is the value to be found. However, the terms $\dot{q}_{CV}$ and $\dot{q}_{RD}$, are usually rather small, and therefore often neglected, especially in cyclic tests [55, 57, 58, 62]. The closer the specimen is to room temperature, the less significant these terms are, 2.2 compares the approximated magnitude of these terms to the overall dissipated heat, for the worst case specimen used in this work. The two concerning terms are approximately two orders of magnitude lower than the measured heat dissipation, and lie well within the experimental scatter. It is, in principle, possible to account for these terms, although it requires better determina-

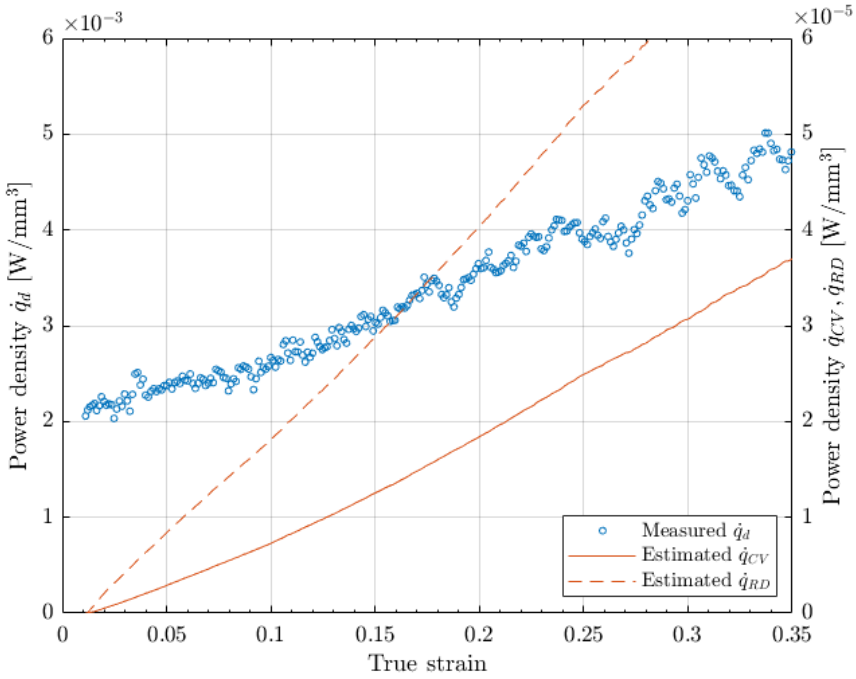

Figure 2.2: Measured infrared power density $\dot{q}_d$ and estimated energy losses due to convection $\dot{q}_{CV}$ and radiation $\dot{q}_{RD}$ (note the difference in the scale of Y-axis)

tion of the coefficients in eqs. (2.5) and (2.7) and will not alter the main conclusions anyway.

Once these terms are neglected, and eq. (2.4) rearranged and combined with the terms describing different contributions, we finally obtain:

$$P_d = \dot{q}_d = \rho_{mat} c_p \frac{\partial T}{\partial t} - \nabla \cdot (k \nabla T) + \alpha_T T \frac{ds}{dt} \tag{2.8}$$

Once plastic deformation prevails over elastic deformation significantly in monotonic testing, the term accounting for the thermoelastic effect in eq. (2.8) has only a minor or even negligible effect; this is illustrated in figure 2.3. The most significant discrepancy occurs in the elastic (pseudo-elastic) regime, where almost no mechanical work is plastically dissipated as heat and where the thermoelastic effect is significant.

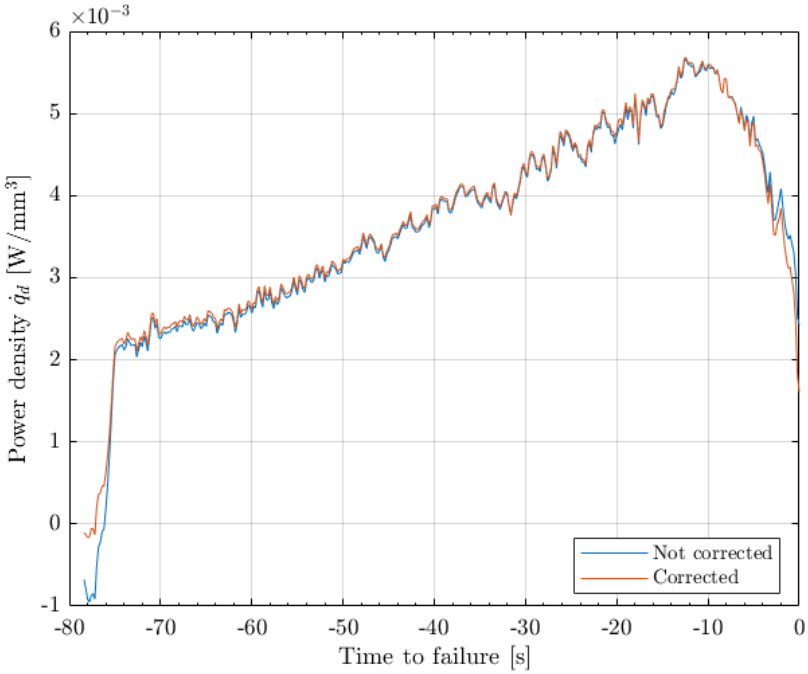

Figure 2.3: Comparison of measured heat dissipation power where the term for thermoelastic effect is neglected (blue curve), and when it is accounted for (orange curve)

2.3 Acoustic Emission

As is briefly explained in article I, Acoustic Emission (AE) is a naturally occurring phenomenon caused by energy release in the form of transient, elastic waves, reflecting rapid local stress relaxation processes in solids. There are several sources of AE during plastic deformation of metals, these include dislocation slip [68–71], mechanical twinning [72–76], deformation- (or temperature-) induced phase transformations [77–81], plastic instabilities of various kinds [82–90], and cracks of various types.

There are four principal wave modes by which elastic waves propagate: longitudinal waves, shear waves, surface waves (Rayleigh waves), and in the case of thin objects, plate waves (Lamb waves) [91]. The generated signal changes due to wave propagation effects and mechanical disturbance [92], so the characteristics are altered before reaching the AE sensor. A sensor consists of a piezoelectric transducer that converts the specific part of the wave - longitudinal or transverse to the surface - to an electric signal. Once the elastic wave leaves the source and reaches the surface, it has to pass through another medium before entering the sensor. Air has rather poor transmitting properties, therefore the signal transfer can be improved by using a "wave-transparent" substance between the sensor and specimen surface, such as vacuum grease or machine oil.

Depending on the frequency response, the AE sensors are usually divided into two categories: broad-band sensors, and narrow-band resonant sensors. Ideally, the former has a flat response that captures and transfers all frequencies equally, whereas the resonant type is excited mainly at the resonance frequencies. Depending on the application, both categories have advantages and disadvantages. For scientific purposes, where the signal source or its evolution is of concern, the wide-band sensors deliver more significant information, however, when noise is present, and the specific frequency of the source is known, a resonant type sensor might be preferred. Besides, the resonant sensors are by far more sensitive than their broad-band counterparts. The strength of the electric signal generated by the sensor is of a few µV. This requires an 20-60 dB amplifier, before the signal can be fed to the data logger and signal processor. Note, that the natural lower bound sensitivity of the sensor is limited by the thermal electric noise, which is typically of 10 µV peak-to-peak on average at the input of the pre-amplifier, depending on the pre-amp input circuit.

The signal can be recorded continuously, or only when it fulfils specific criteria, e.g., when a pre-set voltage threshold is crossed. The threshold based

approach is by far the most popular one due to its simplicity: one can use either a physical electric trigger or a programmable software voltage level. Not only the amount of acquired data is reduced in this way, but also when the threshold is crossed, the user can be confident that the data contains a valid signal. On the other hand, the threshold is arbitrarily (often carelessly) set and there are no scientific grounds to set it rigorously. Besides, some deformation and fracture mechanisms generate a weak signal, and, therefore, will not be captured in this approach. Furthermore, dislocation-mediated mechanisms of plastic deformation usually generate a continuous signal instead of sharp individual bursts. All in all this justifies that the continuous recording method is in general more scientifically justified even if it requires admittedly greater resources. The sampling rate during recording can be selected based on the highest frequency of interest by using the Nyquist theorem. However, it will also affect the frequency resolution when performing Discrete Fourier Transform (DFT).

2.3.1 Acoustic Emission processing

The data processing in this work was done with the Adaptive Sequential k-means Clustering (ASKC) data analysis and clustering algorithm first proposed by Pomponi & Vinogradov [93]. The clustering itself has not been the main task in the present work, and therefore, is not explained here (the interested readers are encouraged to go through [93] for details). However, the ASKC algorithm returns the key AE features of interest - median frequency of the Power Spectral Density (PSD) function, and AE power, which are chosen as the primary descriptive variables on the basis of multivariate factor analysis and the statistical and physical arguments presented in [94]. Both these chosen variables have been shown to be intimately related to the mechanisms generating the signal, including the dislocation motion as will be discussed in what follows. Besides, their instantaneous values are affected by the current state of the dislocations, as they interact with each other. The self-consistent phenomenological model relating the dislocation density with the AE behaviour during strain hardening in metals has been proposed in article III. It has been, in particular, demonstrated that the above mentioned features - AE PSD median frequency and power - can be directly linked to the behaviour of mobile and immobile dislocations. The settings used for AE processing affect the shape of the derived PSD and the properties calculated from it. It is important to be aware of the relation between the settings used and processed data. However, before explaining this influence on the processing, some important concepts need to be

explained.

2.3.1.1 Fourier transform

The first step in understanding the processing of AE data is to understand the Fourier transform of a random time series, or more precisely, the Discrete Fourier Transform (DFT). A short summary is given here, for details see book by Semmlow [95].

To investigate the frequencies, and their magnitudes present in a discrete signal, a DFT is performed, which transforms a signal from the time representation to the corresponding frequency representation. The Fourier coefficients contain information about both the magnitude and the phase of specific frequencies. The problem is, however, that the higher frequency resolution is obtained at the expense of temporal resolution. Simply speaking, more sampling points are required to obtain higher frequency resolution for a fixed sampling rate, but the more points are added, the less precisely we know where in time the frequencies occur.

In general, the assumption is that the signal is stationary and periodic, with a period time T_{ds}, which (in our case) is the duration of the data segment. The frequency components of the Fourier series are dependent on T_{ds} according to the equation below:

$$f_{m_h} = \frac{m_h}{T_{ds}} = m_h f_1 \tag{2.9}$$

where f_{m_h} is the frequency of the m_h'th harmonic number, and $f_1 = 1/T_{ds}$, is the frequency of the segment. If N is the number of sample points, and T_{sample} and f_{sample} are respectively the sample interval and sampling frequency, the total time T_{ds} is

$$T_{ds} = NT_{sample} = \frac{N}{f_{sample}} \tag{2.10}$$

which combined with eq. (2.9) yields

$$f_{m_h} = \frac{m_h f_{sample}}{N} \tag{2.11}$$

Since the frequency resolution is the difference in frequencies between harmonics, it can be found from eq. (2.11) to be

$$f_{resolution} = \frac{f_{sample}}{N} \tag{2.12}$$

As mentioned above, the frequency resolution is dependent on the time length of the data, or N for a fixed sampling rate. It can also be increased by reducing f_{sample}, but it is, however, limited by the Nyquist rate.

2.3.1.2 Zero padding

When computing the DFT there are some other considerations to keep in mind. It is often calculated through Fast Fourier Transform (FFT), an algorithm that is computationally very efficient. Once data is acquired, the number of data points can artificially be increased, by adding additional zeros. The reason is that some algorithms prefer to operate with a number of points equal to a power of 2. There are also some other advantages, adding zeros in the time series, appears to give a spectrum with higher frequency resolution. In reality, it gives an interpolation, which does not contain more information than the original signal, however, the PSD is visually easier to read and compare with each other.

2.3.1.3 Welch's method

Welch's method [96, 97] is a way of estimating power spectra. The general advantage of this approach over full DFT is that it smooths over non-stationary noise, and is robust to some non-stationary artefacts. The downside is reduced spectral precision.

When DFT performs processing over a segment of data, Welch's method divides it instead into smaller sub-segments, which might overlap, depending on the particular approach. Each sub-segment is tapered, as the edges would cause artefacts in the PSD. Tapering is also to some extent motivation to make the windows overlapping, to not lose valid data at the edges of the segments. Next, the periodograms are calculated using FFT, and averaged; this way, non-stationary noise is filtered out of the PSD. The PSD function calculated by Welch's method was further used to calculate AE properties used in this work.

2.3.2 Effect of settings on the AE output parameters

Figure 2.4 is an example of ASKC settings used for processing AE streams. This section will briefly explain how the most significant settings influence

the results of primary AE processing.

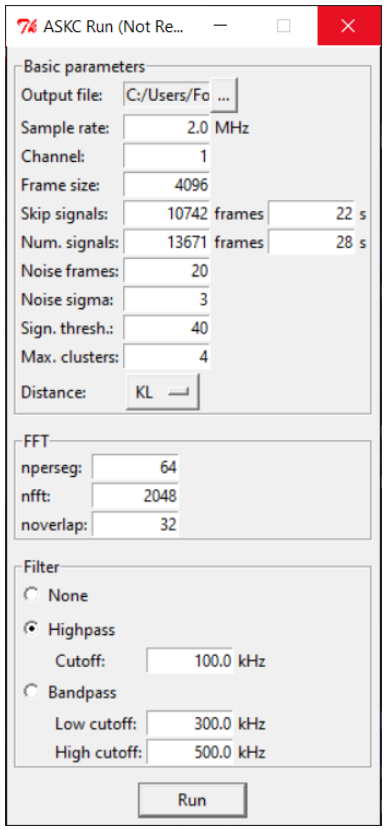

Figure 2.4: AE settings during processing

Sample rate - the hardware (analogue-to-digital converter) sample rate is set in the data acquisition software; the corresponding setting in ASKC must match the hardware sample rate and is not adjustable.

Channel is selected either 0 or 1 for the processing of the corresponding stream in the case if two sensors are used in parallel.

Frame size - the stream is divided into a set of subsequent segments of equal length; Frame size is the number of points each data segment (also commonly termed realisation) consists of; it is usually set a power of 2. There are several strategies when selecting this quantity, one is to select the frame to match the size of a signal feature, e.g. a transient signal. In that case, the PSD calculation is dominated by the properties of the feature. Another approach is to select a relatively large frame (long realisation of the random process) so that it represents an average of the features in the signal. This might be useful for continuous signals, where larger frames result in less scatter.

Skip signals is simply the amount of frames to skip in the beginning of the recording.

Num. signals is the number of frames to process; the software will also skip all frames acquired after Skip signals + Num. signals.

Noise frames is the amount of frames that will be utilised for characterising the noise. This estimate is done on frames captured before the test start, and assumes the noise does not change during the test. If noise is generated by the test machine, this assumption is not valid and this extrinsic noise should be handled by the cluster analysis, which is supposed to be capable

of distinguishing outliers of this kind from both regular background noise and true AE events.

Noise sigma is a statistical variable, characterising the compactness of the noise cluster. This parameter is mathematically equal to the multiplier to the standard deviation of background noise and is typically set at 1, 2 or 3; the resultant product is then used to define the distance, which serves as an initial measure of similarity/dissimilarity between the clusters [93].

Sign. thresh. is an important feature of the clustering algorithm which has not been documented in [93]. The numerical integer value of this parameter is used as a minimum number of accumulated cluster member when the cluster is considered significant, and further merging of this cluster with others is prohibited. Once the significance threshold is exceeded for a given cluster, this cluster cannot be automatically merged with others anymore and will evolve only by welcoming the nearest new arriving events. The use of this parameter helps to avoid the "black hole" like dominance of large, widely distributed, clusters tending to accept all new arriving members. If set at -1, the significance threshold is not used in the clustering procedure.

Max. clusters Is the maximum number of clusters, which ASKC is allowed to distinguish. In principle, ASKC does not require this parameter to be set and determines the number of clusters automatically from the data structure. It is however, convenient to set this parameter reasonably large, e.g., by 1 or 2 greater than the expected number of possible sources (operation mechanisms).

Distance refers to the type of statistical measure of similarity/dissimilarity between the normalised to unity AE PSD functions. Of many possible candidates, the Python's version of the ASKC algorithm implements only three popular measures: Euclidean distance, Spectral Angle Mapper (SAM) distance and Kulback-Leibler (KL) divergence in its symmetrical variant. The latter is used by default and is recommended for most practical situations.

nperseg determines the segment size used for Welch's method explained in section 2.3.1.3. More points in the segment size result in a better frequency resolution, but less noise filtering.

nfft is the number of points used by the FFT algorithm (section 2.3.1.1), and should be at least as big as the number of data-points. If the nfft value is set larger than nperseg, the data is zero padded.

noverlap determines the amount of points by which segments in Welch's method overlap. This setting is dependent on the type of tapering function used, in this particular setting, a 50% overlap is reasonable.

2.4 Methodological challenges

A brief note on the technical challenges faced in the present work is in place. Several methodological issues have been addressed in the course of experimental work. The main ones were traditionally associated with the noise generated by the testing machine which severely affected AE measurements. Due to the nature of thermal measurements the estimation of the second spatial derivative of the temperature was also suffering from noise. These challenges and the countermeasures which helped to alleviate, if not completely eliminate, these issues were described in detail in article I. However, several practical difficulties were not included in the publication for brevity, or they were encountered after the article has been published. These most significant additional challenges are therefore described here.

Effect of paint on thermal measurements
Even though many measurement problems were solved with the emissivity correction procedure, and the careful selection of the paint, some new issues were encountered with the change of the testing material. The alloys like the 316L austenitic stainless steel, Inconel 625, or other materials typically used for thermographic measurements have a relatively low thermal conductivity, whereas in copper and CuZn alloys this property is by orders of magnitude higher. Due to this change, the effect of paint as an insulating layer might affect thermal measurements, as it delays the temperature transfer from the metal surface to the free surface. The impact of this effect is experimentally unknown, but can be estimated through modelling and simulations, in which case, the properties of the coating such as thermal properties and the thickness must be known. This is challenging as the thickness will vary for each specimen, and during the test. The effect of the paint can be fully disposed by adapting a suitable calibration approach, which does not require surface coating. Instead of assuming an emissivity, a calibration curve can be made [98], or by using multi colour (several radiation bands) algorithms to estimate the absolute temperature [99]. The first approach has advantages for high strain rate tests, and for the materials with the high electric and thermal conductivity. The second approach allows to investigate objects with unknown, or varying emissivity. Both do however have disadvantages. If the surface is of a high finish, it works as a mirror, and

reflects the surroundings with very little dispersion. In that case the surroundings should be uniform, which is also difficult to achieve if the camera is located relatively close to the specimen. Deformation of the surface can also shift the reflected part of the surroundings. If the temperatures of the object and the surroundings are relatively similar, and the emissivity is low, these approaches struggle as the signal is dominated by the surroundings. Both approaches also require additional preparations, a calibration curve must be made, or the hardware needs to be adapted to multi-colour measurements with proper spectral filters. The advantage of paint, is that it creates a dispersive, matt texture even though the surface of the specimen is highly reflective with little dispersion. Additional improvements of the experimental methodology are left as further work.

Limitations due to the specimen geometry

The attempts to perform the mechanical testing together with highly sensitive AE, IRT and DIC in situ methods sets additional requirements to the specimen geometry, which, on one hand, has to be compatible with the standard recommendations for uniaxial tensile testing, and, on the other hand, it has to permit the observation of the gauge region by both IRT and DIC cameras. Article I explains how to reach an excellent correspondence between the regions of interest observed by both methods. Nonetheless, it should be noted that the specimen design adopted in article III was not ideal when it comes to the AE results. Since the annealed Cu-Zn alloys have a low yield stress and exhibit the yield point followed by the propagation of the Luder's band, the AE results appeared to be sensitive to the geometry of the shoulder part: the propagating plastic deformation enters the shoulder part far beyond the onset of yielding (at around 10 % plastic strain) leading to a second AE peak in all experiments performed with alloys, regardless of the strain rate and testing machines used (we probed the electrodynamic Instron Electropuls 10000 and the screw-driven MTS Criterion model 42). The reason for it was undoubtedly clarified by DIC as explained in the article. To mitigate, or remove this issue, the specimens should be redesigned. The issue could not be predicted prior to the tests. Due to the second AE peak, the signal did not represent uniform deformation, and had to be removed from the analysis. Although the compromise between the gauge length, shape of the shoulder part, and the visibility and resolution of ROI was not found, this issue did not affect the conclusions drawn in article III. Nonetheless, it was admittedly unfortunate as the signal was strongest at the early stage of deformation, and this factor could be decisive for many other materials.

3 Model for energy partitioning governed by dislocation density

Article II focuses on creating a model for energy partitioning for a material where plastic deformation occurs due to dislocation production and annihilation. The idea is that energy is expanded on material deformation. The energy will be stored in the interatomic bonds, used on dislocation creation, motion, and annihilation. The total energy can be divided into two parts: the internal energy that remains stored in the deformed material in the form of elastic strains surrounding dislocations (and, in principle, other lattice defects generated in the course of plastic deformation), and the rest of it will be dissipated, mostly as heat, but also as acoustic emissions.

The most important finding is that the model, even though it is very simple, manages to precisely predict the proportions of stored and dissipated energies, when compared to experimental in situ measurements. The general solution for expanded power density, as well as the power densities of the stored and dissipated energies, based on the first law of thermodynamics and Taylor relation are summarised below.

$$P_e = \sigma\dot{\varepsilon} \tag{3.1a}$$

$$P_d = \left[\sigma_I + \frac{\dot{\rho}^-}{\dot{\rho}^+}(\sigma - \sigma_I)\right]\dot{\varepsilon} \tag{3.1b}$$

$$P_s = (\sigma - \sigma_I)\left(1 - \frac{\dot{\rho}^-}{\dot{\rho}^+}\right)\dot{\varepsilon} \tag{3.1c}$$

This result might be combined with the single internal variable model presented by Kocks & Mecking [100] (see also [101]), to express the dislocation "birth" and "death". This particular solution also predicts how dislocation interactions affect energy storage, as is presented in equation eq. (3.2).

$$E_s = \frac{\alpha G b^2}{k_1}(\rho - \rho_0)\Phi\left(\frac{\rho_0}{\rho}\right) \tag{3.2a}$$

$$\Phi\left(\frac{\rho_0}{\rho}\right) = \left[1 - \frac{2\sqrt{\frac{\rho_0}{\rho}}}{1 + \sqrt{\frac{\rho_0}{\rho}}}\right] \tag{3.2b}$$

Finally, under the assumption of only one internal variable, namely the total dislocation density, there are only two parameters controlling the process of plastic deformation: the athermal dislocation production rate, k_1, and the thermally-activated dislocation annihilation (dynamic recovery) rate k_2. Once these are known, all other properties are determined, stress, energy storage and dissipation, even properties of AE signal as is step-by-step derived and discussed in article III.

3.1 Independent attainment of dislocation production and annihilation parameters

The focus of article II was on acquiring parameters of the Kocks & Mecking (KM)-model from the stress and strain data, and to relate them to energy partitioning. Article III investigates the relation between AE and the KM parameters. The relation between these allowed to obtain k_2 with reasonable accuracy, purely from AE signal, and the combination with IRT allowed to also obtain k_1. This result closes the loop, and shows, that the parameters governing plastic deformation can indeed be obtained through independent experimental measurements.

4 Conclusions and further work

4.1 Conclusions and final remarks

The present work benefits from a synergy of three modern in situ techniques - Digital Image Correlation (DIC), full-field high resolution Infrared Thermography (IRT) and braodband Acoustic Emission (AE) - and the wealth of information arising from them regarding underlying deformation mechanisms. Numerous hardware and software challenges were addressed, which are inevitable in a contemporary advanced experimental design. The developed experiential methodology is based on open-source and self-made software solutions enabling versatility, and tunability of the entire setup, allowing it to be adapted to any combination of visual and thermal cameras, as well as giving freedom in selecting loading conditions. In addition, the concurrent use of fully synchronised AE measurements together with IRT and DIC , adds one more dimension to the multiscale investigation of mechanics of plasticity and fracture due to the outstanding temporal resolution offered by the AE method. There are still improvements to be done, however, the current state of the methodological work can be regarded as the state-of-the-art and is suitable to address fundamental challenges existing in the modern understanding of the strain hardening phenomenon in materials.

Embedded in the developed experimental design, a thermodynamic modelling methodology is presented. The modelling strategy is footed firmly on the first law of thermodynamics and informed by the dislocation evolution theory inspired by the classic Kocks & Mecking formalism, with the aim of gaining deeper insight into the partitioning of energy of plastic deformation. For the fist time, the first law of thermodynamics is bridged with the the time-proven first-order dislocation kinetics approach, where only physically motivated variables are used. This constitutes the main advantage of the entire modelling approach proposed in this work. The outcome of

the model is a successful prediction of energy partitioning in materials with dislocation mediated plasticity in monotonic deformation. The model was verified with the fcc low-carbon austenitic 316L stainless steel tested at various strain rates, and its power was further confirmed on copper and model CuZn alloys with different Zn content corresponding stacking fault energies controlling the dislocation mobility and microstructure evolution in these alloys.

The energy partitioning is analysed through simple, mathematically traceable expressions, and when combined with the Kocks-Mecking type dislocation evolution model, these constitute the basis for the Taylor-Quinney factor calculations. They can be connected to the same properties measured through experimental in situ techniques, for non-destructive monitoring of damage, and damage evolution in deforming solids. The model can be extended to a wide range of structural materials, some other materials tested, but not reported here include TWIP and TRIP steels, and Inconel 625. The adaptation to bcc or hcp materials is straight forward.

Finally, the combination of IRT, and AE allows to characterise the details of the evolution of dislocation ensemble during plastic deformation through the connection to its kinetic properties. The factors controlling the dislocation production and dynamic recovery rates in the strain hardening process, which are typically derived solely from the approximation of the stress-strain curves by the Kocks & Mecking model solutions, in the present work were recovered for the first time from the model-based AE, and IRT analyses respectively; reasonable accuracy of the calculations made has been observed for the set tested CuZn alloys. Thus, the efficient toolset consisting of the synchronised IRT and AE measurements, equipped with the developed model solutions, can be used for unravelling of the quantitative details of the dislocation microstructure evolution on various scales. Particularly, the toolset can be used for predictive purposes regarding the strain hardening behaviour of a material. The proposed model framework increases the robustness and predictive capability of the developed experimental toolset and put it in a sharper focus as a contemporary technique that permits quantitative evaluation of the dislocation kinetics in situ.

More specific and detailed conclusions are drawn in the dedicated papers, which are integrated in the present thesis.

4.2 Further work

4.2.1 Improvement of methodological challenges

Some methodological challenges have already been addressed, these include calibration procedures for infrared thermography, and a solution was proposed based on the approach adopted by Soares & Hokka [98], or Savino *et al.* [99]. If a calibration procedure would allow to measure temperature distribution precisely without the use of a surface coating, several challenges could be resolved, such as paint cracking or peeling at high strains, or thermal properties of the paint.

Another issue which can easily be improved is the specimen geometry causing non-uniform deformation, which influenced AE measurements.

4.2.2 Further modelling and experimental validation

A natural next step would be to continue the work with monotonic tests, for materials exhibiting strain-rate sensitivity. The model could be strengthened by such a validation.

The methodology for cyclic and crack growth tests has been developed, and has an enormous potential in improving our understanding mechanisms governing fatigue. Common approach to Fatigue Crack Growth (FCG) is to fit experimental data to Paris' law, an empiric relation based on linear elastic fracture mechanics, under the assumption of a **negligible** plastic zone. This approach however is impossible to relate to the mechanisms driving crack growth, as it is a process driven by plastic deformation at crack tip.

Bibliography

1. Pfeifer, M. in *Materials Enabled Designs* (ed Pfeifer, M.) 161–187 (Butterworth-Heinemann, Boston, 1st Jan. 2009). ISBN: 978-0-7506-8287-9.
2. Friedel, J. *Dislocations* [1st English, xxi, 491 p. (Pergamon Press; Oxford, New York, 1964).
3. Gilman, J. J. *Micromechanics of flow in solids* (McGraw-Hill, New York ; London, 1969).
4. Zaiser, M. & Seeger, A. in *Dislocations in Solids* (eds Nabarro, F. R. N. & Duesbery, M.) Nabarro, F. R. N., 1–100 (Elsevier, 2002).
5. Miguel, M. C., Vespignani, A., Zapperi, S., Weiss, J. & Grasso, J.-R. Complexity in Dislocation Dynamics: Model. *Materials Science and Engineering: A. Dislocations 2000: An International Conference on the Fundamentals of Plastic Deformation* **309–310,** 324–327. ISSN: 0921-5093 (15th July 2001).
6. Richeton, T., Weiss, J. & Louchet, F. Breakdown of avalanche critical behaviour in polycrystalline plasticity. *Nature Materials* **4,** 465–469. ISSN: 1476-1122 (2005).
7. Richeton, T., Weiss, J. & Louchet, F. Dislocation avalanches: Role of temperature, grain size and strain hardening. *Acta Materialia* **53,** 4463–4471. ISSN: 1359-6454 (2005).
8. Dimiduk, D. M., Woodward, C., LeSar, R. & Uchic, M. D. Scale-Free Intermittent Flow in Crystal Plasticity. *Science* **312,** 1188–1190 (2006).
9. Cai, B. & Kong, Q. P. Analyses on the Background of Dynamic Internal Friction and the Modulus Defect during Plastic Deformation. *Physica Status Solidi (a)* **173,** 365–373. ISSN: 1521-396X (1999).

10. Vinogradov, A., Yasnikov, I. S. & Estrin, Y. Stochastic dislocation kinetics and fractal structures in deforming metals probed by acoustic emission and surface topography measurements. *Journal of Applied Physics* **115,** 233506. ISSN: 0021-8979 (2014).

11. Vinogradov, A., Yasnikov, I. S. & Estrin, Y. Irreversible thermodynamics approach to plasticity: dislocation density based constitutive modelling. *Materials Science and Technology* **31,** 1664–1672. ISSN: 0267-0836 1743-2847 (2015).

12. Lavrentev, F. F. The Type of Dislocation Interaction as the Factor Determining Work Hardening. *Materials Science and Engineering* **46,** 191–208. ISSN: 0025-5416 (1st Dec. 1980).

13. Vinogradov, A., Merson, D. L., Patlan, V. & Hashimoto, S. Effect of Solid Solution Hardening and Stacking Fault Energy on Plastic Flow and Acoustic Emission in Cu–Ge Alloys. *Materials Science and Engineering: A* **341,** 57–73. ISSN: 0921-5093 (20th Jan. 2003).

14. Weidner, A. *Deformation Processes in TRIP/TWIP Steels* 439. ISBN: 978-3-030-37148-7 (Springer, Cham, Switzerland, 2020).

15. Taylor, G. I. & Quinney, H. The Latent Energy Remaining in a Metal after Cold Working. *Proceedings of the Royal Society of London. Series A* **143,** 307–326 (Jan. 1934).

16. Welber, B. Measurement of the Internal Energy in Copper Introduced by Cold Work. *Journal of Applied Physics* **23,** 876–881. ISSN: 0021-8979 (Aug. 1952).

17. Nabarro, F. R. N. *Theory of Crystal Dislocations* xviii, 821. ISBN: 978-0-19-851244-8 (Clarendon Press, Oxford, 1967).

18. Gilman, J. J. *Micromechanics of Flow in Solids* x,294. ISBN: 978-0-07-023227-3 (McGraw-Hill, New York, Maidenhead, 1969).

19. Blaber, J., Adair, B. & Antoniou, A. Ncorr: Open-Source 2D Digital Image Correlation Matlab Software. *Experimental Mechanics* **55,** 1105–1122. ISSN: 1741-2765 (July 2015).

20. Harilal, R. & Ramji, M. *Adaptation of Open Source 2D DIC Software Ncorr for Solid Mechanics Applications* in (Nov. 2014).

21. Pierré, J.-E., Passieux, J.-C. & Périé, J.-N. Finite Element Stereo Digital Image Correlation: Framework and Mechanical Regularization. *Experimental Mechanics* **57,** 443–456. ISSN: 1741-2765 (1st Mar. 2017).

22. Wang, B. & Pan, B. Subset-Based Local vs. Finite Element-Based Global Digital Image Correlation: A Comparison Study. *Theoretical and Applied Mechanics Letters* **6,** 200–208. ISSN: 2095-0349 (1st Sept. 2016).

23. Bilissi, E., Triantaphillidou, S. & Allen, E. in *The Manual of Photography (Tenth Edition)* (eds Allen, E. & Triantaphillidou, S.) 227–243 (Focal Press, Oxford, 1st Jan. 2011). ISBN: 978-0-240-52037-7.

24. Xing, H. Z., Zhang, Q. B., Braithwaite, C. H., Pan, B. & Zhao, J. High-Speed Photography and Digital Optical Measurement Techniques for Geomaterials: Fundamentals and Applications. *Rock Mechanics and Rock Engineering* **50,** 1611–1659. ISSN: 1434-453X (June 2017).

25. Courtney-Pratt, J. S. A Review of the Methods of High-Speed Photography. *Reports on Progress in Physics* **20,** 379–432. ISSN: 0034-4885 (Jan. 1957).

26. Paúr, M., Stoklasa, B., Hradil, Z., Sánchez-Soto, L. L. & Rehacek, J. Achieving the Ultimate Optical Resolution. *Optica* **3,** 1144–1147. ISSN: 2334-2536 (20th Oct. 2016).

27. Dong, Y. & Pan, B. A Review of Speckle Pattern Fabrication and Assessment for Digital Image Correlation. *Experimental Mechanics* **57,** 1161–1181. ISSN: 1741-2765 (1st Oct. 2017).

28. Kammers, A. D. & Daly, S. Small-Scale Patterning Methods for Digital Image Correlation under Scanning Electron Microscopy. *Measurement Science and Technology* **22,** 125501. ISSN: 0957-0233 (Oct. 2011).

29. Reu, P. All about Speckles: Aliasing. *Experimental Techniques* **38,** 1–3. ISSN: 1747-1567 (2014).

30. Reu, P. All about Speckles: Speckle Size Measurement. *Experimental Techniques* **38,** 1–2. ISSN: 1747-1567 (2014).

31. Pan, B., Xie, H., Wang, Z., Qian, K. & Wang, Z. Study on Subset Size Selection in Digital Image Correlation for Speckle Patterns. *Optics Express* **16,** 7037–7048. ISSN: 1094-4087 (12th May 2008).

32. Lu, H. & Cary, P. D. Deformation Measurements by Digital Image Correlation: Implementation of a Second-Order Displacement Gradient. *Experimental Mechanics* **40,** 393–400. ISSN: 1741-2765 (1st Dec. 2000).

33. Pan, B., Yu, L., Wu, D. & Tang, L. Systematic Errors in Two-Dimensional Digital Image Correlation Due to Lens Distortion. *Optics and Lasers in Engineering* **51,** 140–147. ISSN: 0143-8166 (Feb. 2013).

34. Atkinson, D. & Becker, T. A 117 Line 2D Digital Image Correlation Code Written in MATLAB. *Remote Sensing* **12,** 2906 (8th Sept. 2020).

35. Yu, L. & Pan, B. The Errors in Digital Image Correlation Due to Overmatched Shape Functions. *Measurement Science and Technology* **26,** 045202. ISSN: 0957-0233 (Feb. 2015).

36. Schreier, H. W. & Sutton, M. A. Systematic Errors in Digital Image Correlation Due to Undermatched Subset Shape Functions. *Experimental Mechanics* **42,** 303–310. ISSN: 1741-2765 (1st Sept. 2002).

37. Malesa, M., Szczepanek, D., Kujawińska, M., Świercz, A. & Kolakowski, P. Monitoring of Civil Engineering Structures Using Digital Image Correlation Technique. *The European Physical Journal Conferences* **6** (9th June 2010).

38. Ngeljaratan, L. & Moustafa, M. A. Structural Health Monitoring and Seismic Response Assessment of Bridge Structures Using Target-Tracking Digital Image Correlation. *Engineering Structures* **213,** 110551. ISSN: 0141-0296 (15th June 2020).

39. Nonis, C. *et al. Structural Health Monitoring of Bridges Using Digital Image Correlation* in. SPIE Smart Structures and Materials + Nondestructive Evaluation and Health Monitoring (ed Kundu, T.) (San Diego, California, USA, 17th Apr. 2013), 869507.

40. Quanjin, M., Rejab, M. R. M., Halim, Q., Merzuki, M. N. M. & Darus, M. A. H. Experimental Investigation of the Tensile Test Using Digital Image Correlation (DIC) Method. *Materials Today: Proceedings. First International Conference on Advanced Lightweight Materials and Structures* **27,** 757–763. ISSN: 2214-7853 (1st Jan. 2020).

41. Tong, J., Alshammrei, S., Wigger, T., Lupton, C. & Yates, J. Full-Field Characterization of a Fatigue Crack: Crack Closure Revisited. *Fatigue & Fracture of Engineering Materials & Structures* **41,** 2130–2139. ISSN: 1460-2695 (2018).

42. Vasco-Olmo, J. M., James, M. N., Christopher, C. J., Patterson, E. A. & Díaz, F. A. Assessment of Crack Tip Plastic Zone Size and Shape and Its Influence on Crack Tip Shielding. *Fatigue & Fracture of Engineering Materials & Structures* **39,** 969–981. ISSN: 1460-2695 (2016).

43. Kan, W. H. *et al.* Fracture Toughness Testing Using Photogrammetry and Digital Image Correlation. *MethodsX* **5,** 1166–1177. ISSN: 2215-0161 (1st Jan. 2018).

44. Rahmatabadi, D., Ahmadi, M., Pahlavani, M. & Hashemi, R. DIC-based Experimental Study of Fracture Toughness through R-curve Tests in a Multi-Layered Al-Mg (LZ91) Composite Fabricated by ARB. *Journal of Alloys and Compounds* **883,** 160843. ISSN: 0925-8388 (25th Nov. 2021).

45. Yin, Y., Xie, H. & He, W. In Situ SEM-DIC Technique and Its Application to Characterize the High-Temperature Fatigue Crack Closure Effect. *Science China Technological Sciences* **63,** 265–276. ISSN: 1869-1900 (1st Feb. 2020).

46. Sendrowicz, A., Myhre, A. O., Wierdak, S. W. & Vinogradov, A. Challenges and Accomplishments in Mechanical Testing Instrumented by In Situ Techniques: Infrared Thermography, Digital Image Correlation, and Acoustic Emission. *Applied Sciences* **11,** 6718. ISSN: 2076-3417 (15 Jan. 2021).

47. Planck, M. & Masius, M. *The Theory of Heat Radiation* in collab. with University of California Libraries. 256 pp. (2022) (Philadelphia, P. Blakiston's Son & Co, 1914).

48. Kirchhoff, G. I. On the Relation between the Radiating and Absorbing Powers of Different Bodies for Light and Heat. *The London, Edinburgh, and Dublin Philosophical Magazine and Journal of Science* **20,** 1–21. ISSN: 1941-5982 (1st July 1860).

49. Mountain, D. S. & Webber, J. M. B. *Stress Pattern Analysis By Thermal Emission (SPATE)* in *4th European Electro-Optics Conf* **0164** (International Society for Optics and Photonics, July 1979), 189–196.

50. Pitarresi, G. & Patterson, E. A. A Review of the General Theory of Thermoelastic Stress Analysis. *The Journal of Strain Analysis for Engineering Design* **38,** 405–417. ISSN: 0309-3247, 2041-3130 (1st July 2003).

51. Díaz, F. A., Patterson, E. A., Tomlinson, R. A. & Yates, J. R. Measuring Stress Intensity Factors during Fatigue Crack Growth Using Thermoelasticity. *Fatigue & Fracture of Engineering Materials & Structures* **27,** 571–583. ISSN: 1460-2695 (2004).

52. Tomlinson, R. A. & Olden, E. J. Thermoelasticity for the Analysis of Crack Tip Stress Fields — a Review. *Strain* **35,** 49–55. ISSN: 1475-1305 (1999).

53. Dulieu-Barton, Fulton & Stanley. The Analysis of Thermoelastic Isopachic Data from Crack Tip Stress Fields. *Fatigue & Fracture of Engineering Materials & Structures* **23,** 301–314. ISSN: 1460-2695 (2000).

54. Thatcher, J. E., Crump, D. A., Devivier, C., Bailey, P. B. S. & Dulieu-Barton, J. M. Low Cost Infrared Thermography for Automated Crack Monitoring in Fatigue Testing. *Optics and Lasers in Engineering* **126,** 105914. ISSN: 0143-8166 (1st Mar. 2020).

55. Risitano, A., Corallo, D., Guglielmino, E., Risitano, G. & Scappaticci, L. Fatigue Assessment by Energy Approach during Tensile Tests on AISI 304 Steel. *Frattura ed Integrità Strutturale* **11,** 202–215. ISSN: 1971-8993, 1971-8993 (1st Jan. 2017).

56. Lu, J., Han, X., Newaz, G., Favro, L. & Thomas, R. Study of the Effect of Crack Closure in Sonic Infrared Imaging. *Nondestructive Testing and Evaluation* **22,** 127–135 (1st June 2007).

57. La Rosa, G. & Risitano, A. Thermographic Methodology for Rapid Determination of the Fatigue Limit of Materials and Mechanical Components. *International Journal of Fatigue* **22,** 65–73. ISSN: 0142-1123 (1st Jan. 2000).

58. Meneghetti, G. Analysis of the Fatigue Strength of a Stainless Steel Based on the Energy Dissipation. *International Journal of Fatigue* **29,** 81–94. ISSN: 0142-1123 (1st Jan. 2007).

59. De Finis, R., Palumbo, D. & Galietti, U. A Multianalysis Thermography-Based Approach for Fatigue and Damage Investigations of ASTM A182 F6NM Steel at Two Stress Ratios. *Fatigue & Fracture of Engineering Materials & Structures* **42,** 267–283. ISSN: 1460-2695 (2019).

60. Palumbo, D., De Finis, R., Ancona, F. & Galietti, U. Damage Monitoring in Fracture Mechanics by Evaluation of the Heat Dissipated in the Cyclic Plastic Zone Ahead of the Crack Tip with Thermal Measurements. *Engineering Fracture Mechanics* **181,** 65–76. ISSN: 0013-7944 (1st Aug. 2017).

61. Soares, G., Vázquez-Fernández, N. & Hokka, M. Thermomechanical Behavior of Steels in Tension Studied with Synchronized Full-Field Deformation and Temperature Measurements. *Experimental Techniques* **45,** 627–643. ISSN: 0732-8818, 1747-1567 (Oct. 2021).

62. Meneghetti, G. & Ricotta, M. Evaluating the Heat Energy Dissipated in a Small Volume Surrounding the Tip of a Fatigue Crack. *International Journal of Fatigue. Fatigue Crack Paths 2015* **92,** 605–615. ISSN: 0142-1123 (1st Nov. 2016).

63. Meneghetti, G., Ricotta, M. & Pitarresi, G. Infrared Thermography-Based Evaluation of the Elastic-Plastic J-integral to Correlate Fatigue Crack Growth Data of a Stainless Steel. *International Journal of Fatigue* **125,** 149–160. ISSN: 0142-1123 (1st Aug. 2019).

64. Urbanek, R. & Bär, J. Lock-In Thermographic Stress Analysis of Notched and Unnotched Specimen under Alternating Loads. *Procedia Structural Integrity. 2nd International Conference on Structural Integrity, ICSI 2017, 4-7 September 2017, Funchal, Madeira, Portugal* **5,** 785–792. ISSN: 2452-3216 (1st Jan. 2017).

65. Li, L. *et al.* Local Experimental Investigations of the Thermomechanical Behavior of a Coarse-Grained Aluminum Multicrystal Using Combined DIC and IRT Methods. *Optics and Lasers in Engineering* **81,** 1–10. ISSN: 0143-8166 (1st June 2016).

66. Bergman, T. L., Lavine, A. S., Incropera, F. P. & DeWitt, D. P. *Introduction to Heat Transfer* 2069 pp. ISBN: 978-0-470-50196-2 (John Wiley & Sons, 13th June 2011).

67. *Convection Heat Transfer Coefficients Equations and Calculator* https://www.engineersedge.com/heat_transfer/convection_heat_transfer_coefficients_13855.htm (2022).

68. Kiesewetter, N. Acoustic Emission from Moving Dislocations. *Scripta Metallurgica* **8,** 249–252. ISSN: 0036-9748 (1st Mar. 1974).

69. Kiesewetter, N. & Schiller, P. The Acoustic Emission from Moving Dislocations in Aluminium. *physica status solidi (a)* **38,** 569–576. ISSN: 1521-396X (1976).

70. Vinogradov, A., Yasnikov, I. S. & Estrin, Y. Evolution of Fractal Structures in Dislocation Ensembles during Plastic Deformation. *Physical Review Letters* **108,** 205504 (15th May 2012).

71. Vinogradov, A., Danyuk, A. V., Merson, D. L. & Yasnikov, I. S. Probing Elementary Dislocation Mechanisms of Local Plastic Deformation by the Advanced Acoustic Emission Technique. *Scripta Materialia* **151,** 53–56. ISSN: 1359-6462 (1st July 2018).

72. Muránsky, O., Barnett, M. R., Carr, D. G., Vogel, S. C. & Oliver, E. C. Investigation of Deformation Twinning in a Fine-Grained and Coarse-Grained ZM20 Mg Alloy: Combined in Situ Neutron Diffraction and Acoustic Emission. *Acta Materialia* **58,** 1503–1517. ISSN: 1359-6454 (1st Mar. 2010).

73. Máthis, K. *et al.* On the Dynamics of Twinning in Magnesium Micropillars. *Materials & Design* **203,** 109563. ISSN: 0264-1275 (1st May 2021).

74. Vinogradov, A. *et al.* On the Limits of Acoustic Emission Detectability for Twinning. *Materials Letters* **183,** 417–419. ISSN: 0167-577X (15th Nov. 2016).

75. Vinogradov, A. & Máthis, K. Acoustic Emission as a Tool for Exploring Deformation Mechanisms in Magnesium and Its Alloys In Situ. *JOM* **68,** 3057–3062. ISSN: 1543-1851 (1st Dec. 2016).

76. Vinogradov, A. A Phenomenological Model of Deformation Twinning Kinetics. *Materials Science and Engineering: A* **803,** 140700. ISSN: 0921-5093 (28th Jan. 2021).

77. Baram, J., Avissar, J., Gefen, Y. & Rosen, M. Release of Elastic Strain Energy as Acoustic Emission during the Reverse Thermoelastic Phase Transformation in Au-47.5 at .% Cd Alloy. *Scripta Metallurgica* **14,** 1013–1016. ISSN: 0036-9748 (1st Sept. 1980).

78. Van Bohemen, S. M. C., Sietsma, J., Hermans, M. J. M. & Richardson, I. M. Kinetics of the Martensitic Transformation in Low-Alloy Steel Studied by Means of Acoustic Emission. *Acta Materialia* **51,** 4183–4196. ISSN: 1359-6454 (15th Aug. 2003).

79. Van Bohemen, S. M. C., Sietsma, J., Petrov, R., Hermans, M. J. M. & Richardson, I. M. Acoustic Emission as a Probe of the Kinetics of the Martensitic Transformation in a Shape Memory Alloy. *MATERIALS TRANSACTIONS* **47,** 607–611. ISSN: 1345-9678. (2022) (3 2006).

80. Vives, E., Ràfols, I., Mañosa, L., Ortín, J. & Planes, A. Statistics of Avalanches in Martensitic Transformations. I. Acoustic Emission Experiments. *Physical Review B* **52,** 12644–12650 (1st Nov. 1995).

81. Vinogradov, A., Lazarev, A., Linderov, M., Weidner, A. & Biermann, H. Kinetics of Deformation Processes in High-Alloyed Cast Transformation-Induced Plasticity/Twinning-Induced Plasticity Steels Determined by Acoustic Emission and Scanning Electron Microscopy: Influence of Austenite Stability on Deformation Mechanisms. *Acta Materialia* **61,** 2434–2449. ISSN: 1359-6454 (1st Apr. 2013).

82. Lazarev, A. & Vinogradov, A. About Plastic Instabilities in Iron and Power Spectrum of Acoustic Emission. *Journal of Acoustic Emission* **27,** 144–156 (2009).

83. Shashkov, I. V., Lebyodkin, M. A. & Lebedkina, T. A. Multiscale Study of Acoustic Emission during Smooth and Jerky Flow in an AlMg Alloy. *Acta Materialia* **60,** 6842–6850. ISSN: 1359-6454 (1st Nov. 2012).

84. Vinogradov, A. & Lazarev, A. Continuous Acoustic Emission during Intermittent Plastic Flow in α-Brass. *Scripta Materialia* **66,** 745–748. ISSN: 1359-6462 (1st May 2012).

85. Chmelík, F. *et al.* The Portevin-Le Châtelier Effect in Cu-Al Single Crystals Investigated by Acoustic Emission and Slip Line Cinematography. *Key Engineering Materials* **97–98,** 263–268. ISSN: 1662-9795 (1994).

86. Vinogradov, A. Acoustic Emission in Ultra-Fine Grained Copper. *Scripta Materialia* **39,** 797–805. ISSN: 1359-6462 (1998).

87. Richeton, T., Dobron, P., Chmelik, F., Weiss, J. & Louchet, F. On the Critical Character of Plasticity in Metallic Single Crystals. *Materials Science and Engineering: A* **424,** 190–195. ISSN: 0921-5093 (25th May 2006).

88. Weiss, J. *et al.* Evidence for Universal Intermittent Crystal Plasticity from Acoustic Emission and High-Resolution Extensometry Experiments. *Physical Review B* **76,** 224110 (21st Dec. 2007).

89. Merson, E., Vinogradov, A. & Merson, D. L. Application of Acoustic Emission Method for Investigation of Hydrogen Embrittlement Mechanism in the Low-Carbon Steel. *Journal of Alloys and Compounds. Supplement Issue: Proceedings from the 14th International Symposium on Metal-Hydrogen Systems: Fundamentals and Applications, 2014 (MH2014)* **645,** S460–S463. ISSN: 0925-8388 (5th Oct. 2015).

90. Vinogradov, A. *et al.* Propagation of Shear Bands in Metallic Glasses and Transition from Serrated to Non-Serrated Plastic Flow at Low Temperatures. *Acta Materialia* **58,** 6736–6743. ISSN: 1359-6454 (1st Dec. 2010).

91. Auld, B. A. *Acoustic Fields and Waves in Solids* 432 pp. ISBN: 978-5-88501-343-7 (Рипол Классик, 1973).

92. McLaskey, G. C. & Glaser, S. D. Acoustic Emission Sensor Calibration for Absolute Source Measurements. *Journal of Nondestructive Evaluation* **31,** 157–168. ISSN: 1573-4862 (1st June 2012).

93. Pomponi, E. & Vinogradov, A. A Real-Time Approach to Acoustic Emission Clustering. *Mechanical Systems and Signal Processing* **40,** 791–804. ISSN: 0888-3270 (Nov. 2013).

94. Vinogradov, A. Principles of Statistical and Spectral Analysis of Acoustic Emission and their Application to Plastic Deformation of Metallic Glasses. *J. of Acoustic Emission* **16,** S158–169 (1998).

95. Semmlow, J. in *Circuits, Signals and Systems for Bioengineers (Third Edition)* (ed Semmlow, J.) Third Edition, 169–206 (Academic Press, 2018). ISBN: 978-0-12-809395-5.

96. Welch, P. D. A Direct Digital Method of Power Spectrum Estimation. *IBM Journal of Research and Development* **5,** 141–156. ISSN: 0018-8646 (Apr. 1961).

97. Welch, P. The Use of Fast Fourier Transform for the Estimation of Power Spectra: A Method Based on Time Averaging over Short, Modified Periodograms. *IEEE Transactions on Audio and Electroacoustics* **15,** 70–73. ISSN: 1558-2582 (June 1967).

98. Soares, G. C. & Hokka, M. The Taylor–Quinney Coefficients and Strain Hardening of Commercially Pure Titanium, Iron, Copper, and Tin in High Rate Compression. *International Journal of Impact Engineering* **156,** 103940. ISSN: 0734-743X (1st Oct. 2021).

99. Savino, L. *et al.* Free Emissivity Temperature Investigations by Dual Color Applied Physics Methodology in the Mid- and Long-Infrared Ranges. *International Journal of Thermal Sciences* **117,** 328–341. ISSN: 1290-0729 (1st July 2017).

100. Kocks, U. F. & Mecking, H. Physics and Phenomenology of Strain Hardening: The FCC Case. *Progress in Materials Science* **48,** 171–273. ISSN: 0079-6425 (1st Jan. 2003).

101. Mecking, H. & Kocks, U. F. Kinetics of Flow and Strain-Hardening. *Acta Metallurgica* **29,** 1865–1875. ISSN: 0001-6160 (1st Nov. 1981).

Part II

Article I

applied sciences

MDPI

Article

Challenges and Accomplishments in Mechanical Testing Instrumented by In Situ Techniques: Infrared Thermography, Digital Image Correlation, and Acoustic Emission

Aleksander Sendrowicz *, Aleksander Omholt Myhre *, Seweryn Witold Wierdak and Alexei Vinogradov

Department of Mechanical and Industrial Engineering, Norwegian University of Science and Technology—NTNU, 7034 Trondheim, Norway; seweryn.wierdak@gmail.com (S.W.W.); alexei.vinogradov@ntnu.no (A.V.)

* Correspondence: aleksander.sendrowicz@ntnu.no (A.S.); aleksander.o.myhre@ntnu.no (A.O.M.)

Featured Application: The proposed research is applicable to advanced laboratory mechanical testing in academic or research settings, and it is supposed be applied to the development of novel means for non-destructive testing and condition monitoring in industry.

Abstract: A current trend in mechanical testing technologies is to equip researchers and industrial practitioners with the facilities for non-destructive characterisation of the deformation and fracture processes occurring on different scales. The synergistic effect of such a combination of destructive and non-destructive techniques both widens and deepens existing knowledge in the field of plasticity and fracture of materials and provides the feedback sought to develop new non-destructive testing approaches and in situ monitoring techniques with enhanced reliability, accuracy and a wider scope of applications. The macroscopic standardised mechanical testing is still dominant in the research laboratories and industrial sector worldwide. The present paper reviews multiple challenges commonly faced by experimentalists, aiming at enhancing the capability of conventional mechanical testing by a combination of contemporary infrared thermography (IRT), rapid video imaging (RVI) with non-contact strain mapping possibilities enabled by the digital image correlation (DIC) method, and the acoustic emission (AE) technique providing unbeatable temporal resolution of the stochastic defect dynamics under load. Practical recommendations to address these challenges are outlined. A versatile experimental setup uniting the unique competencies of all named techniques is described alone with the fascinating possibilities it offers for the comprehensive characterisation of damage accumulation during plastic deformation and fracture of materials. The developed toolbox comprising practical hardware and software solutions brings together measuring technologies, data, and processing in a single place. The proposed methodology focuses on the characterisation of the thermodynamics, kinematics and dynamics of the deformation and fracture processes occurring on different spatial and temporal scales. The capacity of the proposed combination is illustrated using preliminary results on the tensile and fatigue behaviour of the *fcc* Inconel-625 alloy used as a representative example. Dissipative processes occurring in this alloy are assessed through the complex interplay between the released heat, acoustic emission waves, and expended and stored elastic energy.

Keywords: acoustic emission; infrared thermography; digital image correlation; rapid video imaging; plastic deformation; fracture

check for updates

Citation: Sendrowicz, A.; Myhre, A.O.; Wierdak, S.W.; Vinogradov, A. Challenges and Accomplishments in Mechanical Testing Instrumented by In Situ Techniques: Infrared Thermography, Digital Image Correlation, and Acoustic Emission. *Appl. Sci.* **2021**, *11*, 6718. https://doi.org/10.3390/app11156718

Academic Editors: Dimitrios Aggelis and Antolino Gallego

Received: 25 June 2021
Accepted: 20 July 2021
Published: 22 July 2021

Publisher's Note: MDPI stays neutral with regard to jurisdictional claims in published maps and institutional affiliations.

1. Introduction

Traditionally, the primary mechanical properties of structural materials are obtained through tensile or cyclic testing. Departing from routine mechanical testing procedures is required whenever the deformation and fracture processes have to be assessed and understood. A wealth of contemporary highly sensitive non-destructive experimental

methods has emerged recently to meet these challenges and to combine the advantages of both precise mechanical testing and in situ characterisation of underlying mechanisms in pseudo-real time scale. The modern high resolution infrared thermography (IRT), rapid video imaging (RVI), digital image correlation (DIC), and acoustic emission (AE) techniques are those to be listed first among many others. Although infrared methods are unique in that they provide direct access to the thermodynamics of plastic flow, strain localisation and fracture, AE offers an unbeatable temporal resolution of characterising rapid dynamics of stress relaxation processes occurring under load. Thus, both these methods reflecting the elastic energy dissipation in solids (albeit in different ways) are complementary to each other. RVI allows to inspect the development of deformation at a micro-second temporal resolution, and a combination with DIC results in the assessment of the deformation and cyclic behaviour of the material.

IRT is a versatile method in materials testing [1]. The traditional application domain of IRT is the non-contact stress analysis, which bears its origin in the thermoelastic effect in materials [2–5]. Under adiabatic conditions, the analysis of the thermoelastic effects provides a direct link between temperature variations and hydrostatic stress variation pattern [6]. In more complex settings, scattering in the infrared imaging can serve as a measure of strain energy fluctuations in the vicinity of the fatigue crack tip, thus, providing the possibility to characterise the J-integral or the stress intensity factor K during fatigue crack growth [7] from non-contact thermographic measurements [8]. Amongst other appealing applications of IRT, the possibility proposed by Risitano to estimate the fatigue limit rapidly with a small number of samples is to be mentioned [9]. The further elaboration of this approach allowed not only the fatigue limit to be estimated, but the entire fatigue life curve to be recovered in a cost-effective way [10]. Another common use of the IRT method relies on the comparison of the temperature response with the load signal. If the adiabatic conditions are met and no cyclic plastic deformation occurs, the temperature change should be proportional to the change in the load signal (with a negative proportionality constant). This behaviour changes when plasticity is present [7]. Being a dissipative process by nature, plastic deformation affects the temperature response. Based on this premise, Ancona et al. [11] used a second order Fourier series to investigate the first- and second-order harmonics of the temperature, which allows to perform thermoelastic stress analysis, locate the crack tip, and gain information regarding plastic deformation. Other authors have focused on the energy sources that cause the dissipation of the thermal energy at the crack tip, and its relation to damage [12]. Many of these analytical approaches can be combined into a common workflow.

RVI has been proven to be a technique enabling direct assessment of the dynamic effects related to plastic deformation and fracture observable at the surface. The rapid observation of the deformation-induced surface morphology permits for the in-depth characterisation of the failure mechanisms occurring at time scales ranging broadly from seconds to micro-seconds. For instance, Ju et al. [13] investigated the effect of the crack velocity in the vicinity of the crack tip, which has not been well understood as yet. The challenges faced frequently by the RVI users include, but are not limited to, (i) adequate illumination, which is particularly important for high shutter speeds; (ii) limited recording time [14]; and (iii) duration of an event, which can be too short to be captured with sufficient resolution [15]. These commonly known issues highlight the significance of an automated triggering system allowing to capture only the moments of interest with a proper reference to external conditions such as load, strain, temperature, etc. The successful attempt to use the acoustic emission technique to trigger the rapid video camera in a mechanical testing setup has been reported in [16].

DIC is a modern non-contact method of local displacement measurements which is gaining greater and greater popularity due to its versatility and high accuracy results of the measurement of the strain tensor components [1], which is comparable to or exceeds that of other conservative methods available to researchers [17]. The DIC technique enables the full-field displacement and strain maps to be obtained in a set of photographs taken

at different stages of deformation by tracking unique features in the images. DIC is an undemanding method that uses a simple set-up permitting for a widely variable sensitivity and resolution, and for high automation of displacement and strain measurements [15]. The report by Gao et al. [15] is one of multiple examples of the extensive use of RVI in conjunction with DIC to obtain displacement and strain fields, as well as to estimate the strain distribution in the vicinity of the crack tip, and the size of the plastic zone. The outstanding sub-micrometre (per pixel) resolution has been achieved with the DIC method in [18], where the plastic strain field was studied near a growing fatigue crack in a nickel-based superalloy. Pan et al. [19] provided a detailed analysis of the DIC measurement accuracy, considering the influence of both experimental conditions and the correlation algorithm itself. The guidelines for achieving high accuracy strain mapping have been provided too. Many of those recommendations were taken into consideration and implemented in the present work.

Both DIC and IRT methods are capable of characterising the local deformation behaviour of materials by full-field measurements, albeit in remarkably different ways as they refer to different physical properties. However, they both have advantages and disadvantages, which have been well understood and documented in abundant literature (for details, interested readers are referred to comprehensive reviews [1,19,20]). A qualitative side-by-side comparison of DIC and IRT techniques was made in [21], where aluminium specimens were subjected to 3-point bending loading with different velocities. It was shown that both methods were capable of visualising a plastic zone quite well, i.e., the region where heat generated occurred during plastic deformation was comparable to the plastic zone determined by DIC. However, the performance of both methods differed dramatically in dependence on the strain rate: the DIC performed notably better under quasi-static conditions, while IRT revealed the plastic zone much better under dynamic loading. Despite good visible agreement between IRT and DIC images, temperature distributions cannot be mapped directly to strain distributions since both methods are footed on fundamentally different principles, and refer to physically different measured quantities—displacements and temperature, respectively.

An AE technique reflecting the rapid local stress relaxation processes in solids has long been acknowledged by materials scientists as a powerful tool enabling the assessment of the dynamic behaviour of defects in real time scale, and the in situ characterisation of the deformation and fracture processes under load [22]. The method has gained popularity due to its extraordinarily high sensitivity to elementary mechanisms of plastic deformation—dislocation slip [23–25], mechanical twinning [26–30], temperature- or deformation-induced phase transformations [31–35], plastic instabilities of various kinds [36–44], and, of course, cracks of various types. Robust discrimination between different potential sources of AE signals is an everlasting and extremely challenging problem in the AE field. The feasibility of using various classifiers and signal- or pattern-recognition techniques to establish a basis for reliable distinguishing between different AE sources and background noise in the same dataset has been demonstrated on many materials, and several classifiers differing by classification methods, features, cost functions, robustness, etc., have been proposed and tested in the past (see, e.g., [45–48]). The method proposed by Pomponi and Vinogradov [49]) is incorporated in the present setup as a tool of choice, as will be discussed in the next section. The acoustic emission elastic waves emitted at the source and propagated towards the sensor fall in the ultrasonic frequency range, and, consequently, the AE method requires high-speed acquisition of broadband waveforms at 1–20 Msamples/s. Continuous data streaming with high acquisition rate is resource-demanding, and particularly challenging in long-term applications, e.g., during fatigue testing. The specific details of the application of AE to the fatigue crack growth monitoring will be reviewed below.

Thus, the combination of the named techniques provides a rich source of detailed information about thermodynamics, kinematics, and dynamics of deformation and fracture processes occurring on different scales. As stated above, each technique is unique, adapted

to a specific purpose, and different from others in its own regard. Although the advantages of all constituent techniques are accumulated in a combined setup, individual disadvantages can be mitigated (if not avoided altogether). The major asset of the IRT technique is that it provides integral, direct access to thermodynamic aspects of plastic deformation and fracture on the macro-scale through the measurements of the local distribution of temperature on the surface—information that is not accessible otherwise. The RVI system clarifies the details of the occurrence of deformation and fracture mechanisms, which are reflected by the surface relief on the scale ranging from macro (a whole specimen) to micro (grain, sub-grain, individual slip lines, deformation twins, microcracks, etc.), depending on the lens used. When powered by DIC, it quantifies the local strain and stress distribution in the region of interest (ROI).

Recognition of unique benefits offered by a combination of these methods has prompted several researchers to implement them in a single experimental setup and explore new possibilities for monotonic and fatigue testing of different structural materials—aluminium alloys [50–52], titanium alloys [50], 316 austenitic stainless steel [53,54], magnesium alloy AZ31 [55], various composites [6,56], concrete [57], and rock [58].

It is known that, while the combination of IRT, AE, and RVI/DIC is a powerful approach, offering a quite unique and comprehensive piece of information regarding various aspects of the deformation and fracture of the testing material, this novel approach poses many challenges faced by laboratory practitioners worldwide. The burgeoning interest and the increasing number of publications exploiting the named techniques in various combinations motivated us to review the existing challenges and good practices to address them based on our first-hand experience. The main challenges to be addressed include: (i) high mechanical noise from the dynamic testing frames affecting AE measurements, (ii) electrical noise and interference between all the devices used in the setup influencing the measured AE signal, (iii) flexible synchronisation of all testing and measuring devices, (iv) movement of the specimen and the region of interest away from the camera's field of view, (v) combination of IRT and DIC images in the common data processing framework, (vi) finding the crack tip position by means of both IRT and DIC, (vii) correcting the thermal measurements for the lower than unity infrared emissivity, (viii) processing of noisy IRT information to calculate the heat dissipation from weak sources, etc. In what follows, we propose a versatile experimental setup addressing the named major and a few other minor (yet frequently faced and annoying) hardware and software challenges, thus enabling the seamless and synchronous operation of the IRT, AE, and RVI/DIC techniques, and report the preliminary results on the characterisation of plastic deformation and fatigue crack growth in the commercial Inconel-625 alloy.

2. Methods and Materials

2.1. Theoretical Background for Data Processing

The fundamentals of DIC, and thermodynamic calculations are briefly explained in Sections 2.1.1 and 2.1.2, respectively, and this theory is further used in the final calculations.

2.1.1. Continuum Mechanics and Digital Image Correlation Measurements

The digital image correlation technique combines image recording by optical cameras and software tracking procedures for accurate measurements of changes occurring in images due to deformation. Full-field displacement and strain maps are obtained by comparing surface images acquired along the deformation path. The algorithm recognises unique surface features and allocates their coordinates to the image pixels. It then tracks the relative displacement of these features in a set of sequentially obtained images and compares it to the first reference image, which often represents the undeformed state. The tracking is based on the iterative optimisation of a deformation vector to achieve a high correlation between the pairs of images. Thus, a stochastic, high contrast pattern on the surface throughout the entire test is required for the DIC method to find unique correlations. This can be obtained by painting the surface of the specimen with a speckle

pattern. However, in many cases, the natural surface morphology inherited from the specimen preparation, e.g., grinding, is sufficient for a successful analysis [59]. The DIC analysis returns a field of displacements **u** expressed in coordinates corresponding to either reference **X** or deformed configuration **x**. Displacements are used to find the deformation gradient **F**, which is a second-order tensor defined as

$$\mathbf{F} = \frac{\partial \mathbf{x}}{\partial \mathbf{X}} = \mathbf{I} + \frac{\partial \mathbf{u}}{\partial \mathbf{X}} \tag{1}$$

containing information about both the stretch and rotation of the body. Here **I** is the identity matrix, and ∂ denotes the partial differential. **F** is commonly used in calculations of virtually any type of strain defined in continuum mechanics.

For elastic energy (or power) density calculations, stresses and strains must be energetically conjugate. For the Cauchy stress tensor $\boldsymbol{\sigma}$, its energetic conjugate is the deformation rate tensor **D**, which, in turn, is calculated from the velocity gradient **L** as

$$\mathbf{D} = \frac{1}{2}(\mathbf{L} \cdot \mathbf{L}^T) \tag{2}$$

The velocity gradient is defined as the spatial derivative of the velocity **v** with respect to coordinates in the deformed configuration **x**

$$\mathbf{L} = \frac{\partial \mathbf{v}}{\partial \mathbf{x}} \tag{3}$$

Tracking the velocity of a given point in the deformed configuration must account for that the point moves with strain or time. To simplify calculations, the velocity gradient **L** can be obtained from the deformation gradient **F** expressed in the reference configuration according to Equation (4). The data given in the reference configuration make it easy to track a point of interest at large deformations and displacements.

$$\mathbf{L} = \dot{\mathbf{F}} \cdot \mathbf{F}^{-1} \tag{4}$$

When the Cauchy stress tensor and the deformation rate tensor are known, the mechanical power density can be calculated as

$$p_M = \boldsymbol{\sigma} : \mathbf{D} \tag{5}$$

2.1.2. Heat Equation and Infrared Thermography

The origin and theory of IRT has been described in detail elsewhere [60,61]. For the sake of completeness, the fundamentals of IRT-based methods are briefly described below.

In the thermographic systems, equilibrium infrared radiation emitted by a body is detected in a non-contact way by an infrared detector. Assuming a black-body model and using Stefan–Boltzmann's law, the temperature of the solid is obtained. When the test object does not satisfy the black body assumption, its emissivity must be considered and accounted for. The infrared emissivity is a function of wavelength, but a IRT camera works in the spectral range where it does not distinguish between wavenumbers. To correct for the non-unit emissivity, a grey body model can be adopted under the assumption that the emissivity is uniformly distributed within the camera's spectral bandpass. Since metals are opaque, the in-band radiance (IBR) received by the camera's sensor can be divided into three part: (i) the radiance emitted by the object surface, (ii) the radiance reflected from the object, and (iii) the radiance emitted by the atmosphere. The last term is often negligible when the distance between the lens and the object is small, while the remaining terms can be approximated as

$$\mathbb{L}_m \cong \overline{\varepsilon_{body}} \times \mathbb{L}_{Pl}(T_{body}) + [1 - \overline{\varepsilon_{body}}] \times \mathbb{L}_{Pl}(T_s) \tag{6}$$

where $\mathbb{L}_m$ is the IBR measured by the system, $\mathbb{L}_{Pl}(T)$ is the IBR of the Planck's function at temperature T, $\overline{\varepsilon_{body}}$ is the average emissivity in the operating spectrum, T_{body}, and T_s

are the temperatures of the object of interest and surroundings, respectively. This equation assumes that the radiance emitted from the object and the surroundings, is represented by Planck's law. The IBR is an integral of radiation over the working spectrum of the camera-lens system. Rearranging these terms gives the following equation

$$\mathbb{L}_{Pl}(T_{body}) \cong \frac{\mathbb{L}_m - [1 - \overline{\varepsilon_{body}}] \times \mathbb{L}_{Pl}(T_s)}{\overline{\varepsilon_{body}}} \tag{7}$$

which allows calculating the black body equivalent IBR of the test object. From the last equation, the temperature of the object can be calculated since $\mathbb{L}_{Pl}(T)$ is a bijective function connecting the radiometric temperature to IBR (for further information, interested readers are referred to [62]).

According to Fourier's law, the differential heat conduction equation for anisotropic materials takes a form

$$\boldsymbol{\Phi}_q = -k\nabla T \tag{8}$$

where $\boldsymbol{\Phi}_q$ denotes the heat flux vector (the flow of heat through a unit area per unit of time), k is the coefficient of heat conductivity, which, in general, can be expressed in a symmetric tensorial form, and ∇T stands for the temperature gradient. Applying this equation to the experimentally measured temperature field permits determining the heat flux. Equation (8) is sufficient to describe heat conduction under stationary conditions, i.e., when the temperature distribution across the solid and the heat flux remain constant in time. To account for the non-steady behaviour, a second independent equation is required. The energy conservation law is commonly used for this purpose in the form of the continuity equation [61]:

$$\frac{\delta Q}{\delta t} = c_p \rho \frac{\partial T}{\partial t} \tag{9}$$

where the change in the internal heat energy with time, i.e., the heat power, is denoted as $\frac{\delta Q}{\delta t}$ (the symbol δ here, and in what follows, highlights that the infinitesimally small increment of heat is not a perfect differential), and it is related to the rate of the temperature change, c_p is the specific heat capacity, and ρ is the material's mass density. Conservation of energy implies that the accumulation of the thermal energy at a given point of the specimen volume is equal to the negative spatial derivative of heat flow at that point, plus any other energy put into the system. Combination of these equations gives the familiar heat conduction equation:

$$\rho c_p \frac{\partial T}{\partial t} = \dot{q} + k\nabla^2 T \tag{10}$$

The term on the left-hand side is the change in the internal heat energy, $\dot{q}$ represents a heat source function that comprises contributions from a variety of existing heat sources or sinks, and the last term on the right-hand side describes the heat energy change due to the heat flow. The term $\dot{q}$ accounts for a wealth of contributors to the energy change (except conduction), such as radiative loss, heat convection on a surface, heat dissipation due to plastic work, thermoelastic effect, and, possibly, other mechanisms that can be involved in a specific case.

When applying Equation (10) to metals undergoing deformation, heat conduction is usually significantly larger than radiative loss, or convection [63] which can often be neglected. In the case of a large temperature difference between the metal and its surroundings, the heat loss due to these terms can be accounted for if necessary. Once these terms are neglected or accounted for, the remaining part of $\dot{q}$ will consist of the thermoelastic contribution, and the part of mechanical power dissipated as heat p_D. The thermoelastic effect occurs as a reversible temperature change caused by the change in the first stress invariant s, and is usually described by the linear equation for the infinitesimally small increment of T as

$$dT = -K_t T ds \tag{11}$$

The thermoelastic parameter K_t is usually assumed to be constant [64] and expressed as

$$K_t = \frac{\alpha_T}{\rho c_p} \tag{12}$$

where α_T is the coefficient of the linear thermal expansion, c_p is the specific heat capacity (at constant pressure), and ρ is the materials density.

An integral of p_D with respect to time gives the energy density dissipated as heat w_D. The same applies to p_M from Equation (5)—the time integral of p_M yields the mechanical work (per unit volume) w_M expended on the deformation. Both the heat energy dissipated by the system w_D and the mechanical work w_M enter the first law of thermodynamics, which relates these two quantities to the change in the stored energy density w_S as

$$dw_S = \delta w_M - \delta w_D \tag{13}$$

2.2. Experimental Setup

Using the same design philosophy, two slightly different experimental setups have been developed for the axial monotonic and cyclic testing under load or displacement control and for fatigue crack growth (FCG) tests. The schematics of both setups are shown in Figure 1. Since the involved key techniques are essentially the same in both arrangements, the tensile setup can be considered as a simplified version of the one for FCG.

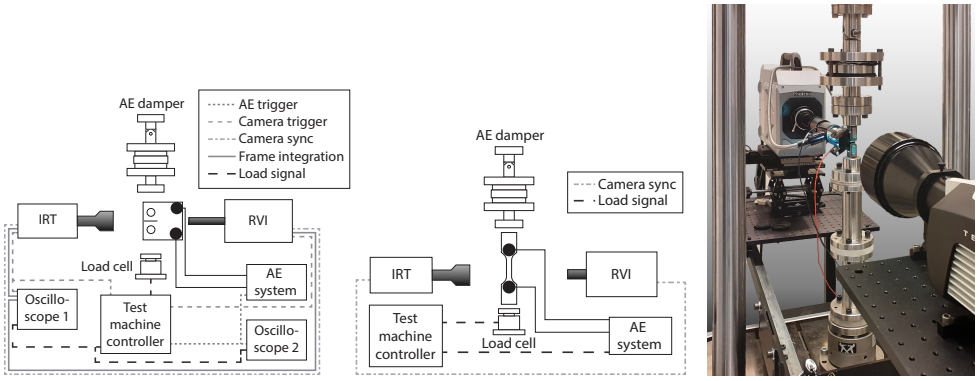

(**a**) Fatigue crack growth setup (**b**) Tensile setup (**c**) Photograph of the fatigue setup.

Figure 1. Schematics (**a**,**b**) and photograph of the setup (**c**).

In addition to the testing machine and the three independent measurement systems representing IRT, AE, and RVI/DIC techniques, the entire setup does, however, require additional instrumentation and preparation to turn it working as desired. Specifically, depending on the testing machine and the grips, measures to reduce the machine noise, which is particularly severe on most commercially available servo-hydraulic frames, is required for the AE acquisition. The AE unit often needs to be galvanically isolated from all other devices to eliminate electrical interference and improve the signal-to-noise ratio (SNR): the sensors with conductive contact surfaces have to be isolated from the specimen, and triggering circuits have to be designed with optical decoupling of all signal connections. In the setup used in the present work, the high-speed CMOS-based camera PHOTRON SA-Z maintaining a square aspect ratio of 1024 × 1024 pixels for frame rates up to 20,000 fps (up to 1,000,000 fps at a reduced resolution) with 64 GB on-board memory was

used. A versatile modular microscopic and microscopic long-focal zoom lens Navitar-6000 with the through-the-lens coaxial high-power Hayashi LA HDF7010RL LED illumination unit was attached to the camera for high-speed shooting. The maximal spatial resolution with this lens system is approximately 0.7 µm. The camera was mounted on a motorised computer-controlled linear stage LNR502E (Thorlabs, Newton, NJ, USA), which allows the camera to move together with the crack tip to measure the crack length precisely even when the surface is polished, and the camera's position and relative motion would be difficult to track.

IRT measurements were performed using a Telops FAST M350 mid-wave, high-speed camera, with an operating spectral range of 1.5 µm to 5.4 µm and the indium antimonide (InSb) cooled sensor. The camera has a typical in the class noise equivalent temperature difference (NETD) value of 20 mK (referring to 30 °C background temperature). Even though, NETD is a quantity that might characterise the inherent property of the sensor at a given reference temperature, when it comes to practical measurements, the NETD parameter represents the upper bound estimate of the thermal resolution of the entire thermographic system. The NETD value depends on the settings, most notably on the temperature of the tested object, the spectral transmittance of the camera optics, f-number characterising the lens aperture (a low f-number means a larger aperture), exposure time, etc. [65,66]. Therefore, the actual NETD value of the experimental setup can be considerably higher. The sensor has a 640 × 512 pixels resolution and the maximum frame rate is 355 fps at full resolution. The internal memory of the camera was 16 GB and a CameraLink interface enabling direct data transfer to an external drive. The camera was firmly mounted on a tripod as shown in Figure 1c. The IRC-LENS-G1-MW 1X microscopic lens ($f/3$) with a working distance of 260 mm was used in the FCG setup. The sensor size is 15 µm, which, in combination with the 1X lens, renders a spatial resolution of 15 µm. The Janos Technology 40,494 25 mm lens ($f/2.3$) with $1/4''$ extension ring was used in the axial setup, although both lens sets can be used interchangeably, depending on the dimensions of the test specimens.

For AE recording, the PC-controlled system based on 18 bits PCI-2 (MISTRAS, Princeton, NJ, USA) data acquisition board with a data streaming capability (see [67] for technical details) was used. The signal from the sensor output is amplified by 60 dB by the low-noise wide-band preamplifier 2/4/6 with the built-in band-pass 30–1200 kHz filter. The background noise level measured peak-to-peak was of 32 µV or less at the sensor output (depending on the sensor used). The MISTRAS F50α 200–800 kHz wideband sensor was used. Molykote 33 silicone-based grease was used as the coupling medium, and the sensor was mounted using a 3D-printed polymeric mechanical clamp. The background noise level at the sensor output was measured with the specimen mounted at zero load as of 3 µV rms (of 31 µV peak-to-peak) in the tensile setup and of 2.6 µV rms (of 27 µV peak-to-peak) in the FCG setup. The AE recording was performed continuously at 2 MHz sampling rate. The preference to use the waveform streaming acquisition mode is given based on the strong arguments unfolded in [68–72]. In brief, AE during plastic deformation and fracture of structural materials appears as a random sequence of arbitrarily spaced individual pulses having different waveforms and amplitudes depending on the properties of the emitting source. The amplitude of AE bursts can vary by several orders of magnitude in the dynamic range exceeding 100 dB. Pulses with a high SNR (e.g., >10 dB) are easily detectable by simple hit-detectors based on the amplitude threshold, which are traditionally built-in in commercial AE apparatus, where a hit is marked when the pre-set amplitude threshold is crossed by the signal [67]. As has been reviewed in [68,70], and more recently in [71], this method suffers from many irrecoverable drawbacks when low-amplitude signals are to be resolved on the background of electric noise or when the low-amplitude transients overlap and form a continuous signal. For instance, if the trigger level is set sensitively low, false alarms are recorded due to fluctuations of noise, which, as stated above, is particularly important in dynamic fatigue setups. Unidentified false triggering burdens the data analysis and can potentially result in misinterpretations and wrong decision making. For example,

a common practice in the AE field of counting the AE activity as the number of AE hits per unit of time suffers particularly strongly from the arbitrary settings of the amplitude threshold. Low-amplitude continuous signals, comparable to the background electric noise, are the most common signatures of plastic deformation due to dislocation slip [24], which not only dominates the strain hardening behaviour during the monotonic tensile or compressive test but is of crucial significance for the evolution of the microstructure in the plastic zone ahead of the propagating fatigue crack. Moreover, it is plastic work that determines the heat dissipation in the cyclic plastic zone [73–76]. In addition, a wealth of powerful signal processing techniques have been developed recently for unveiling and handling low-amplitude signals buried in the background noise, provided the waveform is continuously recorded in a sufficiently wide frequency range (see [69,71] and literature therein). Thus, it is for these reasons the use of thresholdless high-speed data streaming is uncompromising when it comes to the need to investigate the low-amplitude dynamic events in the AE flux.

All measuring devices have to be synchronised and triggered depending on the desired timing and loading conditions, which might be challenging as the definition of moment of interest (MOI) might vary for different devices. To this end, a homemade PC-controlled triggering unit was used for precise temporal synchronisation of both cameras with the current load. Tracking and logging of the external load signal and the load-controlled trigger signal (MOI) were performed by a user-programmable USB digital oscilloscope PicoScope-4284A. Additionally, the AE event-controlled triggering of high-speed and IRT cameras, similar to that proposed in [16], is also possible in the present setup, and is particularly appealing for capturing rapid events, such as the nucleation of brittle cracks, mechanical twinning or Lüders bands, or other plastic instabilities. The spatial alignment of both cameras was achieved with reference points on the surfaces of the specimens, which allows finding the transformation matrix between images acquired by both cameras.

The constituent measuring methods can also have contradictory (if not mutually exclusive) requirements for testing conditions to yield the best results. For example, IRT might need high test frequencies to promote adiabatic conditions, while, on the other hand, the short exposure time and large magnification reduce the SNR. AE can also suffer from dynamic mechanical noise when the test frequency is high but, on the other hand, being proportional to the strain rate, AE due to plastic deformation can benefit from high testing frequencies. These are just a few examples of the trade-offs and multiple issues that must be considered when selecting experimental settings.

2.2.1. Testing Machine and the Noise Reducing Damper

Servo-hydraulic machines, which are most commonly used in fatigue experiments, are known to produce background vibrations on the actuator and a test piece, arising primarily from servovalves [77,78]. These vibrations often cause uncontrollable fluctuating and load-dependent noise at the output of the AE sensor attached to the test specimen, giving rise to false signals, both continuous and transient, which fall in the frequency and amplitude range comparable to damage-related acoustic emissions, thus making it challenging to remove them in the post-mortem analysis.

To reduce the noise-related artefacts in AE data, several methods have been probed in the research community. These include: (i) passive mechanical dampers installed between the frame, actuator, and the test specimen [77]; (ii) guard sensors and sensor arrays locating the AE signals from the region of interest (e.g., close to the crack tip) [79–83]; (iii) load gating and partitioning the signals with respect to the load (e.g., acquiring the signals which appear only close to the peak load) [84,85]; (iv) setting the high amplitude discrimination threshold [86,87]; and (v) post-processing filtering methods including criterion-based feature selection [88], information entropy-based approach [78], and a variety of hierarchical clustering procedures in an attempt to identify outliers according to distributions of specific features [89].

As will be seen shortly, passive damping is universally efficient and is undeniably recommended for any experimental setup based on servohydraulic or electrodynamic frames. In fact, as has been correctly pointed out by Sauerbrunn et al. [78], neither of the other measures taken individually or in any combination can be considered 100% reliable and universal. We share this opinion, supported by our extensive laboratory experience. Even a very appealing technique of locating AE sources within ROI according to signal arrival times between two or more sensors suffers from substantial drawbacks. To be more specific, it cannot be used for small samples, it fails to work with continuous signals, which are common due to plastic deformation of ductile materials, and, besides, the acquisition system is often overloaded and ceased to operate under cyclic loading due to intensive pulse flow from the area outside ROI. The noise signals and damage-related signals can hardly be distinguished by their frequency spectra, thus making frequency-based filtering ineffective. Needless to say that setting the high amplitude threshold does not help much to solve the machine noise problem as a lot of valuable low-amplitude acoustic information is missed in this way.

Therefore, the present experimental setup is based on the 10 kN electrodynamic Instron E10000 Electropulse universal testing machine. Compared to servo-hydraulic testing frames, a family of modern electrodynamic machines are considerably more silent. Nonetheless, the examination of several electrodynamic machines has shown that they are not completely noise-proof in the dynamic regime and a damper-clevis assembly shown in Figure 2 was installed between the actuator and the specimen grip to reduce the machine noise captured by AE. The clevis joints have a small contact area which helps to reduce the noise. A mechanical damper, inspired by Harris and Dunegan's early work [77], was made as a laminated structure consisting of numerous aluminium and felt interfaces. The sketch and the photograph of the damper are shown in Figure 2. The signal on the actuator, the signal on specimen without the damper, and the signal on the specimen with the damper installed during cyclic loading of a non-deformable "dummy" specimen are compared in the same figure. One can see that the noise measured on the specimen with the damper was equivalent to the electric background noise at the sensor output.

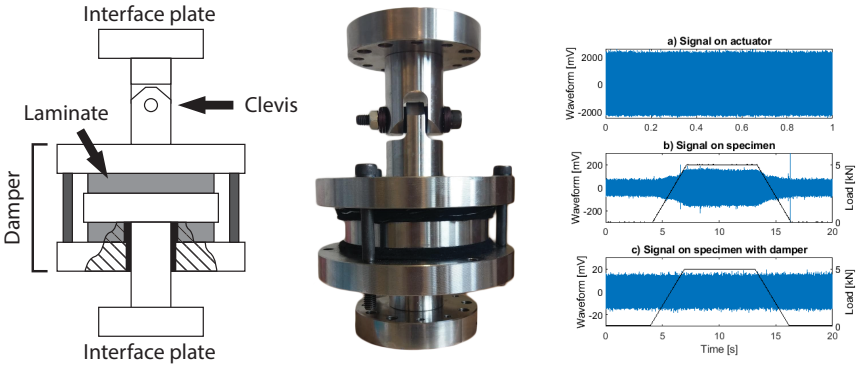

(**a**) Sketch of the damper (**b**) Photograph of the damper (**c**) AE signal at different locations

Figure 2. Clevis damper assembly.

2.2.2. Fatigue Crack Growth Setup

In this setup, the cameras can run at the same frame rates and similar magnifications, if spatial and temporal synchronisation is of particular concern, or they can run with notably different settings otherwise. For the sake of adaptability to a variety of possible testing conditions, the AE system had its own load-controlled triggering system with a digital

oscilloscope to record the load data since the built-in parametric channels in the PCI-2 board operate upon hit-based triggering and are not suitable for continuous recording of external signals. The need for the independent AE trigger is obvious, for a long-term fatigue test, it is virtually impossible to perform the continuous acquisition at 2–5 MSamples/s rate. Therefore, the trigger is programmed to open the AE continuous recording during several consecutive loading cycles. Then, the acquisition stops, and resumes again after the pre-set number of cycles. In this way, the AE system can run independently or synchronously with the cameras.

2.2.3. Tension/Compression Testing Setup

Since the tensile test does not last too long and can be recorded continuously, the main difference between the tensile and FCG setups is in the simplified triggering. A camera with the higher 2448 × 2050 pixel resolution and 15 fps frame rate (Allied Vision Prosilica GC2450 with Tamron 272EN II lens) was used for DIC, if the rapid shooting was not demanded in particular experiments.

2.3. Sample Preparation and Testing Conditions

The material used for the illustration of the capacity of the combination of all chosen in situ techniques with a developed setup was the commercial Inconel-625 alloy with the nominal composition NiCr21Mo8.3Nb3.5 (in wt.%) manufactured by Böhler Edelstahl GmbH & Co KG (Vienna, Austria). The material was annealed at 930 °C for 75 min and quenched in water, resulting in a reasonably uniform microstructure with ≈10 µm grain size. The tensile specimen had a dog-bone geometry with a gauge length of 12 mm, 3 mm width, and 2 mm thickness. The compact tension specimens were made according to the ASTM E647-15e1 standard [90], with 50 mm width W and 4 mm thickness. All specimens were shaped by electric discharge machining.

To facilitate infrared measurements, and improve the signal-to-noise ratio through the increase in the emissivity coefficient of the test object, the dog-bone tensile specimens were coated with a black matt paint (with the emissivity of 0.95) that does not peel off at large strains. The surface facing the DIC camera was additionally covered with white dots sprayed to create a speckle pattern.

The compact tension (CT) specimen for FCG tests were ground down to FEPA #2000 grade. The surface observed by the IRT method was covered with the same black paint, and the RVI side was further treated depending on the purpose of the test. For deformation microstructure observations, the specimens were polished to 1 µm, and optionally etched. For the DIC analysis, the surface was grounded with FEPA #4000 paper in one direction, and random scratches were made with grade #2000 and #4000 papers. If the spatial alignment between the cameras was required, reference lines were made on the surface of the specimen.

Tensile tests were performed under velocity-controlled, nominally constant strain rate of $1 \times 10^{-2}\,s^{-1}$. FCG tests were performed using the pre-cracked CT specimen cyclically loaded under the load-control mode with the maximum and minimum loads of 7000 N and 1400 N, respectively (the fatigue ratio $R = 0.2$).

2.4. Data Processing

2.4.1. Tensile Data Processing

The flowchart of data processing involved in the routine tensile test is shown in Figure 3, where data acquired from all four sensors are colour-marked, and the interactions between different data sub-sets and different processing steps are shown by arrows. Sampled load data were interpolated to be aligned precisely with optical images in time. We have chosen the open-source DIC software Ncorr [91] (http://www.ncorr.com (accessed on 24 June 2021)), which allows for creating and building-in the user-made scripts to facilitate the automation of the data analysis process without compromising the quality of the obtained displacements and strain fields [92]. Numerous studies have demonstrated that

with the appropriate settings, DIC can capture the strain on the surface of tested with the accuracy comparable to that of high precision extensometers or strain gauges attached to the same specimen [93–95]. Specifically, the Ncorr efficiency benefits from the state-of-the art inverse-compositional Gauss–Newton (IC-GN) optimisation algorithm proposed by Pan et al. [96] for fast, robust and accurate full-field displacement tracking with sub-pixel resolution. Leaving the correlation algorithm unchanged, the cross-system data handling and integration software was developed in the present work in MATLAB [97].

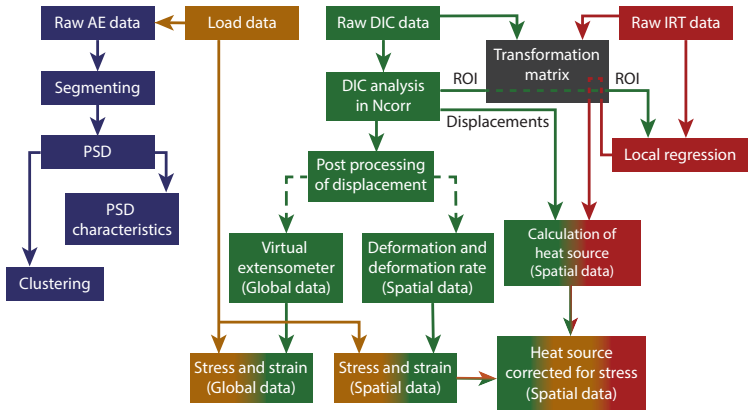

Figure 3. Flow-chart of data processing for the tensile test.

Digital Image Correlation

The first step in the processing of images captured by the visible light camera was the DIC analysis. The reference image corresponded to the undeformed specimen. The subset radius was selected between 20 and 25 pixels, and, since the subset spacing reduces the data size, it was chosen to roughly match the size of the images from IRT. For the high strain analysis, the reference image was updated once the correlation became poor. In a later step, the displacements were formatted to be expressed with respect to the initial reference image. With the automatic seed propagation, a seed which is the initial location used for correlation, seeds are updated too. More information can be found in the Ncorr manual [98].

Once the point-wise displacements were calculated, further processing was divided into two distinct parts. In the first part, a virtual extensometer was applied to measure the global engineering and true strain concurrently with the corresponding engineering and true stress calculated using the load signal and the dimensions of the specimen cross-section. In the second part, local deformations and deformation rates were calculated. Ncorr provides displacement fields in the reference and deformed configurations, from which the deformation gradient can be calculated using Equation (1). The property of primary interests, besides the stress and strain, is the mechanical power, which requires the rate of deformation tensor **D**. This tensor is based on the velocity gradient given in the deformed configuration **L**, as described by Equation (2), so to express it in the reference configuration, the relation between the deformation gradient in reference configuration and velocity gradient in deformed configuration in Equation (4) was used.

After this step, the displacements, deformation, and deformation rate are known. Calculation of engineering stresses is performed from the load signal and samples geometry. To quantify the overall true stress σ_T, the scalar engineering strain ϵ obtained from the virtual extensometer is used, and σ_T calculated conventionally as

$$\sigma_T = \frac{P}{A_0}(1+\epsilon) \tag{14}$$

where P denotes the applied load, A_0 is the initial cross-section. The last expression gives an average value for the region covered by the virtual extensometer in the loading direction. The σ_T value provides a good representation of the flow stress as long as the deformation is homogeneous. As soon as the neck sets in, the 1D extensometer data are not accurate any more. An alternative way of estimating the stress tensor is to use the measured local strains in Equation (14) averaged over the cross-section of interest. As long as the deformation is uniform, the results are the same as those estimated from the extensometer. However, measuring local strains yields significantly better stress estimates when strain localisation occurs. Other than longitudinal components in the stress tensor can be estimated from flow rules [99] or from other correction schemes reviewed by Tu et al. [100], if necessary. Once the stress and the deformation rate are known, the mechanical power can be calculated by Equation (5).

Infrared Thermography

Calculations based on infrared thermography data are dependent on the temperature development over both time and space. Since large deformations can be encountered in a tensile test, it might be challenging to track a point on the specimen surface precisely. The sufficiently accurate tracking, however, can be achieved with DIC. To be able to use DIC to track IRT data, the transformation matrix was found between the DIC and IRT images obtained from specific cameras. The transformation matrix maps coordinates from one image to the other. Assuming the deformation pattern is equal on the both opposite surfaces, the displacement field can be transformed to fit IRT data and vice versa. To find the transformation matrix, calibration points, which simply refer to specific chosen locations in an IRT image and a corresponding DIC image, are needed. If there are 3 points, the software finds an affine transformation, and if there are more, the transformation type is *projective*. The transformation was found using the Matlab embedded function [101]. This procedure and the result are illustrated in Figure 4, where the rightmost image shows a superposition of two images based on the difference between them.

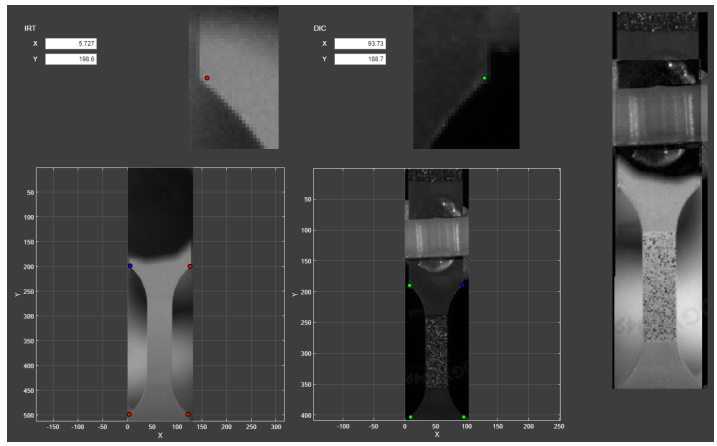

Figure 4. Graphical software used to find the transformation matrix; the coloured points are the operator–chosen reference points.

Once the transformation matrix is found, the ROI can be mapped from the DIC optical domain to the IRT temperature domain.

The challenge, which the practitioners usually face with the heat Equation (10), is related to the second-order spatial derivatives. The temperature field measured by the camera is affected by the quality/ or roughness of the surface [102], the texture of the paint, the emissivity of the paint (which is lower than unity, inhomogeneous, and can possibly change during the test, particularly at large strains when the deformed surface gets rough), sensors, internal noise, etc. The inevitable fluctuations in the temperature distribution make the estimation of the second-order spatial derivative a formidable task. The grey-body emissivity correction method using Equation (7) can be employed to reduce the impact of reflections from surroundings. The method is easy to implement as the emissivity is considered to be constant in the narrow spectral band (3–5 µm due to the lens used). Two main assumptions, however, stand behind this method: (i) the grey-body approximation is valid, and (ii) the reflected radiance is represented by the Planck's function. If the emissivity change appreciably during the test, it must also be accounted for. The error of a black body assumption can be calculated using Equation (6). When the emissivity is high, and the temperature of the specimen is close to the temperature of the reflected surroundings, and the error will be negligible.

Once the temperature field is corrected, noise filtering or noise cancelling procedures are required, although they can introduce some artefacts specific for the filters used. To overcome this problem, the local regression procedure was implemented in the present work. A small circular region close to the point of interest is selected, and a second-order polynomial surface is fitted to it. As long as the heat dissipation is uniform across the chosen region, the temperature within it can be represented very accurately by that polynomial function. However, if the heat dissipation is not uniform, the regression approach causes a smoothing effect: the higher the smoothing factor, the sharper the transitions in the source function. In the tensile test, the heat dissipation is relatively homogeneous as long as plastic deformation is uniform and no local plastic instabilities, such as necking, Lüders bands, or Portevin-Le Chatelier bands show up. In general, the larger the regression radius, the less noise. However, the notice is in place that the regression radius should be small enough to cover the area of the approximately uniform heat dissipation, i.e., the appropriate regression radius depends on the feature size observed in the test. The procedure is illustrated in Figure 5.

The procedure repeats itself for the entire ROI in each image automatically once the operator confirms the satisfactory results of data regression. The results from local regression obtained from IRT data were transformed to fit the DIC data to track the temperature evolution and its Laplacian transform entering Equation (10). The power density of the heat sources is calculated according to Equation (10), and, since the temperature evolution following changes in the heat source was tracked for a given control volume, the power density was integrated over time to find the total energy dissipated at each point of the surface over time. The integration over the volume yields the total power or energy dissipated in the region of interest.

The thermoelastic effect is most significant in the elastic region, and it has only a small effect on the source function in the plastic region. Nevertheless, the source function was corrected for it to give the mechanical power dissipated as heat p_D. Once the mechanical work expended for deformation, and the energy dissipated as heat have been simultaneously measured, the first law of thermodynamics can be used to calculate the stored energy [103–106] (see also a comprehensive review by Bever et al. [107] and references therein). This quantity is of particular interest not only because it relates to the microstructure and deformation mechanisms, but also because it serves as a physically-sound measure of deformation-induced damage. The IRT technique provides a direct estimate of this quantity that is not accessible by in situ measurements otherwise.

As a final note to this session, one can notice that the procedures for joint processing of visual and thermal images could be greatly simplified if thermal and visual cameras were

be equipped with lens sets having the same viewing angle and magnification. However, the use of infrared and optical measurements can have different objectives. For the sake of versatility, it is important to keep the possibility to perform the test using different optics on both systems, thus referring to not necessarily exactly the same but overlapping ROI.

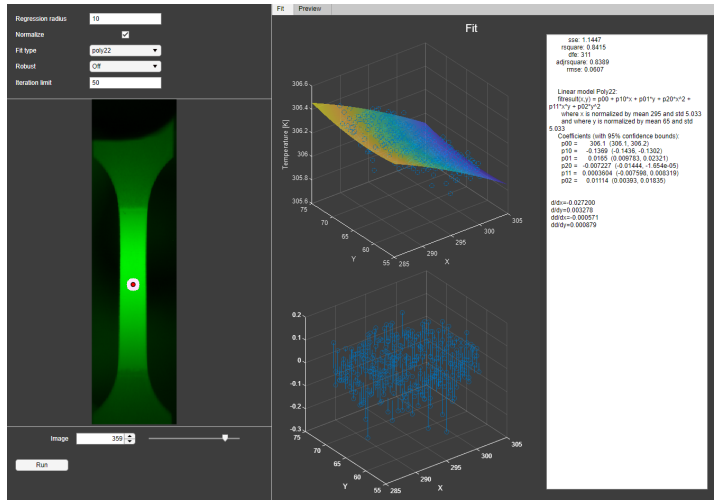

Figure 5. Screenshot of the graphical user interface used for local regression of IRT data. The global temperature distribution across the specimen gauge length is shown in the left panel; the chosen area for local regression at a particular location (red circle) had a diameter of 21 pixels and is shown in white. Temperature readings (blue open circles) and the fitting surface are shown in the middle-up sub-figure, while the result of subtraction of the fitting surface from the data showing the steady thermal noise are displayed in the middle-bottom sub-figure. The fitting model is represented on the right.

Acoustic Emission

The ultimate goal of AE signal processing is to recover properties of the emitting stress relaxation process (or, possibly, multiple processes operating either simultaneously or in a sequence) from the observed data. This pseudo real-time information helps to gain better understanding of underlying accommodative mechanisms active under load. To reduce subjectivity in the interpretation of AE results, the analysis should be non-supervised and data driven. To this end, the processing of the continuously recorded data was performed based on the procedures described in [49]. The continuously streamed acoustic emission data are sectioned into consecutive equal segments of 1024–4096 readings, depending on the temporal scale of the observed transients. After conversion to the frequency domain by the fast fourier transform (FFT), the power spectral density (PSD) function $G(f)$ was estimated using the Welch's method. The AE power P_{AE} of each segment was then calculated as

$$P_{AE} = \int_{f_{min}}^{f_{max}} G(f)\, df \tag{15}$$

where f_{min} is the high-pass filter cut-off frequency, and f_{max} is the Nyquist frequency. The corresponding median frequency, f_m was calculated based on the definition through the implicit equation

$$\int_{f_{min}}^{f_m} G(f)\,df = \int_{f_m}^{f_{max}} G(f)\,df \tag{16}$$

In order to separate the signals originating from distinct sources (including distinguishing between damage-relates sources and possible outliers and false alarms caused by extrinsic mechanical sources and electrical interferences) the cluster analysis can be performed using the non-supervised data driven adaptive sequential *k*-means (ASK) algorithm (for mathematical details details of this classifier, readers are encouraged to review the original publication [49]; several successful examples of the application of the ASK algorithm can be found in [35,108–110]). The procedure uses a normalised PSD $\frac{G(f)}{P_{AE}}$ of each data segment as an input for pairwise comparison. It should be noted that due to strong resonance frequencies, which are pronounced even in the broadband commercial sensors, the shape of the PSD is strongly affected by the frequency response of the sensor itself. Therefore, to distinguish between the AE sources based on the evolution of their Fourier or wavelet spectra, it is desirable to use a sensor with the response as flat as possible. Although the AE signal processing software used here does have the intrinsic capacity to perform a versatile cluster analysis after compensation for the background noise, and for the features of the sensor response, we shall not exemplify it in the present work, and the more detailed AE analysis will be reported elsewhere.

The AE signal was synchronised with the video measurements with respect to the moment of failure, which produced a distinct signal with rapid overshooting, and which is easily and precisely identifiable in the AE data. The maximum synchronisation error, in this way, is equal to half of the time elapsed between the last image before failure, and the first image after failure.

2.4.2. Fatigue Crack Growth Data Processing

Figure 6 shows the overview of DIC and IRT data processing for a FCG test. Since the AE data processing is essentially the same for both tensile and fatigue crack growth tests, it was excluded from the figure for brevity (see Figure 3 for an overview instead). IRT analysis is divided into three primary steps: (i) locating the crack tip, (ii) finding cameras motion and defining a reference point (feature on the surface) to determine the global position of the crack, and (iii) motion compensation, and data smoothing for spatial and temporal calculations. The DIC method utilises a similar approach for finding global crack properties, e.g., the crack length. Details of processing of FCG DIC and IRT data are provided in Sections 2.4.3 and 2.4.4, respectively.

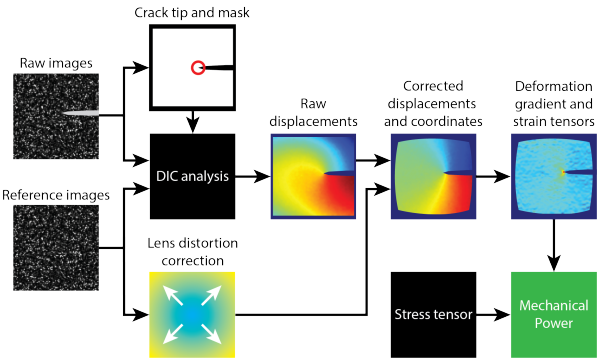

(**a**) Chart of data processing for rapid photography images from a fatigue crack growth test.

Figure 6. *Cont.*

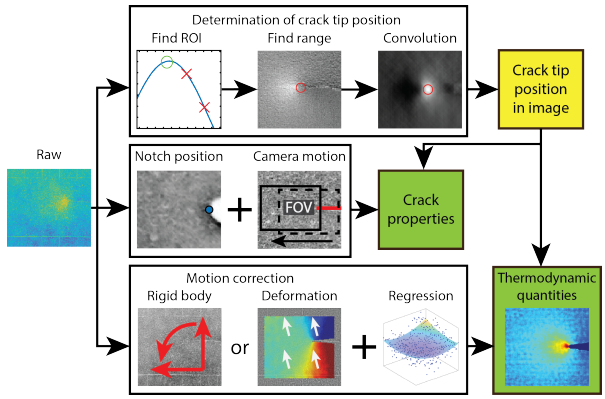

(**b**) Chart of data processing for infrared images from a fatigue crack growth test.

Figure 6. Flowchart illustrating processing of IRT and DIC data for a FCG test.

Rigid Body Motion

The motion of the camera or the specimen during mechanical testing is inevitable and this needs to be compensated by data processing. The corrective procedure is essentially the same for both DIC and IRT images (with only minor differences between these two), and is, therefore, outlined here. Once two images of interest, which are displaced with respect to each other, are selected, Features from Accelerated Segment Test (FAST) [111] are obtained using Matlab routines [112]. If preferred, ROI from which the features have been extracted can be applied. This is of interest when only a part of the image represents rigid body motion. Further, the features are extracted, and matched, which allows to estimate the geometrical transform between images. Displacements described by this transformation matrix might be caused by the motion of the camera or the specimen. In case of IRT images, they were high-pass filtered and re-scaled before the FAST features were found. Figure 7 shows superposition of two IRT images with two different pseudo colours. Since the camera was moved horizontally between the two to follow the growing crack, there is a displacement between them. ROI was reduced to the left half of the image, to exclude the crack visible on the right-hand side. FAST features are marked with the red circles on image 1, and the corresponding green crosses on image 2. The yellow line between the matched points shows the displacement between them, indicating that the motion between the images was dominated by the translation along the horizontal axis.

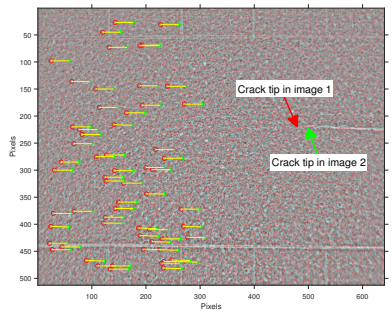

Figure 7. Illustration of FAST points used to find camera motion between two successive recordings.

2.4.3. Rapid Video Imaging and Digital Image Correlation

Optical imaging produces a sequence of images, which was used for the DIC analysis. The majority of modifications in the Ncorr codes were made to automate and accelerate the process without affecting the DIC algorithm itself. Each recording was processed individually. The processing was divided into two parts. We first analysed the entire sequence of images with respect to the "cyclic" reference image taken close to the mean load immediately after the test was paused. In a second part of the analysis, we compared two reference images: the "cyclic" reference image corresponding to the finally deformed state and the one of the undamaged sample. The second step allowed us to find the total strains with respect to the undeformed specimen. However, when plastic deformations are large, the surface becomes so severely deformed that the correlation between the undeformed and finally deformed specimens is not reliable any more or it can disappear completely. Nonetheless, the analysis of the image sequence with respect to the cyclic load can still deliver the rate of the deformation tensor as a function of the number of cycles.

Region of Interest and Mask

To ensure a high quality of strain data in the vicinity of the crack tip, the crack representing discontinuity in strain data must be covered by a virtual mask. If the mask is too wide, valuable data in close proximity to the crack path might become lost, whereas if it does not cover the crack sufficiently, incorrect strain values can be obtained. The precise determination of the crack tip position is, therefore, of crucial importance. There have been many methods proposed in the literature to find the crack tip position (see [15,57,113,114] and references therein). The approach we utilised in the present work is based on the simple observation that the crack was dark, and it was well visible throughout the test. A convolution algorithm was developed to find this dark region, and the end of it was defined as the crack tip. Additionally, the images corresponding to the maximum and minimum load were used to find the motion range within a given recording to make sure the mask was created sufficiently within the borders of the field of view (FOV). An example of the DIC mask created by this algorithm is shown in Figure 8.

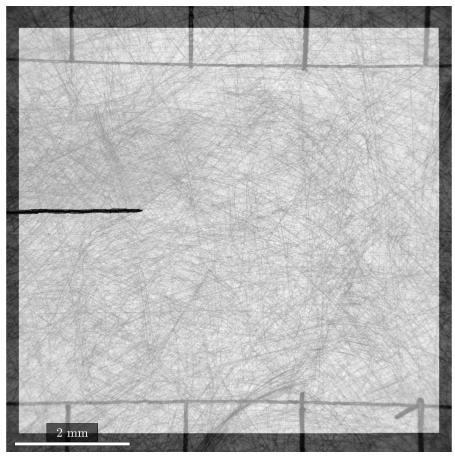

Figure 8. Mask created based on the specimen motion and crack. Lens-induced distortions can be noticed as a curvature of straight judicial lines scratched on the surface.

DIC Analysis

Once the images are chosen for the analysis and the mask is applied, the seed points are selected. The algorithm for that was based on Speeded Up Robust Features (SURF) [115], as the features identified in this way are good candidates for distinct points. A similar approach was used by Wang et al. [116]. SURF points were found in the reference image, and they were classified according to their strength. The number of points corresponding to the number of processor threads was selected. To make sure that they were roughly equally spaced, the chosen points were placed as far away from ROI borders, and from each other as possible. Hence, the region for the analysis was approximately evenly distributed between the CPU threads for efficient computation. Once all of these steps were automatised, the DIC analysis could run automatically.

Correction for Lens Distortion

Like the majority of microscopic lenses, the lens used for FCG tests distorts the image. The Ncorr DIC algorithm has a rather simple way for accounting for the error in displacements caused by lens distortions, provided the lens distortions are known. To quantify and eliminate the distortions, the method proposed by Pan et al. [117] was employed. The linear least-squares algorithm estimates the distortion coefficient from the distorted displacements obtained from the rigid body, in-plane translation DIC analysis. Ncorr utilises this coefficient to correct the distorted displacement fields. Corrected displacements are, however, still in distorted coordinates. This affects the strain calculations, as the Ncorr algorithm assumes an equal and constant spacing between points, which is not the case with non-negligible lens distortions. To express the displacements in undistorted coordinates, first the valid undistorted coordinates within the analysed region were found. The mask containing the valid pixel locations was undistorted, creating a new mask consisting of undistorted coordinates. To find the displacements in the undistorted coordinates, the equivalent distorted coordinates were calculated with the distortion model. Eventually, the displacement data could be interpolated at these locations, resulting in displacements in the equivalent undistorted coordinates. Results for raw and corrected displacements are exemplified and compared in Figure 9: owing to these implemented measures, the improvement of displacement measurements after lens distortion correction is remarkable, which, in turn, results in the enhanced accuracy of strain field estimates.

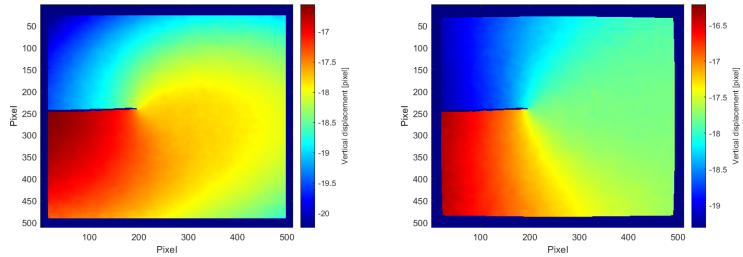

(**a**) Raw displacements (**b**) Corrected displacements

Figure 9. Comparison of raw and corrected displacements.

Deformation Gradient and Strain Tensors

Once the coordinates and displacements have been corrected, the strains can be seamlessly calculated using the deformation gradients calculated by Ncorr. As a result, the displacement vector **u** is obtained in the reference and deformed configurations, **X** and **x**, respectively, as well as the derivatives of the displacement vector with respect to coordinates in both configurations.

The global displacement field between the undeformed and cyclically deformed material is denoted as $\mathbf{u}_{cu}$. Images obtained during cyclic test were processed one by one with respect to the "cyclic reference" image, which was acquired immediately after the cyclic images. The data for this sequential cyclic analysis will be denoted by the subscript index c ($\mathbf{u}_c$, $\mathbf{x}_c$, and $\mathbf{X}_c$), and data from the analysis with undeformed body will have the subscript index u ($\mathbf{u}_u$, $\mathbf{x}_u$, and $\mathbf{X}_u$). Since $\mathbf{u} = \mathbf{x} - \mathbf{X}$, and $\mathbf{X}_c = \mathbf{x}_u$, we can express $\mathbf{u}_u$ as

$$\mathbf{u}_u = \mathbf{X}_c - \mathbf{X}_u \tag{17}$$

The goal is to find the deformation gradient as if the cyclic analysis would be performed with respect to the undeformed state, $\frac{\partial \mathbf{u}_{cu}}{\partial \mathbf{X}_u}$. After differentiating Equation (17) with respect to $\mathbf{X}_c$, and rearranging it, we obtain

$$\frac{\partial \mathbf{X}_c}{\partial \mathbf{X}_u} = \left(\mathbf{I} - \frac{\partial \mathbf{u}_u}{\partial \mathbf{X}_c}\right)^{-1} \tag{18}$$

Since $\frac{\partial \mathbf{u}_{cu}}{\partial \mathbf{X}_c} = \frac{\partial \mathbf{u}_c}{\partial \mathbf{X}_c} + \frac{\partial \mathbf{u}_u}{\partial \mathbf{X}_c}$, and both terms on the right hand side are known from the DIC analysis, it can be combined with Equation (18). Hence, the deformation gradient defined with respect to the undeformed configuration ($\mathbf{F}$) can be expressed as

$$\mathbf{F} = \mathbf{I} + \frac{\partial \mathbf{u}_{cu}}{\partial \mathbf{X}_u} = \mathbf{I} + \frac{\partial \mathbf{u}_{cu}}{\partial \mathbf{X}_c} \cdot \left(\mathbf{I} - \frac{\partial \mathbf{u}_u}{\partial \mathbf{X}_c}\right)^{-1} \tag{19}$$

Once the gradients with respect to both the cyclic reference image and the undeformed material are known, the strain tensors of interest can be calculated. The polar decomposition theorem can be used to decompose the $\mathbf{F}$ tensor into a product of two second-order tensors and, thus, to separate the rotation matrix $\mathbf{R}$ and the right stretch tensor $\mathbf{U}$ as

$$\mathbf{F} = \mathbf{R} \cdot \mathbf{U} \tag{20}$$

Since $\mathbf{R}^T \cdot \mathbf{R} = \mathbf{I}$ (the superscript T denotes the transpose), the rigid body rotations are eliminated, and the right stretch tensor can be determined from the relation

$$\mathbf{U}^2 = \mathbf{U}^T \cdot \mathbf{U} = \mathbf{F}^T \cdot \mathbf{F} = \mathbf{C} \tag{21}$$

which also defines the right Cauchy–Green deformation tensor $\mathbf{C}$. Since $\mathbf{F}$ is known, the deformation rate tensor $\mathbf{D}$ can be calculated straightforwardly by combining Equations (2) and (4).

2.4.4. Fatigue Crack Growth Data from Infrared Thermography

Finding the Crack Tip Position

To determine the crack tip position, we combine the thermoelastic effect and the heat dissipation measurements. The idea is to take the data recorded just after peak load, where the load decreases while the crack closure effect is negligible. At this stage, both the thermoelastic effect and the heat dissipation (if any) contribute to the temperature rise, with the maximum reached at the crack tip. The region behind the crack tip should experience a lower temperature change, as the closure effects are not active, and the stresses are comparatively low. The images taken at the upper and lower limit (marked with red in Figure 10) were stabilised with respect to the cyclic reference image—the image taken immediately after the test interruption at the mean load. The procedure was essentially the same as that described in Section 2.4.2 with one correction: the transformation matrix was used to transform the images with an *affine* transformation to the reference image to find the temperature change between the images. By applying convolution with a specific kernel, which added the data covered by a 90 degree angle in front of a point of interest, and subtracted an equivalent region behind it, the sharp changes are maximised, and the crack tip can be easily located at the brightest point of the convoluted image as illustrated in Figure 11, comparing the temperature change map and the corresponding result of the convolution operation. The image can suffer from noise caused by the uncoated

metallic surfaces at the crack faces. Therefore, the local extreme temperatures in the area outside the high temperature region surrounding the crack tip were replaced with the mean temperature for a given image.

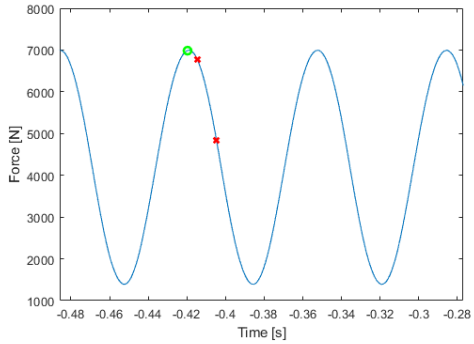

Figure 10. Load signal, and region used to determine crack tip position.

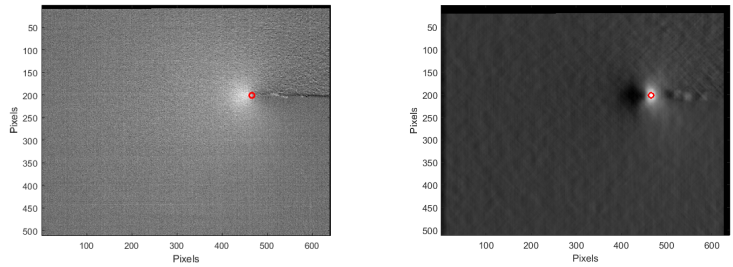

(**a**) Temperature change map (**b**) Result of the convolution

Figure 11. Determination of crack tip position from the image enhanced by the convolution procedure highlighting the crack tip.

Motion Compensation and IRT/DIC Algorithm

To measure and minimise the effect caused by the camera motion between recordings sessions, the cyclic reference image in each session was used. The procedure explained in detail in Section 2.4.2 was used to find the displacement between the images induced by the camera motion. ROI was selected to be approximately equal to half of the image without the crack. Since there is no crack in ROI, all deformations are relatively small, and the rigid body assumption holds. Figure 7 represents an example of finding how far the IRT camera has moved between two successive recordings. The transformation matrices can be combined to express the position of each reference image with respect to the first one (in any coordinate system chosen). Marking the notch position in an image, and finding its transformation matrix with respect to the first reference image, allows determining the crack position with respect to the notch. It is also possible to create a specific user-preferred coordinate system.

Tracking data points in a record can be performed in two ways. The first way is to use a geometric transform (Section 2.4.2) based on the rigid body motion assumption, which is justified for small deformations. Alternatively, one can perform the correlative analysis of images based on IRT data, which can be used to estimate local displacements in many practical situations, where the optical imaging is difficult. The quality of these estimates

depends heavily on the quality of IRT images. A very elegant approach has been proposed by Maynadier et al. [118] who applied the DIC technique to the images captured with an infrared camera in order to obtain perfectly synchronised kinematic and thermal full-field maps solely from the calibrated infrared measurements. Inspired by this work, we propose a simplified algorithm giving rise to similar results, although the quantitative comparison of the accuracy achieved by these two methods has not been performed yet.

In our approach, the DIC/IRT pattern for correlation is based on the texture of the high emissivity paint. The benefit of this approach is that since the whole ROI is painted, the thermal measurements are not affected by low emissivity speckle pattern needed for conventional DIC, and the correlative analysis can be completed using only IRT images with little effort. Some image preparation is, however, required since the temperature data are obtained from a camera in a single precision floating point format, whereas the DIC software works with the 8-bit unsigned integer format. To convert the data to the format digestible by the DIC algorithm, IRT images are filtered by a conventional Gaussian filter with the degree of smoothing adjusted for the feature size. From experience, we set the standard deviation of the Gaussian kernel function at 6 for the cases considered here. The smoothed images were subtracted from the original images, unveiling the paint texture. Any values deviating from means for more than five standard deviations (measured for the distribution of intensity over the entire image) after filtering, were replaced by the five standard deviations limit, to reduce the influence of noise on rescaling of images when converting them to 8 bit format. To proceed with the DIC analysis, a virtual mask covering the crack was applied using the crack location data determined in Section 2.4.4.

The IRT-based DIC processing yields the displacement values evolving during cyclic loading. By subtracting the initial image corresponding to the undeformed state from the sequence of images representing the cyclically deformed state, one obtains the local temperature increments in the reference and deformed configurations. The background image subtraction removed most of the texture visible in the raw images. Figure 12 shows a comparison of the raw image (a), reference image of undeformed sample (b) and the results of subtraction based on rigid body motion correction (c,e), and DIC-based motion correction (d,f). When deformations are small, the rigid body correction scheme might be sufficient (cf. (c,d)), while when the deformations become larger, the rigid body correction gives rise to the noisy texture pattern in the temperature field (e), whereas the IRT/DIC-based correction (f) still shows good results.

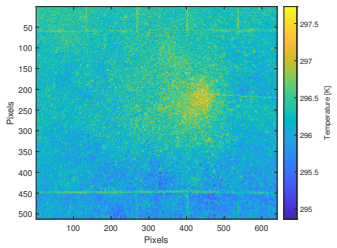

(**a**) Raw image

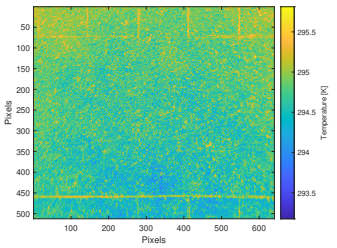

(**b**) Undeformed reference image

Figure 12. *Cont.*

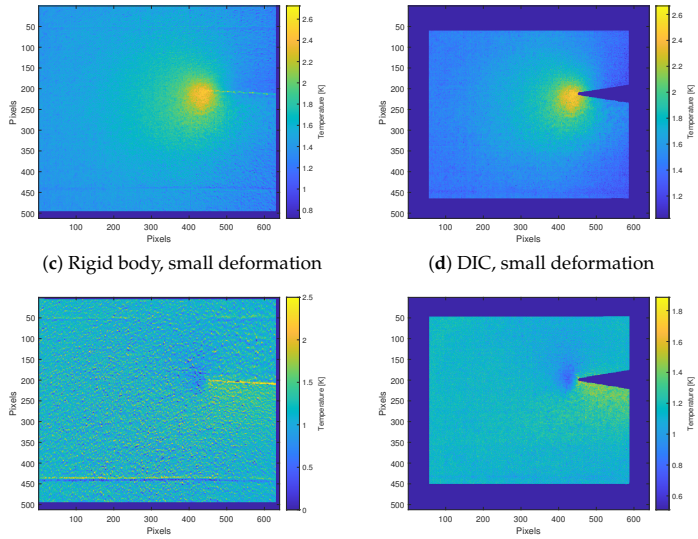

(**c**) Rigid body, small deformation (**d**) DIC, small deformation

(**e**) Rigid body, large deformation (**f**) DIC, large deformation

Figure 12. Comparison of the raw image obtained during cyclic FCG testing (**a**), and the results of background subtraction of the reference image (**b**) using rigid body (**c**,**e**), and IRT/DIC-based image subtraction (**d**,**f**).

Local Regression

The approach for local regression is similar to the one used for the tensile tests. A reference image taken before the beginning of the test was subtracted from all images acquired during cyclic testing, and the ROI from the IRT/DIC analysis for the motion compensation was used. At each pixel position within the global ROI, a smaller circular region was selected with a radius of 10.5 pixels, and the data within that region were used to fit by a second-order polynomial function. The second-order spatial derivative of the temperature, as well as other spatial properties, can be extracted directly from the fitting function afterwards.

2.4.5. Spatial and Temporal Calculations

Aiming at obtaining the source function $\dot{q}$ from the heat Equation (10), one needs to proceed with numerical derivatives of the temperature with respect to time and coordinates. The value of the temperature rate $\frac{\partial T}{\partial t}$ can be calculated based on the motion correction. The input images can be either raw images with or without background subtraction, or the temperature field extracted from the regression analysis. The temperature distribution obtained after regression is smoother, as the regression exerts the effect similar to low-pass filtering. In the particular tests exemplified in the present work, the regression data were used to calculate both the temporal and spatial derivatives of the first and second order, respectively. Ideally, when no heat dissipation occurs, and the temperature field reaches equilibrium, the second derivative should be zero. It is, therefore, possible and reasonable to subtract the Laplacian term obtained for the reference image taken after the test has been paused, i.e., when no heat dissipation occurred, from all images in the recording session. This step allows to remove remaining occasional systematic noise, if it exists and is seen in the Laplacian term.

3. Illustration of the Proposed Approach: Results of Case Studies

The proposed in situ characterisation methodology has been probed on tensile and FCG testing of the Inconel-625 alloy, representing a family of solid solution hardening nickel-based super-alloys having an excellent combination of high strength, ductility, corrosion, and heat resistance. Due to its outstanding properties profile, this alloy has found widespread applications in aeronautic, aerospace, chemical, and petrochemical industries, marine, and nuclear power engineering. For the purpose of the present work, this material was chosen due to a combination of its high density and relatively low electrical and thermal conductivity, favourable for IRT measurements. The microstructure of the Inconel-625 alloy depends on the applied heat treatment [119], and consists typically of the austenitic *fcc* γ-phase matrix containing several secondary strengthening phases including carbides, γ', and γ'' precipitates. The main findings are summarised as follows.

3.1. Tensile Test

Figure 13 shows the true stress-strain curve and the expended mechanical power density p_M (estimated by using DIC mapping and averaged over the entire specimen gauge part) and its variance as a function of strain. The strain hardening rate $\theta(\varepsilon_T) = \frac{d\sigma_T}{d\varepsilon_T}$ was calculated and its fragment is shown in the figure to highlight the crossover with the $\sigma_T(\varepsilon_T)$ indicating the onset of necking according to the Considère criterion (cf. [120–122] for other forms of instability criteria based on the evolution of the total dislocation density)

$$\frac{d\sigma_T}{d\varepsilon_T} = \sigma_T \tag{22}$$

The alloy demonstrates an excellent hardenability resulting in the true strength exceeding 1.3 GPa and uniform strain up to 0.35 before the Considère condition is met.

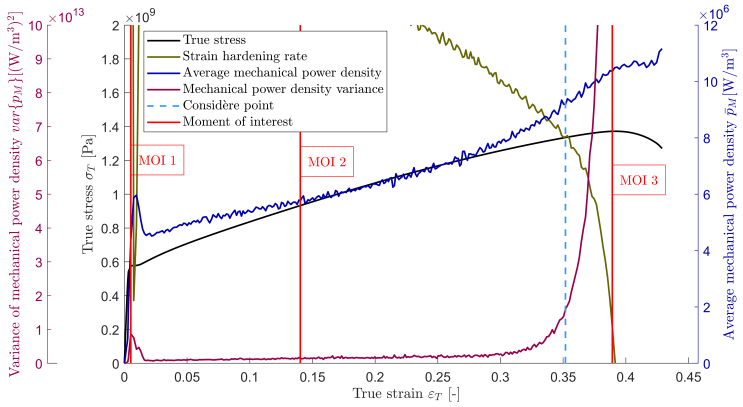

Figure 13. True stress vs. true strain, strain hardening rate, the mechanical power and its variance evolution during tensile testing on the Inconel-625 alloy. The vertical dashed line indicates the Considère point. The solid vertical lines correspond to the moments of interest (MOI) shown in Figure 14.

One can notice that the mechanical power exhibits interesting behaviour, the details of which unveil several deformation stages, as will be discussed in what follows. The distribution of locally measured p_M values is of its own interest, and is shown in Figure 14 representing three typical situations marked in Figure 13: (a,b) the onset of plastic yielding when the Lüders band forms at the upper edge of the gauge part of the specimen; (c,d) the uniform deformation stage; (e,f) the developed necking stage. During uniform deformation,

the p_M distribution has a symmetric Gaussian shape, which is reasonably expected for this stage. Not only does the distribution of p_M become significantly skewed towards the left hand-side of the histograms (i.e., the most probable values lie in the low power domain, indicating that most parts of the specimen do not deform plastically) when the strain localisation occurs, but also its variance can serve as a measure of strain localisation. Indeed, Figure 13 illustrates it explicitly—the variance of the p_M distribution increases dramatically when necking sets in under plane stress domination at the necking strain $\varepsilon_N = 0.35$ (it should be, however, noticed, that the accelerated increase in the p_M variance becomes appreciable even before the macroscopic loss of stability commences according to the mechanistic criterion from Equation (22). Outside of the neck region, the material, however, slightly unloads since the global reaction force decreases in response to the shrinking cross-sectional area within the neck [123], thus resulting in some negative values in the mechanical power distribution shown in Figure 14e.

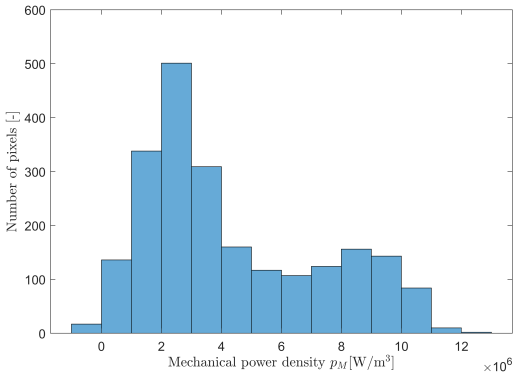

(**a**) MOI 1—onset of the Lüders band nucleation

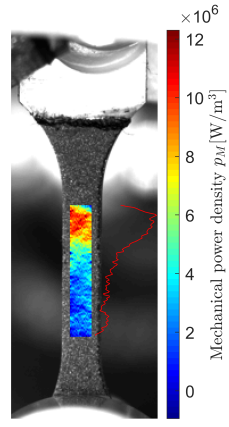

(**b**) p_M map and profile (red line)

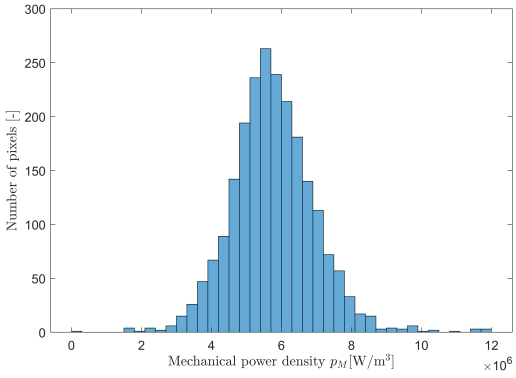

(**c**) MOI 2—uniform deformation

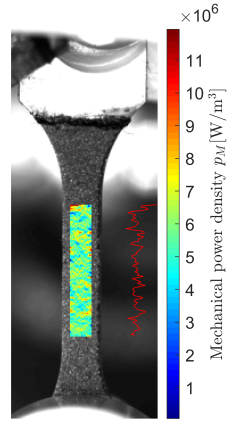

(**d**) p_M map and profile (red line)

Figure 14. *Cont.*

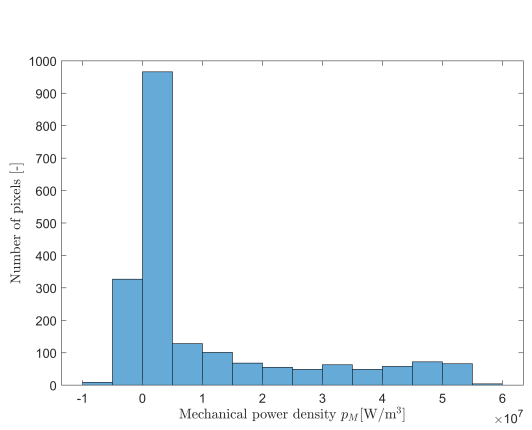

(**e**) MOI 3—necking (**f**) p_M map and profile (red line)

Figure 14. Distribution of the expended mechanical power density for the tensile test at three different points of interest indicated in Figure 13, corresponding to the initiation of the Lüders band (**a**,**b**), uniform deformation stage (**c**,**d**), and necking (**e**,**f**).

Figure 15 compiles the results from all of the methods in a single plot: (i) the average expended mechanical power density is plotted in parallel with the dissipated and stored power, and all curves are synchronised with the stress-strain data. The strain hardening rate is also plotted for comparison.

The typical evolution of the AE signal in the Inconel-625 alloy is illustrated in terms of the dissipated AE power P_{AE} and the median frequency f_m of the PSD function synchronised with the tension loading curves and strain hardening rate. Analysis of Figure 15 reveals that, typically for ductile materials, AE commences already at the relatively low applied stress and peak when the Lüders band nucleates and propagates. Then, the AE level decreases continually until fracture, but never vanishes. Overall, AE exhibits the behaviour typical of metals and alloys with dislocation-mediated plasticity [38,124]. While the power (or energy) reduces with strain in response to strain hardening and the concomitant shortening of the dislocation mean free path, the median frequency f_m of the PSD increases steadily for the same reason in parallel with the flow stress. This trend in the f_m behaviour is confirmed in Figure 15—as long as plastic deformation is uniform, the average f_m value increases steadily. However, when the deformation begins to localise in a neck, the local strain rate increases drastically relative to that outside the neck. In response to this, f_m rises steeply, which is in qualitative agreement with the linear strain rate dependence of the AE median frequency proposed in [124].

The behaviour of the strain hardening rate indicates that uniform plastic deformation proceeds through different stages (the yield point followed by the Lüders band propagation, and stages II and III can be discerned from the $\theta(\varepsilon_T)$ behaviour). The same stages can be seen, in principle, in the evolution of the average total mechanical power p_M. The dissipated p_D and stored p_S powers exhibit opposite trends in the necking region: while the former shows a sharp increase, the latter changes its trend from ascending to descending. The smooth gradual increase in p_D and p_S with strain is observed in parallel with the progressive rise in the AE median frequency changing with the evolution of the dislocation microstructure. The overall strain hardening behaviour is nicely reflected by the AE power, which behaves in general agreement with the predictions of the phenomenological model of AE caused by dislocation-based strain hardening proposed in [125]. Specifically, the increased AE activity is noteworthy at approximately 0.07 strain, where the transition

between Stages II and III can be seen in the behaviour of $\theta(\varepsilon_T)$ and $p_M(\varepsilon_T)$. The in-depth discussion of the observed trends requires a bridge to be built between the thermodynamics of plastic deformation and the underlying microstructural evolution, which is beyond the scope of the present paper and will be discussed elsewhere. Nonetheless, importantly for the purpose of the present work, the proposed methodology, based on a comprehensive in situ monitoring strategy, follows the evolution of the microstructure with strain hardening, and provides the grounds for the progress in the thermodynamic analysis of plastic deformation.

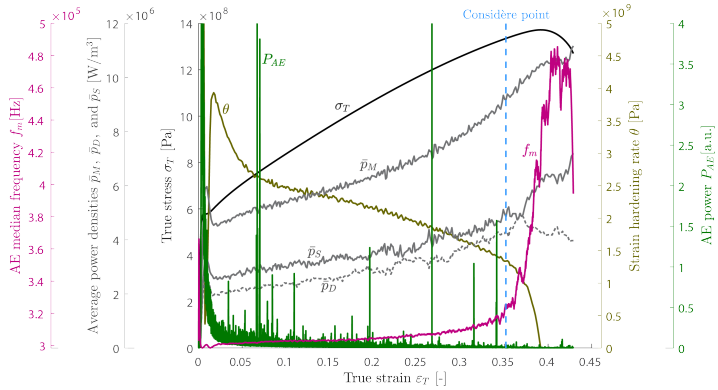

Figure 15. Summary of results of the tensile test, representing the behaviour of the expended and stored mechanical power—p_M and p_S, respectively, dissipated heat p_D, and the strain hardening rate θ, synchronised with the stress-strain curve and the key descriptive AE variables—power P_{AE} and median frequency of the PSD f_m.

3.2. Fatigue Crack Growth Test

In the fracture mechanics approach to the stable fatigue crack propagation, in the vast majority of structural materials, the crack length a increases under cyclic load according to the empiric Paris–Erdogan equation

$$\frac{da}{dN} = C\Delta K^m \tag{23}$$

where $\frac{da}{dN}$ represents the crack growth rate (the crack length increment per cycle), and C and m are experimentally determined material properties known as Paris coefficient and Paris exponent, respectively (both dependent also on the environment, temperature and loading conditions). Figure 16 shows the Paris plots for the crack growth rate $\frac{da}{dN}$ vs. the stress intensity factor range ΔK, which are obtained independently from the IRT (a) or RVI (b) data used to find the crack tip position and estimate the crack length. The vertical lines indicate the validity of the linear elastic fracture mechanics (LEFM) and the ΔK concept according to the ASTM standard [90], which is verified by the criterion:

$$(W - a) \geq \frac{4}{\pi}\left(\frac{K_{max}}{\sigma_{ys}}\right)^2 \tag{24}$$

where W is the effective width of the specimen, a is crack length, K_{max} is the highest stress intensity factor occurring within a cycle, and σ_{ys} is the materials yield stress. The stress intensity factor needs to be calculated within the small scale yielding (SSY) approximation of an elastic-plastic body with a Mode I crack in plane strain. In Figure 17, the results from both techniques are compared. Not only an excellent agreement between both methods is seen, but also the scatter of experimental data for $\frac{da}{dN}$ for each technique is reasonably

small. Both methods yield practically the same Paris parameters C and m of 3.12 ± 0.03. Additionally, for both methods the slight deviation from the LEFM prediction according to the Paris' law becomes visible precisely at ΔK expected from the SSY criterion of 62 MPa$\sqrt{\text{m}}$ corresponding to the crack length a of 24.8 mm.

The reversible thermoelastic effect and the irreversible heat dissipation due to plastic deformation in the cyclic plastic zone are the two main contributors to the heat source function $\dot{q}$ in Equation (10). Since the thermoelastic effect assumes the linearity between the stress and temperature increment, one can make use of the cyclic loading to eliminate this effect from the analysis by performing the integration of the $\dot{q}$ over each loading cycle. An example of the heat dissipation behaviour per cycle is illustrated in Figure 18, where the heat power density $\dot{q}$ at the crack tip is plotted versus the applied load. An example of the map of the energy dissipated during one cycle w_D is shown in Figure 18c, highlighting the cyclic plastic zone ahead of the crack tip.

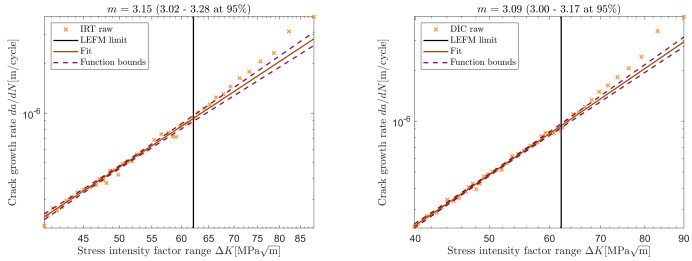

(**a**) IRT (**b**) RVI

Figure 16. Crack growth curves and their linear fit for IRT (**a**) and DIC data (**b**). The vertical line represents the calculated linear elastic fracture mechanics limit according to the small scale yielding criterion.

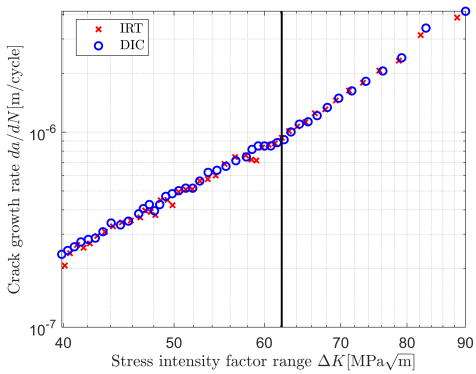

Figure 17. Paris plot obtained from IRT and DIC measurements. Both datasets are plotted for comparison. The vertical line represents the LEFM limit according to the small yielding criterion.

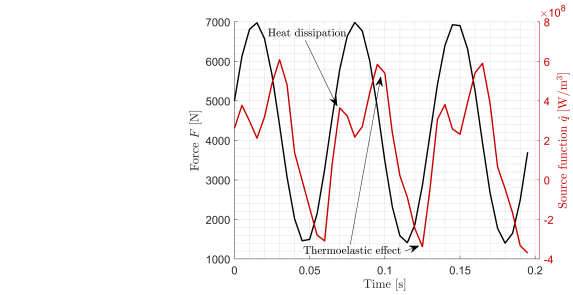

(**a**) Source function at crack tip

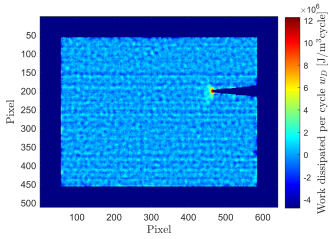

(**b**) Source function at crack tip

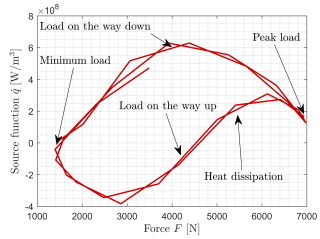

(**c**) Dissipated heat density during one cycle

Figure 18. The source function plotted versus time (**a**) or loading force (**b**): the contributions from the heat dissipation and thermoleastic effect are distinguished, and the separated heat energy dissipation per cycle is shown in (**c**).

The plot compiling the main findings from all three in situ methods is represented in Figure 19, where the average (per cycle) AE energy and median frequency are plotted together with the dissipated heat energy at the crack tip as a function of the crack length, which serves as a damage parameter for FCG. The load gating method was used to select the AE signals at the loads exceeding 0.95 of the peak load, and to remove the signals associated with crack closure on unloading. As a note, AE due to crack closure can be produced by several mechanisms such mechanisms as rubbing of the crack faces due to local compressive stresses from plastic deformation, friction between jagged crack edges and rubbing or breaking of wedged oxides [126–130]. AE induced by crack closure is dependent on many factors including materials properties, environment, and test frequency [86,127]. The ductility of the material affects the roughness of the crack faces, and the susceptibility of a material to oxidation in a given environment will affect the presence of oxides in the crack region. Closure emissions are generally unwanted in the AE analysis of FCG [126], unless the crack closure phenomenon itself is of particular interest. Before discussing the AE findings of the present work, a brief excursion to the FCG related mechanisms would be in place. Acoustic emission from fatigue crack-related mechanisms has been studied experimentally for decades, and AE features specific to crack initiation, crack extension, and crack closure have been identified by many researchers on examples of various materials. Several empiric relations and qualitative explanations of the crack growth behaviour in its relation to AE have been developed, and some are described below. Fracture mechanisms associated with the opening of new surfaces and expansion of the plastic zone during crack extension produce elastic waves. The amplitude of the AE signal depends on the dynamics at the source [131,132], and, in general, brittle fracture mechanisms produce higher amplitude signals than ductile ones [129,133–135]. Brittle fracture mechanisms include intergranular and cleavage fracture. Ductile fracture mechanisms involve microvoid nucleation and coalescence, tearing, and shearing. Pollock [136] considered the elastic energy

conversions of a system during crack growth for characteristic ductile and brittle source events of equal magnitude. The difference in the AE signal amplitudes was explained by partitioning the released energy into three groups: energy of plastic deformation, surface energy or "event" energy associated with AE waves. The plastic deformation term captures the energy expended in creating the plastic zone through the dislocation generation and movement, while the surface energy refers to the disbonding of the single atomic layer to create the new surfaces. It was argued that due to a larger plastic zone and the increased surface energy due to a rougher crack surface, a lesser fraction of the released elastic energy is emitted as AE in the ductile fracture mode compared to brittle fracture of the same magnitude of the energy release at the source. For FCG, Morton et al. [137,138] found a relation between the AE count rate $\frac{dN_{AE}}{dN}$, and ΔK in the form of the power law resembling the Paris–Erdogan FCG Equation (23) (see also [77,139,140], where the first model has been proposed to link the AE count rate with the stress intensity factor):

$$\frac{dN_{AE}}{dN} = C_{AE}\Delta K^{n_{AE}} \tag{25}$$

where C_{AE} is the empiric constant and the exponent n_{AE} is found to be related to the Paris exponent, m, by the relation $n_{AE} \approx m + 2$ as proposed by Lindley et al. [129]. It was suggested that both the energy released during crack extension, and the deformation and fracture related events within the plastic zone ahead of the crack, contribute to AE during FCG, see Heiple and Carpenter [141,142], finding dislocation mechanisms, twin nucleation, and fracture of inclusions to be potent sources of AE in the plastic zone.

For the material under investigation, the mechanisms related to mechanical twinning and fracture of hard particles can be ruled out due to Inconel's high stacking fault energy. Therefore, the primary energy dissipation mechanisms are supposed to be attributed to the crack advance and the dislocation activity in the plastic zone. One can note that, in line with many previous observations, the average (per cycle) AE power increases exponentially as the crack advances. Even though the observed behaviour of the AE power P_{AE} presented in Figure 20 as a function of ΔK can be approximated by a straight line in log-log scale, the linear fit is applicable only for the low ΔK domain. It is interesting that the power relation (25) holds reasonably only up to the critical ΔK value corresponding to the LEFM limit, whereas beyond this point, the AE power tends to increase rapidly with the crack advance, which agrees with the development of the excess plasticity ahead of the crack tip. However, the observed behaviour contradicts the predictions by Lindley et al. [129] since the n_{AE} value of 2.2, which is obtained from the least square fit in Figure 20, is far from being equal to $m + 2$ at relatively small ΔK, as anticipated from the cited work for the AE count rate [129]. Thus, even though there seem to be a reasonable agreement between the AE power and the stress intensity factor range indeed, at least within small scale yielding, there is still no consensus about the n_{AE} index, and there is still a big deal to establish the dependence (if any) of n_{AE} on the microstructure and testing conditions. Figure 19 unveils another interesting correlation between the AE power, the heat dissipation power, and the strain range. The latter quantity assessed by DIC as the difference between maximum and minimum local strain per cycle serves as a measure of the expended mechanical power in the plastic zone. One can notice that the measured strains appeared to be substantially plastic (see the blue curve in Figure 19, which represents the strain range measured by DIC). Therefore, obtaining the expended mechanical power from DIC is not as straightforward as that in the case of uniaxial tension. Nonetheless, the observed correlation is noteworthy and the expended mechanical power can be obtained in a more elaborated approach.

Although the AE power (energy or count rate) has long been recognised to be generally related to the fatigue crack length or the stress intensity factor range, the behaviour of the AE spectral density during fatigue crack propagation has not been explored so far, to the authors best knowledge (that is at sharp contrast to the monotonic tensile testing). In the present work, we illustrate the evolution of the AE PSD function by the behaviour of its median frequency (compare to that in the tensile test, Figure 15). As cycling proceeds and

the crack advances, f_m shows a general trend to decrease (Figure 19). This apparent trend opposes that in monotonic tension, where the f_m value increases with strain hardening, as has been discussed above. According to the statistical interpretation of the median frequency as a property reciprocal to the correlation time in the ensemble of emitting defects proposed by Vinogradov et al. [25] (see also [124]), the increase in the f_m value signifies the increase in randomness of AE sources, while the opposite trend (decreasing f_m) heralds the increase in their temporal correlation or spatial scale. This interpretation appears to be in harmony with the observed behaviour of f_m, since during FCG the plastic zone expands progressively at the expense of the undeformed material, resulting in longer and longer crack jumps. Thus, AE is emitted not from the most heavily deformed plastic zone, but primarily from its expanding periphery, thus involving greater and greater undeformed volume into the process of cyclic plastic zone growth. What should be noticed in the behaviour of the AE median frequency is that it exhibits a local maximum at the intermediate ΔK values. Presumably, this specific behaviour reflects the AE PSD response to the local strain hardening in the growing plastic zone. This process was not visible in the very small plastic zone at the beginning of the crack growth. As the plastic zone increased the contribution of strain hardening became appreciable in the AE PSD evolution. The gradual shift of f_m towards the higher frequency domain was finally overridden by the rapid development of the excess crack tip plasticity beyond the LEFM SSY limit resulting in the rapid expansion of the plastic zone and the reduction in AE PSD.

Concluding this section, a brief discussion regarding uncertainty of the measurements is required. Similarly to many commercially available infrared cameras with cooled quantum sensors, the factory-calibrated TELOPS FAST M350 thermograph used in the present work delivers a radiometric temperature accuracy of 1 K (or $\pm 1\%$ over the entire range), which is not very impressive, yet typical in the class. The energy calculations are, however, based on the spatio-temporal difference in the temperature. The resolution related to the temperature increment is, fortunately, much better, reducing ideally to 20 mK, as has been discussed above. The greatest uncertainty in the estimates of the thermodynamic quantities, such as a stored energy, is known to be associated with the measurements of the temperature rate and the Laplacian of the temperature field. We have not performed the formal differential error analysis of the propagation of uncertainty in our measurements of quantities entering Equations (10) and (13). However, based on the "worst case" analysis, the relative uncertainty in the estimated stored energy does not exceed 15% over the entire range, and this is the most conservative estimate. Furthermore, the calibration procedure applied to the IRT system supports the opinion that 15% can be regarded as the upper boundary in uncertainty, and is likely to be notably smaller. The propagation of error analysis and the details of the calibration procedure, which itself might be of special interest, will be reported elsewhere. In brief, the well-controlled rectangular DC current pulses of 2, 5, 10, 20, and 50 A amplitude and 200 ms duration were passed through the Inconel-625 test specimen (being initially at room temperature), and the corresponding voltage drops and Joule heat dissipation were independently measured. The temperature rise did not exceed 7 K at 20 A, and 55 K at 50 A current. Regardless of the magnitude of the temperature rise, the measured thermal power consistently compared favourably to the measured Joule heat (electric power). This justifies that the obtained estimates of the thermodynamic quantities are reliable that the procedures used to obtain them are adequate.

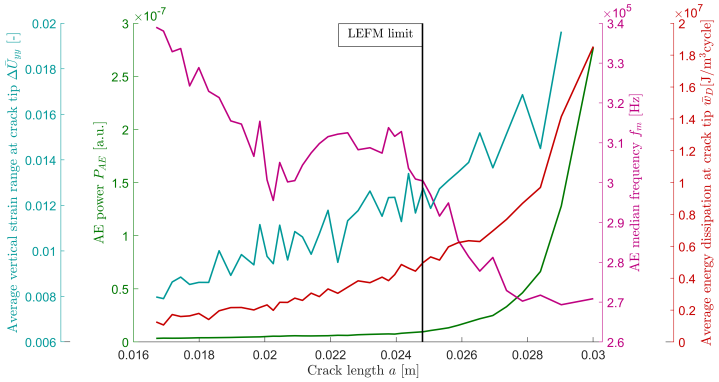

Figure 19. Characterisation of fatigue crack propagation by a combination of IRT, DIC/RVI, and AE techniques. The vertical line indicates the LEFM SSY limit according to Equation (24).

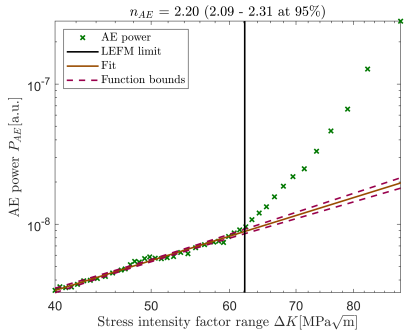

Figure 20. AE power plotted as a function of the stress intensity factor range. The vertical line indicates the LEFM SSY limit according to Equation (24).

4. Summary, Conclusions, and Future Scopes

As a final comment, the preliminary results from the case study on the tensile and fatigue behaviour using the *fcc* Inconel-625 alloy as an example contain a wealth of information regarding underlying deformation and fracture mechanisms. This multifaceted information was enabled due to the integration of several in situ monitoring techniques—infrared thermography, multi-resolution rapid video imaging complemented by the digital image correlation capability, and acoustic emission powered by the spectral analysis and statistical clustering algorithms—into a common framework, addressing multiple hardware and software challenges, which are inevitable in a contemporary advanced experimental design. At variance to the commercially available systems pairing the DIC and IRT techniques (e.g., https://www.infratec.eu/thermography/digital-image-correlation-and-thermographic-measurements/ (accessed on 14 July 2021)), the use of the open-source software architecture offers uncompromised versatility with a balance of efficiency, accuracy, and tunability of the entire system. Not only the proposed system can be adapted to virtually any combination of thermal and visual cameras, and to suit a wide range of load-bearing applications, but also the concurrent use of AE measurements, which are fully synchronised with the two other techniques and the loading device, adds a new dimension to the multiscale research in the field of physics and mechanics of plasticity and fracture.

Admittedly, the presented results show only the tip of the iceberg and leave more questions than answers. Specifically, there is still a great deal of opportunity to improve virtually all metrological aspects and traceability of the results of measurements by the techniques employed. However, we believe that the proposed rigorous methodology documented in significant details in the present communication permits answering many open questions related to damage initiation and propagation in solids under monotonic and cyclic loads. This is the scope of the ongoing research, the results of which will be reported elsewhere. We also believe that the proposed instrumented laboratory experimental platform can serve for future developments of novel practical approaches and means for non-destructive health monitoring of industrial facilities and infrastructure.

Author Contributions: Conceptualisation, A.S. and A.V.; methodology, A.S. and A.O.M.; software, A.S.; validation, A.S.; investigation, A.S., A.O.M. and S.W.W.; writing—original draft preparation, A.S., A.O.M. and S.W.W.; writing—review and editing, A.V., A.S. and A.O.M.; visualisation, A.S.; supervision, A.V. All authors have read and agreed to the published version of the manuscript.

Funding: This work was partially supported by Research Council of Norway, Project No. 294739, Safe Pipelines for Hydrogen Transport (HyLINE).

Institutional Review Board Statement: Not applicable.

Informed Consent Statement: Not applicable.

Data Availability Statement: Data are available from the corresponding author upon reasonable request.

Acknowledgments: The authors gratefully acknowledge to T. Kristensen and SINTEF Industry personnel for their kind help with specimens preparation. Special thanks go to A. Alvaro and F. Berto for encouragement, support, and discussions. We also thank R. Johnsen for providing the material for this study. The authors would like to thank the anonymous reviewers for the insightful comments that helped in improving the manuscript.

Conflicts of Interest: The authors declare no conflict of interest.

Abbreviations

AE	Acoustic emission
DIC	Digital image correlation
FAST	Features from accelerated segment test
FCG	Fatigue crack growth
FFT	Fast Fourier transform
FOV	Field of view
IBR	In-band radiance
IRT	Infrared thermography
LEFM	Linear elastic fracture mechanics
MOI	Moment of interest
NETD	Noise equivalent temperature difference
PSD	Power spectral density
ROI	Region of interest

References

1. Sutton, M.A. Digital Image Correlation for Shape and Deformation Measurements. In *Springer Handbook of Experimental Solid Mechanics*; Sharpe, W.N., Ed.; Springer: Boston, MA, USA, 2008; pp. 565–600. [CrossRef]
2. Mountain, D.; Webber, J. Stress Pattern Analysis by Thermal Emission (SPATE). *Proc. SPIE* **1979**. [CrossRef]
3. De Finis, R.; Palumbo, D.; Galietti, U. A multianalysis thermography-based approach for fatigue and damage investigations of ASTM A182 F6NM steel at two stress ratios. *Fatigue Fract. Eng. Mater. Struct.* **2019**, *42*, 267–283. [CrossRef]
4. Morabito, A.E.; Chrysochoos, A.; Dattoma, V.; Galietti, U. Analysis of heat sources accompanying the fatigue of 2024 T3 aluminium alloys. *Int. J. Fatigue* **2007**, *29*, 977–984. [CrossRef]
5. Berthel, B.; Chrysochoos, A.; Wattrisse, B.; Galtier, A. Infrared image processing for the calorimetric analysis of fatigue phenomena. *Exp. Mech.* **2008**, *48*, 79–90. [CrossRef]
6. Zhou, W.; Han, K.N.; Qin, R.; Zhang, Y.J. Investigation of mechanical behavior and damage of three-dimensional braided carbon fiber composites. *Mater. Res. Express* **2019**, *6*, 085624. [CrossRef]

7. Díaz, F.A.; Patterson, E.A.; Tomlinson, R.A.; Yates, J.R. Measuring Stress Intensity Factors during Fatigue Crack Growth Using Thermoelasticity. *Fatigue Fract. Eng. Mater. Struct.* **2004**, *27*, 571–583. [CrossRef]
8. Meneghetti, G.; Ricotta, M.; Pitarresi, G. Infrared thermography-based evaluation of the elastic-plastic J-integral to correlate fatigue crack growth data of a stainless steel. *Int. J. Fatigue* **2019**, *125*, 149–160. [CrossRef]
9. La Rosa, G.; Risitano, A. Thermographic Methodology for Rapid Determination of the Fatigue Limit of Materials and Mechanical Components. *Int. J. Fatigue* **2000**, *22*, 65–73. [CrossRef]
10. Lipski, A. Rapid Determination of the S-N Curve for Steel by Means of the Thermographic Method. *Adv. Mater. Sci. Eng.* **2016**, *2016*, e4134021. [CrossRef]
11. Ancona, F.; De Finis, R.; Demelio, G.P.; Galietti, U.; Palumbo, D. Study of the Plastic Behavior around the Crack Tip by Means of Thermal Methods. *Procedia Struct. Integr.* **2016**, *2*, 2113–2122. [CrossRef]
12. Fedorova, A.Y.; Bannikov, M.V.; Bannikov, M.V.; Plekhov, O.A.; Plekhova, E.V. Infrared thermography study of the fatigue crack propagation. *Frattura ed Integrità Strutturale* **2012**, *6*, 46–53. [CrossRef]
13. Ju, Y.; Xie, H.; Zhao, X.; Mao, L.; Ren, Z.; Zheng, J.; Chiang, F.P.; Wang, Y.; Gao, F. Visualization method for stress-field evolution during rapid crack propagation using 3D printing and photoelastic testing techniques. *Sci. Rep.* **2018**, *8*. [CrossRef]
14. Hertegård, S.; Larsson, H.; Wittenberg, T. High-speed imaging: Applications and development. *Logop. Phoniatr. Vocol.* **2003**, *28*, 133–139. [CrossRef] [PubMed]
15. Gao, H.; Zhang, Z.; Jiang, W.; Zhu, K.; Gong, A. Deformation Fields Measurement of Crack Tip under High-Frequency Resonant Loading Using a Novel Hybrid Image Processing Method. *Shock Vib.* **2018**, *2018*. [CrossRef]
16. Seleznev, M.; Vinogradov, A. Note: High-speed optical imaging powered by acoustic emission triggering. *Rev. Sci. Instrum.* **2014**, *85*, 076103. [CrossRef] [PubMed]
17. Hosdez, J.; Witz, J.F.; Martel, C.; Limodin, N.; Najjar, D.; Charkaluk, E.; Osmond, P.; Szmytka, F. Fatigue crack growth law identification by Digital Image Correlation and electrical potential method for ductile cast iron. *Eng. Fract. Mech.* **2017**, *182*, 577–594. [CrossRef]
18. Carroll, J.D.; Abuzaid, W.; Lambros, J.; Sehitoglu, H. High resolution digital image correlation measurements of strain accumulation in fatigue crack growth. *Int. J. Fatigue* **2013**, *57*, 140–150. [CrossRef]
19. Pan, B.; Qian, K.; Xie, H.; Asundi, A. Two-dimensional digital image correlation for in-plane displacement and strain measurement: A review. *Meas. Sci. Technol.* **2009**, *20*, 062001. [CrossRef]
20. Maldague, X.P.V. *Nondestructive Evaluation of Materials by Infrared Thermography*; Springer: London, UK, 1993; p. 207. [CrossRef]
21. Krstulović-Opara, L.; Surjak, M.; Vesenjak, M.; Tonković, Z.; Kodvanj, J.; Domazet, Z. Comparison of infrared and 3D digital image correlation techniques applied for mechanical testing of materials. *Infrared Phys. Technol.* **2015**, *73*, 166–174. [CrossRef]
22. Ono, K. Current understanding of mechanisms of acoustic emission. *J. Strain Anal. Eng. Des.* **2005**, *40*, 1–15. [CrossRef]
23. Kiesewetter, N.; Schiller, P. Acoustic-Emission from Moving Dislocations in Aluminum. *Phys. Status Solidi A* **1976**, *38*, 569–576. [CrossRef]
24. Vinogradov, A.; Danyuk, A.V.; Merson, D.L.; Yasnikov, I.S. Probing elementary dislocation mechanisms of local plastic deformation by the advanced acoustic emission technique. *Scr. Mater.* **2018**, *151*, 53–56. [CrossRef]
25. Vinogradov, A.; Yasnikov, I.S.; Estrin, Y. Evolution of Fractal Structures in Dislocation Ensembles during Plastic Deformation. *Phys. Rev. Lett.* **2012**, *108*, 205504. [CrossRef] [PubMed]
26. Muransky, O.; Barnett, M.R.; Carr, D.G.; Vogel, S.C.; Oliver, E.C. Investigation of deformation twinning in a fine-grained and coarse-grained ZM20 Mg alloy: Combined in situ neutron diffraction and acoustic emission. *Acta Mater.* **2010**, *58*, 1503–1517. [CrossRef]
27. Máthis, K.; Knapek, M.; Šiška, F.; Harcuba, P.; Ugi, D.; Ispánovity, P.D.; Groma, I.; Shin, K.S. On the dynamics of twinning in magnesium micropillars. *Mater. Des.* **2021**, *203*, 109563. [CrossRef]
28. Vinogradov, A.; Vasilev, E.; Seleznev, M.; Máthis, K.; Orlov, D.; Merson, D. On the limits of acoustic emission detectability for twinning. *Mater. Lett.* **2016**, *183*, 417–419. [CrossRef]
29. Vinogradov, A.; Máthis, K. Acoustic Emission as a Tool for Exploring Deformation Mechanisms in Magnesium and Its Alloys In Situ. *JOM* **2016**, *68*, 1–6. [CrossRef]
30. Vinogradov, A. A phenomenological model of deformation twinning kinetics. *Mater. Sci. Eng. A* **2021**, *803*, 140700. [CrossRef]
31. Baram, J.; Avissar, J.; Gefen, Y.; Rosen, M. Release of Elastic Strain-Energy as Acoustic-Emission during the Reverse Thermoelastic Phase-Transformation in Au-47.5 at. Percent Cd Alloy. *Scr. Metall.* **1980**, *14*, 1013–1016. [CrossRef]
32. van Bohemen, S.M.C.; Sietsma, J.; Hermans, M.J.M.; Richardson, I.M. Kinetics of the martensitic transformation in low-alloy steel studied by means of acoustic emission. *Acta Mater.* **2003**, *51*, 4183–4196. [CrossRef]
33. van Bohemen, S.M.C.; Sietsma, J.; Petrov, R.; Hermans, M.J.M.; Richardson, I.M. Acoustic emission as a probe of the kinetics of the martensitic transformation in a shape memory alloy. *Mater. Trans.* **2006**, *47*, 607–611. [CrossRef]
34. Vives, E.; Rafols, I.; Manosa, L.; Ortin, J.; Planes, A. Statistics of Avalanches in Martensitic Transformations 1. Acoustic-Emission Experiments. *Phys. Rev. B* **1995**, *52*, 12644–12650. [CrossRef] [PubMed]
35. Vinogradov, A.; Lazarev, A.; Linderov, M.; Weidner, A.; Biermann, H. Kinetics of deformation processes in high-alloyed cast transformation-induced plasticity/twinning-induced plasticity steels determined by acoustic emission and scanning electron microscopy: Influence of austenite stability on deformation mechanisms. *Acta Mater.* **2013**, *61*, 2434–2449. [CrossRef]

36. Lazarev, A.; Vinogradov, A. About plastic instabilities in iron and power spectrum of acoustic emission. *J. Acoust. Emiss.* **2009**, *27*, 144–156.
37. Shashkov, I.V.; Lebyodkin, M.A.; Lebedkina, T.A. Multiscale study of acoustic emission during smooth and jerky flow in an AlMg alloy. *Acta Mater.* **2012**, *60*, 6842–6850. [CrossRef]
38. Vinogradov, A.; Lazarev, A. Continuous acoustic emission during intermittent plastic flow in α-brass. *Scr. Mater.* **2012**, *66*, 745–748. [CrossRef]
39. Chmelík, F.; Dosoudil, J.; Plessing, J.; Neuhäuser, H.; Lukáč, P.; Trojanová, Z. The Portevin-Le Châtelier Effect in Cu-Al Single Crystals Investigated by Acoustic Emission and Slip Line Cinematography. In *Key Engineering Materials*; Plasticity of Metals and Alloys; Trans Tech Publications Ltd.: Bäch, Switzerland, 1995; Volume 97, pp. 263–268. [CrossRef]
40. Vinogradov, A. Acoustic emission in ultra-fine grained copper. *Scr. Mater.* **1998**, *39*, 797–805. [CrossRef]
41. Thiebaud, R.; Dobron, P.; Chmelik, F.; Jerome, W.; Louchet, F. On the critical character of plasticity in metallic single crystals. *Mater. Sci. Eng. A* **2006**, *424*, 190–195. [CrossRef]
42. Weiss, J.; Richeton, T.; Louchet, F.; Chmelik, F.; Dobron, P.; Entemeyer, D.; Lebyodkin, M.; Lebedkina, T.; Fressengeas, C.; McDonald, R.J. Evidence for universal intermittent crystal plasticity from acoustic emission and high-resolution extensometry experiments. *Phys. Rev. B Condens. Matter Mater. Phys.* **2007**, *76*, 224110. [CrossRef]
43. Merson, E.; Vinogradov, A.; Merson, D.L. Application of acoustic emission method for investigation of hydrogen embrittlement mechanism in the low-carbon steel. *J. Alloys Compd.* **2015**, *645*, S460–S463. [CrossRef]
44. Vinogradov, A.; Lazarev, A.; Louzguine-Luzgin, D.V.; Yokoyama, Y.; Li, S.; Yavari, A.R.; Inoue, A. Propagation of shear bands in metallic glasses and transition from serrated to non-serrated plastic flow at low temperatures. *Acta Mater.* **2010**, *58*, 6736–6743. [CrossRef]
45. Godin, N.; Reynaud, P.; Fantozzi, G. Challenges and Limitations in the Identification of Acoustic Emission Signature of Damage Mechanisms in Composites Materials. *Appl. Sci.* **2018**, *8*, 1267. [CrossRef]
46. Vinogradov, A.; Merson, D.L.; Patlan, V.; Hashimoto, S. Effect of solid solution hardening and stacking fault energy on plastic flow and acoustic emission in Cu-Ge alloys. *Mater. Sci. Eng. A* **2003**, *341*, 57–73. [CrossRef]
47. Gutkin, R.; Green, C.J.; Vangrattanachai, S.; Pinho, S.T.; Robinson, P.; Curtis, P.T. On acoustic emission for failure investigation in CFRP: Pattern recognition and peak frequency analyses. *Mech. Syst. Signal Process.* **2011**, *25*, 1393–1407. [CrossRef]
48. Piotrkowski, R.; Castro, E.; Gallego, A. Wavelet power, entropy and bispectrum applied to AE signals for damage identification and evaluation of corroded galvanized steel. *Mech. Syst. Signal Process.* **2009**, *23*, 432–445. [CrossRef]
49. Pomponi, E.; Vinogradov, A. A Real-Time Approach to Acoustic Emission Clustering. *Mech. Syst. Signal Process.* **2013**, *40*, 791–804. [CrossRef]
50. Aggelis, D.G.; Kordatos, E.Z.; Matikas, T.E. Acoustic emission for fatigue damage characterization in metal plates. *Mech. Res. Commun.* **2011**, *38*, 106–110. [CrossRef]
51. Tragazikis, I.; Exarchos, D.; Dalla, P.; Matikas, T. Damage characterization in engineering materials using a combination of optical, acoustic, and thermal techniques. In *SPIE Smart Structures and Materials + Nondestructive Evaluation and Health Monitoring*; International Society for Optics and Photonics: Bellingham, WA, USA, 2016; Volume 9804. [CrossRef]
52. Vanniamparambil, P.A.; Guclu, U.; Kontsos, A. Identification of Crack Initiation in Aluminum Alloys using Acoustic Emission. *Exp. Mech.* **2015**, *55*, 837–850. [CrossRef]
53. Venkataraman, B.; Raj, B.; Mukhopadhyay, C.K.; Jayakumar, T. Correlation of infrared thermographic patterns and acoustic emission signals with tensile deformation and fracture processes. *AIP Conf. Proc.* **2001**, *557*, 1443–1450. [CrossRef]
54. Haneef, T.; Lahiri, B.B.; Bagavathiappan, S.; Mukhopadhyay, C.K.; Philip, J.; Rao, B.P.C.; Jayakumar, T. Study of the tensile behavior of AISI type 316 stainless steel using acoustic emission and infrared thermography techniques. *J. Mater. Res. Technol.* **2015**, *4*, 241–253. [CrossRef]
55. Cuadra, J.A.; Baxevanakis, K.P.; Mazzotti, M.; Bartoli, I.; Kontsos, A. Energy dissipation via acoustic emission in ductile crack initiation. *Int. J. Fract.* **2016**, *199*, 89–104. [CrossRef]
56. Khan, R.M.A.; Saeidiharzand, S.; Emami Tabrizi, I.; Ali, H.Q.; Yildiz, M. A novel hybrid damage monitoring approach to understand the correlation between size effect and failure behavior of twill CFRP laminates. *Compos. Struct.* **2021**, *270*, 114064. [CrossRef]
57. Dai, S.; Liu, X.; Nawnit, K. Experimental Study on the Fracture Process Zone Characteristics in Concrete Utilizing DIC and AE Methods. *Appl. Sci.* **2019**, *9*, 1346. [CrossRef]
58. Tang, J.H.; Chen, X.D.; Dai, F. Experimental study on the crack propagation and acoustic emission characteristics of notched rock beams under post-peak cyclic loading. *Eng. Fract. Mech.* **2020**, *226*, 106890. [CrossRef]
59. McCormick, N.; Lord, J. Digital Image Correlation. *Mater. Today* **2010**, *13*, 52–54. [CrossRef]
60. Hodowany, J.; Ravichandran, G.; Rosakis, A.J.; Rosakis, P. Partition of plastic work into heat and stored energy in metals. *Exp. Mech.* **2000**, *40*, 113–123. [CrossRef]
61. Basaran, C.; Nie, S.; Gomez, J.; Gunel, E.; Li, S.; Lin, M.; Tang, H.; Yan, C.; Yao, W.; Ye, H. Thermodynamic Theory for Damage Evolution in Solids. In *Handbook of Damage Mechanics: Nano to Macro Scale for Materials and Structures*; Voyiadjis, G.Z., Ed.; Springer: New York, NY, USA, 2021; pp. 1–39. [CrossRef]
62. Telops. How to Interpret Images from Infrared Cameras. Technical Notes. 2018. Available online: http://info.telops.com/How-to-Interpret-Images-From-Infrared-Cameras.html (accessed on 12 July 2021).

63. Meneghetti, G.; Ricotta, M. Evaluating the Heat Energy Dissipated in a Small Volume Surrounding the Tip of a Fatigue Crack. *Int. J. Fatigue* **2016**, *92*, 605–615. [CrossRef]
64. Gyekenyesi, A.L.; Baaklini, G.Y. Thermoelastic Stress Analysis: The Mean Stress Effect in Metallic Alloys. In *Nondestructive Evaluation of Aging Materials and Composites III*; International Society for Optics and Photonics: Bellingham, WA, USA, 1999; Volume 3585, pp. 142–151. [CrossRef]
65. Redjimi, A.; Knežević, D.; Savić, K.; Jovanovic, N.; Simović, M.; Vasiljevic, D. Noise Equivalent Temperature Difference Model for Thermal Images, Calculation and Analysis. *Sci. Tech. Rev.* **2014**, *64*, 42–49.
66. Budzier, H.; Gerlach, G. *Thermal Infrared Sensors: Theory, Optimisation and Practice*; Sons: Hoboken, NJ, USA, 2011. [CrossRef]
67. Lowenhar, E.; Carlos, M.; Dong, J. A New Generation of AE System Based on PCI Express Bus. In *Advances in Acoustic Emission Technology*; Shen, G., Wu, Z., Zhang, J., Eds.; Springer International Publishing: Berlin/Heidelberg, Germany, 2017; pp. 29–36. [CrossRef]
68. Bai, F.; Gagar, D.; Foote, P.; Zhao, Y. Comparison of alternatives to amplitude thresholding for onset detection of acoustic emission signals. *Mech. Syst. Signal Process.* **2017**, *84*, 717–730. [CrossRef]
69. Pomponi, E.; Vinogradov, A.; Danyuk, A. Wavelet based approach to signal activity detection and phase picking: Application to acoustic emission. *Signal Process.* **2015**, *115*, 110–119. [CrossRef]
70. Stepanova, L.; Ramazanov, I.; Kanifadin, K. Estimation of time-of-arrival errors of acoustic-emission signals by the threshold method. *Russ. J. Nondestruct. Test.* **2009**, *45*, 273–279. [CrossRef]
71. Agletdinov, E.; Merson, D.; Vinogradov, A. A New Method of Low Amplitude Signal Detection and Its Application in Acoustic Emission. *Appl. Sci.* **2019**, *10*, 73. [CrossRef]
72. Zhang, L.; Ozevin, D.; He, D.; Hardman, W.; Timmons, A. A Method to Decompose the Streamed Acoustic Emission Signals for Detecting Embedded Fatigue Crack Signals. *Appl. Sci.* **2018**, *8*, 7. [CrossRef]
73. Raju, K.N. An energy balance criterion for crack growth under fatigue loading from considerations of energy of plastic deformation. *Int. J. Fract. Mech.* **1972**, *8*, 1–14. [CrossRef]
74. Iziumova, A.; Vshivkov, A.; Prokhorov, A.; Kostina, A.; Plekhov, O. The study of energy balance in metals under deformation and failure process. *Quant. Infrared Thermogr. J.* **2016**, *13*, 242–256. [CrossRef]
75. Ranc, N.; Palin-Luc, T.; Paris, P.C.; Saintier, N. About the effect of plastic dissipation in heat at the crack tip on the stress intensity factor under cyclic loading. *Int. J. Fatigue* **2014**, *58*, 56–65. [CrossRef]
76. Vshivkov, A.; Plekhov, O.; Iziumova, A.; Zakharov, A.; Shlyannikov, V. The experimental study of heat dissipation during fatigue crack propagation under biaxial loading. *Frattura ed Integrità Strutturale* **2019**, *13*, 50–57. [CrossRef]
77. Harris, D.O.; Dunegan, H.L. Continuous Monitoring of Fatigue-Crack Growth by Acoustic-Emission Techniques. *Exp. Mech.* **1974**, *14*, 71–81. [CrossRef]
78. Sauerbrunn, C.; Kahirdeh, A.; Yun, H.; Modarres, M. Damage Assessment Using Information Entropy of Individual Acoustic Emission Waveforms during Cyclic Fatigue Loading. *Appl. Sci.* **2017**, *7*, 562. [CrossRef]
79. Awerbuch, J.; Ghaffari, S. Monitoring Progression of Matrix Splitting During Fatigue Loading Through Acoustic Emission in Notched Unidirectional Graphite/Epoxy Composite. *J. Reinf. Plast. Compos.* **1988**, *7*, 245–264. [CrossRef]
80. Eckles, W.; Awerbuch, J. Monitoring Acoustic Emission in Cross-Ply Graphite/Epoxy Laminates During Fatigue Loading. *J. Reinf. Plast. Compos.* **1988**, *7*, 265–283. [CrossRef]
81. Gagar, D.; Foote, P.; Irving, P.E. Effects of loading and sample geometry on acoustic emission generation during fatigue crack growth: Implications for structural health monitoring. *Int. J. Fatigue* **2015**, *81*, 117–127. [CrossRef]
82. Mazal, P.; Vlasic, F.; Koula, V. Use of Acoustic Emission Method for Identification of Fatigue Micro-cracks Creation. *Procedia Eng.* **2015**, *133*, 379–388. [CrossRef]
83. Roberts, T.M.; Talebzadeh, M. Acoustic emission monitoring of fatigue crack propagation. *J. Constr. Steel Res.* **2003**, *59*, 695–712. [CrossRef]
84. Han, Z.; Luo, H.; Sun, C.; Li, J.; Papaelias, M.; Davis, C. Acoustic emission study of fatigue crack propagation in extruded AZ31 magnesium alloy. *Mater. Sci. Eng. A* **2014**, *597*, 270–278. [CrossRef]
85. Williams, R.S.; Reifsnider, K.L. Investigation of Acoustic Emission During Fatigue Loading of Composite Specimens. *J. Compos. Mater.* **1974**, *8*, 340–355. [CrossRef]
86. Pascoe, J.A.; Zarouchas, D.S.; Alderliesten, R.C.; Benedictus, R. Using acoustic emission to understand fatigue crack growth within a single load cycle. *Eng. Fract. Mech.* **2018**, *194*, 281–300. [CrossRef]
87. Takemura, K.; Fujii, T. Fatigue Damage and Fracture of Carbon Fabric/Epoxy Composites under Tension-Tension Loading. *JSME Int. J. Ser. A Mech. Mater. Eng.* **1994**, *37*, 472–480._472. [CrossRef]
88. Dzenis, Y.A. Cycle-based analysis of damage and failure in advanced composites under fatigue 1. Experimental observation of damage development within loading cycles. *Int. J. Fatigue* **2003**, *25*, 499–510. [CrossRef]
89. Doan, D.D.; Ramasso, E.; Placet, V.; Zhang, S.; Boubakar, L.; Zerhouni, N. An unsupervised pattern recognition approach for AE data originating from fatigue tests on polymer-composite materials. *Mech. Syst. Signal Process.* **2015**, *64–65*, 465–478. [CrossRef]
90. ASTM International. *Standard Test Method for Measurement of Fatigue Crack Growth Rates*; Standard E647-15e1; ASTM International: West Conshohocken, PA, USA, 2015. [CrossRef]
91. Blaber, J.; Adair, B.; Antoniou, A. Ncorr: Open-Source 2D Digital Image Correlation Matlab Software. *Exp. Mech.* **2015**, *55*, 1105–1122. [CrossRef]

92. Harilal, R.; Ramji, M. Adaptation of Open Source 2D DIC Software Ncorr for Solid Mechanics Applications. 2014. Available online: https://www.researchgate.net/publication/267627316_Adaptation_of_Open_Source_2D_DIC_Software_Ncorr_for_Solid_Mechanics_Applications (accessed on 5 June 2021). [CrossRef]
93. Amraish, N.; Reisinger, A.; Pahr, D.H. Robust Filtering Options for Higher-Order Strain Fields Generated by Digital Image Correlation. *Appl. Mech.* **2020**, *1*, 174–192. [CrossRef]
94. Quanjin, M.; Rejab, M.R.M.; Halim, Q.; Merzuki, M.N.M.; Darus, M.A.H. Experimental investigation of the tensile test using digital image correlation (DIC) method. *Mater. Today Proc.* **2020**, *27*, 757–763. [CrossRef]
95. Pan, B. Digital image correlation for surface deformation measurement: Historical developments, recent advances and future goals. *Meas. Sci. Technol.* **2018**, *29*, 082001. [CrossRef]
96. Pan, B.; Li, K.; Tong, W. Fast, Robust and Accurate Digital Image Correlation Calculation Without Redundant Computations. *Exp. Mech.* **2013**, *53*, 1277–1289. [CrossRef]
97. MATLAB. *Version 9.9.0.1467703 (R2020b)*; The MathWorks Inc.: Natick, MA, USA, 2020.
98. Blaber, J.; Antoniou, A. *Ncorr Instruction Manual*; Georgia Institute of Technology: Atlanta, GA, USA, 2017.
99. Hosford, W.F. *Mechanical Behavior of Materials*, 2nd ed.; Cambridge University Press: Cambridge, UK, 2009. [CrossRef]
100. Tu, S.; Ren, X.; He, J.; Zhang, Z. Stress-strain curves of metallic materials and post-necking strain hardening characterization: A review. *Fatigue Fract. Eng. Mater. Struct.* **2020**, *43*, 3–19. [CrossRef]
101. Estimate Geometric Transform from Matching Point Pairs—MATLAB estimateGeometricTransform—MathWorks Nordic. 2013. Available online: https://se.mathworks.com/help/vision/ref/estimategeometrictransform.html (accessed on 21 May 2021).
102. Majchrowski, R.; Rozanski, L.; Grochalski, K. The Surface 3D Parameters to Describe the Diffuse Reflective and Emissive Properties of Selected Dielectrics. In Proceedings of the XXI IMEKO World Congress "Measurement in Research and Industry", Prague, Czech Republic, 30 August–4 September 2015. Available online: https://www.imeko.org/index.php/proceedings (accessed on 10 July 2021).
103. Taylor, G.I.; Quinney, H. The Latent Energy Remaining in a Metal after Cold Working. *Proc. R. Soc. Lond. Ser. A* **1934**, *143*, 307–326. [CrossRef]
104. Oliferuk, W.; Maj, M. Stress–strain curve and stored energy during uniaxial deformation of polycrystals. *Eur. J. Mech.* **2009**, *28*, 266–272. [CrossRef]
105. Fedorova, A.Y.; Bannikov, M.V.; Plekhov, O.A. A study of the stored energy in titanium under deformation and failure using infrared data. *Frat. Ed Integrita Strutt.* **2013**, *24*, 81–88. [CrossRef]
106. Fedorova, A.Y.; Bannikov, M.V.; Terekhina, A.I.; Plekhov, O.A. Heat dissipation energy under fatigue based on infrared data processing. *Quant. InfraRed Thermogr. J.* **2014**, *11*, 2–9. [CrossRef]
107. Bever, M.B.; Holt, D.L.; Titchener, A.L. The stored energy of cold work. *Prog. Mater. Sci.* **1973**, *17*, 5–177. [CrossRef]
108. Vinogradov, A.; Heczko, M.; Mazánová, V.; Linderov, M.; Kruml, T. Kinetics of cyclically-induced mechanical twinning in γ-TiAl unveiled by a combination of acoustic emission, neutron diffraction and electron microscopy. *Acta Mater.* **2021**, *212*, 116921. [CrossRef]
109. Vinogradov, A.; Orlov, D.; Danyuk, A.; Estrin, Y. Effect of grain size on the mechanisms of plastic deformation in wrought Mg–Zn–Zr alloy revealed by acoustic emission measurements. *Acta Mater.* **2013**, *61*, 2044–2056. [CrossRef]
110. Vinogradov, A.; Orlov, D.; Danyuk, A.; Estrin, Y. Deformation mechanisms underlying tension–compression asymmetry in magnesium alloy ZK60 revealed by acoustic emission monitoring. *Mater. Sci. Eng. A* **2015**, *621*, 243–251. [CrossRef]
111. Rosten, E.; Drummond, T. Fusing Points and Lines for High Performance Tracking. In Proceedings of the Tenth IEEE International Conference on Computer Vision (ICCV'05), Beijing, China, 17–21 October 2005; Volume 2, pp. 1508–1515. [CrossRef]
112. Detect Corners Using FAST Algorithm and Return cornerPoints Object—MATLAB detectFASTFeatures—MathWorks Nordic. Available online: https://se.mathworks.com/help/vision/ref/detectfastfeatures.html (accessed on 21 May 2021).
113. Mokhtarishirazabad, M.; Lopez-Crespo, P.; Moreno, B.; Lopez-Moreno, A.; Zanganeh, M. Evaluation of crack-tip fields from DIC data: A parametric study. *Int. J. Fatigue* **2016**, *89*, 11–19. [CrossRef]
114. Zanganeh, M.; Lopez-Crespo, P.; Tai, Y.H.; Yates, J.R. Locating the Crack Tip Using Displacement Field Data: A Comparative Study. *Strain* **2013**, *49*, 102–115. [CrossRef]
115. Bay, H.; Ess, A.; Tuytelaars, T.; Van Gool, L. Speeded-Up Robust Features (SURF). *Comput. Vis. Image Underst.* **2008**, *110*, 346–359. [CrossRef]
116. Wang, Z.; Vo, M.; Kieu, H.; Pan, T. Automated Fast Initial Guess in Digital Image Correlation. *Strain* **2014**, *50*, 28–36. [CrossRef]
117. Pan, B.; Yu, L.; Wu, D.; Tang, L. Systematic Errors in Two-Dimensional Digital Image Correlation Due to Lens Distortion. *Opt. Lasers Eng.* **2013**, *51*, 140–147. [CrossRef]
118. Maynadier, A.; Poncelet, M.; Lavernhe-Taillard, K.; Roux, S. One-shot Measurement of Thermal and Kinematic Fields: InfraRed Image Correlation (IRIC). *Exp. Mech.* **2012**, *52*, 241–255. [CrossRef]
119. Sukumaran, A.; Gupta, R.K.; Anil Kumar, V. Effect of Heat Treatment Parameters on the Microstructure and Properties of Inconel-625 Superalloy. *J. Mater. Eng. Perform.* **2017**, *26*, 3048–3057. [CrossRef]
120. Yasnikov, I.S.; Vinogradov, A.; Estrin, Y. Revisiting the Considère criterion from the viewpoint of dislocation theory fundamentals. *Scr. Mater.* **2014**, *76*, 37–40. [CrossRef]
121. Vinogradov, A.; Yasnikov, I.S.; Matsuyama, H.; Uchida, M.; Kaneko, Y.; Estrin, Y. Controlling strength and ductility: Dislocation-based model of necking instability and its verification for ultrafine grain 316L steel. *Acta Mater.* **2016**, *106*, 295–303. [CrossRef]

122. Yasnikov, I.S.; Estrin, Y.; Vinogradov, A. What governs ductility of ultrafine-grained metals? A microstructure based approach to necking instability. *Acta Mater.* **2017**, *141*, 18–28. [CrossRef]
123. Matic, P.; Kirby, G.C.; Jolles, M.I. The Relation of Tensile Specimen Size and Geometry Effects to Unique Constitutive Parameters for Ductile Materials. *Proc. R. Soc. Lond. Ser. A Math. Phys. Sci.* **1988**, *417*, 309–333.
124. Vinogradov, A.; Yasnikov, I.S.; Estrin, Y. Stochastic dislocation kinetics and fractal structures in deforming metals probed by acoustic emission and surface topography measurements. *J. Appl. Phys.* **2014**, *115*, 233506. [CrossRef]
125. Vinogradov, A.; Yasnikov, I.S.; Merson, D.L. Phenomenological approach towards modelling the acoustic emission due to plastic deformation in metals. *Scr. Mater.* **2019**, *170*, 172–176. [CrossRef]
126. Wang, Z.; Li, J.; Ke, W.; Zheng, Y.; Zhu, Z.; Wang, Z. Acoustic emission monitoring of fatigue crack closure. *Scr. Metall. Et Mater.* **1992**, *27*, 1691–1694. [CrossRef]
127. Ritchie, R. Mechanisms of fatigue-crack propagation in ductile and brittle solids. *Int. J. Fract.* **1999**, *100*, 55–83. [CrossRef]
128. Berkovits, A.; Fang, D. Study of fatigue crack characteristics by acoustic emission. *Eng. Fract. Mech.* **1995**, *51*, 401–416. [CrossRef]
129. Lindley, T.; Palmer, I.; Richards, C. Acoustic emission monitoring of fatigue crack growth. *Mater. Sci. Eng.* **1978**, *32*, 1–15. [CrossRef]
130. Chang, H.; Han, E.; Wang, J.; Ke, W. Acoustic emission study of fatigue crack closure of physical short and long cracks for aluminum alloy LY12CZ. *Int. J. Fatigue* **2009**, *31*, 403–407. [CrossRef]
131. Scruby, C.B.; Wadley, H.N.G.; Hill, J.J. Dynamic elastic displacements at the surface of an elastic half-space due to defect sources. *J. Phys. D Appl. Phys.* **1983**, *16*, 1069–1083. [CrossRef]
132. Wadley, H.N.G.; Scruby, C.B.; Sinclair, J.E. Acoustic emission source characterization. *J. Acoust. Soc. Am.* **1980**, *68*, S103–S104. [CrossRef]
133. Ono, K.; Cho, H.; Takuma, M. The origin of continuous emissions. *J. Acoust. Emiss.* **2005**, *23*, 206–214.
134. Wang, Z.; Li, J.; Ke, W.; Zhu, Z. Characteristics of acoustic emission for A537 structural steel during fatigue crack propagation. *Scr. Metall. Et Mater.* **1992**, *27*, 641–646. [CrossRef]
135. Gong, Z.; DuQuesnay, D.; McBride, S. Measurement and Interpretation of Fatigue Crack Growth in 7075 Aluminum Alloy Using Acoustic Emission Monitoring. *J. Test. Eval.* **1998**, *26*, 567–574. [CrossRef]
136. Pollock, A.A. Material Brittleness and the Energetics of Acoustic Emission. In *Experimental Mechanics on Emerging Energy Systems and Materials*; Proulx, T., Ed.; Springer: New York, NY, USA, 2011; Volume 5, pp. 73–79.
137. Morton, T.; Harrington, R.; Bjeletich, J. Acoustic emissions of fatigue crack growth. *Eng. Fract. Mech.* **1973**, *5*, 691–697. [CrossRef]
138. Morton, T.M.; Smith, S.; Harrington, R.M. Effect of loading variables on the acoustic emissions of fatigue-crack growth. *Exp. Mech.* **1974**, *14*, 208–213. [CrossRef]
139. Han, Z.; Luo, H.; Cao, J.; Wang, H. Acoustic emission during fatigue crack propagation in a micro-alloyed steel and welds. *Mater. Sci. Eng. A* **2011**, *528*, 7751–7756. [CrossRef]
140. Dunegan, H.L.; Harris, D.O.; Tatro, C.A. Fracture analysis by use of acoustic emission. *Eng. Fract. Mech.* **1968**, *1*, 105–110. IN23–IN24, 111–122. [CrossRef]
141. Heiple, C.; Carpenter, S. Acoustic emission produced by deformation of metals and alloys—A review. Part 1. *J. Acoust. Emiss.* **1987**, *6*, 177–204.
142. Heiple, C.R.; Carpenter, S.H. Acoustic emission produced by deformation of metals and alloys—A review. Part 2. *J. Acoust. Emiss.* **1987**, *6*, 215–237.

Article II

Acta Materialia 237 (2022) 118190

Contents lists available at ScienceDirect

Acta Materialia

journal homepage: www.elsevier.com/locate/actamat

Stored and dissipated energy of plastic deformation revisited from the viewpoint of dislocation kinetics modelling approach

A. Sendrowicz[a,*], A.O. Myhre[a], I.S. Yasnikov[b], A. Vinogradov[a,*]

[a] Department of Mechanical and Industrial Engineering, Norwegian University of Science and Technology – NTNU, Trondheim N-7491, Norway
[b] Research Institute of Advanced Technologies, Togliatti State University, Belorusskaya str. 14, Togliatti 445020, Russia

ARTICLE INFO

Article history:
Received 10 March 2022
Revised 9 May 2022
Accepted 18 July 2022
Available online 19 July 2022

Keywords:
Strain hardening
Energy partitioning
Dislocation kinetics
Thermography

ABSTRACT

In the present work, we revisited the classical topic of elastic energy storage during strain hardening of metals from a perspective of the analytically tractable thermodynamic modelling framework inspired by the widely accepted phenomenological single-variable dislocation evolution approach. The model versatility has been extended towards predicting the energy partitioning during plastic flow. With a total dislocation density serving as a principal variable governing strain hardening during constant strain rate tensile tests, we have been able to demonstrate a very good predictive capability of the proposed analytical solutions. Besides the simplicity, the flexibility and predictive power of the obtained analytical solutions suggest that the entire approach can be used for further modelling, where the emphasis should be placed on the integration of various possible mechanisms of heat dissipation into the proposed framework. Although the examples of successful application of the model refer to the low-carbon austenitic stainless 316L steel, their adaptation to other fcc, bcc or hcp metals is rather straightforward.

1. Background and motivation

Plastic deformation is a highly dissipative process involving dislocation production and storage, motion and annihilation. It has long been recognised that most of the mechanical energy expended in plastic straining is converted into heat while the remainder (a few percent only) is stored in the deformed solid as internal energy [1–4]. The first law of thermodynamics axiomatically states that an increment of work δA, which is done on the system, increases its internal energy dU and, in non-adiabatic processes, results in the heat transfer δQ from the system to the reservoir:

$$\delta A = dU + \delta Q \tag{1}$$

The internal energy can be stored in the system in a variety of ways. Generally speaking, heat and work cannot be conserved independently since they both depend on the process (this is reflected symbolically by δ underlying that the increments of heat and work are not perfect differentials in contrast to the internal energy U).

The first attempts to recognise the significance of stored energy in deformation processes get back to pioneering works by Farren and Taylor [5] and Taylor and Quinney [1] in the mid-twenties of the past century. An excellent review of the early experimental efforts relying on temperature measurements by thermocouples or on heat release measurements by deformation or annealing calorimeters employed to assess the behaviour of the stored and dissipated energy during the plastic flow of metals and alloys was provided by Bever et al. [6] in 1973. Recent years have witnessed the boosting research in the field thanks to the advent of the modern highly-sensitive thermographic technology, which renewed the interest in the topic owing to the direct access enabled by infrared systems to the thermodynamics of plastic flow, strain localisation and fracture in monotonic and cyclic deformation through the measurements of the local distribution of temperature on the surface - information that is not accessible otherwise [7–21]. Notably, significant progress has been achieved in fatigue, where thermography has been proven effective for quantifying the crack tip position and characterising the cyclic plastic zone or for the "express" evaluation of the fatigue limit of materials from a monotonic tensile test [12,20,22–25]. When the two full-field measurement techniques – IRT and DIC – are brought together, the synergy arises from the possibility of quantifying the strain and temperature distribution on the microstructural scale [26].

* Corresponding authors.
E-mail addresses: aleksander.sendrowicz@ntnu.no (A. Sendrowicz), alexei.vinogradov@ntnu.no (A. Vinogradov).

https://doi.org/10.1016/j.actamat.2022.118190

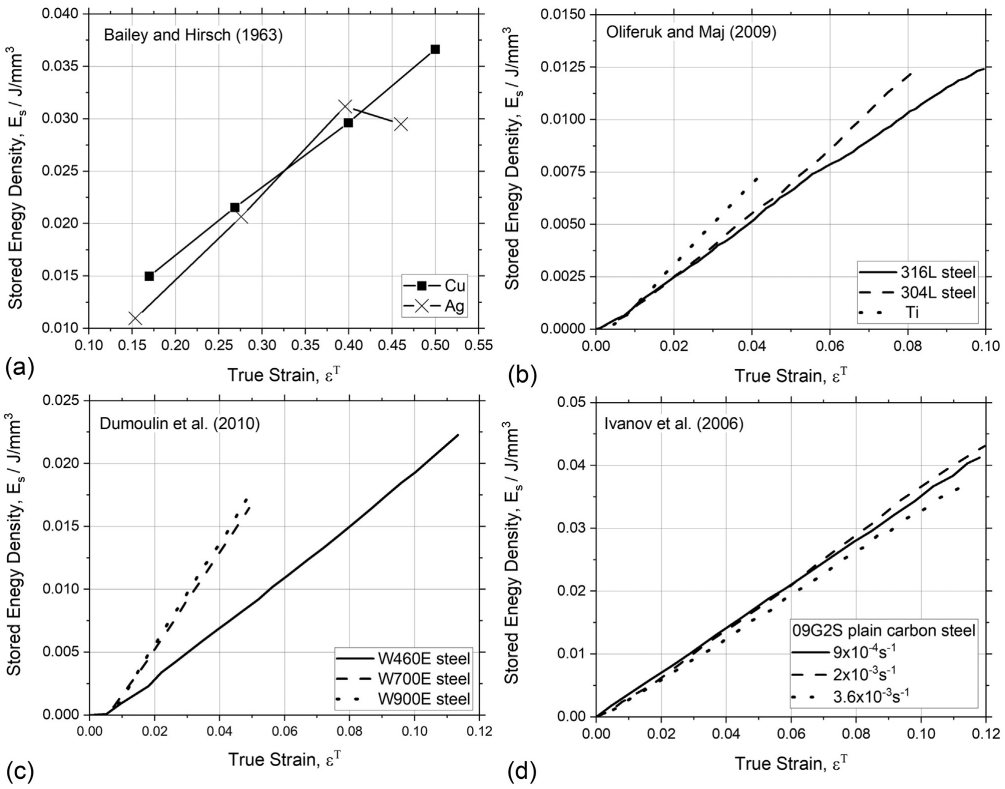

Fig. 1. Experimental data showing the most common behaviour of the stored energy as a function of true strain for different materials under tensile testing: (a) Cu and Ag [32,33], (b) 316L and 304 steels and pure Ti [8], (c) Weldox steels [17], and (d) plain carbon steel [34].

During loading at low homologous temperatures, almost all of the stored energy is attributed to the accumulation of dislocations generated during plastic straining [27]. Thus, the most noticeable difference between the deformed and the initial undeformed states lies in the accumulated population of dislocation and details of the dislocation interactions. The stored energy reflects all the microstructural changes occurring in the course of strain hardening, and the non-dissipated energy is stored mainly in the elastic stress fields of dislocations [28]. Nevertheless, as has been noticed by Nabarro et al. [29] in 1964, measurements of stored energy generally give little guidance in building a work hardening model as it is very insensitive to the arrangement of the dislocations [30]. This message accurately captures the scope of the problem, which has been recognised long ago and remains acute up to date. Indeed, Fig. 1 illustrates the foregoing statement by Nabarro et al. and compiles several results of independent measurements of the stored energy as a function of strain for various structural materials. In spite of the difference in experimental setups, equipment and calculation algorithms used by different investigators, the most prominent result is that the stored energy E_s tends to be nearly linearly dependent on strain regardless of the materials tested, their microstructure, properties, strain hardening behaviour, and mechanisms involved (see also the same conclusion drawn by [31] in their early study based on calorimetric measurements).

These observations can be extended to a wide range of materials [6,35], including TWIP and TRIP steels, Inconel and Cu-based alloys (these results by the present authors are not shown here for brevity and will be reported elsewhere). The linear relation between the stored energy and true (logaritmic) strain ε (from now on, we will confine ourselves to true stress and logarithmic strain, if not stated otherwise) does not necessarily hold precisely, and the $E_s(\varepsilon)$ dependence can exhibit either a slightly concave or convex shape, which can be caused by unclarified experimental issues and regular experimental scatter. Although these observations of dissipation and storage processes cannot help much in developing the strain hardening models, as correctly noticed by Nabarro et al. [29], they can be used to test the consistency of plasticity models aiming, ultimately, at formulating predictive indicators for imminent failure. Even though multiple mechanisms controlling the material's resistance to plastic flow can be named and classified nowadays, most engineering materials are so complicated in the microstructure that it is difficult to specify the relative significance of a given mechanism in a particular set of circumstances up to date. Moreover, measurements of average responses in mechanical and thermodynamic quantities and bridging these responses with the evolution of the microstructure remain indispensable for the development of non-destructive means for real-time monitoring of the damaging processes occurring in loaded structures.

In the present work, we endeavour to propose a phenomenological thermodynamic modelling methodology inspired and informed by the dislocation evolution theory, aiming at gaining a deeper insight into energy partitioning during plastic flow.

2. Stored energy and the evolution of the dislocation ensemble

2.1. A brief overview of the single internal variable model of strain hardening

The latent (or stored) energy is defined as a difference between the energy of the crystal with defects accumulated in the course of plastic deformation and the energy of the initial undeformed crystal. Assuming that during homogeneous uniaxial monotonic deformation, the strain hardening is governed entirely by the microstructural changes caused by dislocations and their interactions with each other, it is the number (or density) of dislocations that determines the stored energy. The total dislocation density in the alloy is related to the flow stress according to the Taylor equation in the form:

$$\sigma(\rho) = \sigma_{SS} + M\alpha Gb\sqrt{\rho} = \sigma_{SS} + \beta\sqrt{\rho} \tag{2}$$

where the first term σ_{SS} refers to the additive contribution from the solid solution strengthening and the second term accounts for the strengthening due to dislocation interactions, b is the magnitude of the Burger's vector of the dislocation, G is the shear modulus, and M is the texture-related Taylor orientation factor converting shear stress τ and strain γ to axial ones as $\tau = \sigma/M, \quad \gamma = \varepsilon M$; $\alpha = \alpha(\dot{\varepsilon}, T)$ is a numerical factor capturing the strain-rate and temperature dependence of the flows stress and dislocation arrangement and ranging typically between 0.1 and 0.5; $\beta = M\alpha Gb$ is used henceforth for brevity. Here, we incorporated the lattice friction stress into the σ_{SS}term for simplicity, as will be discussed below.

Thus, to find the flow stress as a function of plastic strain ε, one needs to know how the dislocation density ρ evolves with time t under a given loading mode, plastic strain rate $\dot{\varepsilon}$ and temperature. This information is derived from the solution of an evolution equation for $\rho = \rho(t)$, which generally reads as

$$\frac{d\rho}{dt} = \frac{d\rho^+}{dt} - \frac{d\rho^-}{dt} \quad or \quad \dot{\rho}(t) = \dot{\rho}^+ - \dot{\rho}^- \tag{3}$$

where the superimposed dot refers to the time derivative; the terms with superscript + and – signs on the right-hand side account for the competitive dislocation storage and annihilation processes, respectively. By using the definition of the plastic strain rate, this kinetic equation is commonly written for $\rho = \rho(\varepsilon)$

$$\frac{d\rho}{d\varepsilon} = \frac{d\rho^+}{d\varepsilon} - \frac{d\rho^-}{d\varepsilon} \tag{4}$$

expressed as a function of plastic strain ε; As has been discussed in [36–38], at variance with strain and stress, the total dislocation density can be regarded as a state variable for the deforming crystalline solid. Therefore, if the density of dislocations in two pieces of the same material is the same, one can plausibly assume that the stored energy in these samples is the same too, regardless of the strain path. This statement is backed by the wealth of experimental data ubiquitously supporting the Taylor-type relation (2), which holds regardless of virtually all conceivable geometrical arrangements of dislocations or specific details of the dislocation-dislocation interactions [33].

In the traditional way of implementing the dislocation "birth and death" approach to the strain hardening modelling, the governing dislocation evolution equation is postulated, considering the rates of dislocation production and disappearance according to the assumed underlying mechanisms. The time-proven recipe calls for a family of simple single internal variable kinetic equations propagated by Kocks and Mecking (KM) [39,40] (see also [41]) in the form

$$\frac{d\rho}{d\gamma} = \frac{d\rho}{Md\varepsilon} = \frac{k_1}{b}\sqrt{\rho} - k_2\rho \tag{5}$$

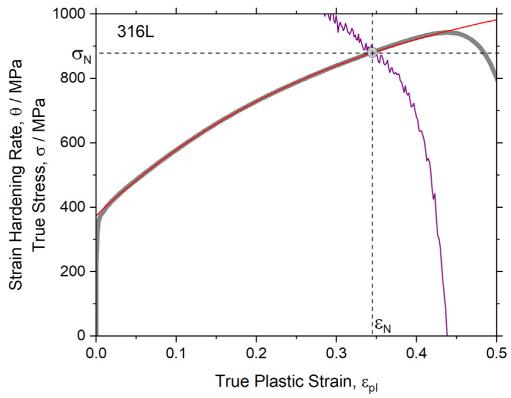

Fig. 2. True stress- logarithmic strain curves and their approximations (red lines) by the Kocks-Mecking model with the input parameters shown in Table 2 for the specimens tested at the nominal strain rate $\dot{\varepsilon}$=10−2 s−1. The dashed line indicates the Considère point and the corresponding necking strain and stress.

with k_1 and k_2 - dimensionless parameters controlling the rates of dislocation production and dynamic recovery, respectively; k_1 is the athermal coefficient, while the term $k_2(\dot{\varepsilon}, T)\rho$ represents the temperature and strain rate dependent dislocation annihilation kinetics. As a note, the governing Eq. (5) can be obtained on the grounds of irreversible thermodynamics applied to dislocation plasticity [36,42] instead of being postulated ad hoc.

The solution of the initial value problem for the homogeneous Eq. (5) with $\rho(\varepsilon = 0) = \rho_0$ provides the explicit relation for the dependence of the total dislocation density on plastic strain:

$$\rho(\varepsilon) = \left(\frac{k_1}{bk_2} + \left(\sqrt{\rho_0} - \frac{k_1}{bk_2}\right)\exp\left(-\frac{k_2 M\varepsilon}{2}\right)\right)^2 \tag{6}$$

When combined with Eq. (2), the flow stress is obtained as a function of strain:

$$\sigma = \sigma_{SS} + \beta\left(\frac{k_1}{bk_2} + \left(\sqrt{\rho_0} - \frac{k_1}{bk_2}\right)\exp\left(-\frac{k_2 M\varepsilon}{2}\right)\right) \tag{7}$$

After introducing new variables:

$$\sigma_S = \frac{\beta k_1}{bk_2} = \frac{\alpha GMk_1}{k_2}, \quad \tilde{\varepsilon} = \frac{2}{k_2 M} \tag{8}$$

Eq. (7) can be rearranged as:

$$\sigma = \sigma_I + (\sigma_\infty - \sigma_I)\left(1 - \exp\left(-\frac{\varepsilon}{\tilde{\varepsilon}}\right)\right) \tag{9}$$

The flow stress tends to saturate asymptotically at $\sigma_\infty = \sigma_{SS} + \sigma_S$ when $\varepsilon \to \infty$. The initial hardening due to contributions from both solid solution and dislocation strengthening mechanisms is, thus, $\sigma_I = \sigma_{SS} + \sigma_0$ at $\varepsilon = 0$. Here $\sigma_0 = \beta\sqrt{\rho_0}$ refers to the hardening due to dislocations residing in the microstructure prior to loading. The parameter $\tilde{\varepsilon}$ governs the necking strain as will be explicit from what follows, according to the findings reported in [37,38,43].

The strain hardening rate $\theta(\varepsilon) = \frac{d\sigma(\varepsilon)}{d\varepsilon}$ is thus obtained as follows:

$$\theta(\varepsilon) = \frac{1}{\tilde{\varepsilon}}(\sigma_S - \sigma_0)\exp\left(-\frac{\varepsilon}{\tilde{\varepsilon}}\right) = \frac{1}{\tilde{\varepsilon}}(\sigma_{SS} + \sigma_S - \sigma(\varepsilon)) = \frac{1}{\tilde{\varepsilon}}(\sigma_\infty - \sigma(\varepsilon)) \tag{10}$$

Fig. 2 shows an example of successful fitting of the KM model to the experimental data obtained in the present work for 316L

Table 1
Model parameters used to approximate the stress-strain data for 316L steel specimens tested in tension at the nominal strain rate $\dot{\varepsilon} = 10^{-2}\text{s}^{-1}$.

Parameter	Specimens		
$\dot{\varepsilon}$, s^{-1}	10^{-2}	$3{\cdot}10^{-3}$	10^{-3}
σ_I, MPa	374	357	393
$\sigma_\infty - \sigma_I$, MPa	779	834	893
$1/\tilde{\varepsilon}$	3.04	2.98	2.52
σ_∞, MPa	1153	1191	1286
$\sigma_S = \sigma_\infty - \sigma_{SS}$, MPa	998	1036	1131
$k_1 = \frac{2\sigma_S}{\alpha G M^2 \tilde{\varepsilon}}$	0.0277	0.0282	0.0260
$k_2 = \frac{2}{M\tilde{\varepsilon}}$	1.99	1.95	1.65
Necking strain ε_N (graph / model)	0.33 / 0.33	0.38 / 0.34	0.39 / 0.35
Necking stress σ_N (graph / model), MPa	876 / 867	934 / 891	960 / 921

austenitic stainless steel, as described in detail in Section 3. The excellent agreement is seen between the experimental stress-strain curve at least up to the point of macroscopic instability when the necking sets in at the necking strain ε_N, i.e., as long as the KM approximations are valid. The critical strain ε_N can be determined from the experimental data according to the Considère criterion [44]

$$\left.\frac{\partial\sigma}{\partial\varepsilon}\right|_{\dot{\varepsilon}} = \sigma \tag{11}$$

The experimental true stress-strain curves were differentiated numerically with respect to strain, and the strain hardening rate $\theta(\varepsilon)$ obtained in this way was plotted together with the $\sigma(\varepsilon)$ curve, as shown in Fig. 2. The intercept between $\sigma(\varepsilon)$ and $\theta(\varepsilon)$ curves marks the necking instability point (ε_N, σ_N). By plugging Eqs.(9) and (10) for $\sigma(\varepsilon)$ and $\theta(\varepsilon)$ derived from the KM model into the Considère criterion (11), one obtains the necking strain and stress, respectively, as (see [37,45] for the detailed discussion)

$$\begin{aligned}\varepsilon_N^{KM} &= \tilde{\varepsilon}\ln\left[\left(1-\tfrac{\sigma_I}{\sigma_\infty}\right)\left(1+\tfrac{1}{\tilde{\varepsilon}}\right)\right] \sim \tilde{\varepsilon}\\ \sigma_N^{KM} &= \tfrac{\sigma_\infty}{\tilde{\varepsilon}+1}\end{aligned} \tag{12}$$

Results of fitting the experimental data to the KM model Eq. (9) are shown graphically in Fig. 2 by red lines superimposed with the $\sigma(\varepsilon)$ curve (shown in black). The main model parameters are listed in Table 1. Other quantities are: $M = 3.06$, $\alpha = 0.4$ and $b = 0.254$ nm. The friction stress characterising the inherent resistance of the γ-iron lattice to dislocation glide is described by the Peierls-Nabarro stress, and it can be calculated as $2 \times 10^{-4}G$ [46]. With $G = 77$ GPa for the 316L austenitic steel under investigation (see Section 3), σ_{PN} is about 15 MPa. Solid solution strengthening for stainless steels can be expressed by the empiric relationship $\tilde{\sigma}_{SS} = \sum_i B_i C_i$, where B_i is the temperature dependent factor for each solute element with the concentration C_i [47]. Using the values of B_i calculated according to [47] for each element listed in Table 2, the $\tilde{\sigma}_{SS}$ value is found to be of 140±3 MPa. Since σ_{PN} and $\tilde{\sigma}_{SS}$ are additive contributions, for further numerical estimates, we combine them into the single $\sigma_{SS} = \sigma_{PN} + \tilde{\sigma}_{SS}$ term entering Eq. (2), which is equal to 155 MPa approximately. $\sigma_0 = \sigma_I - \sigma_{SS}$ is taken to be 220±12 MPa based on the scatter of experimental data.

One can notice that not only does the model approximate the experimental data nicely up to the point of macroscopic instability, but it comes with an important corollary: a remarkably good agreement also exists between the experimentally determined necking stress and strain (ε_N, σ_N) and their model predictions (ε_N^{KM}, σ_N^{KM}) according to Eq. (12). The same observations apply to other strain rates used in the experimental session, c.f., Table 1. Since the current modelling approach relies on the simplistic model, it is essential for further analysis that the theoretical

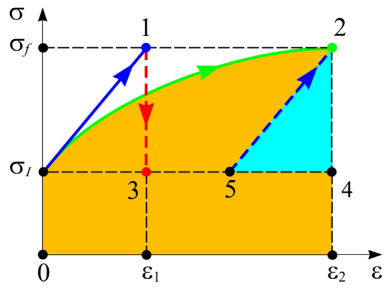

Fig. 3. Schematic illustration of the virtual tensile test up to the same flow stress via two paths: (1) without dislocation annihilation and (2) with dislocation annihilation.

expectations are in harmony with the actual strain hardening behaviour, as seen in Fig. 2 and Table 1. Therefore, we confine ourselves to this basic single internal variable model, which is reasonably applicable up to the modest strains achievable in tensile tests without accounting for dislocation patterning and splitting the total dislocation population into the cell-interior and cell-wall dislocations in cell forming materials [48–60].

2.2. Stored energy in a thought straining experiment

To develop a self-consistent microstructurally motivated, yet purely phenomenological, model of energy dissipation and storage, the following thought experiment is deemed useful.

Consider a hypothetical material that undergoes plastic deformation with work hardening after initial plastic yielding commencing at the σ_I stress, Fig. 3. Let us assume that plastic deformation occurs up to a certain flow stress σ_f, and imagine that the dislocation ensemble can evolve according to either of two virtual scenarios: (1) the dislocations nucleate, move and store in the deforming body along the strain path $\sigma_I \to 1(\varepsilon_1)$ without dynamic recovery, and (2) the dislocations nucleate, move, interact with each other and partly annihilate along the path $\sigma_I \to 2(\varepsilon_2)$.

According to Scenario 1 ($\sigma_I \to 1$), k_2=0, the solution of the initial value problem for Eq. (5) together with Eq. (2) yields a linear strain hardening equation:

$$\begin{aligned}&\sigma_1(\varepsilon) = \sigma_I + \tfrac{\sigma_S}{\tilde{\varepsilon}}\varepsilon \qquad (a)\\ &\sigma_1(\varepsilon_1) = \sigma_f = \sigma_I + \tfrac{\sigma_S}{\tilde{\varepsilon}}\varepsilon_1 \qquad (b)\end{aligned} \tag{13}$$

Here, the subscript index 1 indicates that the deformation occurs according to Scenario 1 without dislocation annihilation. Along this deformation path, the entire mechanical work is expended in the formation of the defect microstructure with the latent energy E_{s1} and heat dissipation according to Eq. (1) $A_1 = E_{s1} + Q_1$. If we isothermally anneal the accumulated defects and return the system to the initial state with the initial dislocation density ρ_0 along the path 1→3, the energy stored by plastic deformation in state 3 will be zero while the residual plastic strain will be ε_1. Thus, the energy stored by plastic deformation at point 1 will be equal to the area of the triangle $\sigma_I - 1 - 3$, while the dissipated heat will be equal to the area of the rectangle $0 - \sigma_I - 3 - \varepsilon_1$ in Fig. 3.

For Scenario 2 $\sigma_I \to 2$, the work done on the specimen is equal to the area of the curvilinear trapezoid $0 - \sigma_I - 2 - \varepsilon_2$, and the energy balance in state 2 reads as $A_2 = E_{s2} + Q_2$. Since the material in the final deformation state obtained according to either of these two scenarios has the same flow stress, therefore, the corresponding state variable – total dislocation density - is the same too. Thus, the stored energies in states 1, E_{s1}, and 2, E_{s2}, are also the

Table 2
Chemical Composition of the AISI 316L steel.

Element	C	Si	Mn	P	S	Cr	Mo	Ni	N	Fe
Wt. %	0.024	0.50	1.75	0.035	0.017	16.89	2.02	10.02	0.052	balance

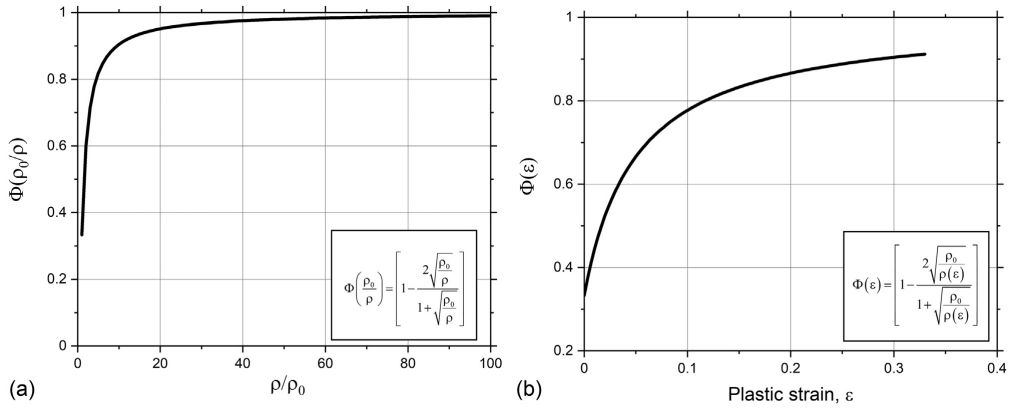

Fig. 4. Schematic illustration of the behaviour of the F function in dependence of the relative dislocation density ρ/ρ_0 (a) and plastic strain ε(b); the experimental data shown in Fig. 2 are used to construct the plot (b).

same. The triangle $\sigma_I - 1 - 3$ depicting the dislocation latent energy accumulation is equivalent to the triangle $2 - 5 - 4$, the area of which represents the stored energy in state 2. The remaining part of the trapezoid $0 - \sigma_I - 2 - \varepsilon_2$ corresponds to the dissipated heat. Stored energies E_{s1} and E_{s2} are easily calculated as

$$E_{s1} = E_{s2} = \frac{1}{2}(\sigma_f - \sigma_I)\varepsilon_1 \tag{14}$$

The relation between strains ε_1 and ε_2 is determined by the obvious relation $\sigma_1(\varepsilon_1) = \sigma_2(\varepsilon_2) = \sigma_f$, which yields:

$$\sigma_I + \frac{\sigma_S}{\tilde{\varepsilon}}\varepsilon_1 = \sigma_f, \quad \Rightarrow \quad \varepsilon_1 = \frac{\tilde{\varepsilon}}{\sigma_S}(\sigma - \sigma_I) \tag{15}$$

By plugging ε_1 into Eq. (14) and dropping the subscript f index, without loss of generality, one obtains the following expression for the stored energy:

$$E_s(\sigma) = \frac{\tilde{\varepsilon}}{2\sigma_S}(\sigma - \sigma_I)^2 \tag{16}$$

Let us recall that various strain hardening theories starting from different premises end up with a similar square dependence of E_s on the flow stress, i.e., $E_s \sim \sigma^2$ (Refs. [6,61,62] represent a few typical examples). For further analysis, Eq. (16) can be rearranged using the Taylor Eq. (2) in terms of the dislocation densities as (see Appendix A for the complete derivation):

$$E_s = \frac{\tilde{\varepsilon}\beta^2}{2\sigma_S}(\rho - \rho_0)\left[1 - \frac{2\sqrt{\frac{\rho_0}{\rho}}}{1 + \sqrt{\frac{\rho_0}{\rho}}}\right] = \frac{\alpha G b^2}{k_1}(\rho - \rho_0)\Phi\left(\frac{\rho_0}{\rho}\right) \tag{17}$$

where the non-linear function $\Phi(\frac{\rho_0}{\rho}) = [1 - \frac{2\sqrt{\frac{\rho_0}{\rho}}}{1+\sqrt{\frac{\rho_0}{\rho}}}]$ is introduced in the right-hand side. This function is bounded between 0 at $\rho = \rho_0$ and 1 at $\rho \gg \rho_0$ (or at $\rho_0 = 0$). The schematic behaviour of the Φ function with ρ increasing by two orders of magnitude from ρ_0 to $100\,\rho_0$ is shown in Fig. 4a. One can see that after a rapid initial growth this function reaches a (quasi-) steady-state plateau, and the stored energy is linear on the increment of the dislocation density $\Delta\rho = \rho - \rho_0$ when $\rho \gg \rho_0$:

$$E_s \approx \frac{\tilde{\varepsilon}\beta^2}{2\sigma_S}(\rho - \rho_0) = \frac{\alpha G b^2}{k_1}(\rho - \rho_0) \tag{18}$$

However, we should emphasise that within the range of strains limiting the uniform deformation stage (c.f., Fig. 2 for the 316L steel), the Φ function is strongly non-linear and cannot be neglected, Fig. 4b.

Using the initial value problem solutions for $\rho(\varepsilon)$, Eq. (6), and $\sigma(\varepsilon)$, Eq. (9), obtained from the KM model (7), Eq. (17) can be easily converted into the dependence of the stored energy on the plastic strain.

An interesting implication inspired by the original works by Kocks and Mecking [39,40] can be obtained from Eq. (17) by differentiating it with respect to strain:

$$\frac{dE_s}{d\varepsilon} = \frac{\tilde{\varepsilon}\beta^2}{2\sigma_S}\frac{d\rho}{d\varepsilon}\left(1 - \sqrt{\frac{\rho_0}{\rho}}\right) = \frac{\alpha G b^2}{k_1}\frac{d\rho}{d\varepsilon}\left(1 - \sqrt{\frac{\rho_0}{\rho}}\right) \tag{19}$$

Neglecting initial hardening in Eq. (2), Kocks and Mecking [39,40] noted that the product $\sigma \cdot \theta$ is related to the dislocation (or energy) storage rate as

$$\sigma\theta = \sigma\frac{d\sigma}{d\varepsilon} = \frac{\beta^2}{2}\frac{d\rho}{d\varepsilon} \tag{20}$$

Using the model data derived from the non-linear model approximation for experimental data shown in Fig. 2, the behaviour of $\rho(\varepsilon)$ and the corresponding storage rate $\frac{d\rho}{d\varepsilon}$ is represented in Fig. 5a. When corrected for the initial dislocation density according to Eq. (19), the storage rate decreases, Fig. 5b, due to the factor $(1 - \sqrt{\frac{\rho_0}{\rho}})$. Finally, the energy storage rate $\frac{dE_s}{d\varepsilon}$ determined by Eq. (19) can be calculated and plotted against strain as shown in Fig. 5b, and can be compared to experimental data derived from thermographic measurements discussed in the following sections. One can see that despite the significant fluctuations of the measured energy storage rate (the reasons of which will be discussed

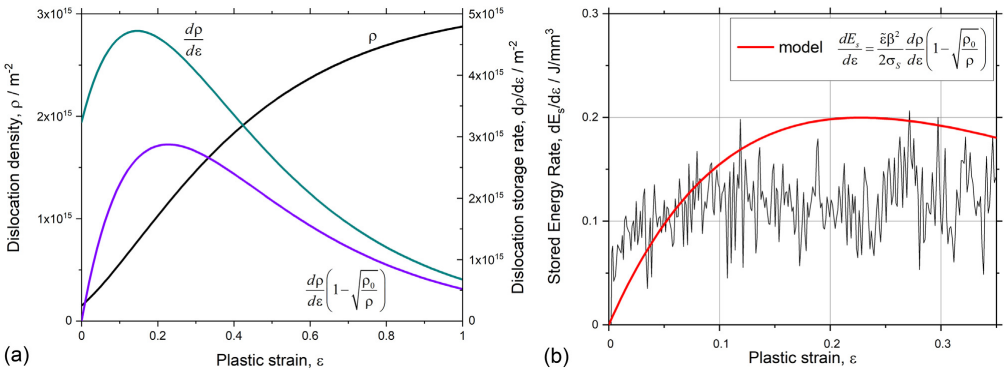

Fig. 5. Schematic illustration of the behaviour of the dislocation density and its storage rate according the KM model and effect of the correcting factor followed from the present model (a), and the behaviour of the stored energy predicted by the present model (red solid line), Eq. (19); the experimental data shown in Fig. 2 are used to construct the model plots (a) and (b); experimental data shown in (b) are discussed in Sections 4 and 5.

below), the experimental data tend to follow the predicted model trend numerically fairly well without any fitting or optimisation procedures. Admittedly, the experimental scatter did not permit recovering the peak in the model $\frac{dE_S}{d\varepsilon}$ behaviour, which is not surprising considering that the measured $\frac{dE_S}{d\varepsilon}$ is as low as 10% of the total mechanical energy rate.

Alternatively, the stored power due to dislocation accumulation can be found by the differentiation of Eq. (16) with respect to time as:

$$P_S = \frac{dE_s}{dt} = \frac{dE_s}{d\varepsilon}\frac{d\varepsilon}{dt} = \frac{\tilde{\varepsilon}}{\sigma_S}(\sigma - \sigma_I)\theta\dot{\varepsilon} \tag{21}$$

One can easily show that this equation is identical with (19). Here we should notice that, in principle, the true strain rate $\dot{\varepsilon} = \dot{\varepsilon}(\varepsilon)$ in the plastically deforming part of the specimen can be not constant, depending on the strain measurement method and the machine response. It is therefore essential to perform the full-field measurements of local strain distributions throughout the test run. By plugging Eq. (10) for the strain hardening coefficient $\theta(\varepsilon)$ into the last equation, the stored power is found as:

$$P_s = \frac{\dot{\varepsilon}}{\sigma_S}(\sigma - \sigma_I)(\sigma_\infty - \sigma) \tag{22}$$

Since the expended mechanical power at a given plastic strain ε is defined simply as:

$$P_e = \frac{\delta A}{dt} = \sigma\dot{\varepsilon} \tag{23}$$

The dissipated power at the same strain, according to the first law of thermodynamics, is found as:

$$P_d = P_e - P_s = \sigma\dot{\varepsilon} - \frac{\dot{\varepsilon}}{\sigma_S}(\sigma - \sigma_I)(\sigma_\infty - \sigma) \tag{24}$$

The expressions (22) and (24) for P_s and P_d, respectively, are notably simple yet very insightful as they bridge both quantities to the dislocation kinetics through the parameter σ_S that is explicitly expressed by k_1 and k_2.

2.3. Partitioning dissipated and stored power densities (first law of thermodynamics approach)

In this complementary approach we rewrite the first law of thermodynamics (1) as:

$$\frac{\delta Q}{dt} + \frac{dU}{d\rho}\cdot\frac{d\rho}{dt} = \sigma\frac{d\varepsilon}{dt} \tag{25}$$

which implies that the change in the internal energy occurs primarily due to the evolution of the total dislocation density ρ, which is regarded as a state variable. Using a general form of the kinetics Eq. (3) for ρ evolving through the coupled "generation and annihilation" processes, the latter equation reads as:

$$\frac{\delta Q}{dt} + \frac{dU}{d\rho}\left(\frac{d\rho^+}{dt} - \frac{d\rho^-}{dt}\right) = \sigma\frac{d\varepsilon}{dt} \tag{26}$$

This equation explicitly states that the internal energy of the plastically deforming solid increases due to the dislocation production and storage term $\frac{dU}{d\rho}\frac{d\rho^+}{dt}$ and decreases due to dynamic dislocation recovery and annihilation expressed as $\frac{dU}{d\rho}\frac{d\rho^-}{dt}$. By identical transformation, the total mechanical work done on the system can be represented as a sum of two components $\sigma\frac{d\varepsilon}{dt} = \sigma_I\frac{d\varepsilon}{dt} + (\sigma - \sigma_I)\frac{d\varepsilon}{dt}$, where the first term is attributed to the fully dissipative process of dislocation production, glide and annihilation without accumulation (in this process, the energy dissipation equals the expended work) in the ideal elastic-viscoplastic material with the initial hardening σ_I, while the second term describes the strain hardening process commencing from σ_I. Eq. (26), therefore, reads as:

$$\frac{\delta Q}{dt} + \frac{dU}{d\rho}\left(\frac{d\rho^+}{dt} - \frac{d\rho^-}{dt}\right) = \sigma_I\frac{d\varepsilon}{dt} + (\sigma - \sigma_I)\frac{d\varepsilon}{dt} \tag{27}$$

Accordingly, it is convenient and physically revealing to split Eq. (27) into a set of two equations describing the preserving and dissipative flows as:

$$\begin{cases} \frac{\delta Q}{dt} = \frac{dU}{d\rho}\frac{d\rho^-}{dt} + \sigma_I\frac{d\varepsilon}{dt} \\ \frac{dU}{d\rho}\frac{d\rho^+}{dt} = (\sigma - \sigma_I)\frac{d\varepsilon}{dt} \end{cases} \tag{28}$$

The first equation in this couple says that heat is produced by the internal energy change due to dynamic dislocation recovery and the dissipative mechanism associated with the viscous flow with the friction caused by pre-existing dislocations, which control the yield stress σ_I according to the deformation path outlined in Fig. 3 as $0 \to \sigma_I \to 4 \to \varepsilon_f$.

By eliminating $\frac{dU}{d\rho}$ from the first equation in (28), the dissipated power is found in a general form as a function of lattice defect's production and annihilation rates:

$$P_d = \frac{\delta Q}{dt} = \sigma_I\dot{\varepsilon} + \frac{\dot{\rho}^-}{\dot{\rho}^+}(\sigma - \sigma_I)\dot{\varepsilon} \tag{29}$$

The stored power density P_s is the difference between the plastic power P_e and the dissipated power P_d at the same accumulated strain. Thus, the following relations hold for P_e, P_d and P_s:

$$\begin{aligned} P_e &= \sigma\dot{\varepsilon} \\ P_d &= \left[\sigma_I + \tfrac{\dot\rho^-}{\dot\rho^+}(\sigma-\sigma_I)\right]\dot\varepsilon \\ P_s &= (\sigma-\sigma_I)\left(1-\tfrac{\dot\rho^-}{\dot\rho^+}\right)\dot\varepsilon \end{aligned} \tag{30}$$

The most appealing aspect of this approach is that it is based on the first law of thermodynamics, assumes that only the storage and annihilation of lattice defects govern the conservative and dissipative energy flows, and does not require any details of the underlying processes to be specified up to this point. These details, however, can be elaborated in a phenomenological way as follows. For example, for the KM approximation, the term $\frac{d\rho^+}{dt} = \frac{k_1}{b}\sqrt{\rho}M\dot\varepsilon$ represents the process of dislocation accumulation (which is, in principle, reversible since the defects induced by strain hardening can be annealed out by appropriate thermal treatment restoring the original microstructure, dislocation density and mechanical properties according to the path $1 \to 3$ indicated in Fig. 3 by the red arrow), and $\frac{d\rho}{dt}^- = k_2\rho M\dot\varepsilon$ is the substantially dissipative term governed by the dislocation annihilation process. Then $\frac{\dot\rho^-}{\dot\rho^+} = \frac{k_2 b}{k_1}\sqrt{\rho} = \frac{k_2 b}{k_1}\frac{\sigma-\sigma_{SS}}{\beta} = \frac{\sigma-\sigma_{SS}}{\sigma_S}$, and the equations for P_s and P_d are expressed through the Kocks and Mecking parameters in exactly the same form as they are given by Eqs. (22) and (24) derived through the thought tensile test. Thus, starting from notably different premises, both approaches render essentially the same results, thus, justifying the assumptions made.

Let us notice that, due to their general formulations, the expressions (30) for P_d and P_s can be conveniently rearranged to gain a better understanding of contributing processes referring only to the rates of dislocation accumulation and disappearance regardless of details of underlying physical mechanisms:

$$\begin{aligned} P_d &= \left[\sigma_I + \frac{\dot\rho^-}{\dot\rho^+}(\sigma-\sigma_I)\right]\dot\varepsilon = \frac{\dot\rho^-}{\dot\rho^+}\sigma\dot\varepsilon + \sigma_I\left(1-\frac{\dot\rho^-}{\dot\rho^+}\right)\dot\varepsilon \\ &= P_d(\sigma_I=0) + \sigma_I\dot\varepsilon - \sigma_I\frac{\dot\rho^-}{\dot\rho^+}\dot\varepsilon \\ P_s &= (\sigma-\sigma_I)\left(1-\frac{\dot\rho^-}{\dot\rho^+}\right)\dot\varepsilon = \sigma\left(1-\frac{\dot\rho^-}{\dot\rho^+}\right)\dot\varepsilon - \sigma_I\left(1-\frac{\dot\rho^-}{\dot\rho^+}\right)\dot\varepsilon \\ &= P_s(\sigma_I=0) - \sigma_I\dot\varepsilon + \sigma_I\frac{\dot\rho^-}{\dot\rho^+}\dot\varepsilon \end{aligned} \tag{31}$$

Here, $P_d(\sigma_I=0) = \frac{\dot\rho^-}{\dot\rho^+}\sigma\dot\varepsilon$ and $P_s(\sigma_I=0) = \sigma(1-\frac{\dot\rho^-}{\dot\rho^+})\dot\varepsilon$ denote the dissipated and stored powers, which would be observed when the initial hardening associated with the combined effect of solute atoms and dislocation interaction is negligibly small (e.g., in well-annealed single- or poly-crystals of pure metals). The immediate corollary from this simplistic derivation is that both $P_d(\sigma_I=0)$ and $P_s(\sigma_I=0)$ are entirely governed by dislocation kinetics, i.e., by the rates of dislocation production $\dot\rho^+$ and annihilation $\dot\rho^-$ (more precisely, by the ratio $\dot\rho^-/\dot\rho^+$): (i) when these two rates equal each other, dislocations are not stored in the deforming body, and the mechanical work is dissipated as heat. Apparently, the expressions (30) and (31) use only the most conceptual form of first-order dislocation kinetics expressed by Eq. (3) in terms of the rates of the generation and annihilation of defects upon straining. It does not refer to a specific dislocation evolution behaviour. However, such details can be straightforwardly integrated into the model, as it has been illustrated above for the KM model.

3. Experimental methods

The low carbon austenitic 316L stainless steel is an important engineering material with an excellent properties profile, qualifying it for use in many industries such as oil and gas, nuclear power generation, as well as the biomedical field. Besides the rewarding mechanical properties, including high strength, ductility, toughness and fatigue resistance, the 316L steel possesses an inherent resistance to corrosion, stress corrosion cracking and hydrogen embrittlement. This steel is often a material of choice for infrared thermographic measurements due to a favourable combination of its high density and relatively low electrical and thermal conductivity. Thus, we used this popular steel in the present study to illustrate the main findings and to verify model predictions. However, it needs to be mentioned that the same set of experiments has been performed using the commercial Inconel-625 alloy, Fe-Cr-Mn-Ni austenitic TRIP/TWIP stainless steels, and Cu-Zn alloys with different concentrations of Zn. Common trends are observed in all materials probed; therefore, the results reported here are not limited to the specific material and are applicable to a wide range of materials obeying the strain hardening behaviour as outlined above. The results obtained on other materials will be reported elsewhere and are not present here for brevity.

The chemical composition of the steel tested is shown in Table 2

The flat dog-bone specimens were shaped by the electric discharge machine to have a gauge length of 12 mm, width of 4 mm and thickness of 2 mm. To relieve the internal stresses inherited from the manufacturing stage, the specimens were annealed in a salt bath at 500 C for 1 h prior to mechanical testing. The mean grain size was of 70–80 μm, as assessed by optical microscopy after mechanical polishing followed by etching performed in accord to the ASTM Standard E407-07 [63] in the solution containing 1/3 HCl, 1/3 HNO_3 and 1/3 H_2O.

The experimental setup and its beneficial features have been described elsewhere in great detail [64]. The measuring system comprises three synchronised devices: the modified electrodynamic Instron Electropuls E10000 tensile machine with the 10 kN load-bearing capacity, the digital image correlation (DIC) system based on the Allied Vision Prosilica GC2450 CCD camera with 5 Mpixel resolution equipped with a Tamron 272EN II macro lens, and the Telops FAST M350 mid-wave, high-speed, high-resolution infrared camera with the Janos Technology 25 mm lens and 1/4″ extension ring. The full-field displacement, strain and strain rate maps were obtained by the DIC technique from a set of images, which were acquired by the optical video camera along the deformation path. The true strain rate averaged over the entire gauge part was evaluated as a function of strain. The plastic strain was calculated using the additive decomposition of the total strain increment into elastic and inelastic (plastic) components in a small-strain theory as $d\varepsilon = d\varepsilon_{el} + d\varepsilon_{pl}$. The elastic component was represented by Hooke's law expressed for the uniform uniaxial straining as $d\varepsilon_{el} = d\sigma/E$ (E denotes the apparent Young's modulus determined experimentally from the stress-strain data acquired during the early loading stage). All details of the original data processing algorithms and the information exchange between DIC and infrared techniques are provided in [64]. In brief, since the adiabatic conditions, which are frequently assumed in dynamic testing [65,66], are not fulfilled in quasistatic loading with relatively slow strain rates, the heat source function $\dot q_d(x,y,t)$ in Cartesian (x,y) coordinates was recovered from the time-dependent temperature distribution field $T(x,y,t)$ by solving the boundary value problem for the heat transfer equation, as has been described in detail in [9–11] (see also [64] for the specific implementation of the approach):

$$\rho_{mat}c_p\frac{\partial T}{\partial t} = \dot q_d + k_T\nabla^2 T \tag{32}$$

where ρ_{mat} is the material's density, c_p is the heat capacity, and k_T is the heat transfer coefficient. The time-dependent tempera-

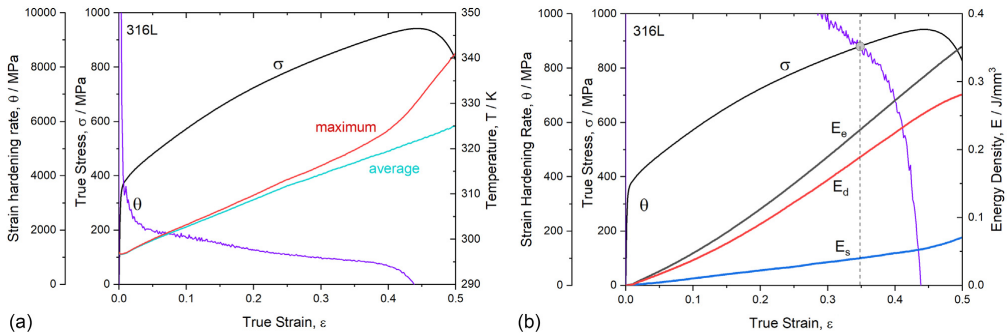

Fig. 6. True stress vs true (logarithmic) strain, strain hardening rate, and temperature evolution (a), and the expended mechanical energy E_e partitioned into dissipated and stored energies $E_d$and E_s, respectively, during tensile testing of 316L steel at the nominal strain rate $\dot{\varepsilon} = 1 \times 10^{-2}\text{s}^{-1}$. A fragment of $\theta(\varepsilon)$ is shown in (b) to highlight the crossover with the true stress-strain curve $\sigma(\varepsilon)$, indicating the onset of necking according to the Considère criterion.

ture distribution maps obtained from the IRT camera were used as input variables. The hardware solutions mitigating the heat losses to the environment and the software algorithms enabling to alleviate the challenges associated with the low signal-to-noise ratio of the temperature distribution data have been discussed in our previous work [64]. Radiation and convection effects are assumed to be negligible. These assumptions are reasonable and justifiable in various circumstances, as exemplified in Supplementary materials for interested readers. The heat losses associated with those effects appear to be orders of magnitude smaller than those due to heat conductivity; note that similar arguments have been presented by Meneghetti and Ricotta [23,25] and Risitano et al. [12,22] for cyclic loading conditions.

One side of the specimens was painted with a matt black lacquer to enhance the emissivity in the infrared spectral domain. The other surface was additionally painted with white paint to create a random, high contrast, speckle pattern suitable for the DIC analysis and accurate measurements of local strains and strain rates. Tensile tests were carried out in air at ambient temperature with the nominal strain rates of 1×10^{-3}, 3×10^{-3} and 1×10^{-2} s^{-1}. The actual strain rates as a function of strain evaluated by the DIC method were used in calculations.

4. Experimental results

Fig. 6 shows the tensile true stress-logarithmic strain curve $\sigma(\varepsilon)$, the corresponding strain hardening rate $\theta = d\sigma/d\varepsilon$ (obtained by the numerical five-point differentiation procedure), and the measured thermodynamic variables: absolute temperature T (a), and the energy densities associated with the plastic work $E_e(\varepsilon)$, dissipated heat $E_d(\varepsilon)$ (calculated by integration of the heat source function obtained from Eq. (32) as described in [64];) and the stored energy $E_s(\varepsilon)$ obtained as a difference between the previous two quantities (b).

All variables representing the partitioning of the energy evolving with strain exhibit similar trends, which are favourably compared with the literature data, c.f., Fig. 1 (for instance, one can notice that the stored energy increases nearly linearly with strain during uniform deformation, beyond which the local temperature increase sharply and the infrared measurements do not reflect the energy dissipation on average over the gauge volume). However, since these energies have been obtained after numerical integration of the corresponding power densities ($E_e(\varepsilon) = \int_0^{\varepsilon} \frac{P_e(\varepsilon')}{\dot{\varepsilon}(\varepsilon')} d\varepsilon'$, $E_d(\varepsilon) = \int_0^{\varepsilon} \frac{P_d(\varepsilon')}{\dot{\varepsilon}(\varepsilon')} d\varepsilon'$), it should be noticed that even a small sporadic experimental error in the estimates of scattered input variables can result in a potentially serious integration error. Therefore, as a matter of caution, we preferably use the power densities for the verification of model predictions in the present work.

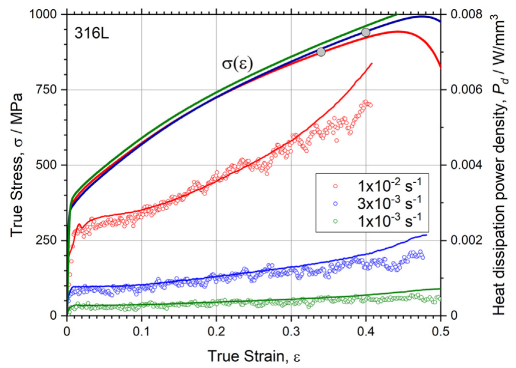

Fig. 7. The loading curves and the corresponding dissipation power density for 316L steel tested at three different strain rates. The solid lines superimposed with experimental data shown by open circles represent the results of model approximations by Eq. (24) (no fitting or optimisation procedures have been applied). The Considère points are indicated by grey circles.

Results of primary calculations of the dissipation power density from the experimentally measured temperature distribution maps are shown in Fig. 7 for three different nominal strain rates (obviously, the higher $\dot{\varepsilon}$, the higher P_d). The tensile stress-strain curves obtained for the three strain rates are almost overlapped (within the regular experimental scatter) in response to the low strain rate sensitivity of fcc metals in general and of the 316L steel in particular. The solid lines superimposed on experimental $P_d$data represent the results of model calculations using Eq. (24) with the KM parameters shown in Table 1. The agreement is especially impressive in that no curve fitting was done: the input variables (k_1 and k_2) were taken directly from the KM approximation of the stress-strain curve, c.f., Fig. 2.

Furthermore, it is interestingly to construct the Taylor-Quinney plot - P_d vs P_e, Fig. 8. One can see that the results of independent

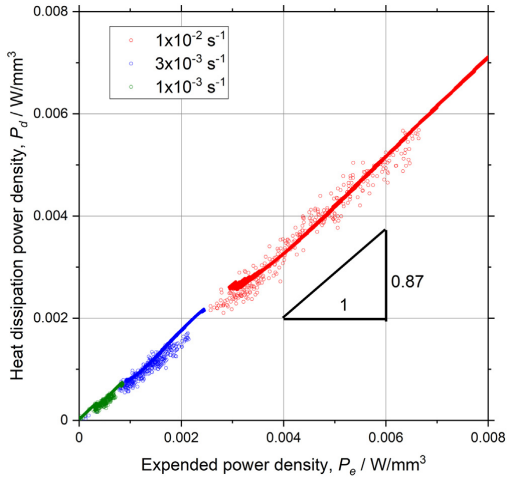

Fig. 8. Heat dissipation power versus plastic power for 316L steel specimens tested at three different strain rates. The solid lines show the results of model calculations by Eqs. (23) and (24).

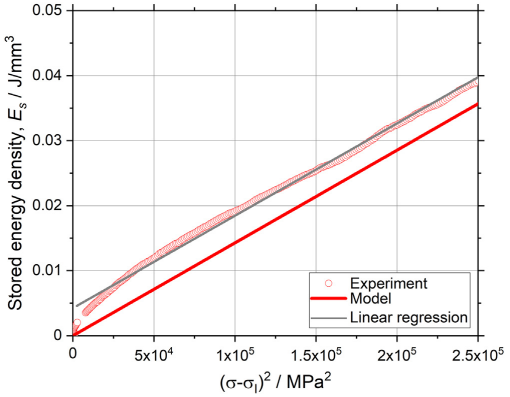

Fig. 9. Stored energy as a function of square flow stress $E_s \sim (\sigma - \sigma_I)^2$ for 316L steel tested at $\dot{\varepsilon} = 1 \times 10^{-2} s^{-1}$: comparison of experimental findings and the model predictions according to Eq. (16).

measurements for three specimens tested at different strain rates align themselves with the same master straight line within a reasonably narrow confidence band. The slope of this line (equal to 0.87) represents the differential Taylor-Quinney coefficient, which is defined as the ratio of dissipated to plastic powers (in its differential form $\beta_{TQ} = \frac{P_d}{P_e}$) or works (in its integral form $\beta_{TQ} = \frac{E_d}{E_e}$). Similarly to the statement made in the paragraph above, this observation is remarkable not only because it is in excellent agreement with the model predictions based on Eqs. (23) and (24) but also because no additional fitting has been applied (the same KM parameters, Table 1, were used to plot the model-representing solid lines in Figs. 7 and 8). Let us notice that the simple observation that, by definition $P_d = \beta_{TQ} P_e = \beta_{TQ} \sigma \dot{\varepsilon}$, i.e., the dissipated power is linear with β_{TQ} (which is the same for all tests), flow stress σ(which exhibits negligible strain rate sensitivity, c.f., Fig. 7) and explains the pronounced dependence of P_d on the strain rate at a given strain.

Recall that the Taylor-Quinney (TQ) factor is generally assumed to be about 0.9 on average [1,67]. Although this value can be considered invariable during tensile testing at modest strain rates for many materials, the deviations from this rule are frequently observed, particularly in high strain rate experiments [68–70]. In fact, the model presented herein predicts that the TQ coefficient evolves slightly as deformation proceeds. The differential TQ-coefficient can be simply found as a function of stress σ or, implicitly, as a function of strain with $\sigma = \sigma(\varepsilon)$:

$$\beta_{TQ} = \frac{P_d}{P_e} = \frac{\left[\sigma_I + \frac{\dot{\rho}^-}{\dot{\rho}^+}(\sigma - \sigma_I)\right]\dot{\varepsilon}}{\sigma \dot{\varepsilon}} = \frac{\sigma}{\sigma_S} + \frac{\sigma_I}{\sigma}\left(1 + \frac{\sigma_{SS}}{\sigma_S}\right) - \left(\frac{\sigma_{SS}}{\sigma_S} + \frac{\sigma_I}{\sigma_S}\right) \quad (33)$$

Taking plausibly that $\sigma_{SS} << \sigma_S$ and $\sigma_\infty \sim \sigma_S$, the last expression is simplified to

$$\beta_{TQ} \approx \frac{\sigma_I}{\sigma} + \frac{\sigma}{\sigma_S} - \frac{\sigma_I}{\sigma_S} \approx \frac{\sigma_I}{\sigma} + \frac{\sigma}{\sigma_\infty} - \frac{\sigma_I}{\sigma_\infty} \quad (34)$$

Here, the flow stress is a parameter that is theoretically bounded within the interval $\sigma_I \le \sigma \le \sigma_\infty$ or, practically, within a narrower range $\sigma_I \le \sigma \le \sigma_N$ confined to the uniform elongation. Elementary numerical estimates show that, within this range, the β_{TQ}value varies between 0.9 and 0.8, with the average around 0.87, which is consistent with abundant literature data, and agrees favourably with the results shown in Fig. 8. The analysis of the $\beta_{TQ}(\sigma)$ function (34) shows that it has a shallow minimum, as has also been envisioned by Zubelewicz [68] and particularly clearly observed by Nieto-Fuentes et al. [69] and Soares and Hokka [70] in high strain rate experiments with various materials such as copper, titanium and iron.

5. Discussion

As has been mentioned above, various strain hardening models converge at that the stored energy is square of stress $E_s \sim \sigma^2$ or, more generally, $E_s \sim (\sigma - \sigma_I)^2$, as it is explicit in the present model, Eq. (16). This equation is supported by the trends observed in the cited above abundant literature; the same trends are suggested by the present model and corroborated by experimental data as seen in Fig. 9, which illustrates the $E_s \sim (\sigma - \sigma_I)^2$relation obtained for the specimen tested at $\dot{\varepsilon} = 1 \times 10^{-2} s^{-1}$. The linear regression (solid grey line) of the experimental data (red circles) exhibits the straight line with the same slope as the model (solid red line); let us reiterate that the model has not been fitted to the experimental data here. Furthermore, the generic behaviour of E_s anticipated from the model and the actual observed E_s *vs* $(\sigma - \sigma_I)^2$ behaviour are in fair agreement with each other, noting that there is still a small gap between the model line and experimental results. In our opinion, this gap, which can be larger or smaller in a set of independent measurements, stems most likely from the integration procedure resulting in the slightly overestimated value of $E_s(\varepsilon)$, which is obtained from the initially calculated $P_s(\varepsilon)$. One should notice that since the stored power is a small fraction (of 13% for Taylor-Quinney coefficient = 0.87) of the mechanical and dissipated power, and since it is calculated from the difference between the latter two, the small measurement error, say 1%, in the mechanical or thermal power will cause of 10% error in the experimentally measured stored power (even a greater error does, therefore, exist in the stored energy for the aforementioned reasons). Notably, the uncertainty is higher in the thermal measurements at low strains/stresses when the dissipation is low. It is exactly for

this reason we preferred testing model findings using power densities, as had been stated above. Another reason for the deviation of the model curve and the experimental data is attributed to the heterogeneity of deformation at the onset of yielding, which is not captured by the model. At that stage, some large favourably oriented grains yield earlier than others. Consequently, those grains deform plastically and dissipate significant heat while others do not produce any heat at all. Nonetheless, despite its simplicity, the model plausibly captures the commonly observed trends in E_s *vs* σ behaviour.

The Eq. (18) relating the stored energy to the dislocation density allows for a transparent physical interpretation: the stored energy refers to the difference between the energies of the crystal deformed and the initial state characterised solely by the dislocation densities ρ and ρ_0, respectively. In this approach, the dislocations can be viewed as a gas of quasi-particles described by their characteristic average energy, thus giving rise to the commonly postulated expressions for the dislocation-related stored energy in the general form $E_s = A \cdot Gb^2 \rho$, see, for example, [6,33,71,72] (here A is constant, depending on the employed model of the energy of dislocations). The self-energy per unit length l_i of an individual dislocation segment i in the crystal of radius r is expressed as (see Ref. [73]):

$$\frac{E_{disl}}{l_i} = \frac{Gb^2}{4\pi\kappa}\left(\ln\frac{r}{r_0}\right) + E_{core} \tag{35}$$

with $\kappa = 1, \quad or \quad 1-\nu$ for screw or edge dislocations, respectively (ν denotes the Poisson ratio), and r_0 refers to the inner cut-off radius below which the continuum mechanics approximation is no longer valid; E_{core} describes the core energy of the dislocation. A variety of modifications of the basic Eq. (35) has been proposed in the literature and reviewed in [6,74,75] to account for different specific dissociation configurations in deformed crystals.

In common, the cumulative dislocation energy per unit volume V is obtained from Eq. (35) simply as

$$E_s = \frac{\sum_i E_i^{disl}}{V} = \frac{Gb^2 \sum_i l_i}{4\pi\kappa V}\ln\frac{r}{r_0} = \frac{Gb^2\rho}{4\pi\kappa}\ln\frac{r}{r_0} \tag{36}$$

Here the summation of self-energies of individual dislocations of the length l_i is made without explicit account for their core energies, explicit interaction between dislocations, screening of elastics stress fields in low-energy dislocation arrangements, etc. With a further assumption that a shielding distance is of the order of the mean dislocation spacing, which scales inversely with the square root of the dislocation density as proposed by Kuhlmann-Wilsdorf [76], the last equation reads as

$$E_s = \frac{Gb^2\rho}{4\pi\kappa}\left(\ln\frac{1}{b\sqrt{\rho}}\right) \tag{37}$$

However, idealisation of the dislocation ensemble in analogy to ideal gases, i.e., without interaction between dislocations, is an oxymoron since dislocations are intrinsically interacting objects whose properties and interrelationships are primarily determined by their long-range elastic stress fields. The contributions from this inter-dislocation interaction to the energy of the crustal are significant and have long been recognised in the literature. For example, Bailey and Hirsch [32,33] concluded that the interactions between dislocations with Burgers vectors of like sign could be accounted for by the additional terms augmenting the Eq. (35) for the dislocation self-energy as:

$$E_s = \frac{Gb^2\rho}{4\pi\kappa}\left(\ln\frac{r_c}{r_0} + 1 + 3\ln\frac{r_c}{r} - \ln 2 - \frac{1}{2}\ln 3\right) \tag{38}$$

with r_c- the interaction distance (of the order of cell size in cell forming materials) and r - the separation distance between dislocation groups (of the order of 200b). Unlike all these formulations (35)–(38) (or similar ones reviewed in [6]) originating from the continuum dislocation theory, Eq. (17) (or (18)) for $\rho \gg \rho_0$), introduces, albeit in a purely phenomenological way, a kind of average energy of dislocations in the ensemble instead of summing up the dislocation self-energies modified for specific dislocation configurations. The notable difference between the proposed models resides primarily in the proportionality coefficient A between E_s and the dislocation "energy factor" Gb^2: $E_s = A \cdot Gb^2 \rho$. While in the family of dislocation-based models A is equal to $1/4\pi\kappa$ multiplied by a logarithmic factor including various terms stemming from dislocation-dislocation interactions, in our model, $A = \frac{\alpha}{k_1}$ is simply proportional to Taylor's coefficient α, which is known to be dependent on the dislocation arrangement and inversely proportional to k_1 governing the dislocation production rate in the KM model. It is instructive to compare the proposed model with the early models assuming the summation of dislocation self-energies and resulting in the relations like $E_s = A \cdot Gb^2 \rho$, e.g., Eqs. (35)–(38). Results of the comparison are shown in Fig. 10 where our model is represented by Eq. (17) for E_s *vs* ρ (red line). The dislocation density increases according to the KM model resulting in Eq. (6) and experimental parameters listed in Table 1. One can notice that in harmony with the results shown in Fig. 9, the experimentally determined $E_s(\varepsilon)$ evolves in parallel with $\rho(\varepsilon)$. Using the same data for ρ, the stored energy was calculated for the Bailey and Hirsch, Eq. (36), and Kuhlmann-Wilsdorf, Eq. (37), models. One can see that although all models capture the anticipated $E_s \sim \rho$ trend reasonably well, the present model exhibits remarkably better agreement with the experimentally measured stored energy[1], while other models show underestimated forecasts for $E_s(\varepsilon)$. Furthermore, one can notice that there is only little numerical difference between the models under consideration at small strains. Recall, that at the onset of plastic yielding when ρ is comparable to ρ_0, Eq. (17) applies rather than (18). This relation effectively accounts the influence of initial strain hardening on the energy of the evolving dislocation ensemble through the Φ function, c.f., Fig. 4. It is intuitively clear that as long as the dislocation density is low,

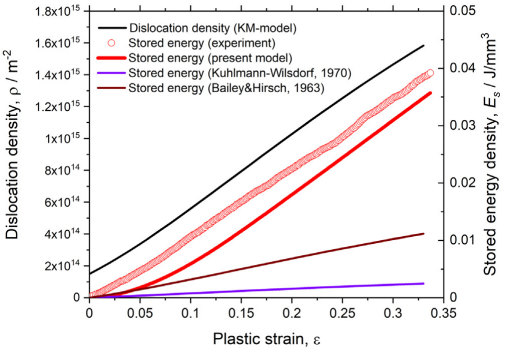

Fig. 10. Experimentally measured stored energy (open circles) as a function of plastic strain for 316L steel tested at $\dot{\varepsilon} = 1 \times 10^{-2} s^{-1}$ compared to the model-predicted evolution of the dislocation density, Eq. (6) (black curve); the stored energy calculated from the present model according to Eq. (16) (red line) in comparison with estimates based on Bailey and Hirsch (Eq. (36)), and Kulhmann-Wilsdorf (Eq. (37)), formulations of dislocation self-energies

[1] The deviation between the model and experimental data can be regarded small, considering the experimental challenges and arguments discussed above.

and the dislocations do not form the screened interacting configurations the summation of individual self-energies of dislocations is better argued than that at higher strains. The plots presented in Fig. 10 corroborate this speculation.

We should also notice that, from the viewpoint of the elastic continuum theory, the dislocation energies are independent of temperature and strain rate, which is confirmed by molecular dynamic simulations [77]. This is, in principle, indirectly supported by the present observations illustrated in Fig. 6, where the Taylor-Quinney type plot P_d vs P_e for different specimens exhibits the same slope between P_d and P_e independently of the strain rate. Furthermore, it is exciting to notice that the proposed model based on Eq. (17) shows that the stored energy does not explicitly depend on the dynamic recovery rate k_2 (which is temperature and strain-rate dependent) and depends only on the athermal coefficient k_1 controlling the dislocation production rate. However, the effect of the strain rate and temperature still resides in the factor α, which is commonly related to the strain rate through the power-law function $\alpha = \alpha(\dot{\varepsilon}, T) = \alpha_0 (\frac{\dot{\varepsilon}}{\dot{\varepsilon}_0})^{\frac{1}{m}}$, which bears its origin in an Arrhenius equation for the plastic strain rate; here m – the strain rate sensitivity, $\dot{\varepsilon}_0$ is a constant, which represents the mechanical resistance to dislocation glide due to dislocation-dislocation interaction at absolute zero temperature. The temperature dependence is associated with thermally activated dislocation glide and is captured by the parameters $\dot{\varepsilon}_0$ and m [39–41,78,79]. Thus, in principle, following the kinetic KM approach, the present model captures the strain rate sensitivity of materials through the α coefficient. Experimental verification of this statement is an exciting task, which is, however, beyond the scope of the present work, and which will be implemented in future studies.

Let us reiterate that there are only two principal microstructurally-controlled "adjustable" phenomenological parameters (k_1, k_2) included in the model equations. Both, in principle, allow for a microscopic interpretation [80,81], albeit further efforts are still required in this regard. Other parameters such as σ_0, M, G can be measured experimentally from the mechanical response and/or microstructural and texture measurements. However, some uncertainty is still there about the exact value of the microstructurally sensitive parameter $\alpha = \alpha(\dot{\varepsilon}, T)$ in Taylor Eq. (2) [82].

As a final note, although the above model considering dislocation recovery and annihilation of a general kind as a primary source of heat dissipation works pretty well, the assumption made is a simplification. However, this study provides a baseline for elaborated modelling efforts. A more complete theory can straightforwardly include contributions of other dissipative mechanisms such as heating at the very localised sources when dislocation avalanches breakaway from their pinning points [83–85], phonon drag [86,87] and acoustic emission [88] during dislocation glide, etc., into the proposed framework. The results of these efforts will be reported in a forthcoming publication.

6. Concluding remarks

In conclusion, the main thrust of the present work was to propose a thermodynamic modelling methodology informed by dislocation evolution theory, aiming at gaining a deeper insight into energy partitioning during plastic flow. Based on the first law of thermodynamics and the time-proven first-order kinetics approach using only physically motivated variables governing dislocation storage and annihilation, the proposed phenomenological modelling approach is demonstrated to be capable of accurately predicting the behaviour of the stored/dissipated power (or energy) in materials with dislocation-mediated plasticity during strain hardening. The model predictions were verified by the infrared thermography during *in situ* testing of the fcc low-carbon austenitic 316L stainless steel tested at different strain rates, albeit in the relatively narrow range 10^{-2}–10^{-3} s^{-1}. However, the main conclusions can be extended to a wide range of structural materials tested by the same authors, including TWIP and TRIP steels, Inconel, and Cu-based alloys (these results are not shown here for brevity and will be reported elsewhere). The adaptation of the model to bcc or hcp metals is rather straightforward. The recipes, which have been proposed for including the Peierls stress and temperature and strain rate sensitivity for the one-internal variable model, can simply be 'borrowed'.

The proposed modelling approach provides a general platform for accounting for various dissipative mechanisms into the measured heat response, thus enabling a new level of synergy between remote non-destructive measurements and underlying deformation and fracture mechanisms. In this context, a conclusion important for experimental methodology was also drawn and deserves special mention here. It was demonstrated that the full-filed thermographic measurements *in situ* during the plastic deformation can be used as a "litmus" test for strain-hardening theories by providing direct access to energy partitioning during plastic deformation.

The simple mathematically tractable expressions were derived for the dissipated and stored power densities (or energies) as well as for the Taylor-Quinney factor on the basis of the Kocks-Mecking type model. They can be practically utilised in connection with *in situ* systems for non-destructive monitoring of damage evolution in solids under load.

Declaration of Competing Interest

The authors declare that they have no known competing financial interests or personal relationships that could have appeared to influence the work reported in this paper.

CRediT authorship contribution statement

A. Sendrowicz: Conceptualization, Methodology, Software, Validation, Writing – original draft, Investigation, Writing – review & editing, Visualization. **A.O. Myhre:** Conceptualization, Methodology, Validation, Investigation, Writing – original draft, Writing – review & editing. **I.S. Yasnikov:** Conceptualization, Investigation, Writing – original draft. **A. Vinogradov:** Conceptualization, Investigation, Writing – original draft, Writing – review & editing, Visualization, Supervision.

Acknowledgments

Internal funding provided by the Department of Mechanical and Industrial Engineering of NTNU is appreciated. The partial support by the Research Council of Norway, Project No. 294739, Safe Pipelines for Hydrogen Transport (HyLINE) is gratefully acknowledged. The author are grateful to Profs. Y. Estrin, and F. Berto and Dr. A. Alvaro for encouragement and insightful discussions.

Supplementary materials

Supplementary material associated with this article can be found, in the online version, at doi:10.1016/j.actamat.2022.118190.

Appendix A (Derivation of Eq. (17))

$$E_s(\sigma) = \frac{\bar{\varepsilon}}{2\sigma_S}(\sigma - \sigma_I)^2 = \frac{\bar{\varepsilon}}{2\sigma_S}([\sigma_{SS} + \beta\sqrt{\rho}] - [\sigma_{SS} + \beta\sqrt{\rho_0}])^2 =$$

$$E_s = \frac{\bar{\varepsilon}\beta^2}{2\sigma_S}(\sigma - \sigma_I)^2 = \frac{\bar{\varepsilon}\beta^2}{2\sigma_S}(\rho - \rho_0) - \frac{\bar{\varepsilon}\sigma_0}{\sigma_S}(\sigma - \sigma_I)$$

$$= \frac{\bar{\varepsilon}}{\sigma_S}\left[\frac{\beta^2}{2}(\rho - \rho_0) - \sigma_0(\sigma - \sigma_I)\right] =$$

$$= \frac{\bar{\varepsilon}}{\sigma_S}\left[\frac{\beta^2}{2}(\rho - \rho_0) - \beta\sqrt{\rho_0}(\sigma - \sigma_I)\right] \Rightarrow \left\langle \begin{matrix} \sigma = \sigma_{SS} + \beta\sqrt{\rho} \\ \sigma_I = \sigma_{SS} + \beta\sqrt{\rho_0} \end{matrix} \right\rangle$$

$$\Rightarrow \frac{\bar{\varepsilon}}{\sigma_S}\left[\frac{\beta^2}{2}(\rho - \rho_0) - \beta^2\sqrt{\rho_0}(\sqrt{\rho} - \sqrt{\rho_0})\right] =$$

$$= \frac{\beta^2\bar{\varepsilon}}{\sigma_S}\left[\frac{1}{2}(\rho - \rho_0) - \sqrt{\rho_0}(\sqrt{\rho} - \sqrt{\rho_0})\right]$$

$$= \frac{\bar{\varepsilon}\beta^2}{2\sigma_S}(\rho - \rho_0)\left[1 - \frac{2\sqrt{\rho_0}(\sqrt{\rho} - \sqrt{\rho_0})}{\rho - \rho_0}\right] =$$

$$= \frac{\bar{\varepsilon}\beta^2}{2\sigma_S}(\rho - \rho_0)\left[1 - \frac{2\sqrt{\rho_0}}{\sqrt{\rho} + \sqrt{\rho_0}}\right] = \frac{\bar{\varepsilon}\beta^2}{2\sigma_S}(\rho - \rho_0)\left[1 - \frac{2\sqrt{\frac{\rho_0}{\rho}}}{1 + \sqrt{\frac{\rho_0}{\rho}}}\right]$$

$$= \frac{\bar{\varepsilon}\beta^2}{2\sigma_S}(\rho - \rho_0)\Phi\left(\frac{\rho_0}{\rho}\right)$$

with

$$\Phi\left(\frac{\rho_0}{\rho}\right) = \left[1 - \frac{2\sqrt{\frac{\rho_0}{\rho}}}{1 + \sqrt{\frac{\rho_0}{\rho}}}\right]$$

References

[1] G.I. Taylor, H. Quinney, The latent energy remaining in a metal after cold working, Proc. R. Soc. Lond. Ser. A 143 (849) (1934) 307–326.
[2] B. Welber, Measurement of the internal energy in copper introduced by cold work, J. Appl. Phys. 23 (8) (1952) 876–881.
[3] F.R.N. Nabarro, Theory of Crystal Dislocations, Clarendon Press, Oxford, 1967.
[4] J.J. Gilman, Micromechanics of flow in solids, McGraw-Hill, New York; London, 1969.
[5] W.S. Farren, G.I. Taylor, in: The heat developed during plastic extension of metals, 107, 1925, pp. 422–451.
[6] M.B. Bever, D.L. Holt, A.L. Titchener, The stored energy of cold work, Prog. Mater. Sci. 17 (0) (1973) 5–177.
[7] W. Oliferuk, M. Maj, Plastic instability criterion based on energy conversion, Mater. Sci. Eng. A 462 (1-2) (2007) 363–366.
[8] W. Oliferuk, M. Maj, Stress–strain curve and stored energy during uniaxial deformation of polycrystals, Eur. J. Mech. A. Solids 28 (2) (2009) 266–272.
[9] A. Chrysochoos, Infrared thermography applied to the analysis of material behavior: a brief overview, Quant. InfraRed Thermogr. J. 9 (2) (2012) 193–208.
[10] A. Chrysochoos, H. Louche, An infrared image processing to analyse the calorific effects accompanying strain localisation, Int. J. Eng. Sci. 38 (16) (2000) 1759–1788.
[11] H. Louche, A. Chrysochoos, Thermal and dissipative effects accompanying Lüders band propagation, Mater. Sci. Eng. A 307 (1-2) (2001) 15–22.
[12] A. Risitano, D. Corallo, E. Guglielmino, G. Risitano, L. Scappaticci, Fatigue assessment by energy approach during tensile tests on AISI 304 steel, Frattura ed Integrita Strutturale 11 (39) (2017) 202–215.
[13] C. Wang, A. Blanche, D. Wagner, A. Chrysochoos, C. Bathias, Dissipative and microstructural effects associated with fatigue crack initiation on an Armco iron, Int. J. Fatigue 58 (2014) 152–157.
[14] J. Hodowany, G. Ravichandran, A.J. Rosakis, P. Rosakis, Partition of plastic work into heat and stored energy in metals, Exp. Mech. 40 (2) (2000) 113–123.
[15] P. Rosakis, A.J. Rosakis, G. Ravichandran, J. Hodowany, A thermodynamic internal variable model for the partition of plastic work into heat and stored energy in metals, J. Mech. Phys. Solids 48 (3) (2000) 581–607.
[16] D. Macdougall, Determination of the plastic work converted to heat using radiometry, Exp. Mech. 40 (3) (2000) 298–306.
[17] S. Dumoulin, H. Louche, O.S. Hopperstad, T. Børvik, Heat sources, energy storage and dissipation in high-strength steels: experiments and modelling, Eur. J. Mech. A Solids 29 (3) (2010) 461–474.
[18] D. Rittel, A.A. Kidane, M. Alkhader, A. Venkert, P. Landau, G. Ravichandran, On the dynamically stored energy of cold work in pure single crystal and polycrystalline copper, Acta Mater. 60 (9) (2012) 3719–3728.
[19] R. De Finis, D. Palumbo, U. Galietti, A multianalysis thermography-based approach for fatigue and damage investigations of ASTM A182 F6NM steel at two stress ratios, Fatigue Fract. Eng. Mater. Struct. 42 (1) (2019) 267–283.
[20] D. Palumbo, R. De Finis, F. Ancona, U. Galietti, Damage monitoring in fracture mechanics by evaluation of the heat dissipated in the cyclic plastic zone ahead of the crack tip with thermal measurements, Eng. Fract. Mech. 181 (2017) 65–76.
[21] G.C. Soares, N.I. Vázquez-Fernández, M. Hokka, Thermomechanical behavior of steels in tension studied with synchronized full-field deformation and temperature measurements, Exp. Tech. 45 (5) (2021) 627–643.
[22] G.L. Rosa, A. Risitano, Thermographic methodology for rapid determination of the fatigue limit of materials and mechanical components, Int. J. Fatigue 22 (1) (2000) 65–73.
[23] G. Meneghetti, M. Ricotta, Evaluating the heat energy dissipated in a small volume surrounding the tip of a fatigue crack, Int. J. Fatigue 92 (Part 2) (2016) 605–615.
[24] G. Meneghetti, M. Ricotta, G. Pitarresi, Infrared thermography-based evaluation of the elastic-plastic J-integral to correlate fatigue crack growth data of a stainless steel, Int. J. Fatigue 125 (2019) 149–160.
[25] G. Meneghetti, Analysis of the fatigue strength of a stainless steel based on the energy dissipation, Int. J. Fatigue 29 (1) (2007) 81–94.
[26] L. Li, J.M. Muracciole, L. Waltz, L. Sabatier, F. Barou, B. Wattrisse, Local experimental investigations of the thermomechanical behavior of a coarse-grained aluminum multicrystal using combined DIC and IRT methods, Opt. Lasers Eng. 81 (2016) 1–10.
[27] J. Humphreys, G.S. Rohrer, A. Rollett, Chapter 2 - the deformed state, in: J. Humphreys, G.S. Rohrer, A. Rollett (Eds.), Recrystallization and Related Annealing Phenomena, 3rd Edition, Elsevier, Oxford, 2017, pp. 13–79.
[28] M. Zaiser, A. Seeger, Long-range internal stresses, dislocation patterning and work-hardening in crystal plasticity, in: F.R.N. Nabarro, M.S. Duesbery (Eds.), Dislocations in Solids, Elsevier, 2002, pp. 1–100.
[29] F.R.N. Nabarro, Z.S. Basinski, D.B. Holt, The plasticity of pure single crystals, Adv. Phys. 13 (50) (1964) 193–323.
[30] H. Kronmüller, Stored energy and recovery of deformed F.C.C. metals AU - Seeger, A, Philos. Mag. A J. Theor. Exp. Appl. Phys. 7 (78) (1962) 897–913.
[31] L.M. Clarebrough, M.E. Hargreaves, G.W. West, The release of energy during annealing of deformed metals, Proc. R. Soc. Lond. Ser. A Math. Phys. Sci. 232 (1189) (1955) 252–270.
[32] J.E. Bailey, The dislocation density, flow stress and stored energy in deformed polycrystalline copper, Philos. Mag. 8 (86) (1963) 223–236.
[33] J.E. Bailey, P.B. Hirsch, The dislocation distribution, flow stress, and stored energy in cold-worked polycrystalline silver, Philos. Mag. 5 (53) (1960) 485–497.
[34] A.M. Ivanov, E.S. Lukin, B.G. Vainer, Evaluation of Storage Energy of the Constructional Steel during Plastic Deformation, QIRT Council, 2006.
[35] R.O. Williams, The stored energy in deformed copper: The effect of grain size and silver content, Acta Metall. 9 (10) (1961) 949–957.
[36] A. Vinogradov, I.S. Yasnikov, Y. Estrin, Evolution of fractal structures in dislocation ensembles during plastic deformation, Phys. Rev. Lett. 108 (20) (2012) 205504.
[37] I.S. Yasnikov, Y. Estrin, A. Vinogradov, What governs ductility of ultrafine–grained metals? A microstructure based approach to necking instability, Acta Mater. 141 (2017) 18–28 Supplement C.
[38] I.S. Yasnikov, A. Vinogradov, Y. Estrin, Revisiting the Considère criterion from the viewpoint of dislocation theory fundamentals, Scr. Mater. 76 (0) (2014) 37–40.
[39] U.F. Kocks, H. Mecking, Physics and phenomenology of strain hardening: the FCC case, Prog. Mater Sci. 48 (3) (2003) 171–273.
[40] H. Mecking, U.F. Kocks, Kinetics of flow and strain-hardening, Acta Metall. 29 (11) (1981) 1865–1875.
[41] Y. Estrin, H. Mecking, A unified phenomenological description of work hardening and creep based on one-parameter models, Acta Metall. 32 (1) (1984) 57–70.
[42] M. Huang, P.E.J. Rivera-Díaz-del-Castillo, O. Bouaziz, S. van der Zwaag, Modelling plastic deformation of metals over a wide range of strain rates using irreversible thermodynamics, IOP Conf. Ser. Mater. Sci. Eng. 3 (1) (2009) 012006.
[43] I.S. Yasnikov, Y. Kaneko, M. Uchida, A. Vinogradov, The grain size effect on strain hardening and necking instability revisited from the dislocation density evolution approach, Mater. Sci. Eng. A 831 (2022) 142330.
[44] A. Considère, Mémoire sur l'emploi du fer et de l'acier dans les constructions, in: Annales des Ponts et Chaussées I Sem, 1885, pp. 574–775.
[45] A. Vinogradov, I.S. Yasnikov, H. Matsuyama, M. Uchida, Y. Kaneko, Y. Estrin, Controlling strength and ductility: dislocation-based model of necking instability and its verification for ultrafine grain 316L steel, Acta Mater. 106 (2016) 295–303.
[46] F.R.N. Nabarro, Fifty-year study of the Peierls-Nabarro stress, Mater. Sci. Eng. A 234-236 (1997) 67–76.
[47] J. Eliasson, R. Sandström, Proof strength values for austenitic stainless steels at elevated temperatures, Steel Res. 71 (6-7) (2000) 249–254.
[48] F.B. Prinz, A.S. Argon, The evolution of plastic resistance in large strain plastic flow of single phase subgrain forming metals, Acta Metall. 32 (7) (1984) 1021–1028.
[49] W. Nix, J. Gibeling, D. Hughes, Time-dependent deformation of metals, Metall. Mat. Trans. A 16 (12) (1985) 2215–2226.
[50] H. Mughrabi, Dislocation wall and cell structures and long-range internal-stresses in deformed metal crystals, Acta Metall. 31 (9) (1983) 1367–1379.
[51] M. Zehetbauer, Cold work hardening in stages IV and V of F.C.C. metals—II. Model fits and physical results, Acta Metall. Mater. 41 (2) (1993) 589–599.
[52] Y. Estrin, L.S. Tóth, A. Molinari, Y. Bréchet, A dislocation-based model for all hardening stages in large strain deformation, Acta Mater. 46 (15) (1998) 5509–5522.
[53] L.S. Toth, A. Molinari, Y. Estrin, Strain hardening at large strains as predicted by dislocation based polycrystal plasticity model, J. Eng. Mater. Technol. 124 (1) (2002) 71–77.
[54] E. Nes, K. Marthinsen, Modeling the evolution in microstructure and properties during plastic deformation of f.c.c.-metals and alloys – an approach towards a unified model, Mater. Sci. Eng. A 322 (1–2) (2002) 176–193.
[55] G.A. Malygin, Kinetic mechanism of the formation of fragmented dislocation structures upon large plastic deformations, Phys. Solid State 44 (11) (2002) 2072–2079.

[56] L.P. Kubin, Y. Estrin, Evolution of dislocation densities and the critical conditions for the Portevin-Le Châtelier effect, Acta Metall. Mater. 38 (5) (1990) 697–708.
[57] F. Barlat, A simple model for dislocation behavior, strain and strain rate hardening evolution in deforming aluminum alloys, Int. J. Plast. 18 (7) (2002) 919–939.
[58] L.P. Kubin, Y. Estrin, G. Canova, Dislocation Patterns and Plastic Instabilities, in: D. Walgraef, N.M. Ghoniem (Eds.), Patterns, Defects and Materials Instabilities, Springer, Netherlands, 1990, pp. 277–301.
[59] F. Roters, D. Raabe, G. Gottstein, Work hardening in heterogeneous alloys—a microstructural approach based on three internal state variables, Acta Mater. 48 (17) (2000) 4181–4189.
[60] E. Nes, Modelling of work hardening and stress saturation in FCC metals, Prog. Mater. Sci. 41 (3) (1997) 129–193.
[61] D. Kuhlmann-Wilsdorf, The theory of dislocation-based crystal plasticity, Philos. Mag. A 79 (4) (1999) 955–1008.
[62] P.B. Hirsch, T.E. Mitchell, Stage II work hardening in crystals, Can. J. Phys. 45 (1967) 663–706.
[63] E407-07, in: Standard Practice for Microetching Metals and Alloys, ASTM International, West Conshohocken, PA, USA, 2015, p. 2015.
[64] A. Sendrowicz, A.O. Myhre, S.W. Wierdak, A. Vinogradov, Challenges and accomplishments in mechanical testing instrumented by in situ techniques: infrared thermography, digital image correlation, and acoustic emission, Appl. Sci. 11 (15) (2021) 6718.
[65] D. Mountain, J. Webber, Stress Pattern Analysis By Thermal Emission (SPATE), SPIE, 1979.
[66] R. Urbanek, J. Bär, Lock-in thermographic stress analysis of notched and unnotched specimen under alternating loads, Procedia Struct. Integr. 5 (2017) 785–792.
[67] D. Rittel, On the conversion of plastic work to heat during high strain rate deformation of glassy polymers, Mech. Mater. 31 (2) (1999) 131–139.
[68] A. Zubelewicz, Century-long Taylor-Quinney interpretation of plasticity-induced heating reexamined, Sci. Rep. 9 (1) (2019).
[69] J.C. Nieto-Fuentes, D. Rittel, S. Osovski, On a dislocation-based constitutive model and dynamic thermomechanical considerations, Int. J. Plast. 108 (2018) 55–69.
[70] G.C. Soares, M. Hokka, The Taylor–Quinney coefficients and strain hardening of commercially pure titanium, iron, copper, and tin in high rate compression, Int. J. Impact Eng. 156 (2021) 103940.
[71] M. Verdier, I. Groma, L. Flandin, J. Lendvai, Y. Bréchet, P. Guyot, Dislocation densities and stored energy after cold rolling of Al-Mg alloys: investigations by resistivity and differential scanning calorimetry, Scr. Mater. 37 (4) (1997) 449–454.
[72] V.L. Berdichevsky, On thermodynamics of crystal plasticity, Scr. Mater. 54 (5) (2006) 711–716.
[73] J.P. Hirth, J. Lothe, Theory of Dislocations, 2nd ed., Wiley, New York, 1982.
[74] N. Hansen, D. Kuhlmann-Wilsdorf, Low energy dislocation structures due to unidirectional deformation at low temperatures, Mater. Sci. Eng. 81 (0) (1986) 141–161.
[75] S. Kolupaeva, M. Semenov, The stored energy of plastic deformation in crystals of face- centered cubic metals, IOP Conf. Ser. Mater. Sci. Eng. 71 (2015) 012077.
[76] D. Kuhlmann-wilsdorf, A critical test on theories of work-hardening for the case of drawn iron wire, Metall. Trans. 1 (11) (1970) 3173–3179.
[77] X.W. Zhou, R.B. Sills, D.K. Ward, R.A. Karnesky, Atomistic calculations of dislocation core energy in aluminium, Phys. Rev. B 95 (5) (2017) 054112.
[78] U.F. Kocks, Laws for work-hardening and low-temperature creep, J. Eng. Mater. Technol. Trans. ASME 98 (1) (1976) 76–85.
[79] Y. Estrin, Unified Constitutive Laws of Plastic Deformation, Academic Press, San Diego, London, 1996.
[80] E.I. Galindo-Nava, P.E.J. Rivera-Díaz-del-Castillo, Thermostatistical modelling of hot deformation in FCC metals, Int. J. Plast. 47 (0) (2013) 202–221.
[81] E.I. Galindo-Nava, J. Sietsma, P.E.J. Rivera-Díaz-del-Castillo, Dislocation annihilation in plastic deformation: II. Kocks–Mecking analysis, Acta Mater. 60 (6–7) (2012) 2615–2624.
[82] H. Mughrabi, The α-factor in the Taylor flow-stress law in monotonic, cyclic and quasi-stationary deformations: dependence on slip mode, dislocation arrangement and density, Curr. Opin. Solid State Mater. Sci. 20 (6) (2016) 411–420.
[83] R.W. Armstrong, C.S. Coffey, W.L. Elban, Adiabatic heating at a dislocation pile-up avalanche, Acta Metall. 30 (12) (1982) 2111–2116.
[84] R.W. Armstrong, W.L. Elban, Temperature rise at a dislocation pile-up breakthrough, Mater. Sci. Eng. A 122 (2) (1989) L1–L3.
[85] R.W. Armstrong, W.R. Grise, Hot spots from dislocation pile-up avalanches, AIP Conf. Proc. 845 (1) (2006) 1033–1036.
[86] D.N. Blaschke, Properties of dislocation drag from phonon wind at ambient conditions, Materials 12 (6) (2019) 948.
[87] V.A. Al'shitz, V.L. Indenbom, Dynamic dragging of dislocations, Sov. Phys. Uspekhi 18 (1) (1975) 1.
[88] A. Vinogradov, I.S. Yasnikov, D.L. Merson, Phenomenological approach towards modelling the acoustic emission due to plastic deformation in metals, Scr. Mater. 170 (2019) 172–176.

Article III

Materials Science & Engineering A 856 (2022) 143969

Contents lists available at ScienceDirect

Materials Science & Engineering A

journal homepage: www.elsevier.com/locate/msea

Dislocation kinetics explains energy partitioning during strain hardening: Model and experimental validation by infrared thermography and acoustic emission

A. Sendrowicz [a], A.O. Myhre [a], A.V. Danyuk [b], A. Vinogradov [a,*]

[a] Department of Mechanical and Industrial Engineering, Norwegian University of Science and Technology – NTNU, N-7491, Trondheim, Norway
[b] Research Institute of Advanced Technologies, Togliatti State University, Togliatti, 445020, Russia

ARTICLE INFO

Keywords:
Strain hardening
Energy partitioning
Dislocation kinetics
Thermography
Acoustic emission
Cu–Zn alloys

ABSTRACT

The energy dissipation and storage during strain hardening of metals have been investigated by means of complementary in situ techniques - infrared thermography (IRT), digital image correlation (DIC) and acoustic emission (AE). Inspired by experimental results obtained in the present work and data available in literature, we proposed the analytically tractable thermodynamic modelling approach, which is conceptually based on a single-variable dislocation evolution approach with a total dislocation density serving as a principal variable governing the strain hardening process. Unified by the kinetic approach involving generation, annihilation and motion of dislocations, the models accounting for the acoustic emission behaviour and heat dissipation under load have been proposed and verified experimentally. For the first time, we were able to demonstrate that the key parameters governing the dislocation storage and annihilation rates can be, in principle, recovered from independent AE and IRT measurements. These results agree favourably with the predictions of the dislocation-based constitutive strain hardening models of the Kocks-Mecking type. The self-consistency, versatility and predictive capacity of the proposed modelling approach are demonstrated in the examples of Cu–Zn alloys with different concentrations of Zn varied from 0 to 30% and correspondingly different stacking fault energies.

1. Background and motivation

Plastic deformation is a highly dissipative process occurring at various scales. Energy dissipation during plastic deformation of metals and alloys occurs as the result of irreversible dissipative processes of dislocation nucleation, motion and annihilation. Thus, the transformation and dissipation of mechanical energy are related to residual deformation and damage associated with the accumulation of defects in the crystalline elastic-plastic solids. The seminal work on plastic dissipation was done by Taylor and Farren in 1925 [1] and Taylor and Quinney in 1934 [2]. They demonstrated that most of the mechanical energy expended in plastic straining is converted into heat while the small remaining energy is stored in the deformed solid as internal energy (see also early works [3–5]). It was two decades later, that Kaiser [6] recognised that a small part of the total mechanical energy is dissipated also in the form of elastic waves commonly referred to as acoustic emissions (AE). A comprehensive review of the early experimental efforts aiming at assessing the energy stored during plastic deformation and relying on either temperature measurements by thermocouples or on heat release measurements by deformation or annealing calorimeters was provided by Bever et al. [7] in 1973. Recent years have seen significant progress in the non-contact full-field thermographic technology. Featured by its high sensitivity, spatial resolution and acquisition rate, this method is unique in providing direct access to the thermodynamic quantities characterising plastic flow, its temporal and spatial evolution up to fracture through the measurements of the local distribution of temperature on the surface [8–21]. Multiple attempts have been made to utilise IRT measurements to characterise various aspects of cyclic deformation and fatigue of structural materials [22–24]. Despite some demonstrated examples, the fatigue limits assessed in this way are often challenged since the physical and microstructural reasons standing behind the estimations have not been understood to date. Overall, although it has been demonstrated that dissipative energy measurements can be used as non-destructive indicators of a material's microstructure evolution during cyclic deformation (see the above sited works [22–24] and references therein), no correlation between the measurable

* Corresponding author.
E-mail address: alexei.vinogradov@ntnu.no (A. Vinogradov).

https://doi.org/10.1016/j.msea.2022.143969
Received 1 July 2022; Received in revised form 2 September 2022; Accepted 6 September 2022
Available online 11 September 2022

thermodynamic quantities and the microstructural state has been firmly established as yet.

Besides heat release, which is assessable by infrared thermography in situ, a distinctive 'companion' of dissipative processes in solids, including the evolution of the dislocation structure, is acoustic emission associated with elastic waves generated during rapid local microstructural changes within a solid under load. Unlike the integral IRT measurements, AE is fundamentally sensitive only to strongly localised sources in the microscopic volumes of the materials. Since the collective defect dynamics on the micro- and meso-scale is reflected in AE, the AE measurements provide access to fine details of the dynamic and statistical properties of elementary plastic events such as movement of dislocations, mechanical twinning or deformation-induced phase transformations in solids [25–32]. It has been well understood that the transient AE signals at the sensor output depend primarily on the magnitude and velocity of local displacements caused by local stress relaxations in the material during plastic deformation [33]. However, although the AE technique has long been developed as a tool sensitive to dislocation dynamics [27], physical foundations for reliable forecasting of approaching failure or transitions in mechanical behaviour are still lacking.

These reasons motivated us to revisit the simple conventional uniaxial monotonic tensile testing to fracture to establish the missing links between the microstructure evolution and energy partitioning assessed independently by contemporary AE and IRT techniques. To this end, we advance several general physical concepts centred around dislocation kinetics and thermodynamics and unite them into a potent diagnostic tool for characterising microstructure evolution during plastic flow. The single-parametric dislocation-based strain hardening theory is synergistically connected with the acoustic emission and heat dissipation analytical models for the first time as the main outcome of the present work.

The paper is structured to cover the various concepts relevant to our approach and finally offer a synthesis of them. Since our work is inspired by many experimental results outlined in the Introduction, in Section 3 (following a brief introduction of experimental techniques in Section 2), we first present a series of results from critical experiments performed on model polycrystalline Cu–Zn alloys as representatives of a wide range of FCC structural materials with dislocation mediated plasticity. The most common experimental findings concerning the IRT and AE behaviour caused by plastic deformation are summarised in this section. In the next part (Section 4), we describe a dislocation-based approach to modelling the thermal and acoustic effects in conjunction with the behaviour of dislocations and associated strain hardening. A link between the model parameters governing the evolution of the dislocation density, the stored energy and the energy dissipated both as heat and AE is established. Finally, in Section 5, this important connection between energy partitioning, AE, and properties of evolving dislocation ensembles is tested against the obtained experimental data, and the self-consistent description consolidating all the concepts is provided before the general conclusions are drawn in Section 6.

2. Experimental

2.1. Materials and microstructure characterisation

The commercially available Cu–Zn alloys from Wieland-Werke AG (Germany) were chosen for the present study. Cu–Zn alloys are typical substitutional solid solutions with the stacking fault energies varying broadly and reducing strongly with the concentration of Zn as will be discussed below in Section 3.1. The single FCC α-Cu-Zn phase covers a wide composition range from 0 to almost 35% Zn [34]. The concentrations of Zn varied from 0 to 30%; the specimens are referred to as Cu, Cu–5Zn, Cu–10Zn, Cu–15Zn, Cu–20Zn and Cu–30Zn, respectively.

The materials were received in the form of rolled plates. The flat dog-bone specimens were shaped by the electric discharge machine to have a 12 mm gauge length, 5 mm width and 2.5 mm thickness (see Figure S1[1] in Supplementary Materials for the exact specimen shape and dimensions). The specimens were cut from the as-received plates parallel to the rolling direction. After machining, the samples were ground and polished to a mirror-like surface. They were then annealed in Argon gas at 500 °C (600 °C was used for Cu) for 1–2 h to relieve internal stresses inherited from the manufacturing stage prior to mechanical testing and to create a homogeneous microstructure.

The microstructure was analysed using the Zeiss SIGMA FEG scanning electron microscope equipped with the EDAX/TSL electron backscatter diffraction (EBSD) detector. In the final step of preparation for EBSD measurements, the sections were ion-polished using Hitachi's IM4000Plus low-energy Ar + ion milling system. EBSD maps were obtained from the plane perpendicular to the rolling direction at different magnifications from the undeformed material as well as from the uniformly deformed gauge areas after the final rupture. Regions of interest (ROI) for SEM/EBSD examinations are indicated on the images of fractured specimens in Fig. S1. All investigated materials were characterised in the backscattered electrons (BSE) imaging mode. The mean grain size was assessed from several EBSD maps with edge grains and twins removed from the statistical analysis.

2.2. Experimental setup and mechanical testing

The experimental setup for tensile testing has been described elsewhere in detail [35]. The measuring system comprises four synchronised devices: (i) the modified electrodynamic Instron Electropuls E10000 tensile machine with the 10 kN load-bearing capacity, (ii) the digital image correlation (DIC) system based on the Allied Vision Prosilica GC2450 CCD camera with 5 Mpixel resolution equipped with a Tamron 272 EN II macro lens mounted on a PC-controlled motorised stage, (iii) the Telops FAST M350 mid-wave, high-speed, high-resolution infrared camera with the Janos Technology 25 mm lens and 1/4″ extension ring, and (iv) broadband AE measuring system with continuous streaming capabilities based on the PCI-2 board from MISTRAS. The photograph of the experimental setup is presented in Fig. S2. One side of the specimens was painted with a matt black lacquer to enhance the emissivity in the infrared spectral region. Images of the temperature distribution along the gauge part of the specimen were obtained at 640 × 512 pixels resolution with a frame rate 30 frames per second (maximum of 355 fps). The fine black and white random speckle pattern was created on the other side for the DIC analysis using the subpixel resolution algorithm (c.f., Fig. S1b). Tensile tests were carried out in air at ambient temperature with the nominal strain rates $\dot{e}$ of 3×10^{-2} s^{-1} and 1×10^{-2} s^{-1} (here and below, the dot denotes the first derivative with respect to time). Two strain rates were probed to validate the measurements since AE and IRT techniques are known to be strongly strain rate sensitive while the strain rate sensitivity of the flow stress in copper-based alloys is not significant. For the same reason, to ensure the reproducibility of results, the tests were repeated using the screw-driven MTS machine. Once we made sure that the collected data followed the expected trends reproducibly, the dataset was qualified for the analysis and, in what follows, the main findings will be illustrated for the tests performed at one strain rate $\dot{e}=3\times10^{-2}$ s^{-1}.

The full-field displacement and strain maps were obtained by the DIC technique from a set of sucessive images acquired by the optical camera at 30 fps rate. The local strain rate distribution, the average strain over the entire gauge part and the corresponding strain rate at a given strain were then evaluated numerically. Cauchy ("true") stress and the work-conjugate logarithmic strain are used in what follows to represent the stress/strain state in the deformed specimens if not stated otherwise. All details of the original data processing algorithms are provided in

[1] Prefix S in figure labels refers to Supplementary Materials throughout the text.

Ref. [35]. The flowchart visualising the information exchange between experimental techniques involved in the present study is given in Fig. S3. Some specific details are provided below for the sake of self-consistency.

2.3. Infrared data processing

The thermal images were processed with a grey body emissivity correction. The heat function $\dot{q}_d(x,y,t)$ accumulating the heat generated by all sources regardless of their origin was calculated from the experimentally acquired time-dependent temperature distribution field $T(x,y,t)$ within the (see also Fig. S6 and Supplementary Video 1 representing the raw $T(x,y,t)$ data from the IRT camera synchronised with the loading curve). To do so, the boundary value problem was solved for the heat transfer equation in Cartesian (x,y) coordinates, as has been described in Refs. [10–12,35] in detail:

$$\rho_{mat} c_p \frac{\partial T}{\partial t} = \dot{q}_d + k_T \nabla^2 T \tag{1}$$

where ρ_{mat} is the material's density, c_p is the heat capacity, and k_T is the heat transfer coefficient. Numerical calculations of time and spatial derivatives of $T(x,y,t)$ are required at this step. To reduce the effect of temporal and spatial fluctuations of the measured temperature field on the calculated source function, (i) the high resolution DIC images were mapped onto IRT images, and (ii) the local smoothing/regression procedures were applied to IRT data (interested readers are referred to Supplementary materials, Note 3, Figs. S4 and S5 and ref. [35] for the software procedures and the hardware solutions mitigating the heat losses to the environment). Radiation and convection effects are assumed to be negligible (see the arguments presented in the companion work [36]). After integration of $\dot{q}_d(x,y,t)$ over the surface (x,y) and correction for the thermoelastic effect, the power dissipated as heat (and its average density P_d) is obtained. The corresponding dissipated energy density is then calculated by integration of $P_d(t)$ with respect to time (see the flowchart shown in Fig. S3).

2.4. Acoustic emission measurements and signal processing

A multi-resonant broadband AE sensor micro-30F by MISTRAS (USA) with a frequency range from 150 to 750 kHz with a peak sensitivity of around 300 kHz (according to the manufacturer's calibration certificate) was used in this study. It was securely mounted using a 3D-printed elastic polymer clamp away from the gauge part of the tensile specimens on an unstrained shoulder part. Silicone vacuum grease was used as a coupling medium to ensure the efficient transfer of elastic waves from the surface to the transducer. The signal was amplified by 60 dB in the frequency band from 50 to 1200 kHz by the low-noise preamplifier 2/4/6 and then transferred to the PC-controlled AE-recording system based on the PCI-2 data acquisition board by MISTRAS. AE recording was performed continuously at a 2 MHz sampling rate.

The continuously streamed data were sectioned into consecutive individual realisations of 4096 samples with 2048 points overlapping. For each realisation, a power spectral density (PSD) function $G(f)$ was calculated using a Welch technique implemented in the ASK algorithm [37]. The following two quantities were introduced to describe the evolution of the PSD with time (strain): the AE power referred to 1 Ohm nominal impedance

$$P_{\mathrm{AE}} = \int_0^\infty G(f)\, df \tag{2}$$

and the *median frequency* f_{m} of the PSD function computed from the definition

$$\int_0^{f_m} G(f)\, df = \int_{f_m}^\infty G(f)\, df \tag{3}$$

Both P_{AE} and f_{m} were obtained from $G(f)$ after subtraction of the PSD of the laboratory noise pre-recorded before the start of loading during each test. For details of the AE signal processing and the rationale standing behind the choice of primary descriptive variables - P_{AE} and f_{m} - used to characterise each realisation of the random AE process, the readers are encouraged to look through the early publications [38–40].

3. Experimental results

3.1. Microstructure

The initial state of the studied Cu–Zn alloys was characterised using scanning electron microscopy. The SEM-EBSD scans reveal the typical annealed grain structure, morphology and orientation. Examples of the initial microstructures for all three categories of alloys studied – Cu (high SFE), Cu–10Zn and Cu–15Zn (intermediate SFE), and Cu–20Zn (low SFE) – are represented in Fig. 1a–d, respectively. Equiaxed grains with random misorientations contain annealing twins, the fraction of which tends to increase with the increasing Zn concentration. Collecting and summing up the data from at least three EBSD scans, mean grain size (excluding edge grains and twins) was estimated as shown in Table 1. The corresponding typical deformation microstructures are shown in Fig. 1e-m. One can notice the appearance of an internal deformation-induced structure within the grains, which is revealed in both back-scattered and electron channelling contrast images (ECCI). The deformation microstructure exhibits a strong dependence on the stacking fault energy that decreases notably with the concentration of Zn. The image quality (IQ) layer (e-h), where the contrast is determined primarily (but not solely, see a comprehensive review by Wright et al. [41]), by residual strain in the diffracting volume, provides useful visualisations of the microstructure developed in the course of plastic deformation: strained areas appear darker than unstrained regions.

The role of metallurgical factors such as solid solution strengthening and stacking fault energy (SFE) in the deformation of fcc metals has been established quite carefully using Cu and its solid solution alloys such as Cu–Al, Cu–Ge, Cu–Zn, etc., [42–48]. SFE determines the width of the stacking fault of dissociated dislocations [42,43,49,50]: higher SFE results in a smaller separation between partials and vice versa, thus controlling the propensity of dislocations to cross-slip. To a lower extent, the difficulty to cross-slip also depends on the short-range order and the yield strength. The high SFE facilitates cross-slip, giving rise to a wavy dislocation arrangement, which tends to transform itself into equiaxed cell-like structures as the strain increases [51,52]. In the cell structures, the majority of dislocations reside in cell walls with low angles of misorientations, while the interior of the cells remains relatively dislocation-free. As opposed to this, a large separation between the partial dislocations, which is observed in low SFE materials, inhibits cross-slip. Therefore, dislocations are confined to major slip planes and tend to organise themselves into planar arrays or slip bands. The measured SFE value γ_{SFE} for copper varies typically in the range of 55–80 mJ/m^2. It decreases significantly when copper is alloyed within the solid solubility range (Fig. S7).

In addition to controlling the dislocation mobility and the evolution of the dislocation substructure, SFE affects the propensity of a material to form stacking faults and deformation twins, with low SFE favouring deformation twinning [48,53–55] and the twinning stress scaling with $\sqrt{\gamma_{\mathrm{SFE}}}$. In the low-SFE alloys, such as Cu–20Zn and Cu–30Zn (c.f., also Fig. S8, where the deformed microstructure of Cu–30Zn is shown), the deformation sequence involves the formation of planar dislocation arrays, stacking faults, mechanical twins, and shear bands. The twin thickness and spacing are governed by SFE and decrease as the SFE value decreases. In the cold-rolled intermediate SFE Cu–10Zn alloy, Hatherly and Malin [51] and Wakefield and Hatherly [52] observed mixed microstructures exhibiting features that were characteristic of both high- and low-SFE materials, i.e., the regions containing equiaxed cells and

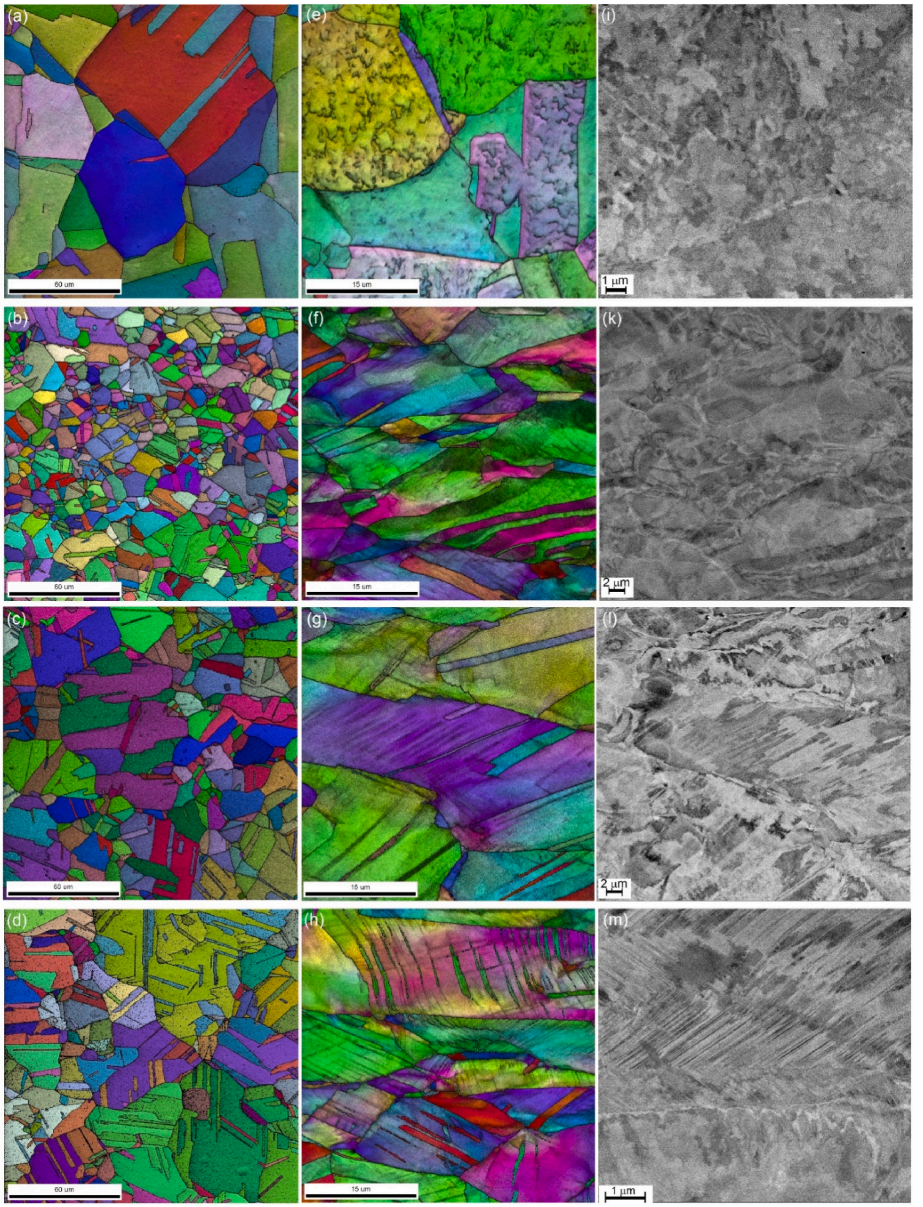

Fig. 1. Typical initial (a–d) deformation (e–m) microstructures represented by EBSD maps in the IPF colours superimposed with the grey-scale IQ maps (a–h) and ECCI micrographs detailing the microstructure at higher magnification (i–m); (a,e,i) Cu, (b,f,k) Cu–10Zn, (c,g,l) Cu–15Zn and (d,h,m) Cu–20Zn – all tested at $\dot{\varepsilon} = 3\times10^{-2}\ s^{-1}$. (For interpretation of the references to colour in this figure legend, the reader is referred to the Web version of this article.)

micro-bands (referred to as copper-type regions) coexist with the regions containing deformation twins (brass-type regions) [51,52]. Grace and Inman [56] (see also [45,57]) concluded that the transition between the cell-type dislocation configuration (high-SFE materials) and the planar-type dislocation configuration (low-SFE materials) occurs between 25 and 36 mJ/m^2. Thus, Cu and Cu–5Zn (high-SFE) represent typical cell-forming materials, Cu–20Zn and Cu–30Zn are examples of materials with the prevailing planar slip, while Cu–10Zn and Cu–15Zn are the alloys with intermediate SFE and mixed microstructures, (see Note 4 and Fig. S7 in Supplementary Materials where the dependence of the SFE value is plotted against the concentration of Zn in the Cu matrix).

Table 1
Materials and their microstructural and mechanical properties at $\dot{\varepsilon} = 3\times10^{-2}$ s^{-1}.

Material	Stacking Fault Energy γ_{SFE} mJ/m^2	Grain size, D μm	Std. Dev. of grain size μm	Shear modulus, G GPa	Yields Stress $\sigma_{0.2}$ MPa	Ultimate tensile strength σ_{UTS} MPa	Uniform Elongation ε_u (eng)	Elongation at break ε_f (eng)
Cu	55–80	34	19	40	33	218	0.44	0.71
Cu5Zn	40	15	–	40	85	264	0.41	0.65
Cu10Zn	35	10	5	44	102	285	0.41	0.64
Cu15Zn	25	20	12	44	100	299	0.42	0.66
Cu20Zn	18	20	14	44	113	324	0.52	0.74
Cu30Zn	14	35	19	45	105	333	0.6	0.81

Note: all mechanical properties were measured in engineering coordinates with an error of less than 3%.

Table 2
Model parameters used to approximate the stress-strain data for Cu–Zn specimens tested in tension at the nominal strain rate 3×10^{-2} s^{-1}.

Material	KM model parameters				Predicted necking strain ε_N^{KM}	Measured necking strain (true) ε_N	σ_S, k_1 and k_2 from IRT and AE measurements		
	k_1 (KM)	k_2 (KM)	σ_S, MPa	σ_0, MPa			σ_S, (IRT) MPa	k_1 (IRT)	k_2 (AE)
Cu	0.0228	3.25	369	44	0.33	0.37	500	0.0309	6.8
Cu–5Zn	0.0264	3.24	437	86	0.32	0.33	410	0.0252	4.4
Cu–10Zn	0.0268	2.94	487	103	0.33	0.34	455	0.0248	5.8
Cu–15Zn	0.0261	2.65	525	111	0.34	0.35	556	0.0273	4.9
Cu–20Zn	0.0259	2.09	623	125	0.38	0.42	588	0.0245	5.1
Cu–30Zn	0.0204	1.23	832	108	0.49	0.43		–	–

Non-surprisingly, the materials investigated in the present work behave in harmony with the described scenario, as is evident from the microstructure evolution illustrated in Fig. 1 for the materials with notably different SFEs: the dislocation distribution in the uniformly, plastically deformed specimens changes markedly with alloying and the SFE reduction from an irregular tangled cell structure in pure copper (high-SFE, Fig. 1e, i) to the coplanar arrangements which became predominant in low-SFE Cu–20Zn and Cu–30Zn (Fig. 1h, m, c.f., also Figs. S2a and b) with mixed microstructural features visible in Cu–10Zn and Cu–15Zn with intermediate SFE.

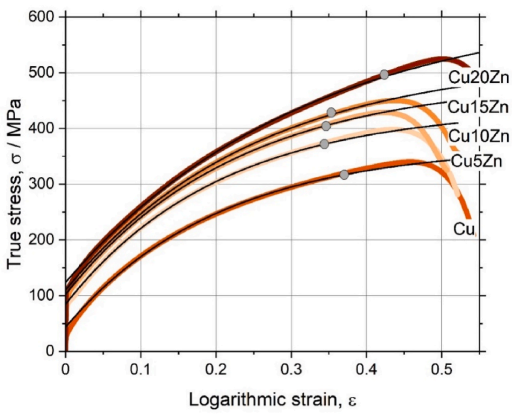

Fig. 2. True stress-strain curves and their approximations (red lines) by the Kocks-Mecking model (see the txt below) with input parameters shown in Table 2 for the specimens tested at the nominal strain rate $\dot{\varepsilon}$=3×10^{-2} s^{-1}. The grey circles indicate the necking points according to the Considère criterion. (For interpretation of the references to colour in this figure legend, the reader is referred to the Web version of this article.)

3.2. Mechanical behaviour

Fig. 2 shows the representative tensile stress-strain curves $\sigma(\varepsilon)$ for Cu–Zn alloys with the concentration of Zn up to 20%. Corresponding strain hardening rates $\theta = d\sigma/d\varepsilon$ are displayed in Supplementary Materials (Fig. S9).

The mechanical behaviour of Cu alloys depends on the Zn content due to a combined effect of solute atoms on the lattice friction for the dislocation motion, stacking fault energy, short-range and chemical order. Tensile strength rises notably with increasing the Zn content, showing an efficient solute-strengthening effect, and the rising tendency slows down above ~20% Zn. The strain hardening behaviour is similar in all materials tested. At the onset of plastic yielding, all alloys (but pure Cu) exhibit a strongly localised Lüders band initiating at one end of the gauge part and propagating towards the other, thus causing the local drop in the strain hardening rate (Fig. S9). The serrated plastic flow is pronounced in the Cu–30Zn alloy as the deformation proceeds (Fig. S9, see also Supplementary Video 2 using the results of the DIC analysis and demonstrating the local fluctuations of the strain rate accompanying the initial Lüders band propagation and Portevin - Le Chatelier bands in Cu–30Zn tested at $\dot{\varepsilon}$=3×10^{-2} s^{-1}). This effect is commonly observed in this alloy [58,59] and is clearly reflected by AE as has been described in abundant literature for various alloy systems [60–63], including Cu–30Zn [64].

3.3. Acoustic emission behaviour

Fig. 3(a–d) provides an overview of acoustic emission streaming waveforms acquired continuously for Cu, Cu–10Zn, Cu–15Zn and Cu–20Zn tested at the nominal strain rate $\dot{\varepsilon} = 3\times10^{-2}$ s^{-1} (all raw streams, including Cu–5Zn and Cu–30Zn can be visually compared in Fig. S10). Similar pictures are observed at the slower strain rate, albeit with the proportional reduction of the root mean square (rms) signal. The signal can be considered as a random time series consisting of a rather intense flow of individual bursts illustrated in more detail by the waveform fragments at a millisecond timescale in Fig. 3(e–h). All these fragments were arbitrarily chosen from the early stage of the strain hardening shortly after the pronounced AE peak. Even though the prominent AE maximum is reached around the conventional

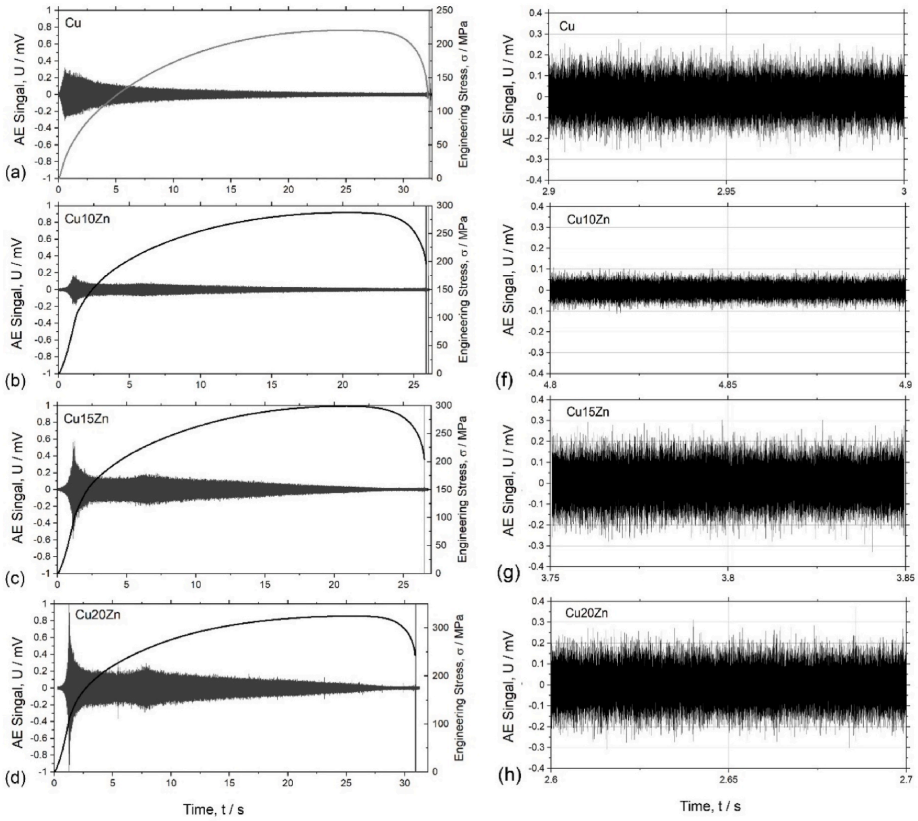

Fig. 3. Raw AE streaming data superimposed with the loading curves ($\dot{\varepsilon} = 3\times10^{-2}\ s^{-1}$) for representative Cu–Zn alloys (a–d) and their typical fragments (e–h) highlighting the continuous nature of AE signal arising in response to dislocation motion during plastic flow.

macroscopic yield stress, the AE signal is considerably higher than the electronic laboratory noise (about 6 μV rms, or 14 μV peak-to-peak measured with the specimen gripped, while the machine was idle prior to starting loading) throughout the test.

Two major factors that affect the AE evolution of the AE peak at the onset of the plastic flow are to be mentioned – the solid solution strengthening and SFE. The interplay between these two controls the final appearance of the AE peak. As it is plausibly expected from the effect of solid solution alloying on AE, which has been quite well understood, see Ref. [65], for example, the AE peak position as a function of the flow stress shifts to higher applied stresses, Fig. 4. The AE signal decreases when 5% Zn or 10% Zn is added to copper since the resistance to dislocation motion by misfitting substitutional solute atoms increases. With the further increase in the Zn content, the reduction of SFE prevails over the effect of substitutional atoms, and the AE tends to increase in harmony with earlier observations performed by Danyuk et al. [66] on several pure metals (Ni, Al, Cu and Ag) with remarkably different SFEs.

Let us notice that the microstructure (both before and after deformation), mechanical behaviour, acoustic emission, and plastic energy dissipation in the Cu–5Zn alloy (high SFE) does not differ significantly from that of pure copper; the overall behaviour of this material follows the common trends in the measured properties lying in between those observed for Cu and Cu–10Zn. Furthermore, the present results confirmed that the AE behaviour in Cu–30Zn was essentially the same as

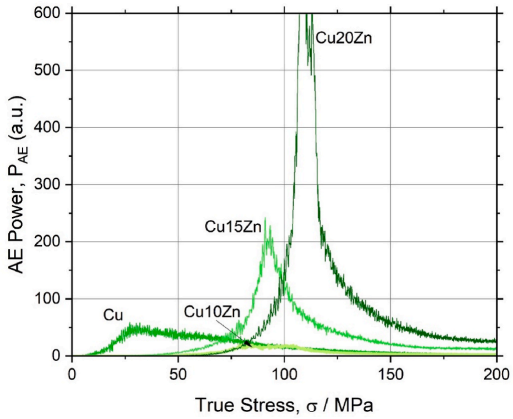

Fig. 4. The AE peak represented as a function of flow stress. The steady shift of the AE peak towards higher stresses is seen with the increasing concentration of the alloying element.

it was reported earlier for α-brass [64] (see Fig. S11). The observed wide serrated flow region limits the applicability of our model, which is proposed for the uniform deformation stage and discussed in the subsequent sections. Bearing in mind that Cu–5Zn and Cu–30Zn alloys follow the trends common for low and high SFE alloys, respectively, without loss of generality, the main part of the model-related discussion will be illustrated using four materials - Cu (high SFE), Cu–10Zn and Cu-15n (intermediate SFE), and Cu–20Zn (low SFE). These alloys represent FCC metals with the remarkably different dislocation behaviour governed by solid solution strengthening and the stacking fault energy.

Analysis of Figs. 3 and 4 unveils that AE commences already at the very low applied stress, i.e., almost immediately after the beginning of loading, thus highlighting the strong inhomogeneity of plastic deformation initiating at coarse favourably oriented grains and involving more and more grains as local strain hardening proceeds. Since the AE signal is seen as a random quasi-stationary process on various temporal scales, it is convenient to call the Fourier spectral decomposition to reveal its statistical features and, therefore, the features of the dynamics in emitting sources.

Fig. 5 illustrates the behaviour of the AE signal in terms of the AE power and the median frequency of the PSD function evolving with strain.

As is typical for many metals and alloys, the AE power peaks shortly after plastic yielding and decays gradually afterwards in response to growing dislocation density and a concomitant decrease in the dislocation mean free path. After the initial transient drop in the AE f_m behaviour corresponding to a very early stage of yielding, the power spectral density tends to shift to a high-frequency domain during the uniform deformation stage. The process, however, is notably not uniform (particularly for the alloys). The unusual observation is that the second AE peak arises in all studied alloys (but not in pure copper) at around 10% plastic strain. The DIC analysis convincingly shows that this peak is actually an experimental artefact irrelevant to any microstructure-related dislocation mechanism. It is merely related to the inhomogeneity of the plastic flow tending to propagate toward the undeformed shoulder part of the specimen being tested; it, therefore, should be excluded from further model analysis. Interested readers are encouraged to review Supplementary Materials Note 9, Fig. S12.

The fluctuating behaviour of the local strain rates, which is particularly pronounced in solid solutions exhibiting the Lüders phenomenon, at the onset of strain hardening is also reflected in the irregular behaviour of the median frequency in Fig. 5. What should be noticed is that the f_m value drops rapidly after the start of the test and reaches its global minimum. It then starts rising again, exhibiting a fluctuating behaviour up to 10% plastic strain where the second AE maximum is observed. The variations of f_m indicate minute features (which are not otherwise visible on the stress-strain diagram) of the deformation behaviour of emitting sources and are attributed to the local inhomogeneities in the plastic flow.

3.4. Infrared thermography

The variables describing partitioning of the mechanical energy with plastic strain (e.g., temperature, stored and dissipated energies and powers) exhibit monotonically ascending trends as is also commonly observed for various structural materials [8–21], including pure copper [67–71]. Results of calculations of the dissipation power density P_d from the experimentally measured temperature distribution maps (c.f., Section 2.3) are shown in Fig. 5 together with the AE data as a function of strain. In Fig. 6, P_d is plotted against the expended mechanical power P_e calculated as $P_e(\varepsilon) = \sigma(\varepsilon)\dot{\varepsilon}(\varepsilon)$ with the account of averaged local strain rates provided by the DIC analysis for a given strain. Within the experimental scatter typical of IRT measurements (see Section 2.3, Fig. S5, and note here that the assessment of thermal effects is particularly challenging in materials like copper and its alloys having a high rate of heat transfer due to high electric and thermal conductivity), all data align themselves with the same master straight line with the slope representing the differential Taylor-Quinney coefficient $\beta_{TQ} = P_d/P_e$. The slope of the linear regression line is close to 0.9, which favourably agrees

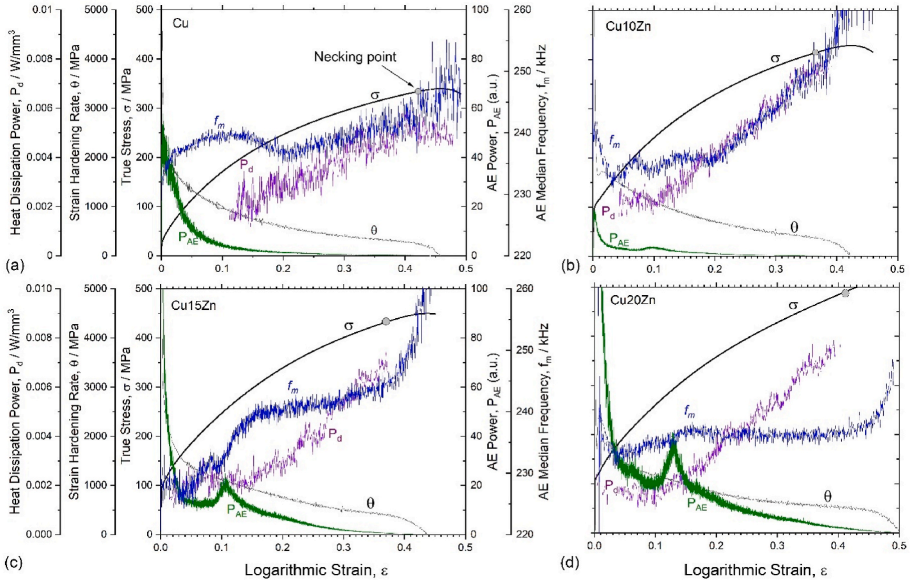

Fig. 5. AE data representing the evolution of the PSD function in terms of the AE power P_{AE} and median frequency $f_{|m}$ synchronised with the tensile loading curves $\sigma(\varepsilon)$, strain hardening rate $\theta(\varepsilon)$ and heat dissipation power $P_d(\varepsilon)$ obtained at $\dot{\varepsilon}=3\times10^{-2}$ s^{-1}.

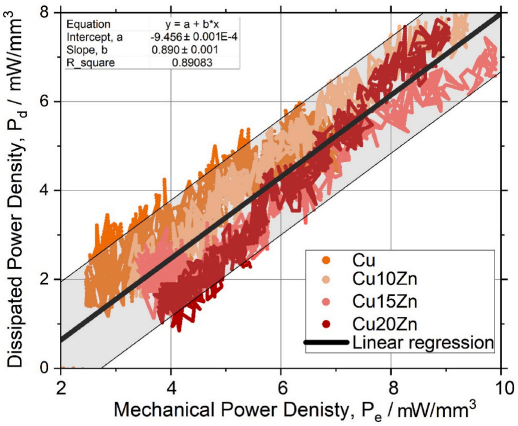

Fig. 6. Heat dissipation power versus plastic power for materials tested. The solid line represents the result of the linear regression.

with that is frequently reported (or assumed) for the β_{TQ} factor in metallic materials. We should note here that since the stored power P_s - a measure of the elastic energy stored in the deforming body per unit time - is a small fraction of the mechanical or dissipated power, and, since it is calculated from the difference between the latter two $P_s = P_e - P_d$, the small measurement error in the mechanical or thermal power will cause a significant error in the experimentally measured stored power. Besides, recall that the expended mechanical energy and the dissipated energy are obtained after numerical integration of the corresponding power densities: $E_e(\varepsilon) = \int \frac{P_e}{\dot{\varepsilon}} d\varepsilon$, $E_d(\varepsilon) = \int \frac{P_d}{\dot{\varepsilon}} d\varepsilon$. Thus, there will be inevitable extra uncertainty due to the integration procedure of scattered input data. Therefore, in what follows, we preferably use the power densities for the model-based calculations.

4. Model description

In the present section, we shall discuss the model efforts made to bridge the dislocation kinetics and the observed features of energy partitioning between heat production, latent energy and acoustic emission accompanying microstructural rearrangements in solids during plastic deformation. Thus, there are three essential ingredients in the modelling process: (i) evolution of the dislocation density and strain hardening, (ii) heat dissipation and energy storage, and (iii) acoustic emission behaviour with strain. For the sake of self-consistency, we briefly recall the basic concepts and ideas involved in all these three modelling steps.

4.1. Strain hardening

Assuming that during homogeneous plastic deformation, the strain hardening is governed entirely by the microstructural changes caused by dislocations and their interactions, it is the density of dislocations that serves as a state variable and determines the stored energy. In a wealth of dislocation-based strain hardening models, the kinetic approach formulated by Kocks and Mecking [72,73] dominates the constitutive modelling philosophy to the present day. The structure of this simple single internal variable model is composed of two equations: the first relates the total dislocation density ρ to the flow stress $\sigma(\rho)$, while the second governs the evolution of the dislocation ensemble with plastic strain, providing the explicit solution for $\rho(\varepsilon)$. For virtually all conceivable geometrical arrangements of dislocations, the flow stress scales with the square root of ρ according to the Taylor equation in the form:

$$\sigma = M\alpha G b\sqrt{\rho} \tag{4}$$

where b is the magnitude of the Burgers vector of the dislocation, G is the shear modulus, and M is the texture-related orientation factor converting shear stress τ and strain γ to axial ones as $\tau = \sigma/M$, $\gamma = \varepsilon M$; $\alpha = \alpha(\dot{\varepsilon}, T)$ is a temperature and strain rate dependent factor ranging typically between 0.1 and 0.5 [74]. Here, we neglected the friction stress for simplicity, which is often a reasonable assumption for FCC metals and alloys.

The first-order differential equation describing the behaviour of the population of dislocations is traditionally postulated in the form $\frac{d\rho}{d\varepsilon} = \frac{d\rho^+}{d\varepsilon} - \frac{d\rho^-}{d\varepsilon}$ accounting for the rates of dislocation production $\frac{d\rho^+}{d\varepsilon}$ and disappearance $\frac{d\rho^-}{d\varepsilon}$ in the righthand side. In the widely accepted model Kocks-Mecking (KM) model, this equation has the following form:

$$\frac{d\rho}{d\gamma} = \frac{d\rho}{Md\varepsilon} = \frac{k_1}{b}\sqrt{\rho} - k_2\rho \tag{5}$$

with k_1 and k_2 - dimensionless parameters controlling the rates of dislocation production and dynamic recovery, respectively. Here k_1 is the athermal coefficient, while the term $k_2(\dot{\varepsilon}, T)\rho$ represents the temperature and strain rate dependent dislocation annihilation kinetics. As a note, this equation does not need to be postulated and can be, in principle, obtained on the grounds of irreversible thermodynamics applied to dislocation plasticity [28,75].

When combined with Eq. (4), the last equation can be rewritten in a compact form for the flow stress as

$$\frac{d\sigma}{d\varepsilon} = \frac{\sigma_S}{\tilde{\varepsilon}} - \frac{\sigma}{\tilde{\varepsilon}} \tag{6}$$

with two coefficients redefined as

$$\sigma_S = \frac{k_1 M\alpha G}{k_2}, \quad \tilde{\varepsilon} = \frac{2}{k_2 M} \tag{7}$$

Here σ_S represents the saturation stress corresponding to the condition $\frac{d\sigma}{d\varepsilon} = 0$ (or $\frac{d\rho}{d\varepsilon} = 0$ in Eq. (5)), and $\tilde{\varepsilon}$ is the parameter controlling the necking strain [76–78]. Solving the initial value problem for the homogeneous differential equation (6) with $\sigma(\varepsilon = 0) = \sigma(\rho_0) = \sigma_0$ yields the explicit relation between the flow stress and plastic strain in the form:

$$\sigma(\varepsilon) = \sigma_0 + (\sigma_S - \sigma_0)\left(1 - \exp\left(-\frac{\varepsilon}{\tilde{\varepsilon}}\right)\right) \tag{8}$$

The strain hardening rate $\theta(\varepsilon) = \frac{d\sigma(\varepsilon)}{d\varepsilon}$ is obtained as follows:

$$\theta(\varepsilon) = \frac{1}{\tilde{\varepsilon}}(\sigma_S - \sigma_0)\exp\left(-\frac{\varepsilon}{\tilde{\varepsilon}}\right) = \frac{1}{\tilde{\varepsilon}}(\sigma_S - \sigma(\varepsilon)) \tag{9}$$

These expressions will be frequently used in the forthcoming sections.

4.2. Stored/dissipated energy

The latent (or stored) energy is defined as a difference between the energy of the crystal with defects accumulated during plastic deformation and the energy of the initial undeformed crystal. Since the dislocations represent the elementary carriers of plastic deformations, which are stored in the deformed body, it is essential to propose a dislocation-based modelling strategy that links the measurable thermodynamic quantities – dissipated and stored energy and/or power - to the evolution of the dislocation density [79].

The first law of thermodynamics states that the work A, which is done on the system, increases its internal energy U and, in non-adiabatic processes, results in the heat transfer Q from the system to the reservoir, which is expressed as:

$$\delta A = dU + \delta Q \tag{10}$$

Here the symbol δ underlines that the infinitesimally small increments of heat and work are not perfect differentials. Assuming that the internal energy of the deforming crystal changes primarily due to the evolution of the total dislocation density $\rho = \rho(t)$ depending on the loading time t, the equality (10) can be rewritten as:

$$\frac{\delta Q}{dt} + \frac{dU}{d\rho}\frac{d\rho}{dt} = \sigma\frac{d\varepsilon}{dt} \tag{11}$$

Using a general form of the kinetics equation $\dot{\rho}(t) = \dot{\rho}^{+} - \dot{\rho}^{-}$ for the total dislocation density evolving through coupled "generation and annihilation" processes described by $\dot{\rho}^{+}$ and $\dot{\rho}^{-}$ terms, respectively, Eq. (11) is transformed to:

$$\frac{\delta Q}{dt} + \frac{dU}{d\rho}\left(\frac{d\rho^{+}}{dt} - \frac{d\rho^{-}}{dt}\right) = \sigma\frac{d\varepsilon}{dt} \tag{12}$$

This equality explicitly states that the internal energy of the plastically deforming solid increases due to the dislocation production and storage term $\frac{dU}{d\rho}\frac{d\rho^{+}}{dt}$ and decreases due to dynamic dislocation recovery and annihilation expressed as $\frac{dU}{d\rho}\frac{d\rho^{-}}{dt}$. By identical transformation, the total mechanical work done on the system can be represented by a sum of two components $\sigma\frac{d\varepsilon}{dt} = \sigma_0\frac{d\varepsilon}{dt} + (\sigma - \sigma_0)\frac{d\varepsilon}{dt}$, where the first term is attributed to the fully dissipative process of dislocation production, glide and annihilation without accumulation (in this process, the energy dissipation equals the expended work) in the ideal elastic-viscoplastic material with the initial hardening σ_0, while the second term describes the strain hardening process commencing with strain hardening from σ_0.

Thus, it is convenient and physically reasonable to split Eq. (12) into a set of two coupled equations describing the preserving and dissipative flows as:

$$\begin{cases} \dfrac{\delta Q}{dt} = \dfrac{dU}{d\rho}\dfrac{d\rho^{-}}{dt} + \sigma_0\dfrac{d\varepsilon}{dt} \\ \dfrac{dU}{d\rho}\dfrac{d\rho^{+}}{dt} = (\sigma - \sigma_0)\dfrac{d\varepsilon}{dt} \end{cases} \tag{13}$$

The first equation in this pair says that heat is produced by the internal energy change due to dynamic dislocation recovery and the dissipative mechanism associated with the viscous flow with the friction caused by pre-existing dislocations, which control the yield stress σ_0. Within the KM approximation, the term $\frac{d\rho^{+}}{dt} = \frac{k_1}{b}\sqrt{\rho}M\dot{\varepsilon}$ and $\frac{d\rho^{-}}{dt} = k_2\rho M\dot{\varepsilon}$. Thus, by eliminating $\frac{dU}{d\rho}$ from the first equation in (13) and bearing in mind that the stored power density P_s is found as the difference between the total expended mechanical power density $P_e = \frac{\delta A}{dt} = \sigma\dot{\varepsilon}$ and the dissipated power density P_d at the same accumulated strain, the following expressions are obtained for P_d and P_s as:

$$P_s = \frac{dE_s}{dt} = \frac{\dot{\varepsilon}}{\sigma_S}(\sigma - \sigma_0)(\sigma_S - \sigma) \tag{14}$$

and

$$P_d = P_e - P_s = \sigma\dot{\varepsilon} - \frac{\dot{\varepsilon}}{\sigma_S}(\sigma - \sigma_0)(\sigma_S - \sigma) \tag{15}$$

These simple expressions for P_d and P_s are insightful as they bridge both quantities to the dislocation kinetics through the parameter σ_S that, in turn, is expressed by k_1 and k_2, Eq. (7). The stored energy density can be obtained as (see Ref. [79] for an alternative derivation):

$$E_s(\sigma) = \frac{\widetilde{\varepsilon}}{2\sigma_S}(\sigma - \sigma_0)^2 \tag{16}$$

One can easily verify this expression by taking the time derivative dE_s/dt, and, then, using Eq. (9), Eq. (15) is reproduced straightforwardly. Equation (16) establishes the functional relation between E_s and flow stress σ, i.e., $E_s \sim (\sigma - \sigma_0)^2$, which is regularly seen in the above-mentioned early models, even though they start from different premises. This ubiquitous relation is well supported experimentally, as will be discussed in what follows (c.f., also Note 10 in Supplementary Materials and Fig. S13, where the experimental results reported by other investigators for pure copper are compiled for comparison). Furthermore, Eq. (16), after elementary algebraic transformations using Taylor's equation (4), can be approximated in terms of the dislocation density as (see Ref. [79]):

$$E_s \approx \frac{\alpha G b^2}{k_1}(\rho - \rho_0) \tag{17}$$

from which it plausibly appears that the energy storage E_s is linear on the increment of the dislocation density $\Delta\rho = \rho - \rho_0$ and is related to the dislocation production rate.

4.3. AE model

The two experimentally measured quantities, which characterise the evolution of dislocation-related AE sources, derived from the AE spectra analysis, are of prime interest - AE power and median frequency. These two fundamentally independent properties of the AE fluxes need to be interrelated to the evolution of the defect microstructure under stress. To this end, inspired by pioneering works of Gillis [80], Tetelman [81] and others [26,27,82,83], we consider AE to be caused by heterogeneous dislocation motion as described in a purely phenomenological model proposed by Vinogradov et al. [84,85].

The entire modelling approach is firmly footed on the common observation that AE fluxes during plastic deformation are represented by randomly fluctuating data, c.f., Fig. 3, which suggests that dissipation of the total mechanical work of plastic deformation stems from local independent stress relaxation processes (events) generating acoustic emissions. Since a mobile dislocation interacts with obstacles of various kinds and different strengths during motion, it experiences considerable fluctuations of the effective local stress, giving rise to the stochastic nature of local stress relaxation. Therefore, the AE time series represented by the output voltage $U(t)$ of the AE sensor appears as a continuous random process, which can be described by the first-order autoregressive Ornstein-Uhlenbeck process satisfying the following stochastic differential equation:

$$\frac{dU}{dt} = -\frac{U}{\tau_r} + \widetilde{\varepsilon}(t) \tag{18}$$

with Gaussian noise $\widetilde{\varepsilon}(t)$ on the right-hand side. Here τ_r denotes a characteristic relaxation time, which serves as a universal measure of temporal correlation between the individual events in the time series. Stochastic features of the Ornstein-Uhlenbeck process are comprehensively determined by the Lorentzian-type power spectral density function [86]:

$$G(f) = 4\sigma_{UU}^2\frac{f_c}{f_c^2 + 4\pi^2 f^2} \sim P_{AE}\frac{f_c}{f_c^2 + 4\pi^2 f^2} \tag{19}$$

where σ_{UU}^2 - the variance of the AE signal - is a measure of the power of the AE random process and $f_c = 1/\tau_r$ is a characteristic frequency determining the effective width of the spectrum – the longer the relaxation time the smaller the f_c value and the narrower the spectrum, and vice versa. Using the definition of the median frequency f_m, one can easily show that for the spectrum given by Eq. (19), $f_c = 2\pi f_m$ [38]. It is exactly for this reason that from among many conceivable frequency characteristics of the AE PSD, we have chosen the median frequency as the preferred companion to the power (note that both properties independently enter Eq. (19)). An increase in the f_m value signifies a decrease in the correlation time in a set of successive AE events. Conversely, a decrease in f_m means increasing the influence of past events on the

present and the future. It has been suggested [85] that the relaxation time τ_r pertinent to dislocation kinetics during uniform elongation can be related to the dislocation mean free path $\langle\Lambda\rangle$ and the average dislocation velocity $\langle v\rangle$:

$$\tau_r = \langle\Lambda\rangle/\langle v\rangle \tag{20}$$

Using Orowan's expression for the plastic strain rate

$$\dot{\varepsilon} = M\rho_m b\langle v\rangle \tag{21}$$

with ρ_m - the mobile dislocation density, and Taylor equation (4), and noticing that for virtually all dislocation configurations emerging in the course of plastic deformation, $\langle\Lambda\rangle$ scales with the dislocation density as $\langle\Lambda\rangle \sim 1/\sqrt{\rho}$ [87], the median frequency is determined as:

$$f_m \sim \frac{M\dot{\varepsilon}}{b\rho_m}\sqrt{\rho} = K_f\frac{\dot{\varepsilon}}{\rho_m}\sigma \tag{22}$$

Here K_f combines all constants from Eqs. (4) and (21), and also incorporates the coefficient accounting for the AE transfer function. Thus, the model predicts that the AE median frequency f_m should be linear in the flow stress $f_m \sim \sqrt{\rho} \sim \sigma$ and strain rate $f_m \sim \dot{\varepsilon}$ as long as plastic deformation is uniform.

The emitted AE power can now be calculated as follows [84]. The energy dissipated by the elementary displacement of a dislocation segment of length L under the action of a Peach-Köhler force F_{PK} per unit time is estimated as:

$$\frac{p_{AE}}{L} \sim \frac{F_{PK}}{L}v = \tau b\dot{\Lambda} \tag{23}$$

where $v = \dot{\Lambda}$ denotes the instantaneous free-flight velocity acquired by a dislocation during the elementary glide with the mean travel inter-obstacle distance Λ. Using the scaling relation $\langle\Lambda\rangle \sim 1/\sqrt{\rho}$ in Eq. (23) together with Taylor and Orowan equations again and summing up the independent contributions from individual dislocations (23) moving in the volume V^* to the cumulative AE power P_{AE}, the expression for P_{AE} was obtained in Ref. [84] as

$$P_{AE} \sim \dot{\varepsilon}\theta\Lambda\rho_m V^* = K_{AE}\rho_m\frac{\theta}{\sigma}\dot{\varepsilon} = K_{AE}\rho_m\frac{\dot{\sigma}}{\sigma} \tag{24}$$

The last expression predicts proportionality between the experimentally measurable quantities $-P_{AE}$ and the reduced hardening rate $\dot{\sigma}/\sigma = \frac{d\ln\sigma}{dt}$, provided ρ_m is constant. The coefficient K_{AE}, similarly to K_f, lumps all constants, including the AE transfer function coefficient.

5. Verification of the model, discussion, and implications

5.1. Strain hardening – comparison between the model and experimental data

The predictive power of the KM model has been undeniably demonstrated on many occasions. For the purpose of the present work, the values of the KM model parameters have to be evaluated. Results of fitting the experimental data to the KM equation (8) are shown graphically in Fig. 2 by solid red lines superimposed with the $\sigma(\varepsilon)$ curves for respective materials. The obtained in this way model parameters are listed in Table 2. The agreement between the model and experimental true stress-strain curves is very good up to the point of macroscopic instability where the neck sets in at a critical necking strain ε_N. This critical strain limiting the validity of all forthcoming considerations can be determined from the experimental data according to the Considère criterion [88].

$$\left.\frac{\partial\sigma}{\partial\varepsilon}\right|_{\dot{\varepsilon}} = \sigma \tag{25}$$

From the true stress-strain curves and the corresponding strain hardening rate $\theta(\varepsilon)$ shown in Fig. S4 (Supplementary Materials), the necking strain ε_N was determined according to the last equation, and the corresponding necking points are marked on the diagrams shown in Fig. 2. By plugging Eqs. (8) and (9) for $\sigma(\varepsilon)$ and $\theta(\varepsilon)$, respectively, derived from the KM model into the Considère criterion (25), one obtains the model-predicted values for the necking instability strain (see Refs. [77,89] for the detailed discussion) as

$$\varepsilon_N^{KM} = \tilde{\varepsilon}\ln\left[\left(1-\frac{\sigma_0}{\sigma_S}\right)\left(1+\frac{1}{\tilde{\varepsilon}}\right)\right] \sim \tilde{\varepsilon} \tag{26}$$

A remarkable result is not only that the model approximated the stress-strain curves quite well but also that it reasonably predicts the occurrence of the necking instability: the experimentally determined necking strain ε_N and their model predictions ε_N^{KM} shown in Table 2 are in fair agreement with each other. Similarly, good agreement is observed for different strain rates used in the experimental session.

5.2. Dislocation storage and IRT measurements

Various strain hardening models reviewed in Ref. [7] converge at that the stored energy is a square form of stress $E_s \sim \sigma^2$ or, more generally, $E_s \sim (\sigma-\sigma_0)^2$, as it is also explicit in the present model, Eq. (16). Fig. 7 supports these common observations, illustrating the $E_s \sim (\sigma-\sigma_0)^2$ type relation for the Cu–Zn specimens tested at $\dot{\varepsilon} = 3\times10^{-2}$ s^{-1}. The linear regression of the experimental data exhibits the straight line in excellent agreement with model predictions (see Ref. [79], where similar findings have been reported and discussed in more detail for 316L austenitic steel). Besides, it is important to notice that the presented results are in fair agreement with earlier findings reported for pure copper, e.g. Refs. [67–71], (see also Fig. S8 and Note 8 in Supplementary Materials).

Despite the difference in experimental setups, equipment and calculation methods used by different investigators, the observed linearity between E_s and σ^2 is apparently the most prominent and common result, which is plausibly explained by the proposed model through Eq. (16).

During loading at low homologous temperatures, almost all stored energy is attributed to the accumulation of dislocations generated during plastic straining [90] and inter-dislocation interactions affecting the overall stored energy [91]. Considering that for virtually all conceivable dislocation configurations, the dislocation contribution to flow stress

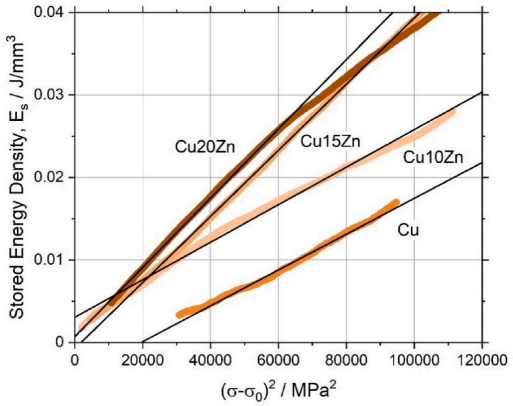

Fig. 7. Stored energy as a function of square flow stress $E_s \sim (\sigma-\sigma_0)^2$ for the alloys (closed circles represent experimental data, and black straight lines are the results of linear regression).

scales with the square root of the total dislocation density $\sigma \sim \sqrt{\rho}$, Eq. (4), the generally expected has a form (see Refs. [7,68,92,93] for multiple examples)

$$E_s = A \cdot G b^2 \rho \tag{27}$$

with A - constant (or a weakly dependent on ρ function) depending on the employed model of the energy of dislocations. In the simplest case, the equation in this form can be postulated by assuming the summation of the self-energies of individual dislocations; in this way, neglecting the inter-dislocation interactions, the stored energy density is expressed as [94]:

$$E_{\text{disl}} = \frac{Gb^2\rho}{4\pi\kappa}\left(\ln\frac{r}{r_0}\right) + E_{\text{core}} \tag{28}$$

with $\kappa = 1, \quad or \quad 1-\nu$ for screw or edge dislocations, respectively (ν denotes the Poisson ratio), and r and r_0 refer to the outer and inner cut-off, and E_{core} describes the core energy of the dislocation. The comparable to (27) equation relating the stored energy to the dislocation density (17) derived from Eq. (16) has the same structure. The favourable comparison of the proposed model against the early models based on Eqs. 27 and 28 and their modifications with different forms of A reviewed in Ref. [7] has been carried out carefully in Ref. [79]. It was also demonstrated that the proposed model expressions for the stored and dissipated energy and power, such as Eqs. (15) and (16), with the coefficients k_1 and k_2 derived from the stress-strain curves for 316L austenitic stainless steel, were in excellent agreement with the experimental values measured by infrared thermography.

5.3. AE model verification and discussion

The proposed in the previous section phenomenological modelling approach is very transparent and intuitive. However, only limited verification has been conducted so far. The fact that during strain hardening of metals and alloys, the AE spectral density shifts to a high-frequency domain has been noticed in the early works by Hatano [95], Rouby and Fleischmann [96] and other researchers. However, the rational link between this behaviour and the evolution of the dislocation structure has been provided only recently in Ref. [85] so far. A considerable drop in the f_m magnitude at the onset of yielding has been observed consistently for several pure polycrystalline metals and alloys, including Cu and Al [85], TRIP and TWIP steels [32,97], as well as in Ni, Ag, 316L steel, Inconel-625 alloy (unpublished results from the author's group). This result is plausibly explained in the present model through Eq. (22) by the rapid multiplication of mobile dislocations at the onset of plastic yielding. Besides, the common result for many observations performed on various materials is that as long as the deformation occurs homogeneously, the magnitude of f_m is proportional to the flow stress σ. Irregular variations of the f_m values up to about 10% strain observed in the present work for Cu–Zn alloys, c.f., Fig. 5, are explained by the strong spatial inhomogeneity of the onset plastic flow in the specimens tested as has been mentioned above and

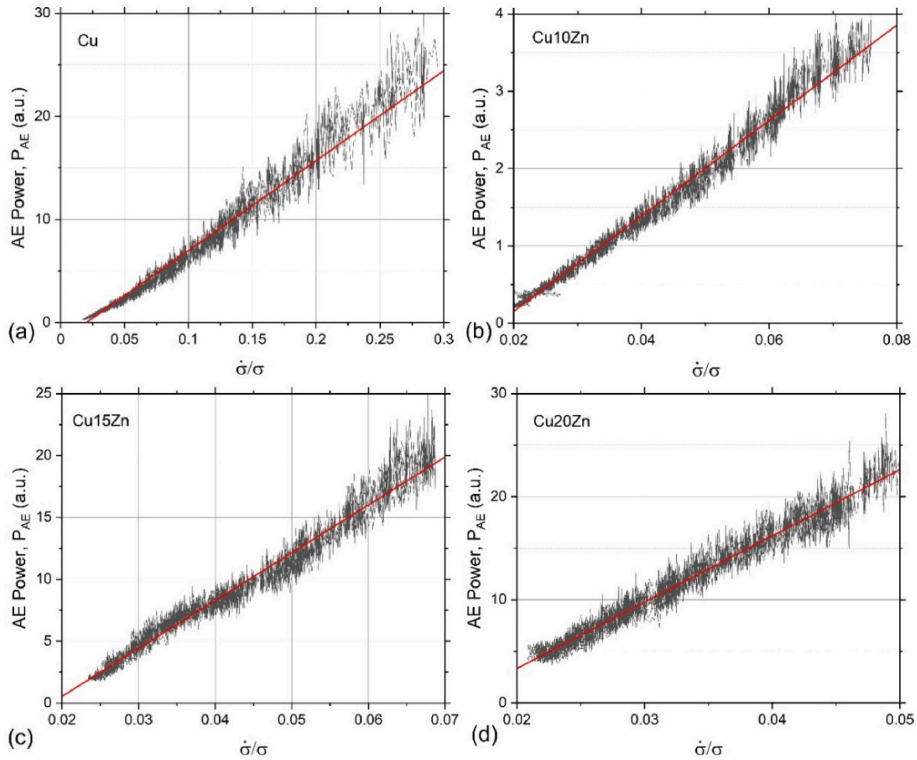

Fig. 8. AE power plotted against the reduced stress rate $\dot{\sigma}/\sigma$ during the unform deformation stage of Cu (a), Cu–10Zn (b), Cu–15Zn (c) and Cu–20Zn (d). Solid red lines represent the result of linear regression that compares favourably with the model prediction, Eq.(24). (For interpretation of the references to colour in this figure legend, the reader is referred to the Web version of this article.)

illustrated in Supplementary Materials, Fig. S7).

Moreover, although the linear relation between P_{AE} and $\dot{\varepsilon}$ has long been recognised, e.g. Refs. [85,95,98], the anticipated proportionality $P_{AE} \sim \dot{\sigma}/\sigma$ has been reported only for pure copper so far [84]. Fig. 8 fully supports the proposed model by showing that the $P_{AE} \sim \dot{\sigma}/\sigma$ relationship holds during uniform deformation for all Cu–Zn alloys tested. It is important that in the above considerations based on Eq. (24) we have tacitly assumed that the ρ_m value remains nearly constant during most of the uniform deformation stage, i.e., that ρ_m tends to saturate (or increases only a little with strain) shortly after initial accumulation. This is a strong yet not unreasonable assumption, which has been frequently used for monotonic testing at moderate strain rates and temperatures [99] and which is indirectly supported by strain rate change experiments [100] (see also the insightful discussion by Argon in Ref. [101]). In the present experiments, this assumption is corroborated by the observed empiric $f_m \sim \sigma$ relation, which would not hold otherwise, i.e., if the condition $\rho_m = const$ is not satisfied (c.f., at the very beginning of plastic yielding in the studied alloys).

Furthermore, rewriting Eq. (22) in a form convenient for verification as $f_m - f_0 = K_f \frac{\dot{\varepsilon}}{\rho_m} \sigma$ (with f_0 - the experimentally determined initial median frequency depending on the frequency response of the transducer and the initial yielding conditions), one can notice that the product

$$P_{AE}\,(f_m - f_0) = K_{AE} K_f \dot{\sigma}\dot{\varepsilon} = K_{AE} K_f \theta \dot{\varepsilon}^2 \tag{29}$$

eliminates uncertainty with the unknown density of mobile dislocations and offers an alternative way of independent experimental verification of the entire approach. The plot displaying the dependence of $P_{AE}\,(f_m - f_0)$ on $\theta\dot{\varepsilon}^2$ is shown in Fig. 9. The impressive result is that the linear trend is evident despite notable experimental scatter (each point on the plot corresponds to one 4k AE realisation of 2 ms duration, for which P_{AE} and f_m are calculated). We should notice that the scatter in the results shown in Fig. 9 is not surprising, considering the random nature of the AE signal reflected in P_{AE} and f_m on the one hand and the uncertainty associated with the digital differentiation of stress-strain data and fluctuations of $\dot{\varepsilon}$ on the other.

Thus, we do believe that, backed by the experimental evidence obtained from different independent approaches reported above, the present model has a unique potential to fulfil the long-standing dream of bridging the AE phenomenon with dislocation kinetics in an explicit and verifiable way. Besides, there are several new, intriguing aspects of the proposed approach. By plugging the expression for the stress and strain hardening rate derived within the KM model, Eqs. (8) and (9), into Eq. (29), and using the relation $\sigma_S \gg \sigma_0$ which is ubiquitously fulfilled for annealed materials, we obtain

$$P_{AE}\,(f_m - f_0) = K_{AE} K_f \theta \dot{\varepsilon}^2 = K_{AE} K_f \dot{\varepsilon}^2 \frac{\sigma_S - \sigma_0}{\dot{\varepsilon}} \exp\left(-\frac{\varepsilon}{\dot{\varepsilon}}\right) \approx$$
$$\approx K_{AE} K_f \dot{\varepsilon}^2 \frac{\sigma_S}{\dot{\varepsilon}} \exp\left(-\frac{\varepsilon}{\dot{\varepsilon}}\right) = \frac{1}{2} K_{AE} K_f M^2 \alpha G \dot{\varepsilon}^2 k_1 \exp\left(-\frac{k_2 M \varepsilon}{2}\right) = K \exp\left(-\frac{k_2 M \varepsilon}{2}\right) \tag{30}$$

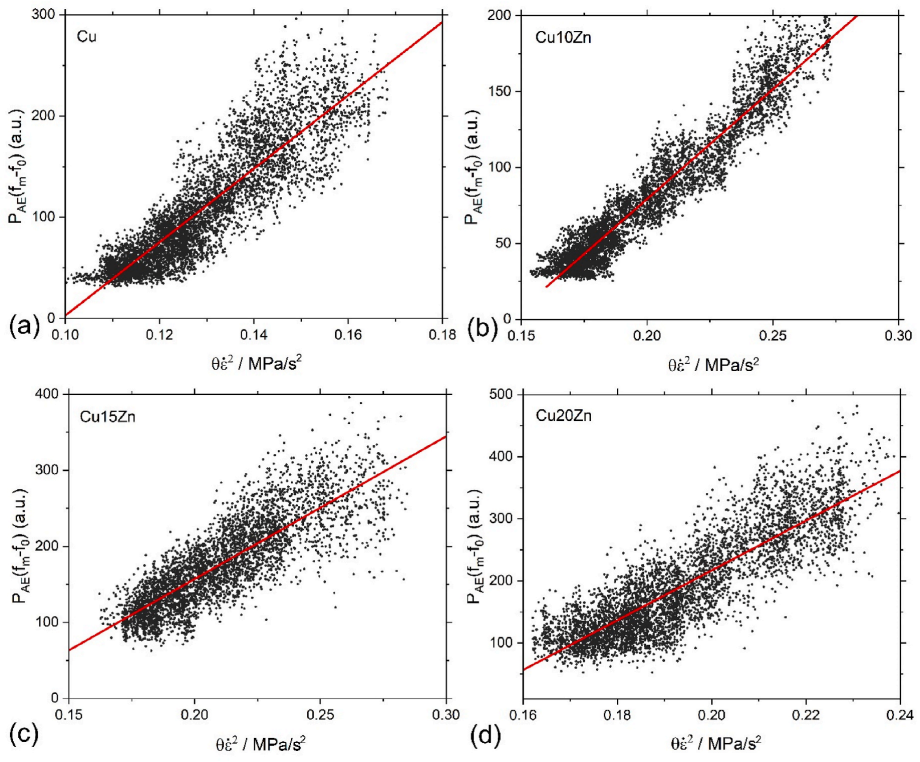

Fig. 9. *A product $P_{AE}(f_m - f_0)$ plotted against $\theta\dot{\varepsilon}^2$ according to Eq.* (29) estimated *during the uniform deformation stage of Cu (a), Cu–10Zn (b), Cu–15Zn (c) and Cu–20Zn (d). Solid red lines represent the result of linear regression that compares favourably with the model prediction, Eq.*(29). (For interpretation of the references to colour in this figure legend, the reader is referred to the Web version of this article.)

with $K = \frac{1}{2}K_{AE}K_f M^2 \alpha G \dot{\varepsilon}^2 k_1$ - constant for the constant strain rate testing conditions. Taking the logarithm from both sides of the last equation, one finds that

$$\ln(P_{AE} \cdot (f_m - f_0)) = \ln(K) - \frac{k_2 M \varepsilon}{2} \tag{31}$$

i.e., $\ln(P_{AE} \cdot (f_m - f_0))$ should be a linear function in ε. By plotting this logarithmic term as a function of strain, one can see, Fig. 10, that during the strain hardening stage up to the necking point, the relation predicted by Eq. (31) holds quite well. The most intriguing inference stemming from Eq. (31) is that the slope of the linear regression lines in Fig. 10 is supposed to be proportional to the key parameter of the KM model - k_2. Let us also note that the intercept of the straight line at Y-axis is, in principle, dependent on k_1. However, the value of K in Eq. (30) also incorporates coefficients K_{AE} and K_f, which are hard to determine experimentally without a specially designed calibration procedure, which has yet to be developed.

From the linear regression analysis applied to the AE data shown in Fig. 10, the k_2 values were estimated as summarised in Table 2. For all materials tested, the values of k_2 evaluated in this way appear to be in the reasonable range, albeit somewhat overestimated (by a factor of 2 or so) if compared to those obtained by the least square KM approximation to the stress-strain curves. The result is nonetheless surprising, considering the great impact of experimental conditions on the general AE measurements and the lack of any specific measures to optimise or calibrate these measurements in the present work. The most influencing factor, in our opinion, is the sensor response, for which there is a lot to be desired to get it more sensitive, wideband, and flat. Nonetheless, the exciting and promising general conclusion can be drawn that, in principle, if the AE measurements are refined to the state when the dislocation recovery rate can be reliably calculated from the AE data, this method can have a unique capacity to predict the imminent strain localisation as follows from the relationship between k_2 and ε_N, which is expected from the model, Eq. (26), and verified experimentally in the present work as well as in early publications [76,77,79,89].

Although, as discussed above, the other model parameter k_1 cannot be simply recovered from the AE data solely, the companion method - infrared thermography – can be used to this end. Let us rearrange Eq. (15) for the dissipated heat power as

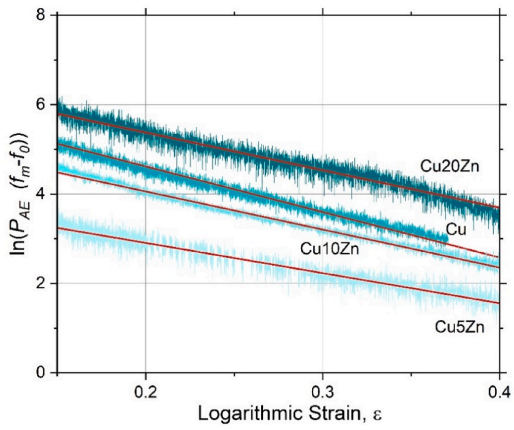

Fig. 10. $\ln(P_{AE} \cdot (f_m - f_0))$ versus logarithmic strain illustrating the linear relation anticipated from Eq. (31) for Cu–Zn alloys tested. *Solid red lines represent the result of linear regression that compares favourably with the model according to Eq.* (31). (For interpretation of the references to colour in this figure legend, the reader is referred to the Web version of this article.)

$$\frac{P_d}{\dot{\varepsilon}} = \sigma_0 - \frac{\sigma_0 \sigma}{\sigma_S} + \frac{\sigma^2}{\sigma_S} \tag{32}$$

By approximating the experimentally determined dependence $\frac{P_d}{\dot{\varepsilon}} = \frac{dE_d}{d\varepsilon}$ on the flow stress by Eq. (32), one can evaluate the saturation stress σ_S and then calculate k_1, provided the magnitude of k_2 is known from independent measurements. Fig. 11 shows the plots of the dissipated energy rate $\frac{dE_d}{d\varepsilon}$ vs flow stress with the superimposed results of non-linear curve fitting. The values of the saturation stresses σ_S and k_1 coefficients calculated from these approximations are shown in Table 2 and can be compared to those recovered from the stress-strain data. One can see that despite the simplicity of the model and the inevitable scattering in the experimental data, the k_1 values obtained in this way agree favourably with KM model predictions. This is a remarkable result not only in that it strongly supports the assumptions made in the present approach but also in that the IRT method is shown for the first time to be able to recover the principal numeric parameter characterising the dislocation kinetics with quite a reasonable accuracy. It also indirectly supports our conclusion that the difference between the AE-measured and KM-based k_2 values is not related to the model itself but is rather attributed to the AE measurements.

6. Summary and conclusions

As the primary outcome of this work, it can be concluded that the combination of two in situ techniques – high-resolution infrared thermography (IRT) and acoustic emission (AE) - opens a way for a quantitative assessment of the intimate details of the evolution of the dislocation ensemble through the access to its kinetic properties.

Bonded by the Kocks-Mecking constitutive modelling philosophy, the analytical and experimental solutions are proposed for the evaluation of the energy dissipated via heat and acoustic emissions during tensile plastic deformation. Using the IRT and AE measurements, the developed models have been verified in several independent ways, furnishing strong support for the entire approach and approximations made. To demonstrate the power of the described unified approach, the Kocks-Mecking parameters controlling the dislocation kinetics and strain hardening, k_1 and k_2, have been recovered for the first time from independent full-field infrared and acoustic emission measurements, respectively. Excellent agreement with model predictions has been observed in the results of tensile testing of Cu–Zn alloys with notably different stacking fault energies and correspondingly different kinetics of dislocations and deformation microstructures. Due to the versatility of the approach, the model in its present form can be applied to a wide range of structural materials with the dislocation-mediated plasticity for which the main conclusions remain unaltered.[2] Other than the simplistic single internal variable Kocks-Mecking strain hardening models can be conceptually employed within the proposed methodological framework, albeit with the loss of analytical transparency.

Thus, the synchronised IRT and AE methods equipped with the proposed analytical model solutions bring benefits as a powerful toolset for unveiling the quantitative details of the evolution of the dislocation structure of the material during plastic flow on various scales. The proposed analytical model solutions increase the robustness and predictive capability of this toolset and put it in a sharper focus as a contemporary technique that permits quantitative evaluation of the dislocation kinetics in situ.

As a future scope, it is essential to improve the AE sensing technique by utilising the transducers with a broader band and flatter frequency response (an everlasting wish of AE practitioners …) and designing a

[2] The same authors have tested pure nickel, aluminium, silver, TWIP and TRIP steels, 316L steel and Inconel alloy and found generally good agreement with the proposed model. The results will be published elsewhere.

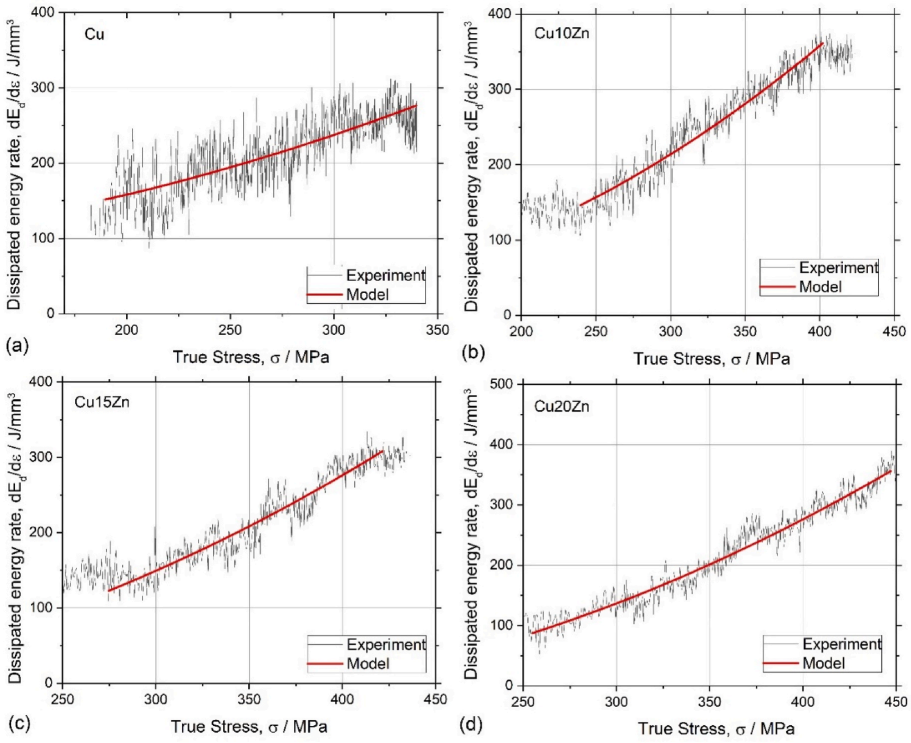

Fig. 11. *Dissipated energy rate $dE_d/d\varepsilon$ vs flow stress for materials tested: (a) Cu, (b)Cu–10Zn, (c) Cu–15Zn and (d) Cu–20Zn. The solid red lines represent the non-linear approximation by the Eq.*(32). (For interpretation of the references to colour in this figure legend, the reader is referred to the Web version of this article.)

specific calibration procedure to measure the characteristic spectral frequencies more precisely.

CRediT authorship contribution statement

A. Sendrowicz: Conceptualization, Methodology, Software, Validation, Visualization, Investigation, Writing - original draft, Writing - review & editing. **A.O. Myhre:** Methodology, Investigation, Writing – original draft, Writing – review & editing, Visualization, Writing – original draft, Writing – review & editing, Visualization, Writing – original draft. **A.V. Danyuk:** Investigation. **A. Vinogradov:** Conceptualization, Visualization, Supervision, Investigation, Writing - original draft, Writing - review & editing.

Declaration of competing interest

The authors declare that they have no known competing financial interests or personal relationships that could have appeared to influence the work reported in this paper.

Data availability

Data will be made available on request.

Acknowledgements

Internal funding provided by the Department of Mechanical and Industrial Engineering of NTNU is appreciated. The partial support by the Research Council of Norway, Project No. 294739, Safe Pipelines for Hydrogen Transport (HyLINE) is gratefully acknowledged.

The authors would like to thank Wieland-Werke AG (Germany) for providing the materials critical for this work, and Berit Vinje Kramer, who was of great help during laboratory activities related to sample preparation. Special thanks go to Profs Y. Estrin and I. Yasnikov for their encouraging interest and stimulating discussions.

Appendix A. Supplementary data

Supplementary data to this article can be found online at https://doi.org/10.1016/j.msea.2022.143969.

References

[1] W.S. Farren, G.I. Taylor, Proceedings of the Royal Society of London. Series A 107 (1925) 422–451.
[2] G.I. Taylor, H. Quinney, Proceedings of the Royal Society of London. Series A 143 (1934) 307–326.
[3] B. Welber, Journal of Applied Physics 23 (1952) 876–881.
[4] F.R.N. Nabarro, Theory of Crystal Dislocations, Clarendon Press, Oxford, 1967.
[5] J.J. Gilman, Micromechanics of Flow in Solids, McGraw-Hill, New York ; London, 1969.
[6] J.E. Kaiser, München Technische Hochschule, 1950. München, FRG.
[7] M.B. Bever, D.L. Holt, A.L. Titchener, Progress in Materials Science 17 (1973) 5–177.
[8] W. Oliferuk, M. Maj, Materials Science and Engineering: A 462 (2007) 363–366.
[9] W. Oliferuk, M. Maj, European Journal of Mechanics - A/Solids 28 (2009) 266–272.
[10] A. Chrysochoos, Quantitative InfraRed Thermography Journal 9 (2012) 193–208.

[11] A. Chrysochoos, H. Louche, International Journal of Engineering Science 38 (2000) 1759–1788.
[12] H. Louche, A. Chrysochoos, Materials Science and Engineering A 307 (2001) 15–22.
[13] A. Risitano, D. Corallo, E. Guglielmino, G. Risitano, L. Scappaticci, Frattura ed Integrita Strutturale 11 (2017) 202–215.
[14] C. Wang, A. Blanche, D. Wagner, A. Chrysochoos, C. Bathias, International Journal of Fatigue 58 (2014) 152–157.
[15] J. Hodowany, G. Ravichandran, A.J. Rosakis, P. Rosakis, Exp. Mech. 40 (2000) 113–123.
[16] P. Rosakis, A.J. Rosakis, G. Ravichandran, J. Hodowany, Journal of the Mechanics and Physics of Solids 48 (2000) 581–607.
[17] D. Macdougall, Exp. Mech. 40 (2000) 298–306.
[18] S. Dumoulin, H. Louche, O.S. Hopperstad, T. Børvik, European Journal of Mechanics - A/Solids 29 (2010) 461–474.
[19] D. Rittel, A.A. Kidane, M. Alkhader, A. Venkert, P. Landau, G. Ravichandran, Acta Materialia 60 (2012) 3719–3728.
[20] R. De Finis, D. Palumbo, U. Galietti, Fatigue and Fracture of Engineering Materials and Structures 42 (2019) 267–283.
[21] D. Palumbo, R. De Finis, F. Ancona, U. Galietti, Engineering Fracture Mechanics 181 (2017) 65–76.
[22] G. Meneghetti, M. Ricotta, G. Pitarresi, International Journal of Fatigue 125 (2019) 149–160.
[23] A. Risitano, G. Risitano 36 (2013) 631–639.
[24] M. Ricotta, G. Meneghetti, B. Atzori, G. Risitano, A. Risitano, Metals 9 (2019) 677.
[25] P.P. Gillis, Materials Research and Standards 11 (1971) 11–&.
[26] N. Kiesewetter, Scripta Metallurgica 8 (1974) 249–252.
[27] K. Ono, Acoustic emission arising from plastic deformation and fracture, in: K. Ono (Ed.), Fundamentals of Acoustic Emission, Univeristy of California, CA, UCA, 1979.
[28] A. Vinogradov, I.S. Yasnikov, Y. Estrin, Physical Review Letters 108 (2012), 205504.
[29] A. Vinogradov, A.V. Danyuk, D.L. Merson, I.S. Yasnikov, Scripta Materialia 151 (2018) 53–56.
[30] A. Vinogradov, E. Vasilev, M. Seleznev, K. Máthis, D. Orlov, D. Merson, Materials Letters 183 (2016) 417–419.
[31] A. Weidner, A. Vinogradov, M. Vollmer, P. Krooß, M.J. Kriegel, V. Klemm, Y. Chumlyakov, T. Niendorf, H. Biermann, Acta Materialia 220 (2021), 117333.
[32] A. Vinogradov, A. Lazarev, M. Linderov, A. Weidner, H. Biermann, Acta materialia 61 (2013) 2434–2449.
[33] C.B. Scruby, H.N.G. Wadley, J.J. Hill, Journal of Physics D: Applied Physics 16 (1983) 1069–1083.
[34] H. Baker, ASM international. Alloy phase diagram committee, in: ASM International. Handbook Committee., Alloy Phase Diagrams, ASM International, Materials Park, Ohio, 1992.
[35] A. Sendrowicz, A.O. Myhre, S.W. Wierdak, A. Vinogradov, Applied Sciences 11 (2021) 6718.
[36] A. Sendrowicz, A.O. Myhre, I.S. Yasnikov, A. Vinogradov, Acta Materialia 237 (2022), 118190.
[37] E. Pomponi, A. Vinogradov, Mech. Syst. Signal Proc. 40 (2013) 791–804.
[38] A.V. Vinogradov, V. Patlan, S. Hashimoto, Philosophical Magazine A 81 (2001) 1427–1446.
[39] A. Vinogradov, D.L. Merson, V. Patlan, S. Hashimoto, Materials Science and Engineering A 341 (2003) 57–73.
[40] A. Vinogradov, M. Nadtochiy, S. Hashimoto, S. Miura, Materials Transactions JIM 36 (1995) 426–431.
[41] S.I. Wright, M.M. Nowell, D.P. Field, Microscopy and Microanalysis 17 (2011) 316–329.
[42] C.B. Carter, I.L.F. Ray, The Philosophical Magazine: A Journal of Theoretical Experimental and Applied Physics 35 (1977) 189–200.
[43] C.B. Carter, I.L.F. Ray, The Philosophical Magazine: A Journal of Theoretical Experimental and Applied Physics 29 (1974) 1231–1235.
[44] A. Howie, P.R. Swann, The Philosophical Magazine: A Journal of Theoretical Experimental and Applied Physics 6 (1961) 1215–1226.
[45] P.G.J. Gallagher, Y.C. Liu, Acta Metallurgica 17 (1969) 127–137.
[46] A. Rohatgi, K.S. Vecchio, Materials Science and Engineering: A 328 (2002) 256–266.
[47] A. Rohatgi, K.S. Vecchio, G.T. Gray, Metall and Mat Trans A 32 (2001) 135–145.
[48] M.A. Meyers, O. Vöhringer, V.A. Lubarda, Acta Materialia 49 (2001) 4025–4039.
[49] A. Cottrell, Dislocations and Plastic Flow in Crystals, Clarendon Press, Oxford, 1953.
[50] J. Friedel, Dislocations, 1st English ed., Pergamon Press, Oxford, New York, 1964.
[51] M. Hatherly, A.S. Malin, Metals Technology 6 (1979) 308–319.
[52] P.T. Wakefield, M. Hatherly, Metal Science 15 (1981) 109–115.
[53] S. Mahajan, G.Y. Chin, Acta Metallurgica 21 (1973) 1353–1363.
[54] J.A. Venables, Journal of Physics and Chemistry of Solids 25 (1964) 693–700.
[55] N. Narita, J. Takamura, The Philosophical Magazine: A Journal of Theoretical Experimental and Applied Physics 29 (1974) 1001–1028.
[56] F.I. Grace, M.C. Inman, Metallography 3 (1970) 89–98.
[57] P.C.J. Gallagher, Metallurgical Transactions 1 (1970) 2429–2461.
[58] A. Korbel, Scripta Metallurgica 8 (1974) 609–612.
[59] M. Mayer, O. Vöhringer, E. Macherauch, Scripta Metallurgica 9 (1975) 1333–1339.
[60] J.M. Robinson, M.P. Shaw, International Materials Reviews 39 (1994) 113–122.
[61] M.M.K. Krishtal, K. A, A.A. Razuvaev, I.S. Demin, Deformation and Fracture of Materials 2008 (2008) 28–34.
[62] M.A. Lebyodkin, N.P. Kobelev, Y. Bougherira, D. Entemeyer, C. Fressengeas, T. A. Lebedkina, I.V. Shashkov, Acta Materialia 60 (2012) 844–850.
[63] I.V. Shashkov, M.A. Lebyodkin, T.A. Lebedkina, Acta Materialia 60 (2012) 6842–6850.
[64] A. Vinogradov, A. Lazarev, Scripta Materialia 66 (2012) 745–748.
[65] M.A. Krishtal, D.L. Merson, A.V. Katsman, M.A. Vyboyschchik, Phys Met Metallogr+ 66 (1988) 169–175.
[66] A.V. Danyuk, D.L. Merson, I.S. Yasnikov, E.A. Agletdinov, M.A. Afanasiev, A. Vinogradov, Lett. Mater. 7 (2017) 437–441.
[67] J.E. Bailey, Philosophical Magazine 8 (1963) 223–236.
[68] J.E. Bailey, P.B. Hirsch, Philosophical Magazine 5 (1960) 485–497.
[69] R.O. Williams, Acta Metallurgica 9 (1961) 949–957.
[70] A. Wolfenden, Acta Metallurgica 19 (1971) 1373–1377.
[71] J. Gil Sevillano, E. Aernoudt, Materials Science and Engineering 86 (1987) 35–51.
[72] U.F. Kocks, H. Mecking, Progress in Materials Science 48 (2003) 171–273.
[73] H. Mecking, U.F. Kocks, Acta Metallurgica 29 (1981) 1865–1875.
[74] H. Mughrabi, Current Opinion in Solid State and Materials Science 20 (2016) 411–420.
[75] M. Huang, P.E.J. Rivera-Díaz-del-Castillo, O. Bouaziz, S. van der Zwaag, IOP Conference Series: Materials Science and Engineering 3 (2009), 012006.
[76] I.S. Yasnikov, A. Vinogradov, Y. Estrin, Scripta Materialia 76 (2014) 37–40.
[77] I.S. Yasnikov, Y. Estrin, A. Vinogradov, Acta Materialia 141 (2017) 18–28.
[78] I.S. Yasnikov, Y. Kaneko, M. Uchida, A. Vinogradov, Materials Science and Engineering: A 831 (2022), 142330.
[79] A. Sendrowicz, A.O. Myhre, I.S. Yasnikov, A. Vinogradov, (under publication), (2022).
[80] P.P. Gillis, Dislocation Motions and Acoustic Emissions Acoustic Emission, ASTM International, West Conshohocken, PA, 1972.
[81] A.S. Tetelman, US-Japan Joint Symposium on Acoustic Emission, Japan Industrial Planning Association, 1972, pp. 1–46. English volume.
[82] K. Malen, L. Bolin, Physica Status Solidi B-Basic Research 61 (1974) 637–645.
[83] N. Kiesewetter, P. Schiller, Physica Status Solidi a-Applied Research 38 (1976) 569–576.
[84] A. Vinogradov, I.S. Yasnikov, D.L. Merson, Scripta Materialia 170 (2019) 172–176.
[85] A. Vinogradov, I.S. Yasnikov, Y. Estrin, Journal of Applied Physics 115 (2014), 233506.
[86] J.S. Bendat, A.G. Piersol, Random Data : Analysis and Measurement Procedures, third ed., Wiley, New York, 2000.
[87] D.L. Holt, Journal of Applied Physics 41 (1970) 3197–3201.
[88] A. Considère, Annales des ponts et chaussées, I sem, 1885, pp. 574–775.
[89] A. Vinogradov, I.S. Yasnikov, H. Matsuyama, M. Uchida, Y. Kaneko, Y. Estrin, Acta Materialia 106 (2016) 295–303.
[90] J. Humphreys, G.S. Rohrer, A. Rollett, Chapter 2 - the deformed state, in: J. Humphreys, G.S. Rohrer, A. Rollett (Eds.), Recrystallization and Related Annealing Phenomena, third ed., Elsevier, Oxford, 2017, pp. 13–79.
[91] M. Zaiser, A. Seeger, Long-range internal stresses, dislocation patterning and work-hardening in crystal plasticity, in: F.R.N. Nabarro, M.S. Duesbery (Eds.), Dislocations in Solids, Elsevier, 2002, pp. 1–100.
[92] M. Verdier, I. Groma, L. Flandin, J. Lendvai, Y. Bréchet, P. Guyot, Scripta Materialia 37 (1997) 449–454.
[93] V.L. Berdichevsky, Scripta Materialia 54 (2006) 711–716.
[94] J.P. Hirth, J. Lothe, Theory of Dislocations, second ed., Wiley, New York, 1982.
[95] H. Hatano, Journal of Applied Physics 47 (1976) 3873–3876.
[96] D. Rouby, P. Fleischmann, Physica Status Solidi a-Applied Research 48 (1978) 439–445.
[97] S. Martin, A. Weidner, C. Ullrich, C. Schimpf, M. Motylenko, R. Lehnert, H. Biermann, D. Rafaja, A. Vinogradov, Y. Estrin, Materials Characterization 184 (2022), 111667.
[98] R.M. Fisher, J.S. Lally, Canadian Journal of Physics 45 (1967) 1147–1159.
[99] W.G. Johnston, J.J. Gilman, Journal of Applied Physics 30 (1959) 129–144.
[100] J.T. Michalak, Acta Metallurgica 13 (1965) 213–222.
[101] A.S. Argon, Materials Science and Engineering 3 (1968) 24–32.

Article III supplementary material

Supplementary Materials

Dislocation Kinetics Explains Energy Partitioning during Strain Hardening: model and experimental validation by infrared thermography and acoustic emission

A. Sendrowicz, A. O. Myhre, A.V. Danyuk and A. Vinogradov

Materials Science and Engineering A (2022)

Note 1. Specimen's shape and dimensions

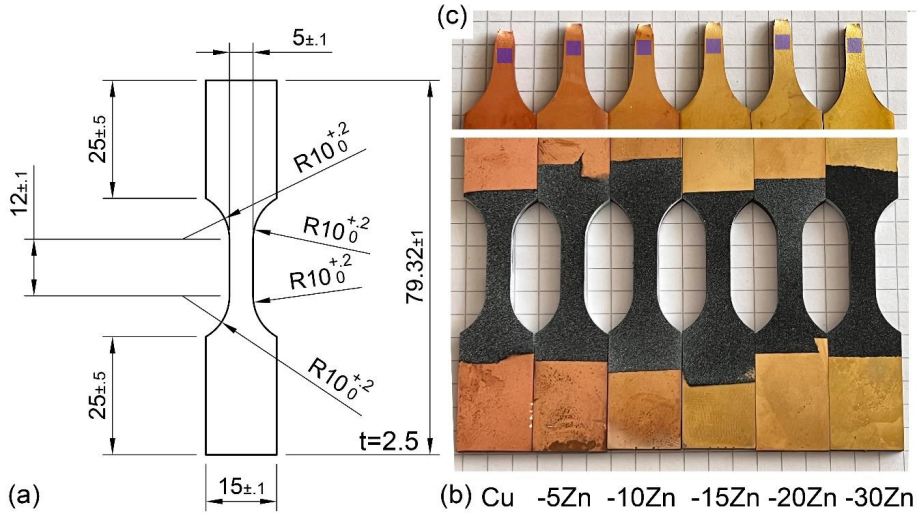

Figure S1. Specimen's shapes dimensions: (a) CAD drawing (b) a set of specimens with different Zn content and with a speckle pattern painted on the surface for DIC measurements and (c) fractured specimens with paint removed; the regions of interest (ROI) for SEM/EBSD examinations of the deformed microstructures are indicated in blue. The surface of the ROI was polished mechanically and, finally, by ion milling prior to SEM/EBSD observations.

Note 2. Experimental Setup and Basic Data Processing Flowchart

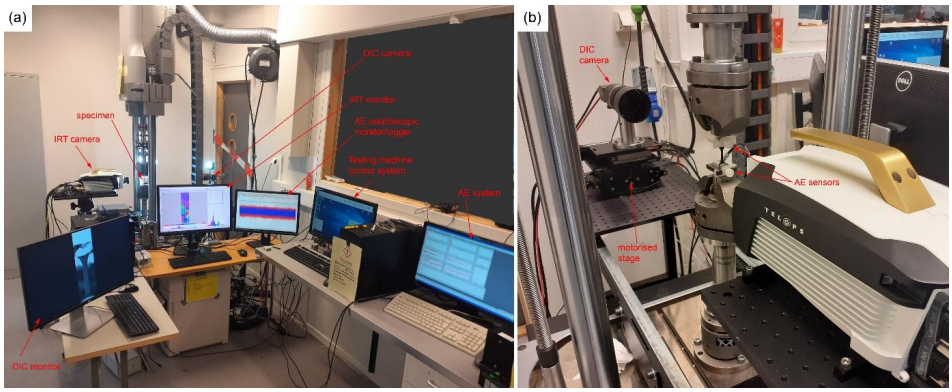

Figure S2. Experimental setup; (a) a general view and (b) a view of the specimen area; see [1] for the detailed description.

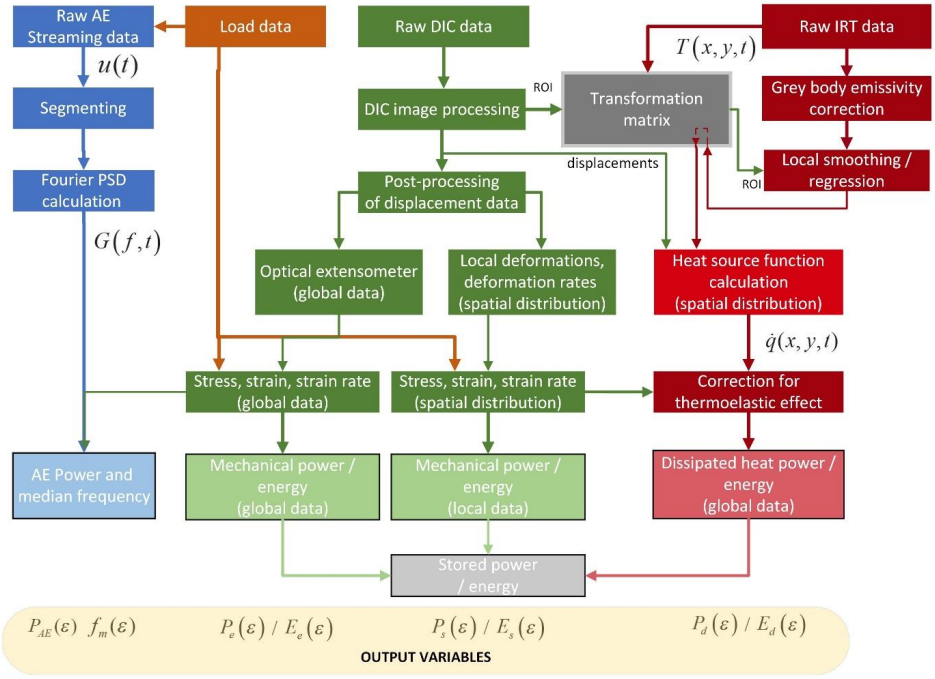

Figure S3. A flowchart illustrating the essential steps of data processing and interactions between different measurement techniques

Note 3. Essentials of infrared data processing

The synergy is obatined from the use of DIC data to track the changes in the IRT images with respect to strain. To this end, the transformation matrix was found between the DIC and IRT images, assuming the deformation pattern is equal on the opposite surfaces during uniform elongation. This procedure and the result are illustrated in Figure S4 below, where images from both measureing cameras are presneted, and the rightmost image shows a superposition of two images. Once the transformation matrix is found, the ROI can be mapped from the DIC optical domain to the IRT temperature domain.

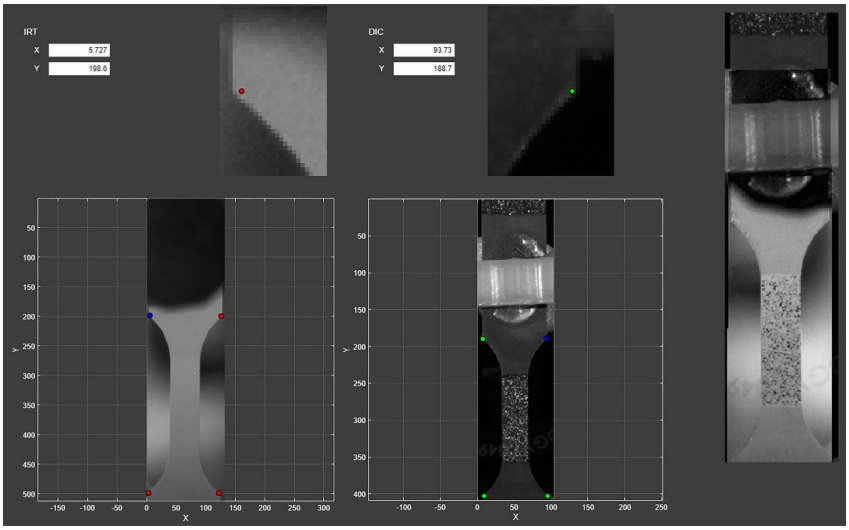

Figure S4. A screenshot illustrating the essential data processing step - calculation of the transformation matrix between the DIC and IRT images (processing software has been developed by A. Sendrowicz)

ROI is limited to the gauge part of the specimen, and the local regression smoothing method is performed in the present work to find the second spatial derivative necessary to solve the heat equation (Eq. (1) in the main text). Figure S5 illustrates this process in the original Matlab-based software. Data from a small circular region surrounding a point of interest is used to perform a non-linear regression and a second-degree polynomial surface represents the local data. The second spatial derivative of the smooth surface is then calculated to find the Laplacian of the temperature field at the point of interest. The process is repeated for all the points in ROI.

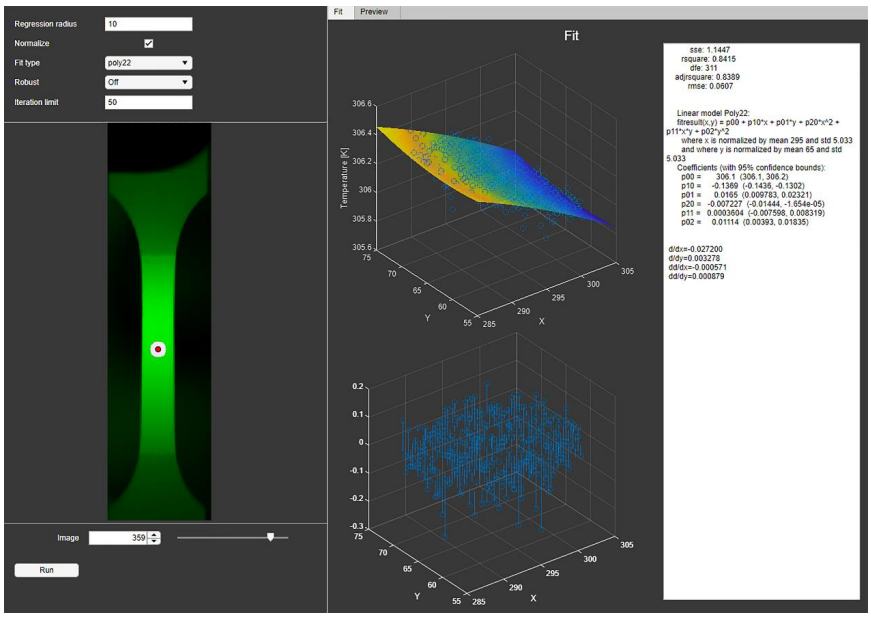

Figure S5. A screenshot illustrating the local smoothing/regression procedure for IRT images; ROI around the selected point is marked by the white circle; the approximation surface is shown in the upper-right image while the noise in the original raw IRT data is shown in the lower-right image (processing software has been developed by A. Sendrowicz)

The filtered temperature distribution in the region of interest for the specimen Cu-20Zn is illustrated in Figure S6. The whole video showing the evolution of temperature with strain can be found in Supplementary Video 1.

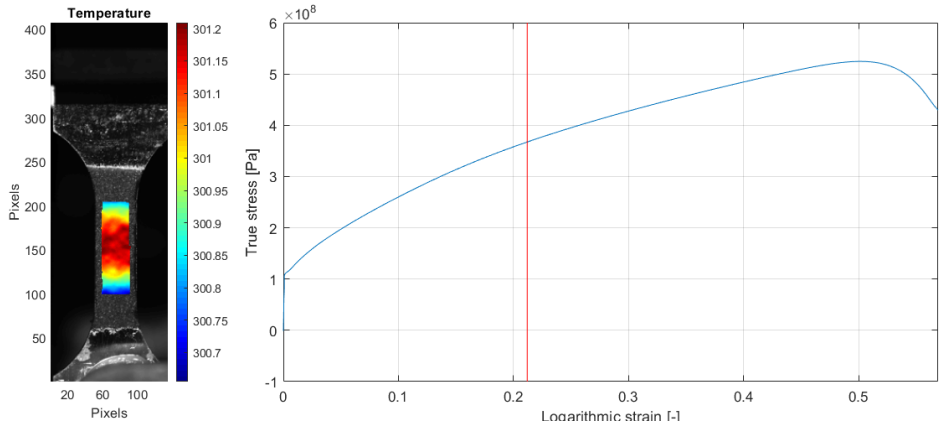

Figure S6. A fragment of the video showing the temperature distribution in ROI (highlighted in the lefthand side image of the specimen) for Cu-20Zn under tension with the nominal strain rate of 3×10^{-2} s^{-1}. The vertical line indicates the strain corresponding to the IRT image.

Note 4. Staking fault energy of Cu-Zn alloys.

Gallagher [2, 3] related the SFE to the electron/atom (e/a) ratio in copper alloys and arrived at the following expression, which links the concentration of solutes with the SFE value in copper solid solutions:

$$\ln\left(\frac{\gamma_{SFE}}{\gamma_{SFE\_Cu}}\right) = K_C\left(\frac{c}{1+c}\right)^2 \quad (1)$$

where γ_{SFE_Cu} denotes the SFE of the solvent metal (copper), c is the ratio $c = C / C_{max}$, with C - the concentration of solute atoms and C_{max} - the solubility limit at high temperature, and K_C is a constant for a given alloy system. One can see, Figure S7b, that this empiric relation fits the experimental data used for the alloys in the present study very well.

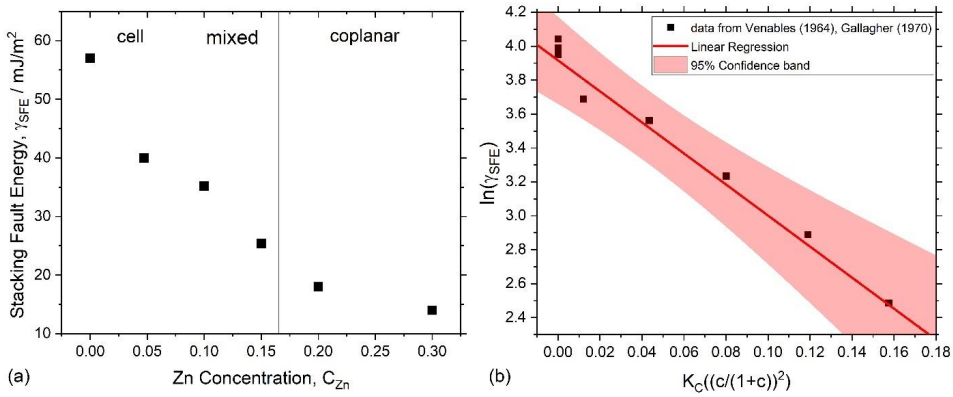

Figure S7. Stacking fault energy as a function of the concentration of solute atoms in Cu-Zn alloys (data from [2, 3], see also [4, 5]).

Note 5. Microstructure of the alloy Cu-30Zn

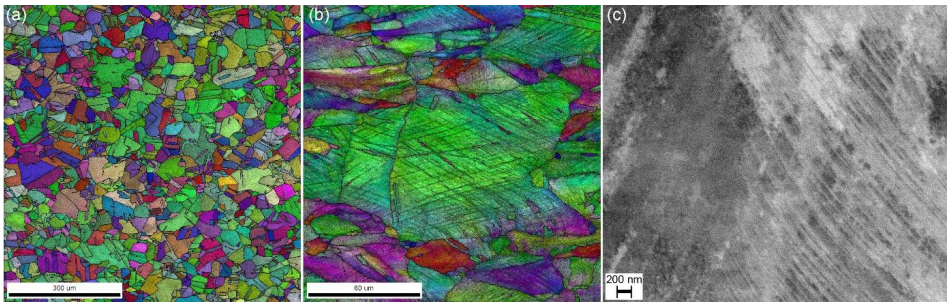

Figure S8. Initial annealed microstructure (a) and typical deformation microstructure of the alloy Cu-30Zn tested at 3×10^{-2} s^{-1} nominal strain rate: (a,b) EBSD maps in the IPF colours superimposed with the grey-scale IQ maps, and (c) ECCI micrograph revealing the dislocation microstructure at higher magnification

The planarity of dislocation arrangement in this low stacking fault energy alloy after deformation is evident in the micrographs taken from the uniformly elongated region of the gauge part of the specimen.

Note 6. Stress-strain curves and strain hardening curves for Cu-Zn alloys

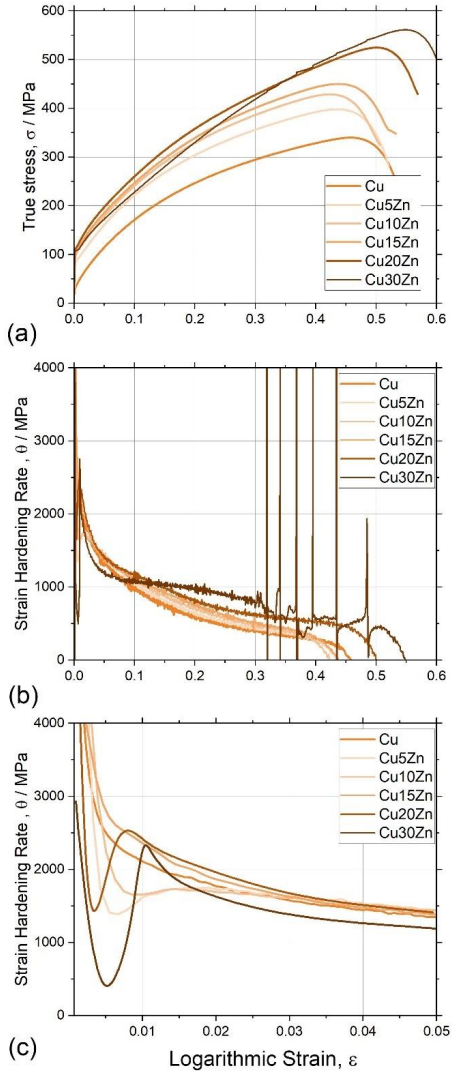

Figure S9. True stress vs true (logarithmic) strain curves (a), strain hardening rate (b) and its fragment (c) corresponding to the onset of yielding and Lüders band propagation in Cu-Zn alloys tested in tension with the nominal strain rate of $3x10^{-2}$ s^{-1}.

The strains and strain rates were estimated by using DIC mapping and measuring local displacements between two subsequent optical images of the deforming specimen, followed by calculations of local strains and strain rates, which were finally averaged over the specimen's gauge part. The correpsonding strain hardening rate $\theta = d\sigma / d\varepsilon$ were obtained by the numerical five-point differentiation procedure.

Note 7. Raw AE streams for all materials tested

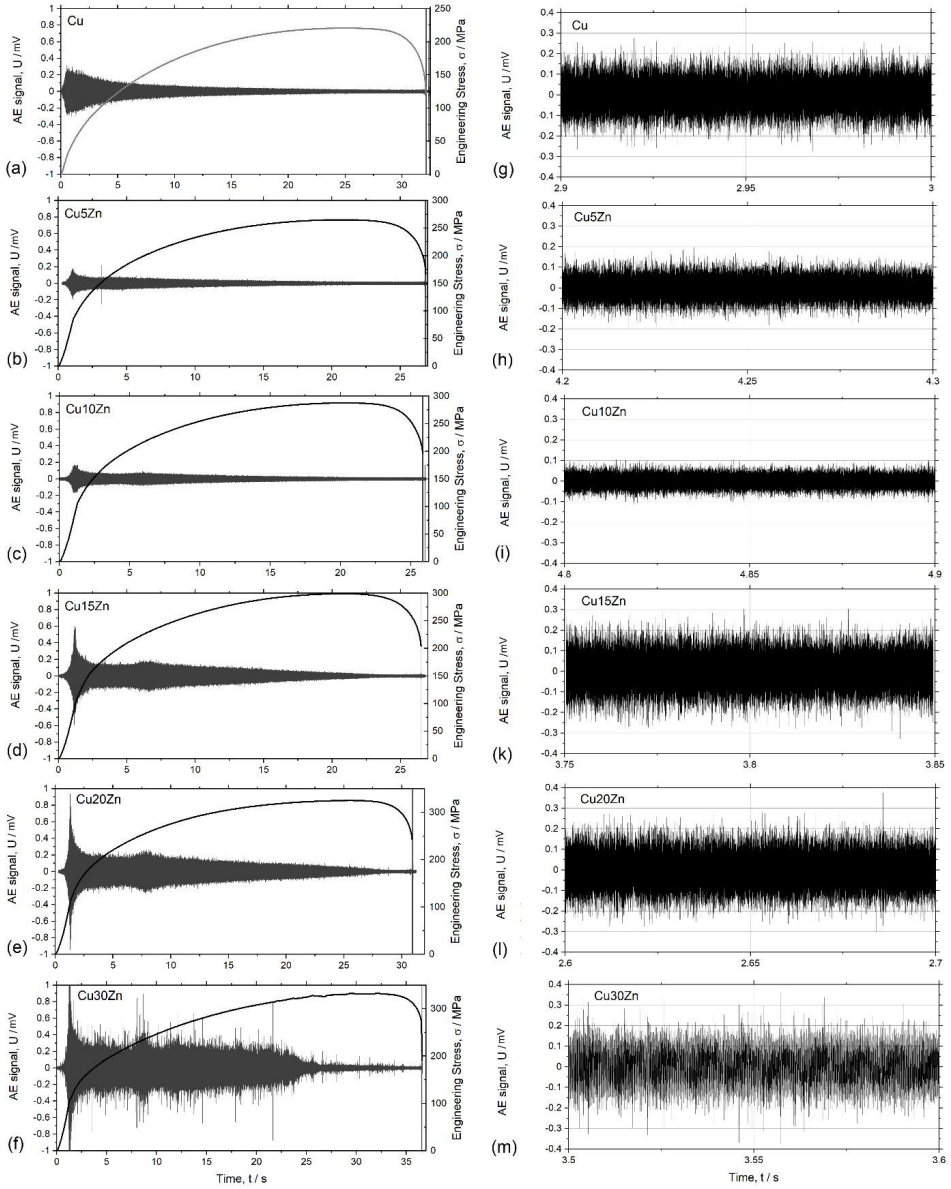

Figure S10. Raw AE streaming data superimposed with the loading curves ($\dot{\varepsilon}$ =3×10^{-2} s^{-1}) for the alloys studied (a-e) and their typical fragments highlighting the continuous nature of AE signal arising in response to dislocation motion during plastic flow.

Note 8. AE and heat energy dissipation in α-brass (Cu-30Zn)

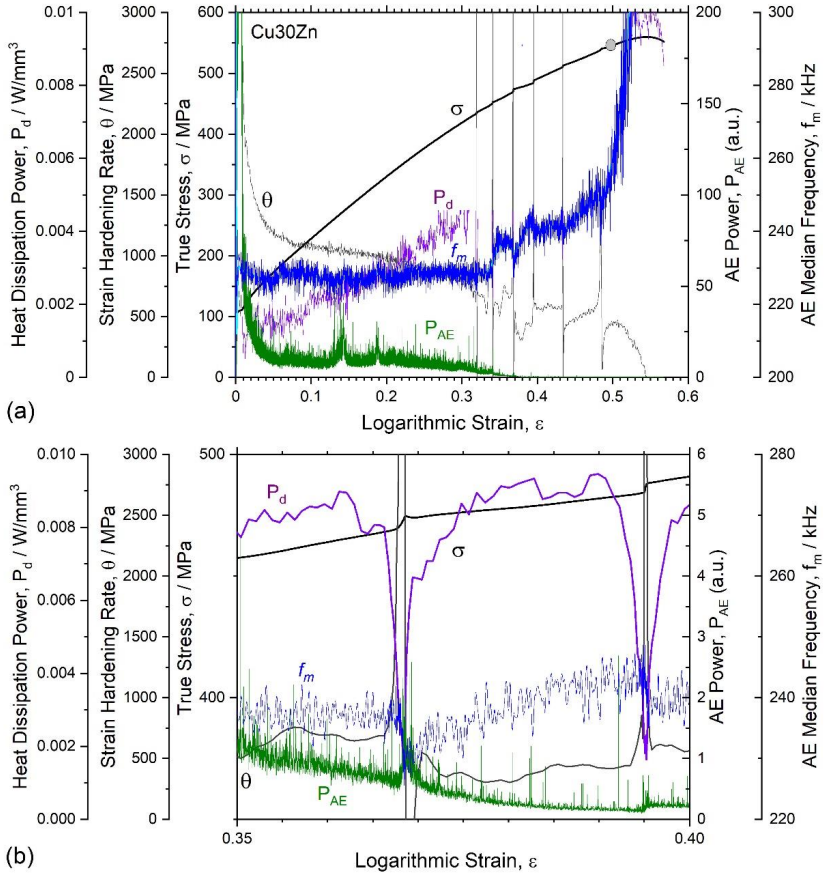

Figure S11. AE data representing the evolution the PSD function in terms of the AE power P_{AE} and median frequency $f_{|m}$ synchronised with the tensile loading curves $\sigma(\varepsilon)$ and the strain hardening rate $\theta(\varepsilon)$ in the alloy Cu-30Zn ($\dot{\varepsilon}$ =3×10^{-2} s^{-1}).

The present results agree well wit the results reported for the similar Cu-30Zn alloy in [6]. AE appears as a smooth continuous random process even during the intermittent plastic flow at the strain rates used in the present work . No significant transient AE signals have been observed at different time scales. There is a strong correlation between the AE power and the median frequency during the intermittent plastic flow stage - local maxima of AE signal are accompanied by considerable drops in the median frequency and the overall heat dissipation due to strain localisation in PLC (Portevin-Le Chatelier) bands. Thus, as a common signature of plastic instabilities, the AE power spectral density function systematically shifts to lower frequencies during the development of propagating fronts of localised deformation. This shift serves as a clear indicator of the increasing correlation in dislocation dynamics.

Note 9. On the nature of the second AE peak.

The DIC measurements undoubtedly reveal that beyond the yield point followed by the nucleation of the initial Lüders band propagating from one edge of the specimen to the other, plastic deformation keeps evolving inhomogeneously across the gauge part of the specimen. This is convincingly evidenced by the images obtained from the DIC analysis applied to consecutive frames of videos captured during the tensile deformation of the specimens, Figure S12. Figures S12a and b illustrate the typically observed distribution of local strain rates in the alloy Cu-10Zn (or quantitatively through the behaviour of the strain rate variance as a function of strain; not shown here for brevity). The DIC maps are synchronised with the loading and AE history and correspond to two different strains randomly chosen at the beginning of the strain hardening stage, marked by the vertical lines on the $\sigma(\varepsilon)$ and AE diagrams. Similar behaviour is noticed for all alloys tested in the present work. Furthermore, the fluctuating deformation front determined at 0.2% plastic strain tends to propagate through the undeformed shoulder part of the specimen as is illustrated on the strain distribution map in Fig. S12c (the propagating plastic front is marked by colour lines near the lower shoulder part of the specimen; the colour – pink, red, green – corresponds to different strains indicated on the righthand side of Fig. S12c by vertical lines coloured in the same way.

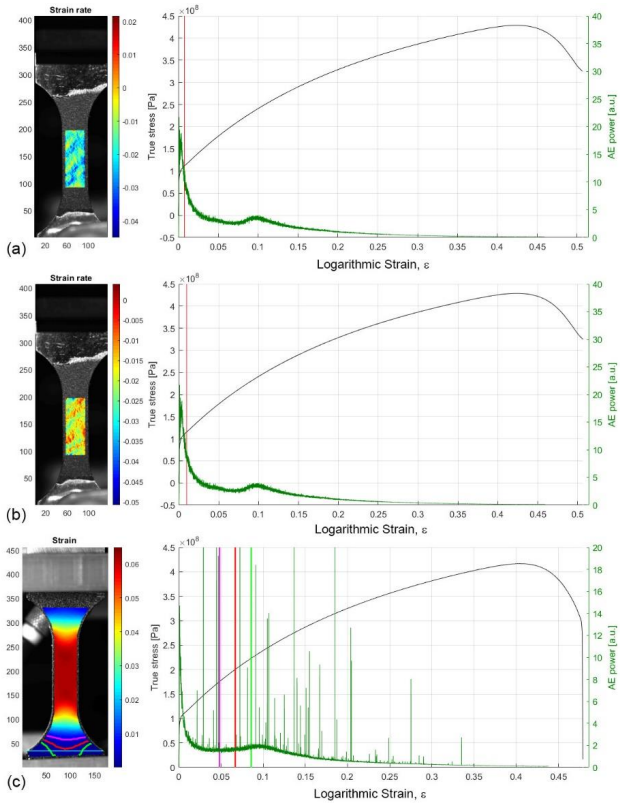

Figure S12. DIC images (left-hand side) corresponding to the synchronised loading and AE diagrams (right-hand side) with the vertical lines marking the average true (logarithmic) strain at which the snapshots were taken.

Note 10. Data on the stored energy for pure Cu compiled from the literature survey.

Figure S13 compiles the results of several relevant early works by different authors *[7-11]*, representing E_s as a function of the square flow stress for pure copper. Despite the difference in experimental setups, equipment and calculation methods used by different investigators, the observed linearity between E_s and σ^2 is apparently the most prominent and common result that is plausibly explained by the proposed model throuth the derived equation $E_s(\sigma)=\frac{\tilde{\varepsilon}}{2\sigma_S}(\sigma-\sigma_0)^2$ (Eq.**Feil! Fant ikke referansekilden.** in the main text).

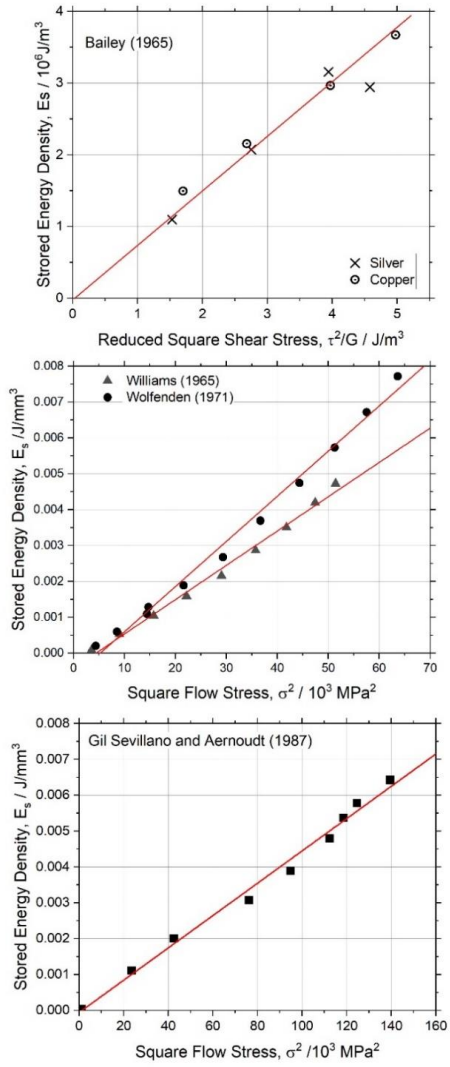

Figure S13. Experimental data showing the stored energy as a function of true strain for pure copper; the data adapted from [7, 8] *(a), [9] and [10] (b), and [11] (c).*

Supplementary References

[1] A. Sendrowicz, A.O. Myhre, S.W. Wierdak, A. Vinogradov, Applied Sciences, 11 (2021) 6718.
[2] P.C.J. Gallagher, Metallurgical Transactions, 1 (1970) 2429-2461.
[3] P.G.J. Gallagher, Y.C. Liu, Acta Metallurgica, 17 (1969) 127-137.
[4] J.A. Venables, Philosophical Magazine, 6 (1961) 379-396.
[5] J.A. Venables, Journal of Physics and Chemistry of Solids, 25 (1964) 693-700.
[6] A. Vinogradov, A. Lazarev, Scripta Materialia, 66 (2012) 745-748.
[7] J.E. Bailey, Philosophical Magazine, 8 (1963) 223-236.
[8] J.E. Bailey, P.B. Hirsch, Philosophical Magazine, 5 (1960) 485-497.
[9] R.O. Williams, Acta Metallurgica, 9 (1961) 949-957.
[10] A. Wolfenden, Acta Metallurgica, 19 (1971) 1373-1377.
[11] J. Gil Sevillano, E. Aernoudt, Materials Science and Engineering, 86 (1987) 35-51.

ISBN 978-82-326-6591-4 (printed ver.)
ISBN 978-82-326-6272-2 (electronic ver.)
ISSN 1503-8181 (printed ver.)
ISSN 2703-8084 (online ver.)

NTNU

Norwegian University of
Science and Technology